UNIVERSIDADE FEDERAL DO CEARÁ
CENTRO DE TECNOLOGIA
DEPARTAMENTO DE ENGENHARIA DE TELEINFORMÁTICA
PROGRAMA DE PÓS-GRADUAÇÃO EM ENGENHARIA DE TELEINFORMÁTICA

DISSERTAÇÃO DE MESTRADO

MULTI-USER RECEIVER PROCESSING FOR INTER-CELL INTERFERENCE REDUCTION IN PUCCH LTE

Author:

Ícaro Leonardo Jerônimo da Silva

Advisor:

Francisco Rodrigo Porto Cavalvanti
Co-advisors:

André Lima Férrer de Almeida and Robert Baldemair

Dissertação apresentada à Coordenação do Programa de Pós-Graduação em Engenharia de Teleinformática da Universidade Federal do Ceará como parte dos requisitos exigidos para obtenção do grau de Mestre em Engenharia de Teleinformática.

Fortaleza–Ceará
Novembro–2009

Acronyms

3GPP	3rd. Generation Partnership Project
PSK	Phase-Shift Keying
BPSK	Binary Phase-Shift Keying
2G	Second Generation
3G	Third Generation
4G	Fourth Generation
AD	analog-to-digital
ACK	Acknowledgement
ALS	Alternating Least Squares
LS	Least Squares
ARQ	Automatic Repeat Request
AWGN	Additive White Gaussian Noise
BER	Bit Error Rate
BLAST	Bell Labs Layered Space-Time

BLER	Block Error Rate
CDMA	Code-Division Multiple Access
CoMP	Cooperative Multi-Point
CONFAC	Constrained PARAFAC
CP	Cyclic Prefix
CQI	Channel Quality Indication
CRC	Cyclic Redundancy Check
CSI	Channel State Information
IDFT	Inverse DFT
DFT	Discrete Fourier Transform
DA	Data-aided
DFTS-OFDM	DFT-spread OFDM
DL	Downlink
DS	Data Signal
DL-SCH	Downlink Shared Channel
DRS	Demodulation Reference Signals
DS-CDMA	Direct-Sequence CDMA
E-UTRA	Evolved Universal Terrestrial Radio Access
FD	Frequency-domain
FDMA	Frequency Division Multiple Access
FEC	Forward Error Correction
FER	Frame Error Rate
FFT	Fast Fourier Transform
GSM	Global System for Mobile Communications

GPRS	Global Packet Radio Services
GTEL	Wireless Telecommunications Research Group
HARQ	Hybrid Automatic Repeat Request
HSDPA	High Speed Downlink Packet Access
HSUPA	High Speed Uplink Packet Access
HSPA	High Speed Packet Access
IMT	International Mobile Telecommunications
IMT-2000	International Mobile Telecommunications - 2000
IFFT	Inverse Fast Fourier Transform
ICI	inter-carrier interference
IP	Internet Protocol
ISI	Inter Symbol Interference
ITU	International Telecommunication Union
LTE	Long Term Evolution
MAC	Medium Access Control
MSE	Mean-Squared-Error
MMSE	Minimum-Mean-Squared-Error
MIMO	Multiple Input Multiple Output
MRC	Maximal Ratio Combining
ML	Maximum Likelihood
NACK	Negative Acknowledgement
OFDM	Orthogonal Frequency Division Multiplexing
OFDMA	Orthogonal Frequency Division Multiple Access
OSI	Open Systems Interconnection

PARAFAC	Parallel Factor Analysis
PAPR	Peak-to-Average Power Ratio
PRB	Physical Resource Block
PDCP	Packet Data Convergence Protocol
PHY	Physical Layer
PMI	Precoding Matrix Indication
PUCCH	Physical Uplink Control Channel
PUSCH	Physical Uplink Shared Channel
QAM	Quadrature Amplitude Modulation
QPSK	Quadrature Phase Shift Key
QoS	Quality of Service
RAN	Radio Access Network
RF	Radio Frequency
RI	Rank Indication
RM	Rate Maximization
RS	Reference Symbol
SINR	Signal-to-Interference plus Noise Ratio
SAE	System Architecture Evolution
SORTD	Space Orthogonal-Resource Transmit Diversity
SC-FDMA	Single Carrier FDMA
SC-OFDM	Single Carrier OFDM
SM	Spatial Multiplexing
SMS	Short Message Service
SNR	Signal-to-Noise Ratio

SINR	Signal-to-Interference plus Noise Ratio
SMS	Short Message Service
STBC	Space-Time Block Code
SFBC	Space-Frequency Block Code
STP	Space-Time Precoding
SVD	Singular Value Decomposition
TSTP	Tensor-based Space-Time Precoding
TD	Time-domain
TDL	Tapped Delay Line
TSG	Technical Specification Group
UE	User Equipment
UL	Uplink
UL-SCH	Uplink Shared Channel
UMTS	Universal Mobile Telecommunications System
UTRA	UMTS Terrestrial Radio Access
UTRAN	UMTS Terrestrial Radio Access Network
V-BLAST	Vertical Bell Labs Layered Space-Time
ZF	Zero Forcing receiver
WCDMA	Wideband CDMA
RLC	Radio Link Control
TREP-1	Tensor-based Receiver for PUCCH Format 1
TREP-2	Tensor-based Receiver for PUCCH Format 2
MMSE	Minimum Mean Square Error
ZF	Zero-Forcing

Notation

In this thesis the following conventions are used. Scalar variables are denoted by lower-case letters ($a, b, \ldots, \alpha, \beta, \ldots$), vectors are written as boldface lower-case letters ($\mathbf{a}, \mathbf{b}, \ldots, \boldsymbol{\alpha}, \boldsymbol{\beta}, \ldots$), matrices correspond to boldface capitals ($\mathbf{A}, \mathbf{B}, \ldots$), and tensors are written as calligraphic letters ($\mathcal{A}, \mathcal{B}, \ldots$). The meaning of the following symbols are, if nothing else is explicitly stated:

$\mathbb{C}$	set of complex-valued numbers
$\mathbb{C}^I$	set of complex-valued I-dimensional vectors
$\mathbb{C}^{I \times J}$	set of complex-valued $(I \times J)$-matrices
$\mathbb{C}^{I_1 \times \cdots \times I_N}$	set of complex-valued $(I_1 \times \cdots \times I_N)$-tensors
a^*	complex conjugate of $a \in \mathbb{C}$
$\lvert\mathbf{a}\rvert$	modulus of $\mathbf{a}$
$\lVert\mathbf{a}\rVert_1$	l-1 norm of $\mathbf{a}$
$\lVert\mathbf{a}\rVert$	l-2 norm of $\mathbf{a}$
$\mathbf{A}^T$	transpose of $\mathbf{A}$
$\mathbf{A}^H$	Hermitian transpose of $\mathbf{A}$
$\mathbf{A}^{-1}$	inverse of $\mathbf{A}$
$\mathbf{A}^\dagger$	Moore-Penrose pseudo-inverse of $\mathbf{A}$
$\lVert\mathbf{A}\rVert_F$ ($\lVert\mathcal{A}\rVert_F$)	Frobenius norm of $\mathbf{A}(\mathcal{A})$
$\mathbf{1}_N$	"All-ones" vector of dimension N.
$\mathbf{I}_N$	Identity matrix of dimension N.

$\mathbf{e}_n^{(N)}$	n-th canonical vector in $\mathbb{R}^N$, i.e. a unitary vector containing an element equal to 1 in its n-th position and 0's elsewhere.
$E^{(N)} = \{\mathbf{e}_1^{(N)}, \ldots, \mathbf{e}_N^{(N)}\}$	Canonical basis in $\mathbb{R}^N$.
$[\mathbf{A}]_{i_1,i_2} = a_{i_1,i_2}$	(i_1, i_2)-th element of matrix $\mathbf{A} \in \mathbb{C}^{I_1 \times I_2}$.
$[\mathbf{A}]_{i_1 \cdot}$ ($[\mathbf{A}]_{\cdot i_2}$)	i_1-th row (i_2-th column) of $\mathbf{A}$.
$[\mathcal{A}]_{i_1,i_2,i_3} = a_{i_1,i_2,i_3}$	(i_1, i_2, i_3)-th element of tensor $\mathcal{A}$.
$\mathbf{A}_{i_1 \cdot \cdot} \in \mathbb{C}^{I_2 \times I_3}$	i_1-th first-mode matrix-slice of tensor $\mathcal{A}$.
$\mathbf{A}_{\cdot i_2 \cdot} \in \mathbb{C}^{I_3 \times I_1}$	i_2-th second-mode matrix-slice of tensor $\mathcal{A}$.
$\mathbf{A}_{\cdot \cdot i_3} \in \mathbb{C}^{I_1 \times I_2}$	i_3-th third-mode matrix-slice of tensor $\mathcal{A}$.
$\mathbf{a} \circ \mathbf{b}$	Outer product between $\mathbf{a} \in \mathbb{C}^{I_1}$ and $\mathbf{b} \in \mathbb{C}^{I_2}$. $\mathbf{a} \circ \mathbf{b} = \begin{bmatrix} a_1 b_1 & \cdots & a_1 b_{I_2} \\ \vdots & & \vdots \\ a_{I_1} b_1 & \cdots & a_{I_1} b_{I_2} \end{bmatrix} \in \mathbb{C}^{I_1 \times I_2}$.
$\mathbf{A} \otimes \mathbf{B}$	The Kronecker product of $\mathbf{A} \in \mathbb{C}^{I \times J}$ with $\mathbf{B} \in \mathbb{C}^{K \times L}$, $\mathbf{A} \otimes \mathbf{B} = \begin{bmatrix} a_{1,1}\mathbf{B} & a_{1,2}\mathbf{B} & \cdots & a_{1,J}\mathbf{B} \\ a_{2,1}\mathbf{B} & a_{2,2}\mathbf{B} & \cdots & a_{2,J}\mathbf{B} \\ \vdots & \vdots & & \vdots \\ a_{I,1}\mathbf{B} & a_{I,2}\mathbf{B} & \cdots & a_{I,J}\mathbf{B} \end{bmatrix} \in \mathbb{C}^{IK \times JL}$.
$\mathbf{A} \diamond \mathbf{B}$	The Khatri-Rao (column-wise Kronecker) product. For $\mathbf{A} \in \mathbb{C}^{I \times K}$ and $\mathbf{B} \in \mathbb{C}^{J \times K}$, $\mathbf{A} \diamond \mathbf{B} = [\mathbf{A}_{\cdot 1} \otimes \mathbf{B}_{\cdot 1},\ \ldots,\ \mathbf{A}_{\cdot K} \otimes \mathbf{B}_{\cdot K}] \in \mathbb{C}^{IJ \times K}$.
$\text{vec}(\mathbf{A})$	The vectorization operator. For $\mathbf{A} \in \mathbb{C}^{I \times J}$: $\text{vec}(\mathbf{A}) = \begin{bmatrix} \mathbf{A}_{\cdot 1} \\ \vdots \\ \mathbf{A}_{\cdot J} \end{bmatrix} \in \mathbb{C}^{IJ}$.
$\text{diag}(\mathbf{a})$	Diagonal matrix with diagonal entries given by the elements of $\mathbf{a}$.

Contents

List of Figures

List of Tables

Introduction

Motivation

In the past few years, developing wireless system has become very complex task undertaken by global standards-developing organizations such as the 3rd. Generation Partnership Project (3GPP). While in the begginning of the 1980s the first analog wireless systems[1] have been deployed to support basically traditional telephony services like voice, nowadays a range of new data-based services became possible with the advent of the Third Generation (3G) [1, 2].

A lot of research has been deployed over the years to handle the 3G a reality, even after it has been deployed in practice, being the standardization an ongoing process. In 2002, with the advent of High Speed Packet Access (HSPA) system, the radio access defined by 3GPP, so-called UMTS Terrestrial Radio Access (UTRA), goes beyond the definition of 3G mobile system and also encompasses broadband mobile data, starting a new reality in mobile communications[2].

The lastest step being studied and developed in 3GPP is an evolution of 3G into

[1] They were the analog NMT system (*Nordic Mobile Telephony*) and AMPS (*Advanced Mobile Phone Service*).

[2] The 3G radio access development is today handled in 3GPP, however its initial steps were taken in the early 1990s, long before 3GPP was formed.

an evolved radio access network referred to as *Long-Term Evolution* (LTE) and an evolved packet access core network in the *System Architecture Evolution* (SAE) specified in Release 8 [3]. By 2010-2011, Long Term Evolution (LTE) and System Architecture Evolution (SAE) are expected to be first deployed, however, 3GPP continues to evolve LTE towards LTE Advanced (to be appeared in Release 10). It is worth pointing out that the research advances on cellular areas (i.e. advanced signal processing tools, new access technologies) influence continuously the design choice of LTE [1, 2].

Physical Uplink Control Channel (PUCCH) LTE

In LTE Release 8, physical uplink control channel PUCCH carries some control signals fed back to the eNodeB. It consists of two basic transmission formats, i.e. Format 1 and Format 2, carrying some control signals fed back to eNodeB, e.g. ACK/NACK related to downlink data transmission packets and channel-status reports for downlink channel-dependent scheduling.

In both PUCCH formats, the User Equipment (UE)s are multiplexed with the aid of frequency-domain orthogonal codes working as a Code Division Multiplexing (CDM) scheme in a portion of the uplink bandwidth. The codes are composed by a cell-specific base sequences that are made orthogonal within the same cell through a UE-specific phase rotation.

In single-cell scenarios, the sequences can be made completely orthogonal, and, conventional receivers based on Maximal Ratio Combining (MRC) can perfectly cancel the intra-cell interference. However, in multi-cell scenarios, conventional receivers do not completely cancel the inter-cell interference, as the cell-specific base sequences have a non-null mutual correlation. This remaining interference can significantly degrade the performance of terminals in the cell edge.

An issue in order to reduce this inter-cell interference is to consider interference randomization techniques [4, **?**]. However, we propose to improve the performance of PUCCH LTE reducing the inter-cell interference at the receiver side.

Objectives

The primary objective of this master thesis is to conceive a multi-user receiver for inter-cell interference reduction in PUCCH LTE. In order to justify that our proposal can be implemented in LTE eNodeBs, the receiver must include the

following features:

- It must be applicable for PUCCH Format 1 and PUCCH Format 2
- It must work in both single-cell and multi-cell scenarios
- It must be configurable to a conventional LTE setting, where the neighboring eNodeBs only exchange mobile management information
- It must be scalable in case the eNodeB is equipped with more than 2 receive antennas [3]

In addition to these features, it is suitable that the proposed receiver is scalable in case i) a variable number of terminals are equipped with multiple transmit antennas and ii) the network is configurable to Cooperative Multi-Point (CoMP), where neighboring eNodeBs (or the access points) exchange some additional network information.

Methodology

The alternative we propose in this thesis is to reduce the inter-cell interference at the receiver side using some advanced signal processing technique. Then, we resort to the tensor modeling approach, proposed in a seminal work to blind multi-user detection in multi-antenna Code-Division Multiple Access (CDMA) systems [5].

Once the model is posed, a tensor estimation algorithm based on successive least squares problems can be applied so that channel estimation and signal separation are improved at each iteration. The interest of considering tensor models to solve this problem, relies on its inherent uniqueness when some mild conditions concerning the system parameters are respected [5]. In this case, the performance of PUCCH can be improved at each iteration as the convergence of the algorithm is guaranteed. Furthermore, the algorithm can be applied in a semi-blind configurations, which is one of the requirements that must be fulfilled.

In the following, we summarize the steps we have followed in order to accomplish the proof of concept concerning the proposed receiver. Concerning PUCCH Format 2 we have:

[3]The eNodeBs are typically equipped with two receive antennas.

1. Modeling the baseband transmission on PUCCH Format 2 using the classical Parallel Factor Analysis (PARAFAC) tensor model
2. Application of a tensor estimation algorithm to improve the channel estimation and separate the multiple signals
3. Evaluation of the channel estimation accuracy and the algorithm convergence
4. Analyze the impact of the uniqueness conditions of the PARAFAC model
5. Performance evaluation of PUCCH Format 2 in the single-cell
6. Performance evaluation of PUCCH Format 2 in multi-cell scenarios for both configurations: conventional LTE setting and LTE CoMP

Concerning PUCCH Format 1 we have the following steps:

1. Conception of a new tensor model to fit the baseband transmission PUCCH Format 1
2. Extension of the tensor estimation algorithm to this proposed tensor model
3. Application of this new algorithm to improve the channel estimation and separate the multiple signals
4. Evaluation of the channel estimation accuracy and the algorithm convergence
5. Derivation of the uniqueness conditions of this new tensor model and analyze the impact in the proposed application
6. Evaluation the performance improvements of PUCCH Format 1 in the single-cell
7. Evaluation the performance improvements of PUCCH Format 1 in multi-cell scenarios for both configurations: conventional LTE setting and LTE CoMP

Scientific production

Throughout the master thesis course, we have published some scientific contributions some of them concerning directly the subject of this thesis.

A United States provisional patent of a version of the proposed receiver was filled with the following information:

- *Multi-User Receiver for Inter-Cell Interference Reduction in PUCCH LTE*, **I. L. J. da Silva**, R. Baldemair, A. L. F. de Almeida, S. Falahati, F. R. P. Cavalcanti. Registration Date: 2009-1-12, Registration number: 61/265, 463.

A list with conference publications follows below:

- *Improved Data-Aided Channel Estimation in LTE PUCCH Using a Tensor Modeling Approach*; **I. L. J. da Silva**, A. L. F. de Almeida, F. R. P. Cavalcanti, R. Baldemair, S. Falahati. Submitted to the IEEE International Conference on Communications (ICC'2010), Cape Town-South Africa, June 2010;

- *Tensor Decompositions and Applications in Wireless Communication Systems*; **I. L. J. da Silva**, A. L. F. de Almeida, Joo C. M. Mota. Tutorial presented at the 27th Brazilian Symposium on Communications (SBrT'09), Blumenau-Brazil, September 2009;

- *Tensor-Based Precoding With Blind MIMO Channel Estimation and Transmit Antenna Selection*; **I. L. J. da Silva**, A. L. F. de Almeida, F. R. P. Cavalcanti. Proc. IEEE Workshop on Signal Processing Advances in Wireless Communications (SPAWC'08), Recife-Brazil, July 2008;

We also have produced the following book chapter:

- *MIMO Transceiver Design for Enhanced Performance Under Limited Feedback*; **I. L. J. da Silva**, A. L. F. de Almeida, F. R. P. Cavalcanti., G. Favier. Chapter 12. In F. R. P. Cavalcanti, Sören Andersson. (Eds.), Optimizing Wireless Communication Systems, ISBN: 978-1-4419-0154-5, Springer, 2009.

Document Structure

The remainder of this document is organized as follows:

Chapter 1: We provide the tensor basics essential to the understanding of this work. Firstly, we show how to interpret a signal in several domains as a tensor, followed by the step by step procedure to conceive a tensor model. Hereafter, we present the classical tensor model called PARAFAC (Parallel Factor Analysis).

Chapter 2: We reviewed the most important features of the 3GPP LTE Radio Access Network (RAN), focusing at the second part in the uplink control channel PUCCH. We also present a general overview of LTE physical layer, which makes this Chapter an interesting survey about the subject.

Chapter 3: We model the baseband transmission in PUCCH Format 2 using the PARAFAC tensor approach. Taking advantage of it, we propose a multi-user receiver for inter-cell interference reduction in PUCCH LTE Format 2. We conclude the chapter presenting some preliminary results.

Chapter 4: We propose a new tensor decomposition, derived from PARAFAC, to model the baseband transmission in PUCCH Format 1. This new tensor model relies on a fixed constrained matrix that take into account the particular design of Format 1. We also propose a multi-user receiver for inter-cell interference reduction in PUCCH LTE Format 1. We conclude the chapter presenting some preliminary results.

Chapter 5: We evaluate the error performance of PUCCH LTE through simulations when the proposed tensor-based receivers are respectively applied to Format 1 and Format 2. The proposed receivers are compared to conventional ones composed by a Least Squares (LS) channel estimation (based on Reference Symbol (RS)) and MRC for data detection.

Final Remarks: We conclude the thesis showing the objectives that have been achieved. We present the perspectives about this work.

CHAPTER 1

Background on Tensors and the PARAFAC Decomposition

A tensor can be intuitively defined as an array that represents a data set in multiple domains, extrapolating the concept of vectors and matrices. In this introductory chapter we provide the tensor basics essential to the understanding of this work. Over the entire document tensor algebra is applied to model the baseband transmission on PUCCH of Third Generatin Partnership Project (3GPP) Long Term Evolution (LTE) system. We have decided to present the tensors by extending some familiar concepts from classical linear algebra to tensor algebra. Firstly, we show how to interpret a signal in several domains as a tensor, followed by the step by step procedure to conceive a tensor model. Hereafter, we present the classical tensor decomposition called PARAFAC (Parallel Factor Analysis), explaining how it can be interpreted as a generalization for tensors of the well known SVD (Singular Value Decomposition). In contrast to SVD, where there is the problem of rotational freedom, PARAFAC can be essentially unique, up to scaling and permutation indeterminacy. This interesting property is exploited later in Chapters 3 and 4, and a semi-blind receiver based on a classical tensor estimation algorithm is proposed. We conclude this chapter presenting the general structure of this algorithm.

1 Tensor Basics

1.1 Interpreting a signal as a tensor

In signal processing models a data set with N elements is commonly represented in a $N \times 1$ column *vector* $\mathbf{x}$. This vector $\mathbf{x}$ could be, e.g., the set of N samples in the time-domain of a given signal transmitted over a wireless channel. In case the received signal of the previous example is transmitted over P subcarriers, the complete data set may be organized in a $N \times P$ matrix expressed as $\mathbf{X} = [\mathbf{x}_1, \cdots, \mathbf{x}_P]$. In this example $\mathbf{X}$ is formed by the concatenation of P vectors $\mathbf{x}_p \in \mathbb{C}^{N\times 1}$. At this point, our matrix model represents a signal in two domains: time and frequency.

This practical problem illustrates the extension from a model that represents the signal in a single domain (using a vector) to a model that represents the signal in two domains (using a matrix). However, what would become our signal model if an additional domain must be taken into account (e.g., suppose a receiver equipped with K antennas)?

An alternative to this problem is to model this signal using a *tensor* of dimension $N \times P \times K$ denoted $\mathcal{X} \in \mathbb{C}^{N\times P\times K}$ since tensor models appear to be a suitable alternative to represent data in more than two domains.

Several approaches exist in the literature to define formally the term *tensor*, which depends on the scientific domain in which tensors are used. In data analysis [1], branch of linear algebra which originated the seminal applications in signal processing, a tensor is defined as a mathematical entity that enjoys the *multilinear property* after a change of coordinate system [6]. A F-th order tensor (which represents a signal in F domains) is interpreted herein as an *array* that exhibits a linear dependency with respect to F vector spaces, and of which the elements are accessed via F indices.

In this thesis, a high-order tensor is intuitively defined as an abstract mathematical structure that represents a data set in more than two domains [2], so that vectors and matrices can be seen as *first-order and second-order tensors* respectively. This

[1] Data analysis is a process of gathering, modeling, and transforming data with the goal of highlighting useful information, suggesting conclusions, and supporting decision making.

[2] A formal definition of a high-order tensor is given in the Appendix (**A.1**)

work focuses on *third-order tensors* that are usually depicted as a 3-D object. The tensor $\mathcal{X}$ of the previous example can be represented, e.g, as a parallelepiped of dimension $N \times P \times K$. These intuitive extensions are depicted in Fig. 1.1, Fig. 1.2 and Fig. 1.3.

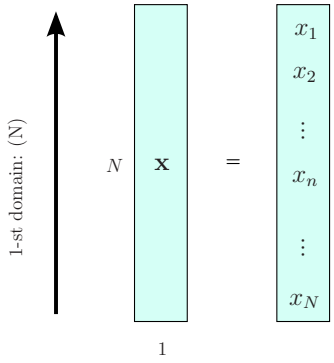

Figure 1.1: $N \times 1$ vector or first-order tensor

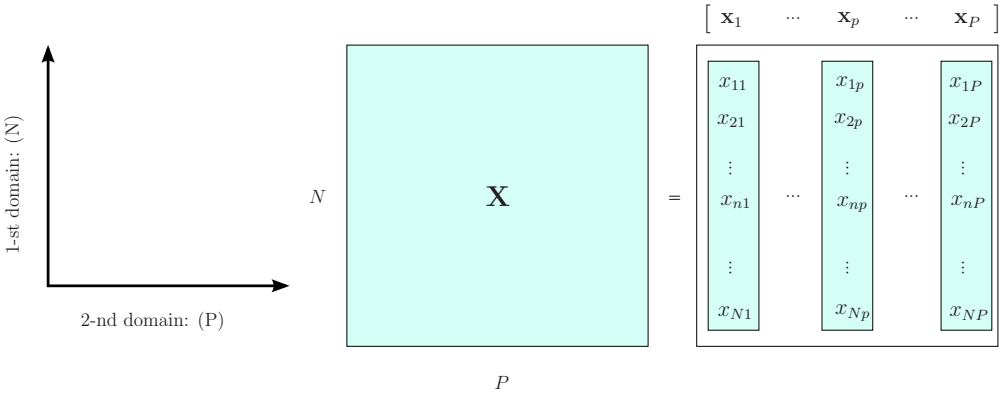

Figure 1.2: $N \times P$ matrix or second-order tensor

In the same manner a term x_n of the vector $\mathbf{x}$ is accessed through a single index n, any term $x_{n,p}$ of the matrix $\mathbf{X}$ is accessed through the two indexes n and p. Thus, any term of the third-order tensor $\mathcal{X}$ is accessed through three indexes n, p, k, as defined in the following.

Definition 1.1 (scalar notation) *Let $\mathcal{X} \in \mathbb{C}^{N \times P \times K}$ be a third-order tensor. A scalar component of $\mathcal{X}$ is specified as*

$$x_{n,p,k} = [\mathcal{X}]_{n,p,k}\,, \tag{1.1}$$

where n, p and k are associated respectively with the first, second and third domains of $\mathcal{X}$.

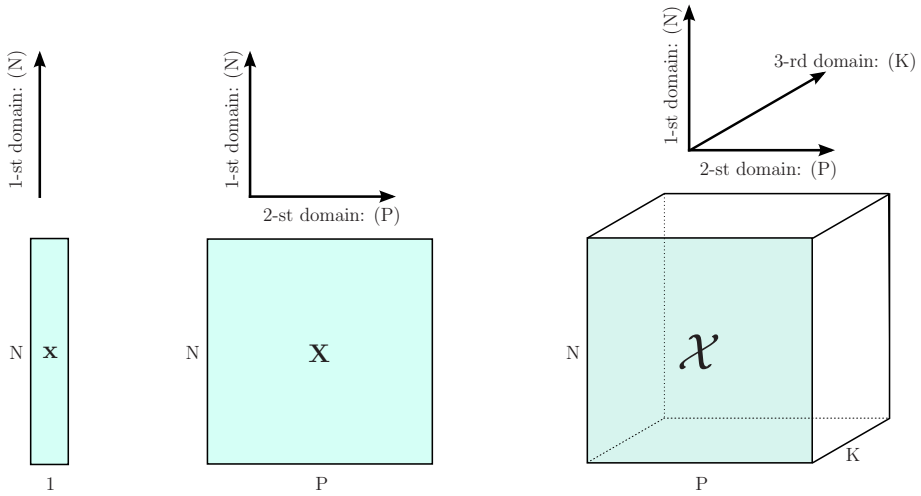

Figure 1.3: first-order tensor (vector), second-order tensor (matrix) and third-order tensor

Example 1.1 A third-order tensor $\mathcal{X}$ of dimensions $2 \times 2 \times 2$ is depicted as a cube in Fig. 1.4. The elements on the frontal surface are indexed as $x_{1,1,1} = 1$, $x_{1,2,1} = 2$, $x_{2,1,1} = 3$, $x_{2,2,1} = 4$. In the same way, the elements from the back are accessed as follows $x_{1,1,1} = 5$, $x_{1,2,1} = 6$, $x_{2,1,1} = 7$, $x_{2,2,1} = 8$.

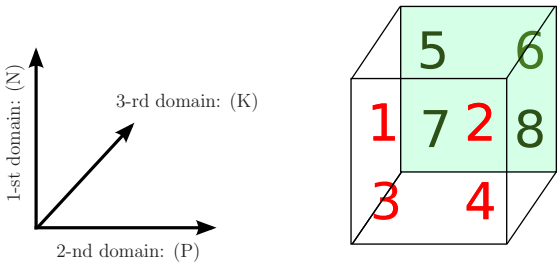

Figure 1.4

Unfolded Representations of a Tensor

Drawing a parallelepiped everytime one needs to manipulate a tensor can become a hard task. In addition, there is any geometric solid to represent tensors with order greater than three. To solve this problem we resort to the unfolded representations of a tensor, but firstly we show how this concept is employed in matrix algebra.

In Fig. 1.1, the time-domain samples ordered in the column vector $\mathbf{x} \in \mathbb{C}^{N \times 1}$ can be alternatively represented in a row vector denoted by $\mathbf{x}^{'} = \mathbf{x}^{T} \in \mathbb{C}^{1 \times N}$. Correspondingly, the matrix $\mathbf{X}$, described as a concatenation of column vectors in Fig. 1.2, can be written as a concatenation of row vectors (see Fig. 1.5). Note that

although we have these two different representations, they remain the same signal.

Extending this notion, a third-order tensor may be represented in three manners, consisting of 3 sets of ordered matrices. These matrices are so-called *slices* since each set can be viewed as a set of slices of the 3-D object that represents the tensor[3]. They are called *unfolded representations*.

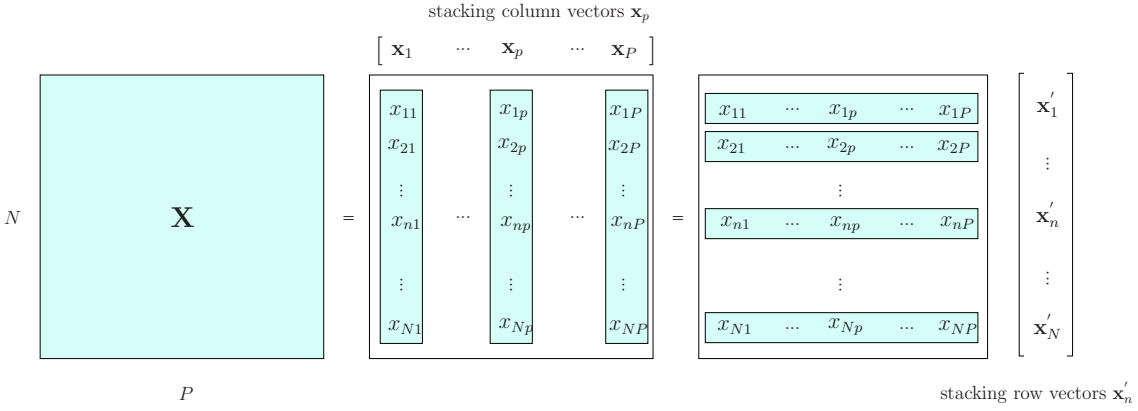

Figure 1.5: $N \times P$ matrix as a concatenation of P column vectors $N \times 1$ or N row vectors $1 \times P$

Definition 1.2 (unfolded representations) *The third-order tensor* $\mathcal{X} \in \mathbb{C}^{N \times P \times K}$ *has three matricidal representations* $\mathbf{X}_1$, $\mathbf{X}_2$ *and* $\mathbf{X}_3$ *as follows:*

$$\mathbf{X}_1 = \begin{bmatrix} X_{1..} \\ \vdots \\ X_{N..} \end{bmatrix} \in \mathbb{C}^{NP \times K},\ \mathbf{X}_2 = \begin{bmatrix} X_{.1.} \\ \vdots \\ X_{.P.} \end{bmatrix} \in \mathbb{C}^{PK \times N} \text{ and } \mathbf{X}_3 = \begin{bmatrix} X_{..1} \\ \vdots \\ X_{..K} \end{bmatrix} \in \mathbb{C}^{KN \times P}, \tag{1.2}$$

where $X_{n..} \in \mathbb{C}^{P \times K}$ *is the* n*-th slice considering the first domain fixed, and* $X_{.p.} \in \mathbb{C}^{K \times N}$ *is the* p*-th slice in the second domain, and* $X_{..k} \in \mathbb{C}^{N \times P}$ *is the* k*-th slice in the third domain.*

At this point, it must be clear that $\mathbf{X}_1, \mathbf{X}_2$ and $\mathbf{X}_3$ are not tensors, but matrices that represents the same tensor $\mathcal{X}$. The unfolded representations of $\mathcal{X}$ are depicted in Fig. 1.6.

[3]Each slice matrix of this set corresponds to the part of the data set whose its components represent the information in two domains while the other domain is fixed.

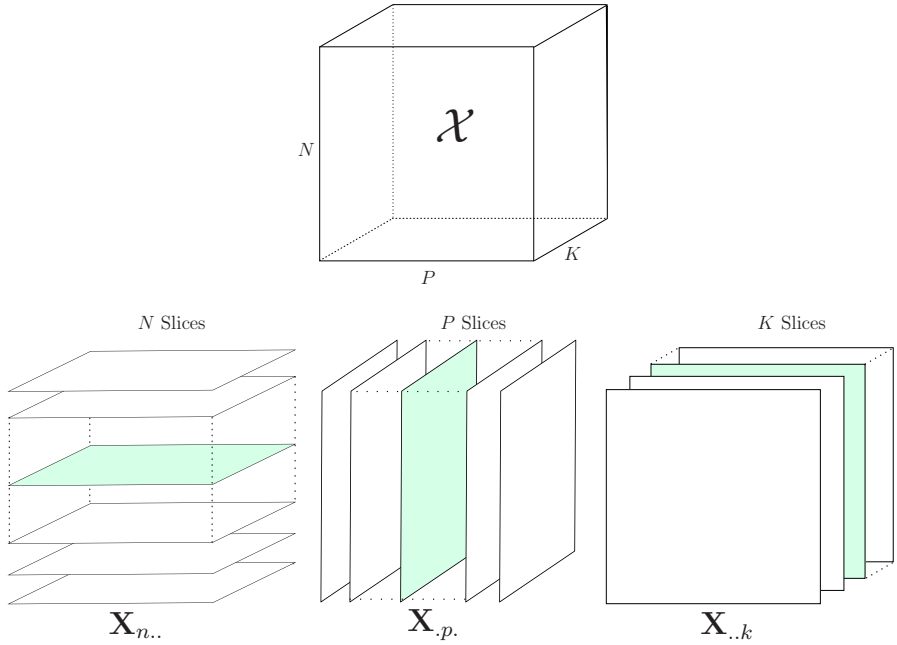

Figure 1.6: Unfolded representations of a $N \times P \times K$ third-order tensor

Example 1.2 (received signal in three domains) In this example, a signal transmitted on $P = 2$ subcarriers during $N = 2$ symbol periods is represented in a 2×2 matrix. If the receiver is equipped with K antennas are used at this receiver, the signal is written as third-order tensor of dimensions $2 \times 2 \times K$ as illustrated in Fig. 1.7

Example 1.3 (unfolded and scalar representations) In this example, we consider the tensor from the previous example where $K = 2$. The received signal is shown in the cube of Fig. 1.8, where we can see the three unfolded representations $\mathbf{X}_1$, $\mathbf{X}_2$ and $\mathbf{X}_3$.

Until this point, we have shown how to interpret a signal in 3 domains as a third-order tensor and its representations using matrices. Before proposing a tensor model, we need to understand the tensor basic operations and properties. In the following some linear algebra operations and results are generalized to tensor algebra.

1.2 Building a signal tensor

A matrix can be constructed from two vectors through the operation defined below.

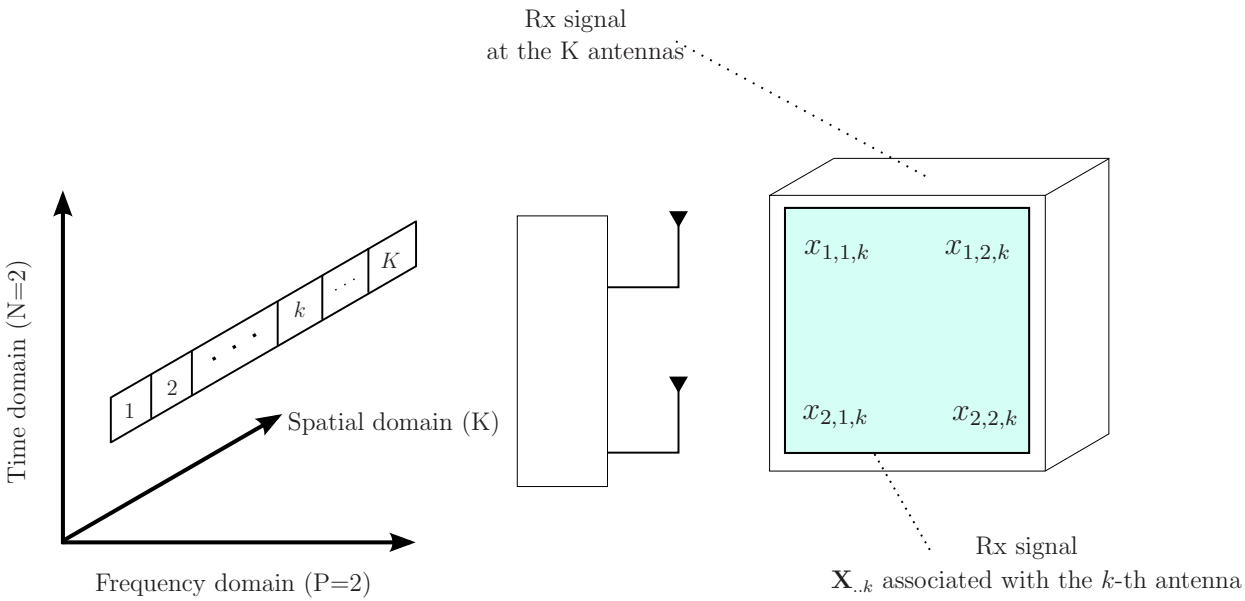

Figure 1.7: Received signal in time × frequency × spatial domains

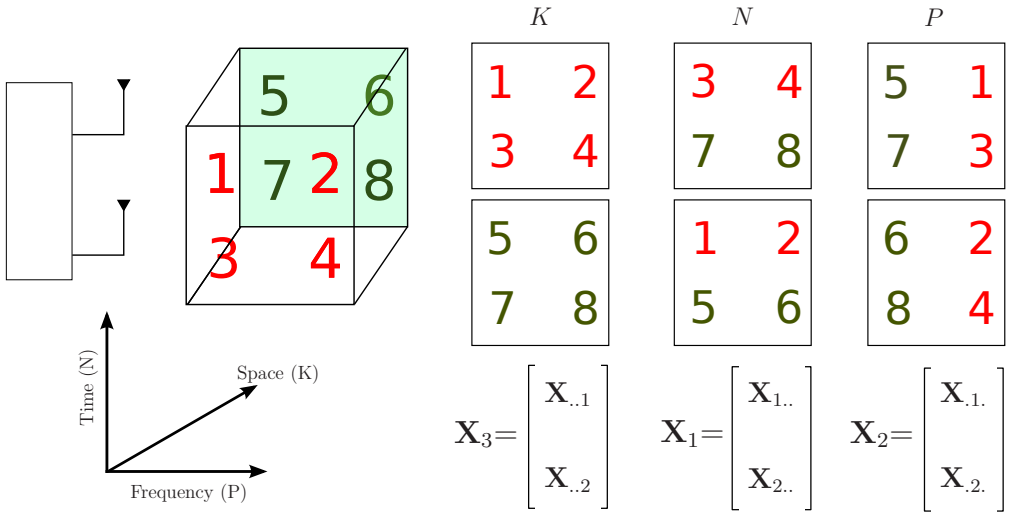

Figure 1.8: Unfolded representations of a third-order tensor on space × frequency × time

Definition 1.3 (outer product of two vectors) *Let* $\mathbf{a} \in \mathbb{C}^{N\times 1}$ *and* $\mathbf{b} \in \mathbb{C}^{P\times 1}$ *be*

two columns vectors. The outer product between $\mathbf{a}$ *and* $\mathbf{b}$ *is given by:*

$$\mathbf{a}\circ\mathbf{b} = \mathbf{a}\mathbf{b}^T = \begin{bmatrix} a_1 \\ a_2 \\ \vdots \\ a_N \end{bmatrix} \begin{bmatrix} b_1 & b_2 & \cdots & b_P \end{bmatrix} = \begin{bmatrix} a_1.b_1 & a_1.b_2 & \cdots & a_1.b_P \\ a_2.b_1 & a_2.b_2 & \cdots & a_2.b_P \\ \vdots & \vdots & \vdots & \vdots \\ a_N.b_1 & a_N.b_2 & \cdots & a_N.b_P \end{bmatrix} \in \mathbb{C}^{N\times P}$$

or in scalar notation $[\mathbf{a}\circ\mathbf{b}]_{n,p} = a_n \cdot b_p$.

Definition 1.4 (column-rank of a matrix) *Let* $\mathbf{X} \in \mathbb{C}^{N\times P}$ *be a matrix formed by stacking column vectors* $\mathbf{x}_1, \cdots, \mathbf{x}_P$ *with* $\mathbf{x}_p \in \mathbb{C}^{N\times 1}$ *written as* $\mathbf{X} = [\mathbf{x}_1 \ \cdots \ \mathbf{x}_P]$. *The column-rank of* $\mathbf{X}$*, denoted by rank(*$\mathbf{X}$*) is the maximal number of vectors* $\mathbf{x}_p$ *that are linearly independent* [4]*. If rank(*$\mathbf{X}$*)=R,* $\mathbf{X}$ *is called a rank-R matrix.*

The concept of rank is very important in linear algebra. The rank of matrix defines the smallest number of vectors that represents the subspace generated by a given matrix [7]. The result of the outer product of Def. 1.3 is a rank-one matrix since the generated column vectors are all linearly dependent. Each column can be factored as a function of vector $\mathbf{a}$, as shown in Fig. 1.9. The subspace generated by this matrix is identical to the subspace generated by the vector $\mathbf{a}$.

Property 1.1 (rank of the sum) Let $\mathbf{X}$ and $\mathbf{Y}$ two matrices with the same dimensions. Then,

$$\text{rank}\,(\mathbf{X}+\mathbf{Y}) \leq \text{rank}\,(\mathbf{X}) + \text{rank}\,(\mathbf{Y})$$

Let $\mathbf{c} \in \mathbb{C}^{N\times 1}$ and $\mathbf{d} \in \mathbb{C}^{P\times 1}$ be other two column vectors so that $\mathbf{a}, \mathbf{c}$ and $\mathbf{b}, \mathbf{d}$ are linearly independent. We define $\mathbf{X} = \mathbf{a}\circ\mathbf{b}$ and $\mathbf{Y} = \mathbf{c}\circ\mathbf{d}$ and the previous property guarantees that $\mathbf{X}+\mathbf{Y}$ is a rank-two matrix. The next example shows this property for $N = P = 2$.

Example 1.4: (constructing a rank-two matrix of dimensions 2×2) Consider the following sum of rank-one matrices

$$\mathbf{a}\circ\mathbf{b} + \mathbf{c}\circ\mathbf{d} = \begin{bmatrix} a_1 \\ a_2 \end{bmatrix} \begin{bmatrix} b_1 & b_2 \end{bmatrix} + \begin{bmatrix} c_1 \\ c_2 \end{bmatrix} \begin{bmatrix} d_1 & d_2 \end{bmatrix} \tag{1.3}$$

[4] A set of P vectors $\mathbf{x}_1, \cdots, \mathbf{x}_P$ is said linearly independent when taking out any vector $\mathbf{x}_p$ from the P vectors, it is not possible to write it as linear combination of the remaining $P-1$ vectors. Otherwise, the set is said linearly dependent.

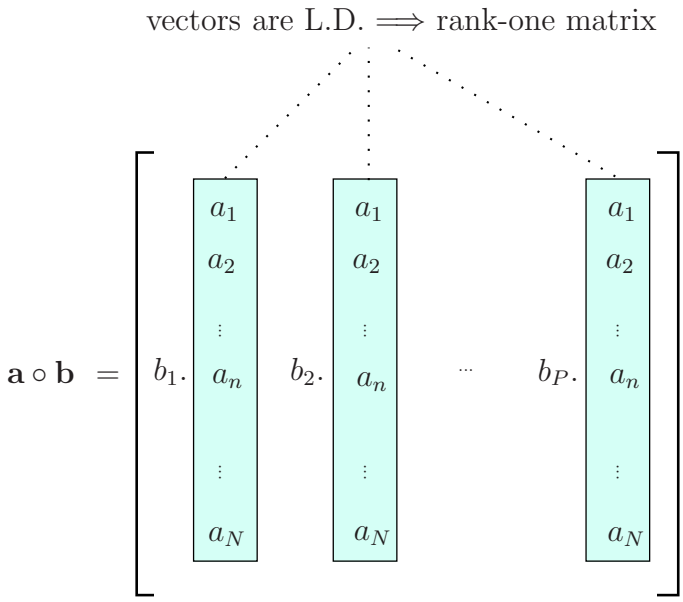

Figure 1.9: Factored representation of $\mathbf{a} \circ \mathbf{b}$

where the vectors $\mathbf{a}, \mathbf{c} \in \mathbb{C}^{2\times 1}$ and $\mathbf{b}, \mathbf{d} \in \mathbb{C}^{2\times 1}$ are linearly independent. The resulting rank-two matrix can be interpreted as the matrix that generates the subspace generated by $\mathbf{a}$ and $\mathbf{c}$.

In the data analysis, these couples of vectors $\mathbf{a}, \mathbf{c}$ and $\mathbf{b}, \mathbf{d}$ are called *parallel factors* as there is any crossed interaction, i.e., each term a_n is summed with c_n and each term b_p with d_p, as depicted in Fig. 1.10. Then, the sum of Eq.(1.3) results in:

$$\mathbf{a} \circ \mathbf{b} + \mathbf{c} \circ \mathbf{d} = \begin{bmatrix} b_1\mathbf{a} + d_1\mathbf{c} & b_2\mathbf{a} + d_2\mathbf{c} \end{bmatrix} \tag{1.4}$$

$$= \begin{bmatrix} b_1 a_1 + d_1 c_1 & b_2 a_1 + d_2 c_1 \\ b_1 a_2 + d_1 c_2 & b_2 a_2 + d_2 c_2 \end{bmatrix}. \tag{1.5}$$

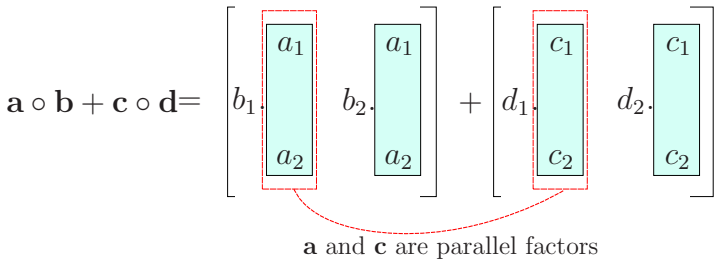

Figure 1.10

This sum of parallel factors can be alternatively written as the product of two matrices $\mathbf{A}$ and $\mathbf{B}^T$ defined as $\mathbf{A} = [\mathbf{a}\ \mathbf{c}] \in \mathbb{C}^{2\times 2}$ and $\mathbf{B} = [\mathbf{b}\ \mathbf{d}] \in \mathbb{C}^{2\times 2}$. This product is shown in Fig. 1.11, where each matrix has two parallel factors.

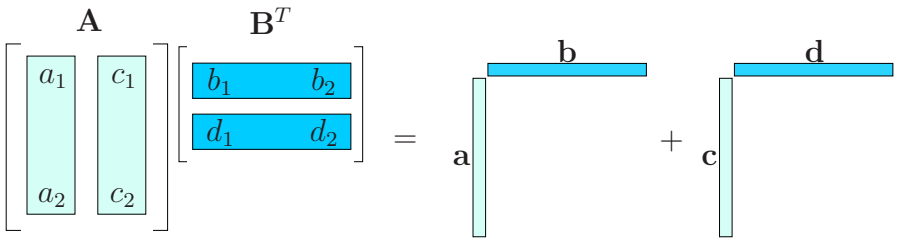

Figure 1.11

In the last example, we have shown that the sum of two rank-one matrices can be factored as the product of two matrices. This result can be generalized to the sum R rank-one matrices in the form $\mathbf{X}^{(r)} = \mathbf{a}^{(r)} \circ \mathbf{b}^{(r)}$ such a way that:

$$\mathbf{X} = \sum_{r=1}^{R} \mathbf{X}^{(r)} = \mathbf{A}\mathbf{B}^T \tag{1.6}$$

where $\mathbf{A} = [\mathbf{a}^{(1)} \cdots \mathbf{a}^{(R)}] \in \mathbb{C}^{N\times R}$ and $\mathbf{B} = [\mathbf{b}^{(1)} \cdots \mathbf{b}^{(R)}] \in \mathbb{C}^{P\times R}$ with $\mathbf{a}^{(r)} \in \mathbb{C}^{N\times 1}$ and $\mathbf{b}^{(r)} \in \mathbb{C}^{P\times 1}$.

In the following, some definitions generalizing these concepts to tensors will be presented.

Rank-one tensor

Definition 1.6 (outer product of three vectors) *Let* $\mathbf{a} \in \mathbb{C}^{N\times 1}$, $\mathbf{b} \in \mathbb{C}^{P\times 1}$ *and* $\boldsymbol{\sigma} \in \mathbb{C}^{K\times 1}$ *be three columns vectors. The outer product of* $\mathbf{a}$, $\mathbf{b}$ *and* $\boldsymbol{\sigma}$ *composes the* $N \times P \times K$ *third-order tensor given by:*

$$\mathcal{X} = \mathbf{a} \circ \mathbf{b} \circ \boldsymbol{\sigma} \tag{1.7}$$

where $[\mathcal{X}]_{n,p,k} = a_n \cdot b_p \cdot \sigma_k$.

From Def. 1.2, one of the unfolded representations of tensor (1.5) is depicted below:

$$\mathbf{X}_3 = \begin{bmatrix} \mathbf{X}_{..1} \\ \mathbf{X}_{..2} \\ \vdots \\ \mathbf{X}_{..K} \end{bmatrix} = \begin{bmatrix} \sigma_1.(\mathbf{a} \circ \mathbf{b}) \\ \sigma_2.(\mathbf{a} \circ \mathbf{b}) \\ \vdots \\ \sigma_K.(\mathbf{a} \circ \mathbf{b}) \end{bmatrix} \tag{1.8}$$

which is the concatenation of the matrices $\mathbf{a} \circ \mathbf{b}$ weighted by σ_k with $k = 1, \cdots, K$. Each slice of $\mathbf{X}_3$ is depicted in Fig. 1.12. The two other unfolded representations

$$\mathbf{X}_{..k} = \sigma_k.(\mathbf{a} \circ \mathbf{b}) \quad = \quad \sigma_k \left[b_1. \begin{bmatrix} a_1 \\ a_2 \\ \vdots \\ a_n \\ \vdots \\ a_N \end{bmatrix} \quad b_2. \begin{bmatrix} a_1 \\ a_2 \\ \vdots \\ a_n \\ \vdots \\ a_N \end{bmatrix} \quad \cdots \quad b_P. \begin{bmatrix} a_1 \\ a_2 \\ \vdots \\ a_n \\ \vdots \\ a_N \end{bmatrix} \right]$$

Figure 1.12

$\mathbf{X}_1$ and $\mathbf{X}_2$ related to $\mathcal{X}$ (1.5) are shown below:

$$\mathbf{X}_1 = \begin{bmatrix} \mathbf{X}_{1..} \\ \mathbf{X}_{2..} \\ \vdots \\ \mathbf{X}_{N..} \end{bmatrix} = \begin{bmatrix} a_1.(\mathbf{b} \circ \boldsymbol{\sigma}) \\ a_2.(\mathbf{b} \circ \boldsymbol{\sigma}) \\ \vdots \\ a_N.(\mathbf{b} \circ \boldsymbol{\sigma}) \end{bmatrix} \tag{1.9}$$

$$\mathbf{X}_2 = \begin{bmatrix} \mathbf{X}_{.1.} \\ \mathbf{X}_{.2.} \\ \vdots \\ \mathbf{X}_{.P.} \end{bmatrix} = \begin{bmatrix} b_1.(\boldsymbol{\sigma} \circ \mathbf{a}) \\ b_2.(\boldsymbol{\sigma} \circ \mathbf{a}) \\ \vdots \\ b_P.(\boldsymbol{\sigma} \circ \mathbf{a}) \end{bmatrix}. \tag{1.10}$$

In the same way a matrix $\mathbf{X}$ composed by the outer product of two vectors is a rank-one matrix, a tensor $\mathcal{X}$ composed by the outer product of three vectors is called a rank-one tensor. Equivalently to the column vectors that form a rank-one matrix, the slices of any of the three unfolded representations of $\mathcal{X}$ are said linearly dependent as they differ only by a multiplicative term, e.g the slices that compose

$\mathbf{X}_3$ differ only by σ_k.

In the following we define the rank of a tensor. Then, we generalize (1.6) to compose a tensor of rank R.

Definition 1.7 (rank of a tensor) *The rank of a third-order $N \times P \times K$ tensor $\mathcal{X}$, denoted by rank($\mathcal{X}$), is the minimum number of rank-one tensors necessary to express $\mathcal{X}$ as a linear combination of rank-one tensors*[5]*. In other words, a rank-R tensor can be written as*

$$\mathcal{X} = \sum_{r=1}^{R} \mathcal{X}^{(r)} = \sum_{r=1}^{R} \mathbf{a}^{(r)} \circ \mathbf{b}^{(r)} \circ \boldsymbol{\sigma}^{(r)} \tag{1.11}$$

where $\mathcal{X}^{(r)} = \mathbf{a}^{(r)} \circ \mathbf{b}^{(r)} \circ \boldsymbol{\sigma}^{(r)}$ is a $N \times P \times K$ rank-one tensor with $\mathbf{a}^{(r)} \in \mathbb{C}^{N \times 1}$, $\mathbf{b}^{(r)} \in \mathbb{C}^{P \times 1}$ and $\boldsymbol{\sigma}^{(r)} \in \mathbb{C}^{K \times 1}$.

Constructing a tensor of rank R of dimension $N \times P \times K$

A rank-two tensor can be constructed by summing two rank-one tensors where each tensor is composed by the outer products $\mathbf{a} \circ \mathbf{b} \circ \boldsymbol{\sigma}$ and $\mathbf{c} \circ \mathbf{d} \circ \boldsymbol{\lambda}$ such that:

$$\mathcal{X} = \mathbf{a} \circ \mathbf{b} \circ \boldsymbol{\sigma} \quad + \quad \mathbf{c} \circ \mathbf{d} \circ \boldsymbol{\lambda}. \tag{1.12}$$

where $\mathbf{a},\ \mathbf{c} \in \mathbb{C}^{N \times 1}$ and $\mathbf{b},\ \mathbf{d} \in \mathbb{C}^{P \times 1}$ and $\boldsymbol{\sigma},\ \boldsymbol{\lambda} \in \mathbb{C}^{K \times 1}$ are couples of linearly independent vectors.

Then, one of the unfolded representation of $\mathcal{X}$ is given by:

$$\mathbf{X}_3 = \begin{bmatrix} \mathbf{X}_{..1} \\ \mathbf{X}_{..2} \\ \vdots \\ \mathbf{X}_{..K} \end{bmatrix} = \begin{bmatrix} \sigma_1.(\mathbf{a} \circ \mathbf{b}) \\ \sigma_2.(\mathbf{a} \circ \mathbf{b}) \\ \vdots \\ \sigma_K.(\mathbf{a} \circ \mathbf{b}) \end{bmatrix} + \begin{bmatrix} \lambda_1.(\mathbf{c} \circ \mathbf{d}) \\ \lambda_2.(\mathbf{c} \circ \mathbf{d}) \\ \vdots \\ \lambda_K.(\mathbf{c} \circ \mathbf{d}) \end{bmatrix}. \tag{1.13}$$

[5]The sum of two $N \times P \times K$ third-order tensors $\mathcal{X}_1$ and $\mathcal{X}_2$ is a $N \times P \times K$ third-order tensor denoted by $\mathcal{X}_1 + \mathcal{X}_2$ and given by $[\mathcal{X}_1 + \mathcal{X}_2]_{n,p,k} = [\mathcal{X}_1]_{n,p,k} + [\mathcal{X}_2]_{n,p,k}$

Notice that the k-th slice $\mathbf{X}_{..k}$ of $\mathbf{X}_3$ can be factored as follows:

$$\begin{aligned}
\mathbf{X}_{..k} &= \sigma_k \left(\mathbf{a} \circ \mathbf{b}\right) + \lambda_k \left(\mathbf{c} \circ \mathbf{d}\right) && (1.14)\\
&= \sigma_k \left(\mathbf{a}\mathbf{b}^T\right) + \lambda_k \left(\mathbf{c}\mathbf{d}^T\right) && (1.15)\\
&= \sigma_k \left[\mathbf{a} \;\; \mathbf{c}\right] + \lambda_k \left[\mathbf{b} \;\; \mathbf{d}\right]^T && (1.16)\\
&= \sigma_k \mathbf{A} + \lambda_k \mathbf{B}^T = && (1.17)\\
&= \mathbf{A} \begin{bmatrix} \sigma_k & 0 \\ 0 & \lambda_k \end{bmatrix} \mathbf{B}^T. && (1.18)
\end{aligned}$$

where $\mathbf{A} = [\mathbf{a}\,\mathbf{c}] \in \mathbb{C}^{N \times 2}$, $\mathbf{B} = [\mathbf{b}\,\mathbf{d}] \in \mathbb{C}^{P \times 2}$ and $\mathbf{\Sigma} = [\boldsymbol{\sigma} \;\; \boldsymbol{\lambda}] \in \mathbb{C}^{K \times 2}$.

Let $D_k(\cdot)$ be the *diagonal operator* that builds a diagonal matrix from the k-*th* row of its matrix argument, such that:

$$\mathbf{X}_{..k} = \mathbf{A} D_k \left(\mathbf{\Sigma}\right) \mathbf{B}^T. \tag{1.19}$$

Thus, the unfolded represention $\mathbf{X}_3$ can be written as:

$$\mathbf{X}_3 = \begin{bmatrix} \mathbf{X}_{..1} \\ \mathbf{X}_{..2} \\ \vdots \\ \mathbf{X}_{..K} \end{bmatrix} = \begin{bmatrix} \mathbf{A} D_1 \left(\mathbf{\Sigma}\right) \mathbf{B}^T \\ \mathbf{A} D_2 \left(\mathbf{\Sigma}\right) \mathbf{B}^T \\ \vdots \\ \mathbf{A} D_K \left(\mathbf{\Sigma}\right) \mathbf{B}^T \end{bmatrix} = \begin{bmatrix} \mathbf{A} D_1 \left(\mathbf{\Sigma}\right) \\ \mathbf{A} D_2 \left(\mathbf{\Sigma}\right) \\ \vdots \\ \mathbf{A} D_K \left(\mathbf{\Sigma}\right) \end{bmatrix} \mathbf{B}^T. \tag{1.20}$$

In the previous equation, the matrix on the left that multiplies $\mathbf{B}^T$, is called Khatri-Rao product and is denoted by $(\mathbf{\Sigma} \diamond \mathbf{A})$ so that, $\mathbf{X}_3$ can be expressed as:

$$\mathbf{X}_3 = \left(\mathbf{\Sigma} \diamond \mathbf{A}\right) \mathbf{B}^T. \tag{1.21}$$

In the same manner, the two other unfolded representations of $\mathcal{X}$ can be also be factored using the Khatri-Rao product notation, as indicated below:

$$\mathbf{X}_1 = \begin{bmatrix} \mathbf{X}_{1..} \\ \mathbf{X}_{2..} \\ \vdots \\ \mathbf{X}_{N..} \end{bmatrix} = \begin{bmatrix} \mathbf{B} D_1 \left(\mathbf{A}\right) \\ \mathbf{B} D_2 \left(\mathbf{A}\right) \\ \vdots \\ \mathbf{B} D_N \left(\mathbf{A}\right) \end{bmatrix} \mathbf{\Sigma}^T = \left(\mathbf{A} \diamond \mathbf{B}\right) \mathbf{\Sigma}^T \tag{1.22}$$

$$\mathbf{X}_2 = \begin{bmatrix} \mathbf{X}_{.1.} \\ \mathbf{X}_{.2.} \\ \vdots \\ \mathbf{X}_{.P.} \end{bmatrix} = \begin{bmatrix} \mathbf{\Sigma} D_1(\mathbf{B}) \\ \mathbf{\Sigma} D_2(\mathbf{B}) \\ \vdots \\ \mathbf{\Sigma} D_P(\mathbf{B}) \end{bmatrix} \mathbf{A}^T = (\mathbf{B} \diamond \mathbf{\Sigma}) \mathbf{A}^T. \tag{1.23}$$

Example 1.5 : (Factored representation of $\mathbf{X}_3$) In this example, $N = P = K = 2$ and a $2 \times 2 \times 2$ tensor is composed summing two rank-one tensors. The factored representation of the unfolded representation $\mathbf{X}_3$ is illustrated in Fig. 1.13 and Fig. 1.14.

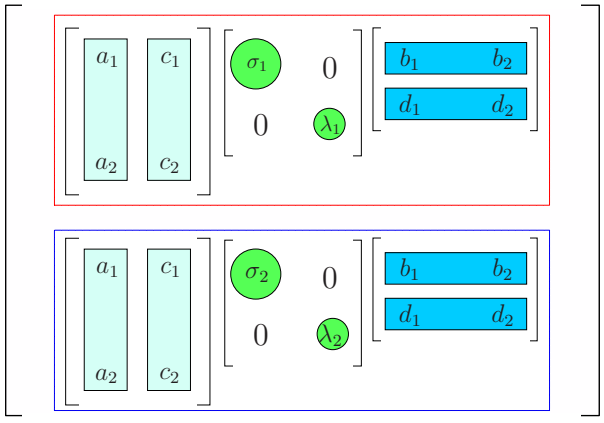

Figure 1.13

Similarly to the factored representation of (1.6), where parallel factors are couples of vectors $\mathbf{a}, \mathbf{b}$ and $\mathbf{c}, \mathbf{d}$, in the factored tensor of (1.21)-(1.23), the triplet of vectors $\mathbf{a}, \mathbf{b}, \boldsymbol{\sigma}$ and $\mathbf{c}, \mathbf{d}, \boldsymbol{\lambda}$ are also called parallel factors as each term a_n interacts only with c_n and σ_n, being the same procedure valid for the other triple. This notion of parallel factors is represented in Fig. 1.15 and Fig. 1.16 to the $2 \times 2 \times 2$ tensor from the previous example.

Therefore, the sum of R rank-one tensors can be factored as in Eq. (1.21)-(1.23) such that $\mathbf{A} = [\mathbf{a}^{(1)}, \cdots, \mathbf{a}^{(R)}] \in \mathbb{C}^{N \times R}$, $\mathbf{B} = [\mathbf{b}^{(1)}, \cdots, \mathbf{b}^{(R)}] \in \mathbb{C}^{P \times R}$ and $\mathbf{\Sigma} = [\boldsymbol{\sigma}^{(1)}, \cdots, \sigma^{(R)}] \in \mathbb{C}^{K \times R}$ are called the component matrices having R parallel factors each one. This will be treated in the following, where we present the PARAFAC tensor decomposition [8].

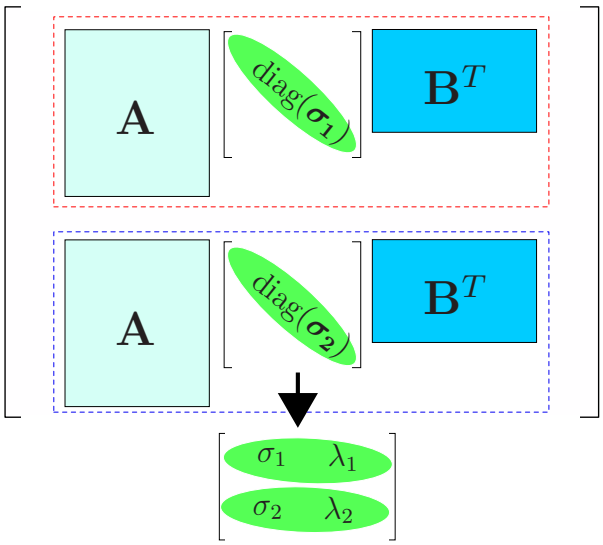

Figure 1.14: Unfolded representation $\mathbf{X}_1$ factored

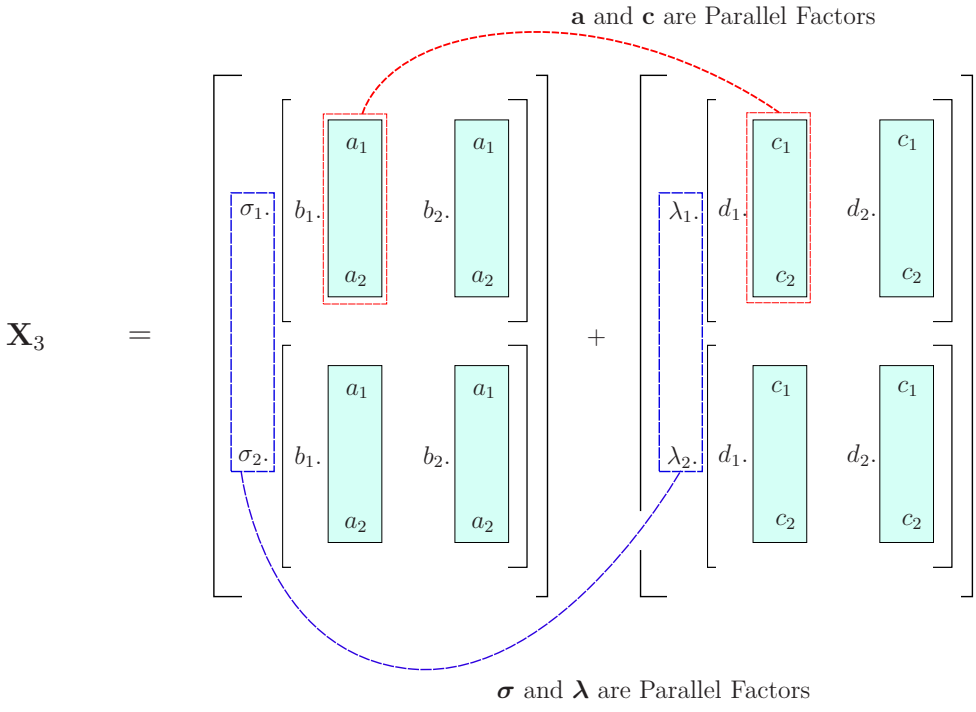

Figure 1.15

2 SVD versus PARAFAC

In this part, we dispose some comments on Singular Value Decomposition (SVD). Then, the PARAFAC tensor decomposition is presented as an extension of SVD

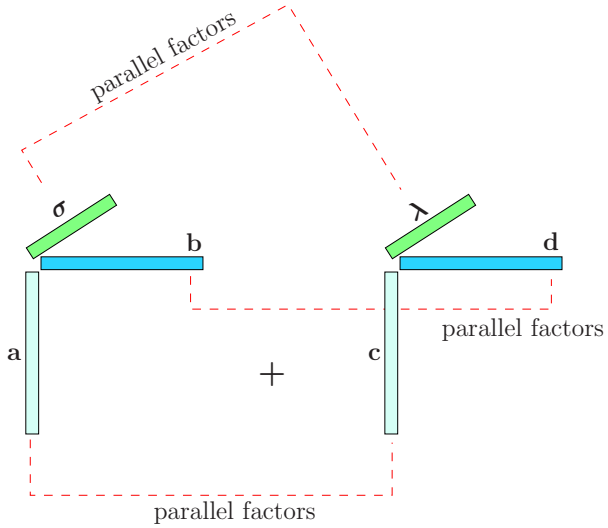

Figure 1.16

to signals represented in more than two domains.

Definition 1.7 (Singular Value Decomposition) *Let* $\mathbf{X} \in \mathbb{C}^{N \times P}$ *be a matrix of rank* R*. Then, the Singular Value Decomposition (SVD) of* $\mathbf{X}$ *is given by:*

$$\mathbf{X} = \mathbf{A} D(\boldsymbol{\sigma}) \mathbf{B}^H \tag{1.24}$$

where $\mathbf{A} = [\mathbf{a}^{(1)}, \cdots, \mathbf{a}^{(R)}]$ *is an* $N \times R$ *unitary matrix (*$\mathbf{A}\mathbf{A}^H = \mathbf{I}_R$*),* $\mathbf{B} = [\mathbf{b}^{(1)\,*}, \cdots, \mathbf{b}^{(R)\,*}]$ *is an* $P \times R$ *unitary matrix (*$\mathbf{B}\mathbf{B}^H = \mathbf{I}_R$*) and* $D(\boldsymbol{\sigma}) = diag(\sigma^{(1)}, \cdots, \sigma^{(R)})$ *is a* $R \times R$ *diagonal matrix.*

Considering the notation of parallel factors, the SVD of $\mathbf{X}$ can be written using the same notation of (1.14), i.e., as a sum of weighted outer products of the input and output eigenvectors of $\mathbf{X}$ as shown below:

$$\mathbf{X} = \sum_{r}^{R} \mathbf{X}^{(r)} = \sum_{r=1}^{R} \sigma^{(r)} \cdot \left(\mathbf{a}^{(r)} \circ \mathbf{b}^{(r)}\right). \tag{1.25}$$

This sum is illustrated in Fig. 1.17.

Notice from the previous equation that SVD decomposes a rank-R matrix $\mathbf{X}$ in a sum of R matrices of rank one. Each one of these rank-one matrix represents a basis element of the subspace generated by matrix $\mathbf{X}$, which is weighted by the singular values $\sigma^{(1)}, \cdots, \sigma^{(R)}$.

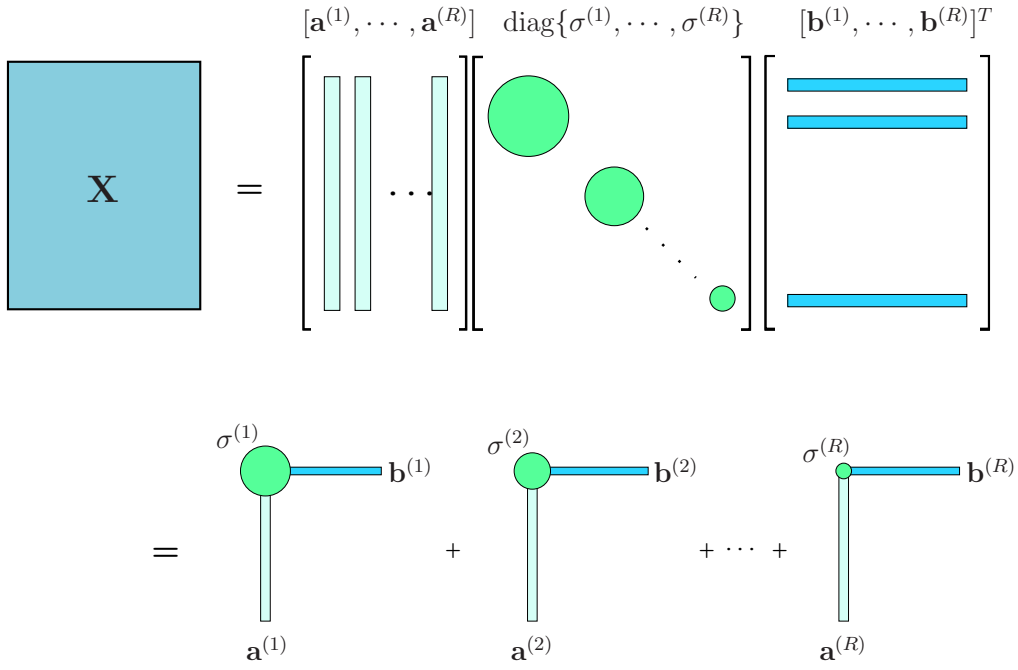

Figure 1.17: SVD

Knowing each of theses basis and their respective singular values, we are able to identify the most important subspaces (or directions) that compose the signal $\mathbf{X}$ which handle SVD very meaningful as an data analysis tool. On the other hand, the inherent rotational ambiguity of SVD create some bounds in its possible applications.

Property 2 (rotational ambiguity of SVD) *Let $\mathbf{X} \in \mathbb{C}^{N \times P}$ a rank-R matrix with SVD given by $\mathbf{X} = \mathbf{A}D(\boldsymbol{\sigma})\mathbf{B}^T$. Then, SVD can be written as:*

$$\mathbf{X} = (\mathbf{AQ})\, D(\boldsymbol{\sigma})\, (\mathbf{BQ})^H \tag{1.26}$$

where $\mathbf{Q} \in \mathbb{C}^{R \times R}$ is an unitary rotation matrix, which means that $\mathbf{QQ}^H = \mathbf{I}_R$.

In many signal processing problem, the signal part of a postulated model that lies in a so-called signal subspace, while the parameters of interest are in one-to-one correspondence with a certain basis of this subspace [9]. The signal subspace can often be reliably estimated from measured data, but the particular basis of interest cannot be identified without additional problem-specific structure. Then, we can say that this represents a bound of SVD.

In the next part we introduce the PARAFAC tensor decomposition. One of its distinguish features is that differently from SVD, PARAFAC is unique under mild conditions. This has meaningful implications in signal processing problems which deal with such data modeling.

2.1 PARAFAC (Parallel Factor Analysis)

Definition 1.8 (PARAFAC decomposition) *Let $\mathcal{X} \in \mathbb{C}^{N\times P\times K}$ a tensor of rank R. Then, $\mathcal{X}$ can be decomposed as a sum of rank-one tensors $\mathcal{X}^{(r)}$ as follows:*

$$\mathcal{X} = \sum_{r=1}^{R} \mathcal{X}^{(r)} = \sum_{r=1}^{R} \mathbf{a}^{(r)} \circ \mathbf{b}^{(r)} \circ \boldsymbol{\sigma}^{(r)} \tag{1.27}$$

where $\boldsymbol{\sigma}^{(r)}, \mathbf{a}^{(r)}$ and $\mathbf{b}^{(r)}$ are called parallel factors.

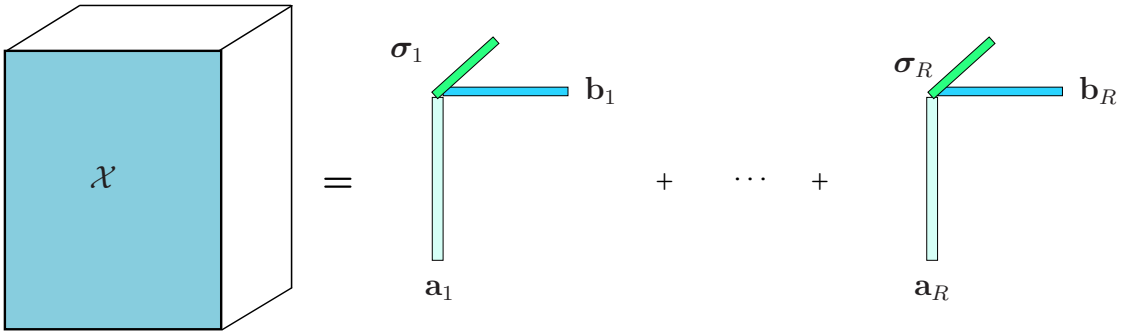

Figure 1.18: PARAFAC decomposition

The parallel factors are stacked in three matrices so-called component matrices:

$$\mathbf{A} = \left[\mathbf{a}^{(1)} \;\; \mathbf{a}^{(2)} \;\; \cdots \;\; \mathbf{a}^{(R)}\right] \in \mathbb{C}^{N\times R} \tag{1.28}$$

$$\mathbf{B} = \left[\mathbf{b}^{(1)} \;\; \mathbf{b}^{(2)} \;\; \cdots \;\; \mathbf{b}^{(R)}\right] \in \mathbb{C}^{P\times R} \tag{1.29}$$

$$\boldsymbol{\Sigma} = \left[\boldsymbol{\sigma}^{(1)} \;\; \boldsymbol{\sigma}^{(2)} \;\; \cdots \;\; \boldsymbol{\sigma}^{(R)}\right] \in \mathbb{C}^{K\times R} \tag{1.30}$$

The unfolded representations of the decomposition can be factored as shown below:

$$\mathbf{X}_1 = \mathbf{Z}_1 \boldsymbol{\Sigma}^T \tag{1.31}$$

$$\mathbf{X}_2 = \mathbf{Z}_2 \mathbf{A}^T \tag{1.32}$$

$$\mathbf{X}_3 = \mathbf{Z}_3 \mathbf{B}^T \tag{1.33}$$

where

$$\mathbf{Z}_1 = (\mathbf{A} \diamond \mathbf{B}), \quad \mathbf{Z}_2 = (\mathbf{B} \diamond \mathbf{\Sigma}), \quad \mathbf{Z}_3 = (\mathbf{\Sigma} \diamond \mathbf{A}).$$

In contrast to SVD, PARAFAC decomposition does not suffer from the rotational ambiguity [8]. In other words, a model composed by the sum of R rank-one tensors is identifiable under mild conditions. The conditions are related to the rank of the component matrices $\mathbf{A}, \mathbf{B}$ and $\mathbf{\Sigma}$ as will be discussed in the following.

Uniqueness of PARAFAC

Definition 1.9 (k-rank of a matrix) *Consider a matrix $\mathbf{X} \in \mathbb{C}^{N \times P}$. If $rank(\mathbf{X}) = r$, then $\mathbf{X}$ constains a collection of r linearly independent columns. Moreover, if every $l \leq P$ columns of $\mathbf{X}$ are linearly independent, but it does not hold for every $l+1$ columns , then $\mathbf{X}$ has k-rank $k_{\mathbf{X}} = l$. Note that $k_{\mathbf{X}} \leq rank(\mathbf{X}), \forall \mathbf{X}$*

Example 1.6 (rank and k-rank of a matrix) Consider the following two matrices:

$$\mathbf{X} = \begin{bmatrix} \alpha & 1 & 0 \\ \beta & 0 & 1 \end{bmatrix}, \mathbf{Y} = \begin{bmatrix} \alpha & 1 & 0 \\ 0 & 0 & 1 \end{bmatrix}.$$

For $\alpha, \beta \neq 0$, rank($\mathbf{X}$)=2 and k-rank($\mathbf{X}$)=2, whereas $rank(\mathbf{Y}) = 2$ but k-rank($\mathbf{Y}$)=1. In other words, k-rank=2 requires that every two columns are linearly independent, whereas rank=2 requires that there exists at least one pair of linearly independent columns.

Theorem 1 (indentifiability of PARAFAC [8, 10]) *Consider the matrices $\mathbf{A} \in \mathbb{C}^{N \times R}$, $\mathbf{B} \in \mathbb{C}^{P \times R}$ and $\mathbf{\Sigma} \in \mathbb{C}^{K \times R}$ which compose a tensor $\mathcal{X} \in \mathbb{C}^{N \times P \times K}$ such that*

$$\mathcal{X} = \sum_{r=1}^{R} \mathbf{a}^{(r)} \circ \mathbf{b}^{(r)} \circ \boldsymbol{\sigma}^{(r)}.$$

If

$$k_{\mathbf{A}} + k_{\mathbf{B}} + k_{\mathbf{\Sigma}} \leq 2(R+1) \tag{1.34}$$

then $\mathbf{A}$, $\mathbf{B}$ and $\mathbf{\Sigma}$ are unique up to permutation and scaling of columns, which means that

$$\bar{\mathbf{A}} = \mathbf{A}\mathbf{\Pi}\mathbf{\Delta}_1, \;\; \bar{\mathbf{B}} = \mathbf{B}\mathbf{\Pi}\mathbf{\Delta}_2, \;\; \bar{\mathbf{\Sigma}} = \mathbf{\Sigma}\mathbf{\Pi}\mathbf{\Delta}_2 \tag{1.35}$$

where $\mathbf{\Pi}$ is a permutation matrix, and $\mathbf{\Delta}_{1,2,3}$ are diagonal scaling matrices satisfying

$$\mathbf{\Delta}_1\mathbf{\Delta}_2\mathbf{\Delta}_3 = \mathbf{I}. \tag{1.36}$$

The result holds for $R = 1$, irrespective of condition (1.31), as long as $\mathcal{X}$ does not contain an identically zero slice along any dimension. Note that for finite R, the set of permutation matrices is finite, as opposed to the set of unitary rotation matrices from SVD, which is infinite.

2.2 Bilinear Model versus Trilinear model

A signaling model can be defined as an approximation of a data set consisting of two parts: a structural part describing the structure in data and a residual one expressing the part of the data which is not captured by the structural part [11]. In signal processing applications to wireless communications, this structural part can be modeled, e.g., as a signal to be detected while the residual part the interference plus noise.

Definition 1.10 (bilinear model) Let $\mathbf{Y} \in \mathbb{C}^{N\times P}$ a measured data set. A bilinear model that describes this data set consists of two matrices $\mathbf{A} = \begin{bmatrix}\mathbf{a}^{(1)} & \mathbf{a}^{(2)} & \cdots & \mathbf{a}^{(R)}\end{bmatrix} \in \mathbb{C}^{N\times R}$ and $\mathbf{B} = \begin{bmatrix}\mathbf{b}^{(1)} & \mathbf{b}^{(2)} & \cdots & \mathbf{b}_R\end{bmatrix} \in \mathbb{C}^{P\times R}$ and a residual error $\mathbf{E} \in \mathbb{C}^{N\times P}$ such that:

$$\mathbf{Y} = \mathbf{A}\mathbf{B}^T + \mathbf{E} \tag{1.37}$$

or in scalar notation

$$y_{n,p} = \sum_{r=1}^{R} a_n^{(r)} \cdot b_p^{(r)} + e_{n,p}, \tag{1.38}$$

where structural part is factored as in Eq.(1.4).

The analysis of residuals quantifies how well a model fits the data. The minimization of the mean squared error is often considered to identify a bilinear model, which gives a Least Squares (LS) problem, represented as:

$$\underset{\mathbf{A}\in\mathbb{C}^{N\times R},}{\arg}\ \underset{\mathbf{B}\in\mathbb{C}^{P\times R}}{\min} \|\mathbf{Y} - \mathbf{A}\mathbf{B}^T\|_F^2. \tag{1.39}$$

A theorem from linear algebra guarantees that the best low-rank approximation of a bilinear model in the LS sense is given by SVD [7]. In other words, a bilinear model with R factors is best represented by the SVD of $\mathbf{Y}$ accounting the

R strongest singular values. Principal component analysis (PCA) is a data analysis tool that exploits this results to find the strongest R components from the measured data set in $\mathbf{Y}$ [7]. Despite the great potential of bilinear models and its tools, the indentifiability problem still remains, once there is an inherent rotational ambiguity. Note that, the solution to the optimization problem (2.2) is given by an infinite set of matrices $\mathbf{U} = \mathbf{A}\mathbf{Q}^H$ and $\mathbf{V} = (\mathbf{\Sigma}\mathbf{B}\mathbf{Q})^H$ with $\mathbf{A}$ and $\mathbf{B}$ from (1.21) and $\mathbf{Q}$ any unitary rotational matrix (1.23). To exploit the uniqueness inherent from tensor decompositions (no rotational ambiguity), models based on tensors can be used.

Definition 1.11 (trilinear model) Let $\mathcal{Y} \in \mathbb{C}^{N\times P\times K}$ a data set. A trilinear model for $\mathcal{Y}$ consists of three matrices $\mathbf{A} = \begin{bmatrix}\mathbf{a}^{(1)} & \mathbf{a}^{(2)} & \cdots & \mathbf{a}^{(R)}\end{bmatrix} \in \mathbb{C}^{N\times R}, \mathbf{B} = \begin{bmatrix}\mathbf{b}^{(1)} & \mathbf{b}^{(2)} & \cdots & \mathbf{b}^{(R)}\end{bmatrix} \in \mathbb{C}^{P\times R}$ and $\mathbf{\Sigma} = \begin{bmatrix}\boldsymbol{\sigma}^{(1)} & \boldsymbol{\sigma}^{(2)} & \cdots & \boldsymbol{\sigma}^{(R)}\end{bmatrix} \in \mathbb{C}^{K\times R}$ and a residual error $\mathcal{E} \in \mathbb{C}^{N\times P\times K}$ such that:

$$\mathcal{Y} = \mathcal{X} + \mathcal{E} = \sum_{r=1}^{R} \mathcal{X}_r + \mathcal{E} = \sum_{r=1}^{R} \mathbf{a}^{(r)} \circ \mathbf{b}^{(r)} \circ \boldsymbol{\sigma}^{(r)} + \mathcal{E} \tag{1.40}$$

or in scalar notation

$$y_{i,j,k} = \sum_{r=1}^{R} a_n^{(r)} \cdot b_p^{(r)} \cdot \sigma_k^{(r)} + e_{n,p,k}. \tag{1.41}$$

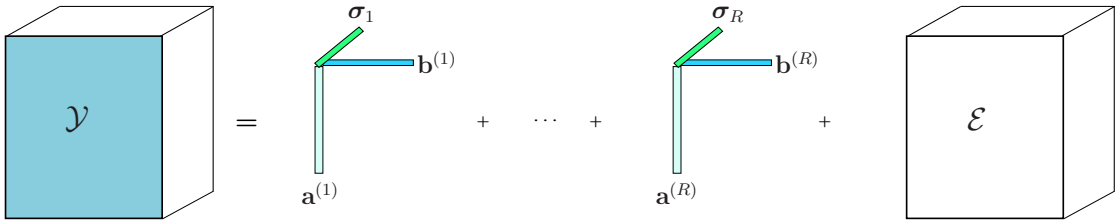

Figure 1.19: Trilinear model: sum of rank-one tensor + residual error tensor

The structural part of a trilinear model has basically the same structure of PARAFAC decomposition and a trilinear model can be also called a PARAFAC model [8]. Then, the structural part has the same unfolded representations that can be factored as in (1.25), (1.26) and (1.27):

$$\mathbf{Y}_1 = \mathbf{X}_1 + \mathbf{E}_1 = (\mathbf{A} \diamond \mathbf{B})\,\mathbf{\Sigma}^T + \mathbf{E}_1 \tag{1.42}$$

$$\mathbf{Y}_2 = \mathbf{X}_2 + \mathbf{E}_2 = (\mathbf{B} \diamond \mathbf{\Sigma})\,\mathbf{A}^T + \mathbf{E}_2 \tag{1.43}$$

$$\mathbf{Y}_3 = \mathbf{X}_3 + \mathbf{E}_3 = (\mathbf{\Sigma} \diamond \mathbf{A})\,\mathbf{B}^T + \mathbf{E}_3 \tag{1.44}$$

where $\mathbf{E}_1 \in \mathbb{C}^{NP\times K}$, $\mathbf{E}_2 \in \mathbb{C}^{PK\times N}$ and $\mathbf{E}_3 \in \mathbb{C}^{KN\times P}$ are the unfolded representations on the three domains with dimensions N, P and K of the tensor $\mathcal{E} \in \mathbb{C}^{N\times P\times K}$. The major interest on trilinear models relies on the uniqueness result of PARAFAC decomposition showed in (1.28).

Finding an algorithm that provides an analytical solution to PARAFAC decomposition is a very hard task. In some special conditions, the algorithms are iterative, consisting of several diagonalization problems [12, 13, 14]. Generalizations of this approach, as new algorithms that provide analytical solutions are under on going research. In the following, a classical algorithm used to identify a tensor model, relying on least squares estimations, is presented. It provides a numerical solution which is useful in most of the cases. Hereafter, references to alternative algorithms are briefly listed.

3 The Alternating Least Squares (ALS)

The Alternating Least Squares (ALS) is an iterative algorithm that estimates the component matrices $\mathbf{A} \in \mathbb{C}^{N\times R}, \mathbf{B} \in \mathbb{C}^{P\times R}$ and $\mathbf{\Sigma} \in \mathbb{C}^{K\times R}$ of a PARAFAC model [5]. It consists of fitting a third-order tensor model to the detected data by alternatively minimizing three least square problems per iteration. ALS makes use of the three unfolded representations (1.36)-(1.38) to identify the structural part of the model.

At each step of this algorithm, one component matrix is estimated in the LS sense, while the two others are fixed to their values obtained at the previous steps. At least two initialization approaches exist. The component matrices can be initialized randomly or constructed using some a prior information. Assuming the initialization of the component matrices such that $\mathbf{A}_{i=0}$, $\mathbf{B}_{i=0}$ and $\mathbf{\Sigma}_{i=0}$, ALS is composed of three estimation steps which are summarized as follows:

1. Set $i = 0$; Initialize $\hat{\mathbf{A}}_{i=0}, \hat{\mathbf{B}}_{i=0}$ and $\hat{\mathbf{\Sigma}}_{i=0}$;
2. $i = i + 1$;
3. Using $\mathbf{Y}_1$, find an LS estimate of $\mathbf{\Sigma}$:

$$\hat{\mathbf{\Sigma}}_{(i)}^T = \left[\hat{\mathbf{A}}_{(i-1)} \diamond \hat{\mathbf{B}}_{(i-1)}\right]^{\dagger} \mathbf{Y}_1$$

4. Using $\mathbf{Y}_2$, find an LS estimate of $\mathbf{A}$:

$$\hat{\mathbf{A}}_{(i)}^T = \left[\hat{\mathbf{B}}_{(i-1)} \diamond \hat{\mathbf{\Sigma}}_{(i)}\right]^\dagger \mathbf{Y}_2$$

5. Using $\mathbf{Y}_3$, find an LS estimate of $\mathbf{B}$:

$$\hat{\mathbf{B}}_{(i)}^T = \left[\hat{\mathbf{\Sigma}}_{(i)} \diamond \hat{\mathbf{A}}_{(i)}\right]^\dagger \mathbf{Y}_3$$

6. Repeat steps 2-5 until convergence

The convergence of the algorithm at the i-th iteration is declared when the squared error between the true received signal tensor and its version reconstructed from the estimated component matrices does not significantly change between iterations i and $i+1$. This measured squared error is defined as follows:

$$|\varepsilon_{(i+1)}| = \frac{\|\mathbf{Y}_2 - (\hat{\mathbf{B}}_{(i+1)} \diamond \hat{\mathbf{\Sigma}}_{(i+1)})\hat{\mathbf{A}}_{(i+1)}^T\|_F^2}{N \times P \times K} \tag{1.45}$$

and the convergence is achieved when

$$|\varepsilon_{(i+1)}| - |\varepsilon_{(i)}| \leq \epsilon \tag{1.46}$$

where ϵ is a specified threshold value (e.q. 10^{-5}).

The conditional update of each matrix may either improve or maintain but can not worsen the current fit. It is worth noting that ALS algorithm strongly depends on the initialization, and convergence to local minimum can occur [8, 5]. This is the case when some a prior information about the system is known and considered in the initialization procedure. Otherwise, some alternatives have been studied over the past few years [15]. A different approach considers a fixed number of iterations of ALS, which can reduce the complexity of the algorithm.

The practical interest of ALS is its simplicity. Respecting the uniqueness conditions of PARAFAC decomposition shown in Eq. (1.28), associated component matrices can be estimated even when the initialization of ALS is random. Several applications in blind multiuser detection exploiting the PARAFAC model and ALS have been proposed [5, 16, 17, 18, 19, 20, 21, 22, 23]. where $\mathbf{A}, \mathbf{B}$ and $\mathbf{\Sigma}$ are, respectively, the symbol, channel and code matrices.

There exist alternative algorithms to identify a third-order tensor [24]. However, over this thesis, only algorithms derived from ALS are considered.

CHAPTER 2

Physical Uplink Control Channel (PUCCH) LTE

In this thesis, we deal with a practical problem regarding the physical layer of 3GPP LTE system. More specifically, we model the baseband transmission on the uplink control channel of LTE so-called PUCCH using the tensor approach presented in Chapter 1. Thanks to this modeling, we propose multi-user receivers for inter-cell interference reduction in PUCCH LTE. Although over this thesis we focus in the PUCCH signaling, we provide in the first part of Chapter 2 a general overview of LTE physical layer, which makes this Chapter an interesting survey about the subject. Concepts like Orthogonal Frequency Division Multiplexing (OFDM) and DFT-spread OFDM (DFTS-OFDM) (respectively the transmission schemes of LTE downlink and uplink) are elucidated over the text. The impact of these schemes are also explained into the context of LTE radio interface. At the second part of this Chapter we concentate our attention on the PUCCH signaling. We detaile the design of both formats are the the kind of information carried on. In addition to this, we also discuss the relevance of such information to the system performance.

1 Overview of 3GPP LTE

3GPP is a partnership project formed by standards bodies consisting of several *Technical Specification Groups* (TSGs), being 3GPP TSG RAN the technical specification group that has developed Wideband CDMA (WCDMA), its evolution HSPA, as well as LTE, and its forefront of technology. Technical Specification Group (TSG) RAN consists of five working groups (WG). In this thesis we are interested in two of them:

- RAN WG1 dealing with the physical layer specifications.
- RAN WG2 dealing with the layer 2 and layer 3 radio interface specifications.

The 3GPP documents are divided into releases, where each release has a set of added features compared to the previous one. The specifications of all releases can be updated after each set of TSG meetings. Before a specification is closed, the documents are proposed in form of technical reports (TR) sorted by the TSG. The references concerning LTE in this thesis are precisely releases and technical reports of 3GPP.

The Evolved UTRAN (LTE) and the related SAE, e.g., have been included in Release 8. The LTE specification was approved in December 2007, but 3GPP TSG RAN did not stop working on LTE when the first version of the specifications was completed. In fact, 3GPP continues to evolve LTE towards LTE Advanced (to be appeared in Release 10). It is worth pointing out that the research advances on cellular areas (i.e. advanced signal processing tools, new access technologies) influence continously the design choice of LTE [1, 2].

LTE RAN Architecture

For the purpose of this work, it suffices to note that the LTE radio-access architecture consists of a single node so-called the eNodeB[1]. The eNodeB communicates with one or multiple mobile terminals, also referred herein as UEs. This is illustrated in Fig. 2.1. A deep discussion about the LTE architecture can be found in [1, 2].

[1]The term eNodeB is introduced in LTE to indicate the additional functionality placed in the eNodeB compared to the functionality in the NodeB in WCDMA/HSPA

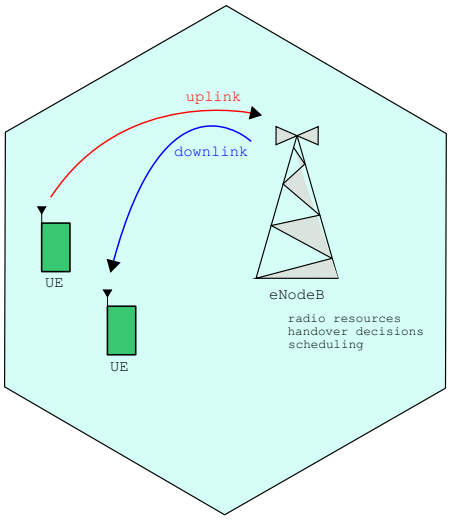

Figure 2.1: Simplified LTE Radio Access Architecture

As most of other modern communication systems, the processing specified for LTE is structured into different protocol layers, several of them similar to those used for WCDMA/HSPA. The LTE protocol architecture is equivalent for both uplink or downlink[2], as depicted in Fig. 2.2. The first two layers called Packet Data Convergence Protocol (PDCP) and Radio Link Control (RLC) are basically responsible for i) Internet Protocol (IP) header compression and ii) segmentation/concatenation, retransmission handling, and in sequence delivery to higher layers respectively.

The Medium Access Control (MAC) layer is responsible for retransmission error schemes and scheduling functionality while the Physical Layer (PHY) layer handles coding/decoding, modulation/demodulation, and other typical physical layer functions. The PHY layer offers services to the MAC layer in the form of *transport channels*.

Definition 2.1 (transport channel) *A transport channel is defined by* ***how*** *and* ***with what characteristics*** *the information is transmitted over the radio interface.*

The Uplink Shared Channel (UL-SCH) is the main transport channel used for transmission of uplink data in LTE. In the downlink, its equivalent is the Down-

[2]Not all the entities are presented in this simplified description.

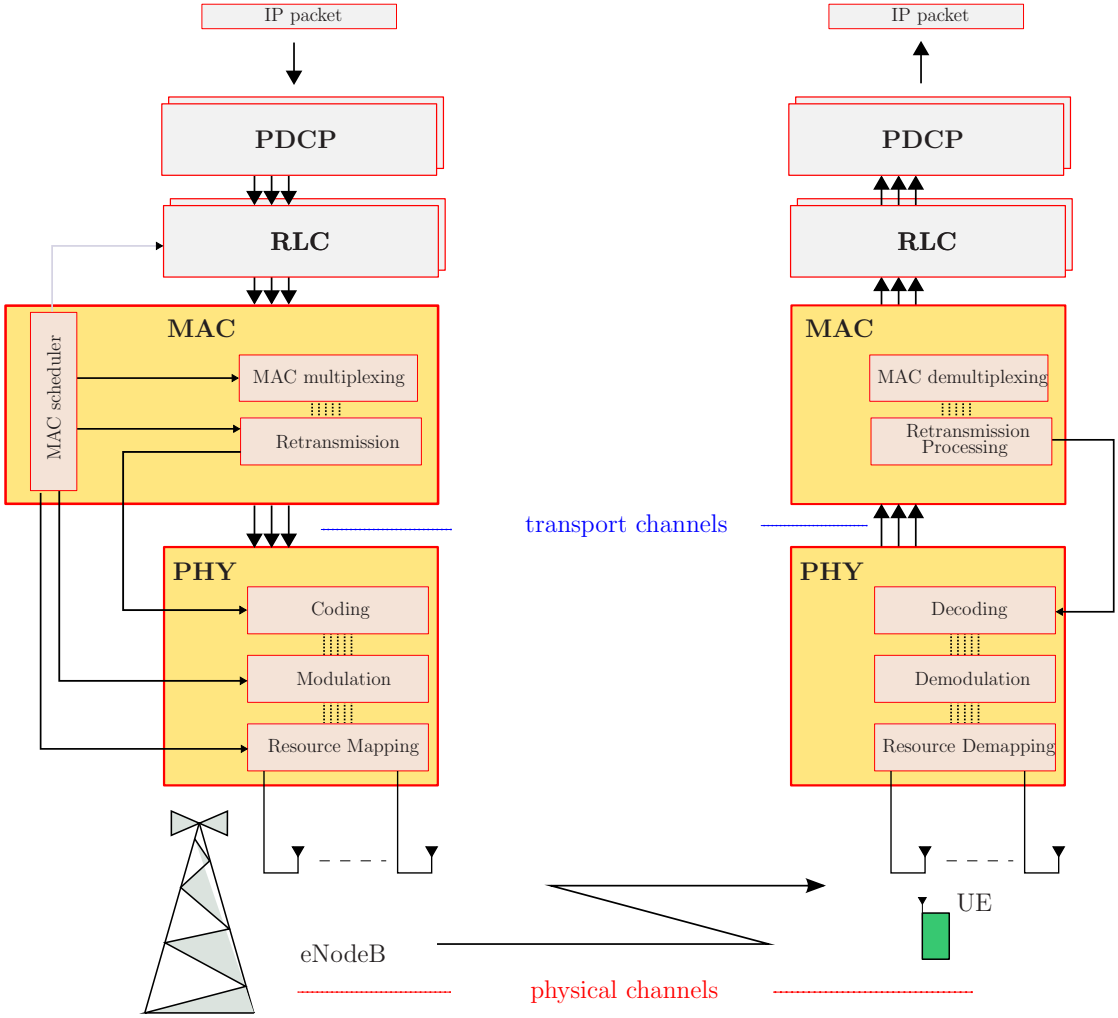

Figure 2.2: Simplified LTE Protocol Architecture (downlink)

link Shared Channel (DL-SCH). A transport channel is always associated with a *physical channel*, as explained in the following.

Definition 2.2 (physical channel) *A physical channel corresponds to the set of physical resources (in the time and frequency domains, as it will be clear in the following) used for transmission of a particular transport channel. Each transport channel is mapped to a corresponding physical channel.*

The physical channel associated with UL-SCH is Physical Uplink Shared Channel (PUSCH), that shares data and control information in the same physical resource when uplink resources have been assigned to a given UE.

In addition to the physical channels with a corresponding transport channel, there are also physical channels without a corresponding transport channel. These channels, known as *L1/L2 control channels*, are used to transmit control information, providing the eNodeB (or the terminal) with the necessary information for proper detection and decoding of the downlink (uplink) data transmission. This is depicted for uplink in Fig.2.3. The focus of this work is the modeling of the baseband

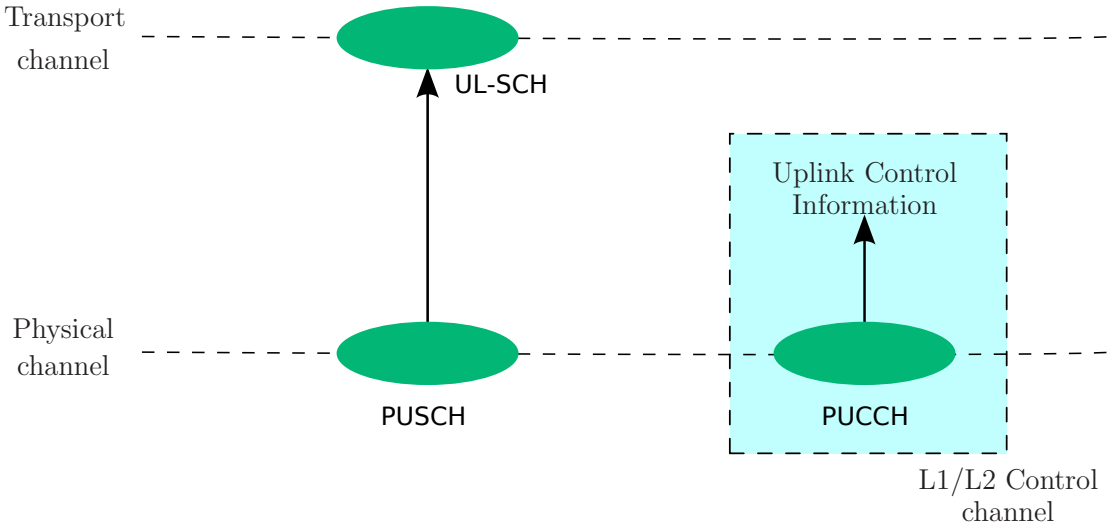

Figure 2.3: Uplink channel mapping

transmission on PUCCH, which is a L1/L2 control channel in the uplink. However, before starting this item, we take a deep look inside some important features of PHY and MAC layers of the LTE protocol stack.

2 LTE PHY Layer

2.1 LTE Downlink Transmission

OFDM

Multipath propagation is a typical phenomenon of a wireless channel, as shown in Fig. 2.5. As a consequence of multipath, the signal arriving at the receiver consists of a sum of delayed and faded copies of the transmitted signal, as illustrated in Fig. 2.5. When the maximum multipath delay exceeds one symbol interval (i.e. the interval between two successive transmitted signal samples), the wireless channel is said to be time-dispersive, introducing Inter Symbol Interference (ISI) [25].

This frequency selectivity will corrupt the frequency-domain structure of the transmitted signal, leading to higher error rates for a given Signal-to-Interference plus Noise Ratio (SINR).

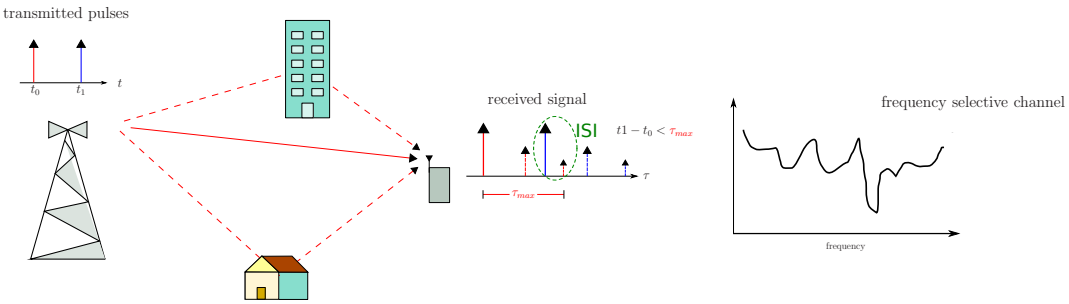

Figure 2.4: Propagation via multipath

Receiver-side equalization has for many years been considered to counteract the ISI [9]. Equalization has been shown to provide satisfactory performance with reasonable complexity at least up to bandwidths corresponding to the WCDMA bandwidth of 5 MHz [26]. However, if the transmission bandwidth is increased up to 20 MHz (the maximum target of LTE), the complexity of high performance equalization becomes a serious issue.

An interesting alternative to this problem, adopted in many emerging wireless communication systems, is the use of *multicarrier modulation* as part of the physical layer specifications. On multicarrier transmission, instead of transmitting a single wideband signal, multiple narrowband signals are frequency multiplexed and jointly transmitted over the same radio link. This is illustrated in Fig. 2.5.

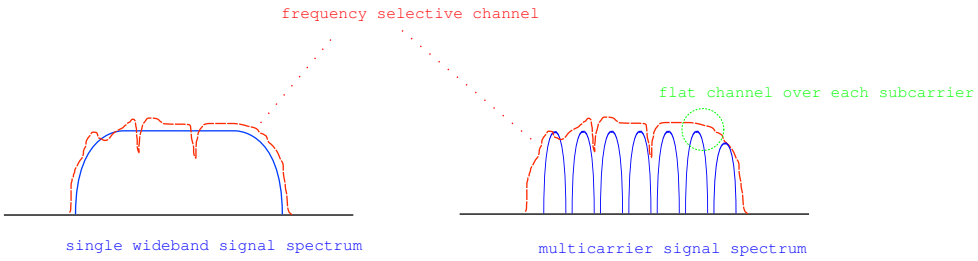

Figure 2.5: Multicarrier modulation

The downlink transmission of LTE is based on OFDM, a multicarrier modulation scheme that consists in transmitting a set of modulation symbols $u_{n,1}, u_{n,2}, \cdots, u_{n,P}$ in parallel through P orthogonal subcarriers [3, 27]. In OFDM, each symbol $u_{n,p}$ from a given complex constellation modulates a subcarrier $e^{j2\pi p\Delta ft}$

with the pulse shaping of Fig. 2.6 such that the subcarrier spacing is given by $\Delta f = 1/T_u$. In complex baseband notation, we call an *OFDM symbol* $u_n(t)$ during

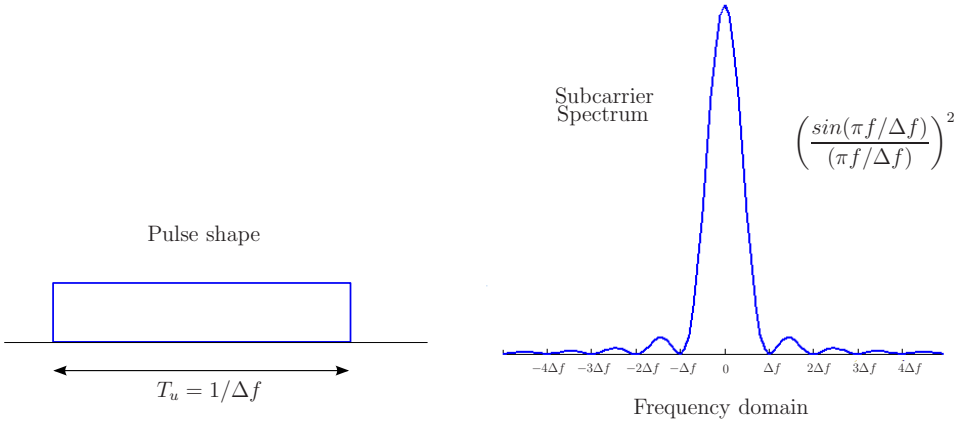

Figure 2.6: Per-symbol subcarrier pulse shape and spectrum per-subcarrier

the interval $nT_u \leq t < (n+1)T_u$ the contribution of the P modulated subcarriers, expressed as:

$$u_n(t) = \sum_{p=1}^{P} u_{n,p}(t) = \sum_{p=1}^{P} u_{n,p} e^{j2\pi p \Delta f t}. \tag{2.1}$$

where $u_{n,p}(t)$ is the p-th modulated subcarrier with frequency $f_p = p\Delta f$. Fig. 2.7 illustrates the composition of an OFDM symbol with P=12 subcarriers.

Once the modulation symbols are transmitted in parallel, the spectrum of the OFDM signal is given by the aggregation of the spectrum of all subcarriers, as shown in Fig. 2.8.

The main feature of OFDM compared to other multicarrier schemes is the fact that two modulated subcarriers $e^{j2\pi p_1 \Delta f t}$ and $e^{j2\pi p_2 \Delta f t}$ are mutually orthogonal over the time interval $nT_u \leq t < (n+1)T_u$, i.e.:

$$\int_n^{n+1} (e^{j2\pi p_1 \Delta f t})(e^{j2\pi p_2 \Delta f t})^* dt = \int_n^{n+1} e^{j2\pi p_1 \Delta f t} e^{-j2\pi p_2 \Delta f t} dt = 0. \tag{2.2}$$

The impact in terms of signal corruption due to radio-channel frequency selectivity depends on the bandwidth of each subcarrier. Having a smaller frequency bandwidth for each channel is equivalent to a greater time period and then better resistance to multipath propagation compared to single carrier signals.

For 3GPP LTE, the basic subcarrier spacing equals $\Delta f = 15$ kHz and downlink

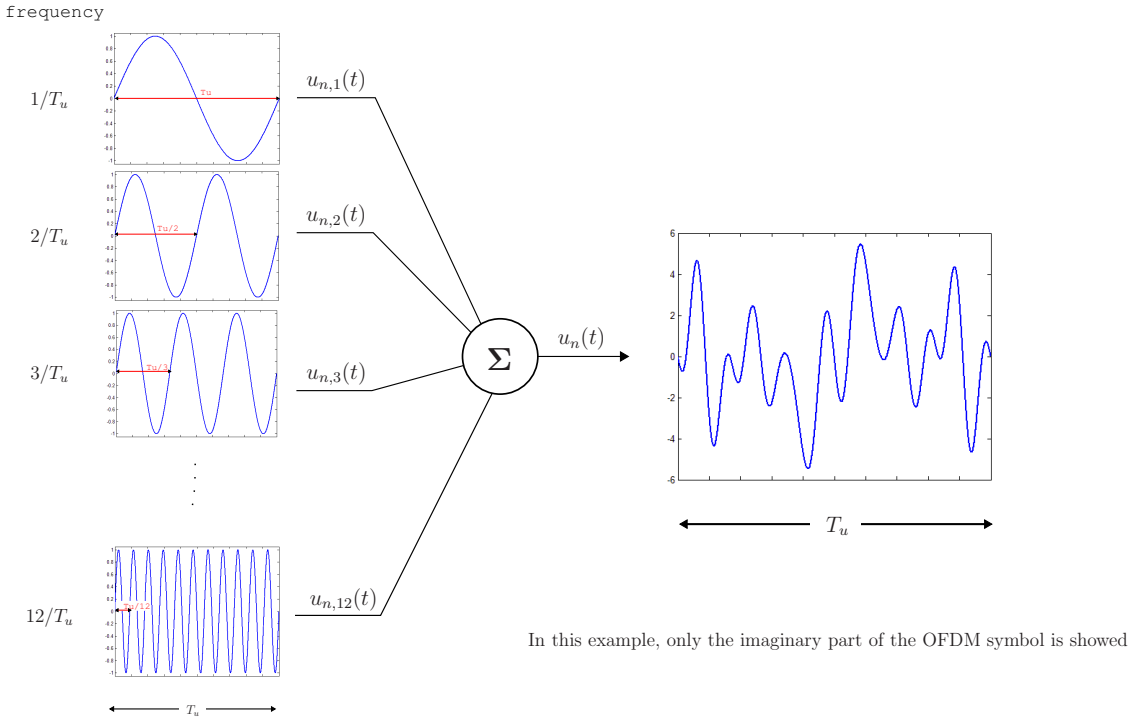

Figure 2.7: Generation of an OFDM symbol with P=12

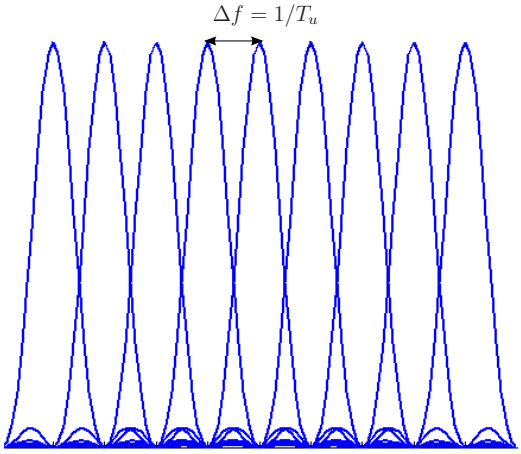

Figure 2.8: Spectrum of an OFDM symbol

subcarriers are grouped into *resource blocks*, where each resource block consists of 12 consecutive subcarriers, occupying 180 kHz [28]. In addition, there is an unused DC-subcarrier in the center of the downlink band, because it may be subject to

high interference, for example, due to local oscillator leakage [29].

In digital systems, the composition of an OFDM symbol is done by applying the Inverse Fast Fourier Transform (IFFT) to the input symbol stream $u_{n,1}, \cdots, u_{n,P}$. This represents a low-complexity implementation which is equivalent to i) modulate the orthogonal subcarriers generating the OFDM symbol of Eq.(2.1) and ii) sample this OFDM symbol with a rate f_s multiple of the subcarrier spacing Δf, i.e. $f_s = 1/T_s = N_{ft} \cdot \Delta f$ such that:

$$u_n[m] = u_n(mT_s) = \sum_{p=1}^{P} u_{n,p} e^{j2\pi p \Delta f (mT_s)} = \sum_{p=1}^{P} u_{n,p} \cdot e^{j2\pi pm/N_{ft}} = \sum_{p=1}^{N_{ft}} u'_{n,p} \cdot e^{j2\pi pm/N_{ft}} \tag{2.3}$$

where $u'_{n,p} = u_{n,p}$ if $0 \leq p < P$ or $u'_{n,p} = 0$ if $P \leq p < N_{ft}$. The term $u_n[m]$ is the m-th sample of the n-th OFDM symbol which has a total of N_{ft} samples, equivalent to a duration of T_u as illustrated in Fig. 2.9.

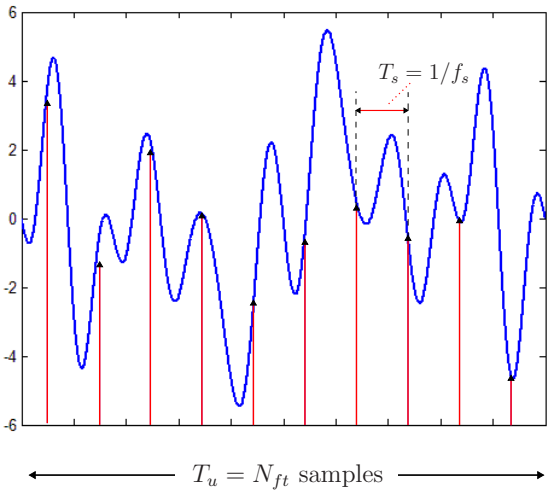

Figure 2.9: OFDM symbol sampled with sampling frequency $f_s = 1/T_s$ through a size-N_{ft} IFFT

As $P\Delta f$ can be seen as the nominal bandwidth of the OFDM signal, this implies that N_{ft} should exceed P with a sufficient margin and the sampling theorem must be fulfilled [9]. At the receiver side, efficient Fast Fourier Transform (FFT) processing can be used for OFDM demodulation after the analog-to-digital (AD) conversion at a sampling rate $f_s = 1/T_s$.

Cyclic-prefix insertion

OFDM modulation handles the spectrum associated with each OFDM subcarrier very tight so that the channel associated with each modulation symbol can be assumed to be flat in the frequency domain [27]. In case of a time-dispersive channel there will be either inter-OFDM-symbol and inter-carrier interference (ICI). To deal with this problem and to make an OFDM signal truly insensitive to time dispersion the so-called *Cyclic Prefix (CP) insertion* is typically used. CP insertion implies that the last part of the OFDM symbol is copied and inserted at the beginning of each OFDM symbol. This technique increases the length of the OFDM symbol from T_u to $T_u + T_{CP}$, where T_{CP} is the length of the CP, with a corresponding reduction in the OFDM symbol rate. In LTE, two CP lengths are defined: the normal and the extended [28]. Although less efficient from a CP-overhead point-of-view, a longer CP can be beneficial in specific environments with very large delay spread, for example in very large cells. [3]. The CP insertion is illustrated in Fig. 2.10 and Fig. 2.11.

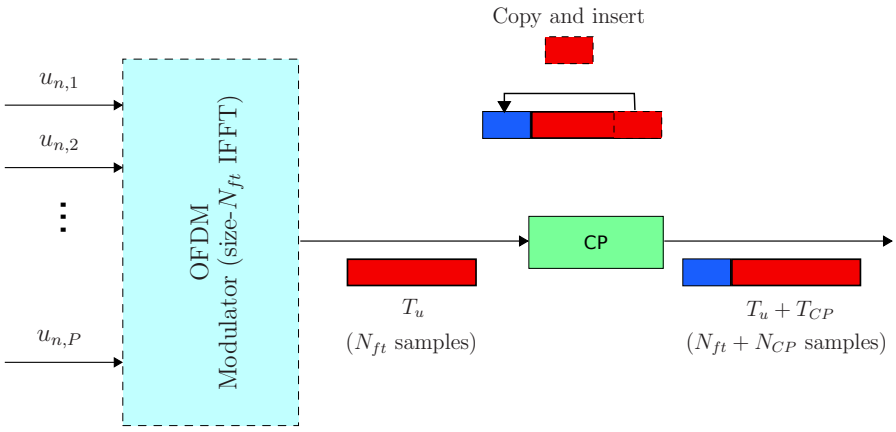

Figure 2.10: Cyclic-prefix insertion

The complete OFDM modulator and demodulator are depicted respectively in Fig. 2.12 and Fig 2.13.

[3] If in large cells the link performance is limited by noise rather than signal corruption due to residual time dispersion not covered by the CP, the additional robustness to radio-channel time dispersion, due to the use of extended CP, may not justify the corresponding loss in terms of reduced received signal energy.

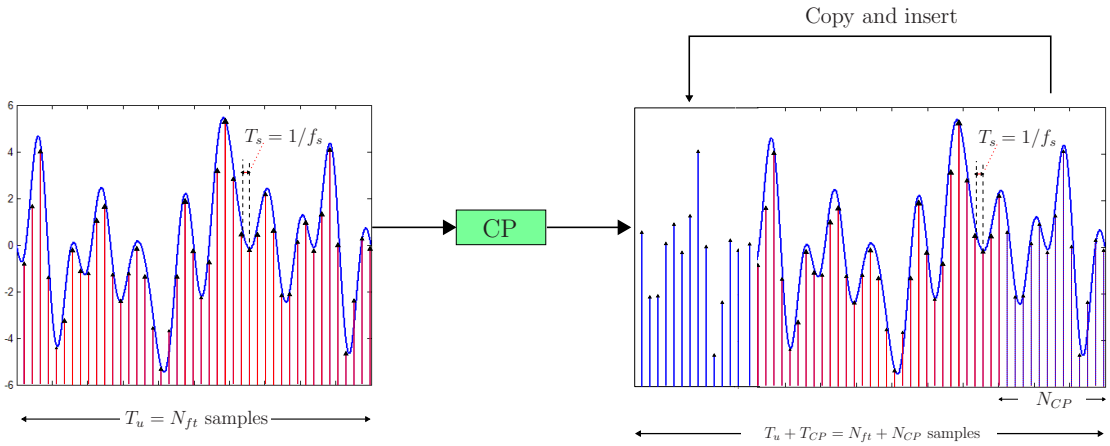

Figure 2.11: Cyclic-prefix insertion

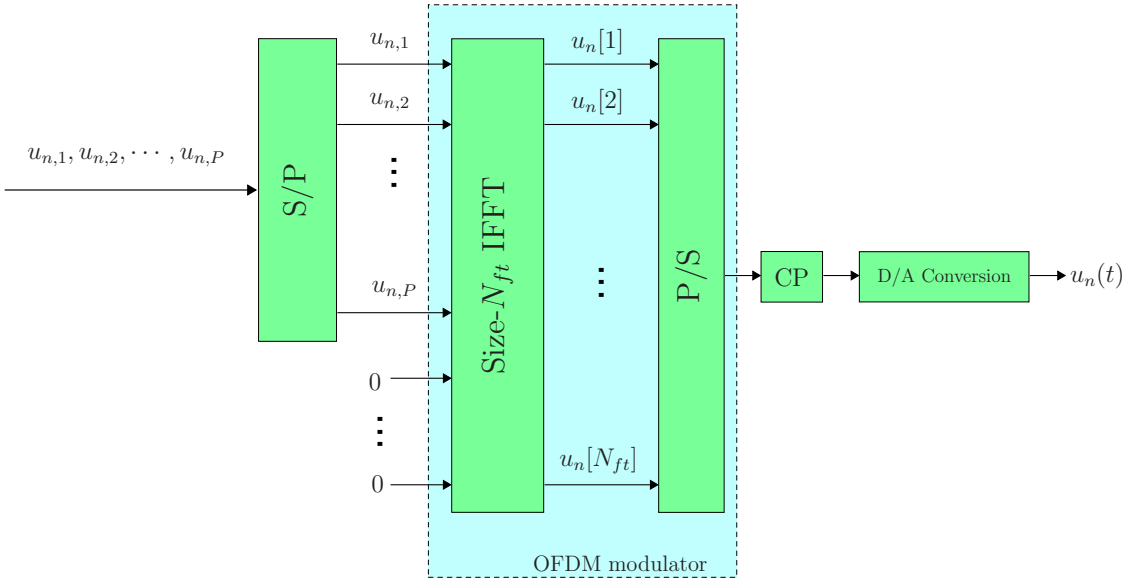

Figure 2.12: OFDM modulation by means of IFFT processing

LTE Time-Domain Structure

The time-domain structure of LTE transmission consist of radio frames of $T_{frame} =$ 10 ms divided in 10 subframes, each with $T_{subframe} = 1$ ms as depicted in Fig. 2.14 Each subframe is composed by two slots of length $T_{slot} = 0.5$ ms and each slot contains 7 and 6 OFDM symbols for normal and extended CP respectively [28]. A detailed description is given in Fig. 2.15.

According to the previous discussion about OFDM, a subcarrier spacing of

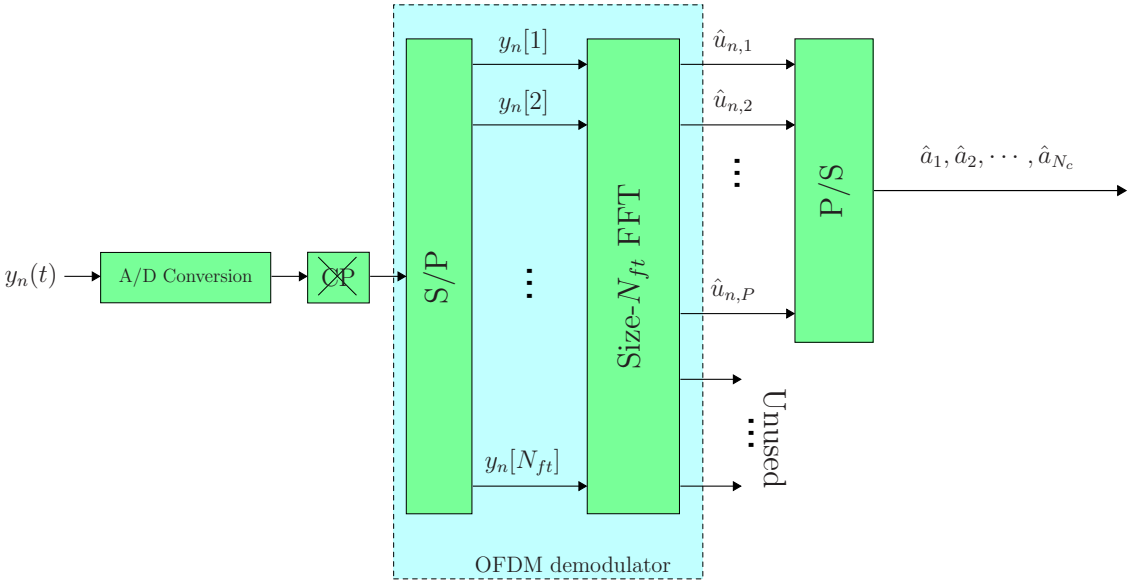

Figure 2.13: OFDM demodulation by means of FFT processing

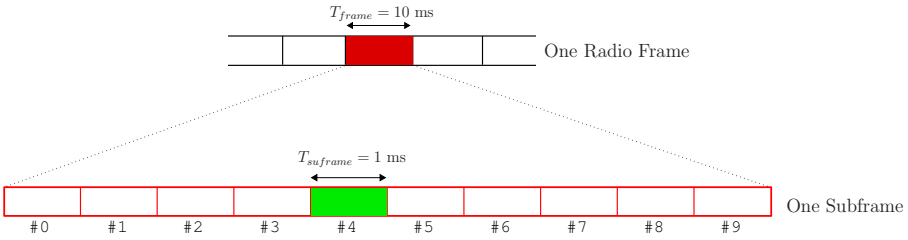

Figure 2.14: LTE high-level time-domain structure

Δf=15kHz corresponds to a useful symbol time of approximately $T_u = 1/\Delta f \simeq 66.7\mu s$. Taking also into account the time-domain structure of OFDM, the LTE *resource blocks* mentioned previously consist of 12 subcarriers during a 0.5ms slot, and is often illustrated in a time-frequency grid. Each resource block thus consists of 84 (7×12) resource elements in case of normal CP and 72 (6×12) resource elements in case of extended CP. Although resource blocks are defined over one slot, the basic time-domain unit for dynamic scheduling in LTE is one subframe, consisting of two consecutive slots (also called a *resource-block pair*). This is illustrated in Fig. 2.16.

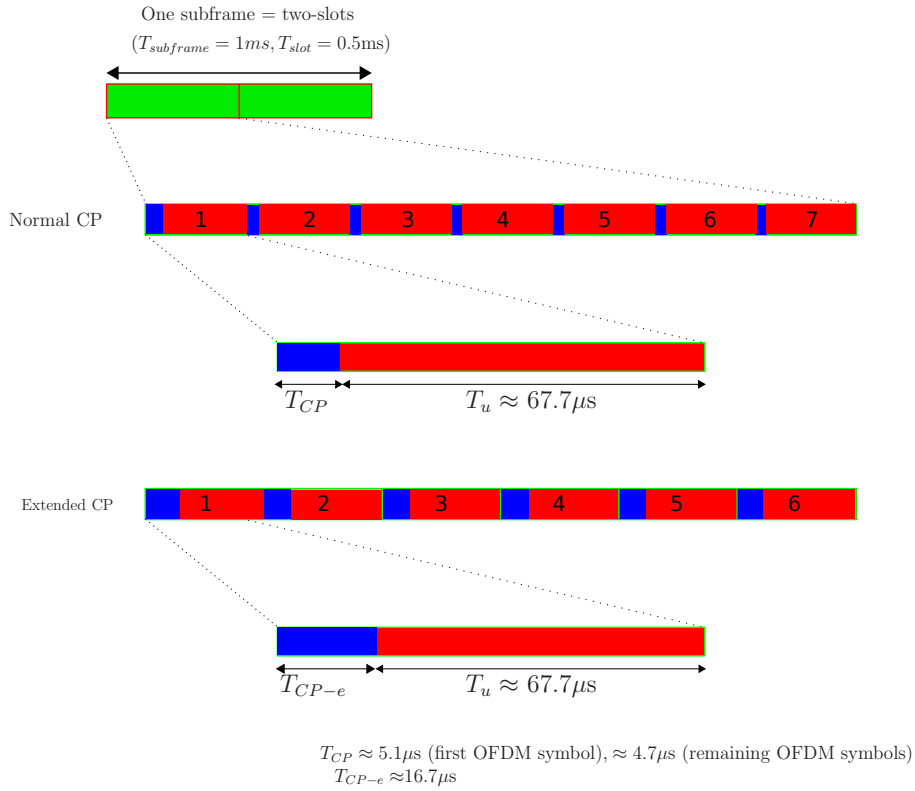

Figure 2.15: Detailed time-domain structure for LTE downlink transmission

Baseband model of OFDM transmission

The time-dispersive channel described in the beginning of this section can be modeled as the following tapped-delayed line (TDL) channel [9]:

$$h(t,\tau) = \sum_{l=0}^{L-1} h_l(t) \cdot \delta(\tau - \tau_l) \tag{2.4}$$

where $h_l(t)$ is the time-varying channel coefficient associated with the l-th path with delay equals τ_l. The term L represents the number of maximum paths. Thus, considering the transmission of the OFDM symbol of Eq. (2.1) through this channel, the received signal, in absence of noise, can be represented by the following linear convolution between $h(t,\tau)$ and $u_n(t)$ [9]:

$$y_n(t) = h(t,\tau) * u_n(t) = \int_{-\infty}^{\infty} h(t,\tau) u_n(t-\tau) d\tau. \tag{2.5}$$

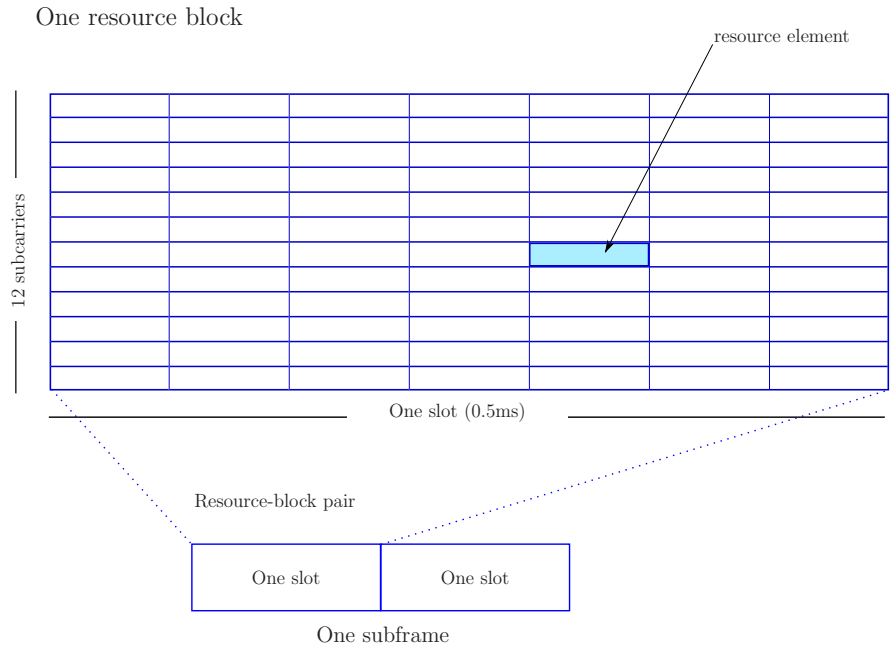

Figure 2.16: Downlink resource block assuming normal CP (i.e. seven OFDM symbols per slot). With extended CP there are six OFDM symbols per slot.

When this signal is sampled at the frequency $f_s = N_{ft}\Delta f$ this can be represented by the following discrete convolution:

$$y[m] = \mathbf{h}_n * \mathbf{u}_n = \sum_{l=0}^{L-1} h_n[m,l]u_n[m-l]. \tag{2.6}$$

where $\mathbf{h}_n = [h_n[1] \;\; h_n[2] \;\; \cdots h_n[N_{ft}]]$ is the vector containing the channel impulse response sampled at rate f_s.

Assuming a sufficiently large CP, the linear convolution of a time-dispersive radio channel will appear as a circular convolution during the demodulation interval T_u [27]. Thus, the combination of OFDM modulation (IFFT processing), a time-dispersive radio channel, and OFDM demodulation (FFT processing) is equivalent to a flat fading model in the frequency-domain, as illustrated in Fig. 2.17. The channel coefficients $h_{n,1}, \cdots, h_{n,P}$ are associated with each subcarrier and can be directly derived from the channel impulse response.

We can represent the baseband model of downlink tranmsision in a resource-element basis of LTE where $u_{n,p}$ is the modulation symbol transmitted over the $p-$th subcarrier ($p = 1, \cdots, 12$) and at the $n-$th OFDM symbol ($n = 1, \cdots, 7$ for normal CP or $n = 1, \cdots, 6$ for extended CP) of a given time-slot. Then, in a

resource-block with 84=7 × 12 resource elements, 84 modulation symbols can be transmitted (in groups of 12) and the equation below:

$$y_{n,p} = u_{n,p} \cdot h_{n,p} + v_{n,p} \tag{2.7}$$

represents a flat fading model per subcarrier.

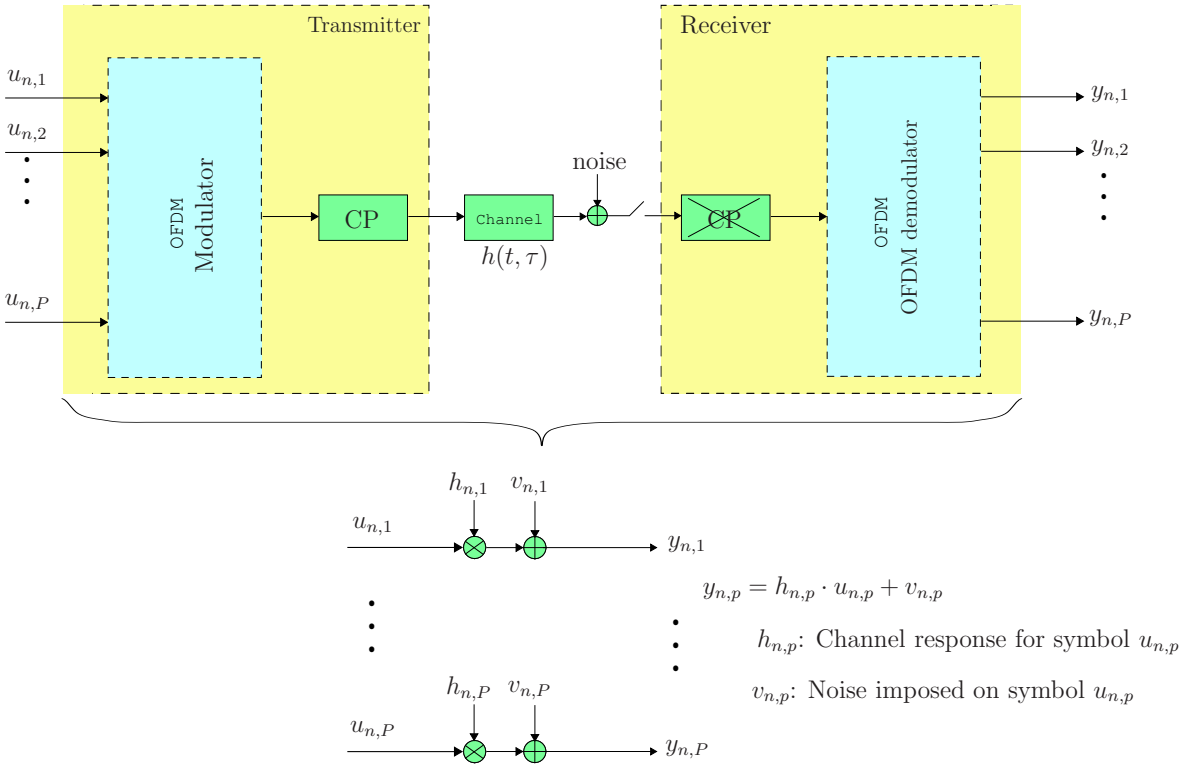

Figure 2.17: Frequency-domain model of OFDM transmission/reception

To properly recover the transmitted symbol for further processing (e.g. data demodulation and channel decoding) the receiver should multiply $y_{n,p}$ by $h^*_{n,p}/|h_{n,p}|^2$ as illustrated in Fig 2.18 and shown below:

$$\hat{u}_{n,p} = \frac{h^*_{n,p}}{|h_{n,p}|^2} y_{n,p} = u_{n,p} + \frac{h^*_{n,p}}{|h_{n,p}|^2} v_{n,p}. \tag{2.8}$$

Channel estimation

To obtain the frequency-domain channel response $h_{n,p}$ we need to consider some channel estimation method. An straightforward approach to estimate the

frequency-domain channel taps $h_{n,p}$ consists in inserting known RS (also called pilot symbols) at regular intervals within the OFDM time-frequency grid. Using knowledge about the RS, the receiver can estimate the frequency-domain channel around the location of these symbols. They should have a sufficiently high density in both the time and the frequency domain to be able to provide estimates for the entire time/frequency grid also in case of radio channels subject to high frequency and/or time selectivity.

Different algorithms can be used for channel estimation, ranging from simple averaging in combination with linear interpolation to Minimum Mean Square Error (MMSE) estimation relying on more detailed knowledge of the channel time/frequency-domain characteristics [27].

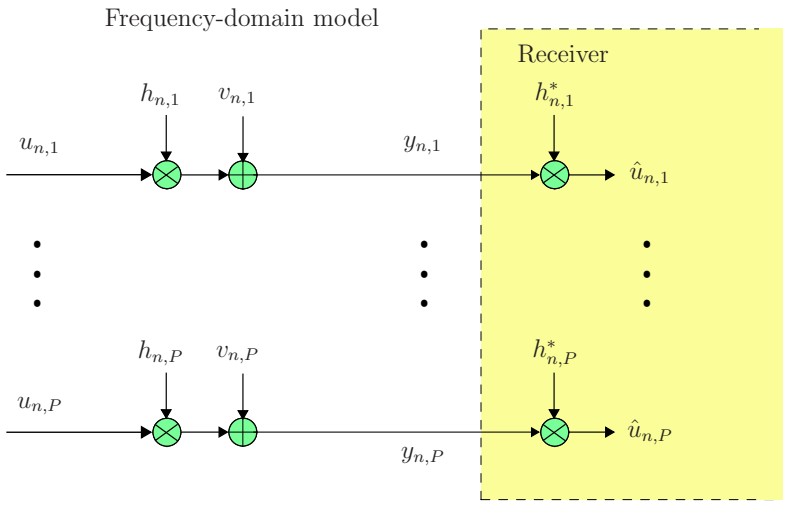

Figure 2.18: Frequency-domain model of OFDM transmission/reception with one-tap equalization at the receiver

2.2 LTE Uplink Transmission

DFT-Spread OFDM (DFTS-OFDM)

A drawback of OFDM modulation is the large variation in the instantaneous power of the transmitted signals. This implies in a reduced power-amplifier efficiency and power-amplifier cost which is particularly critical in the uplink [2, 1]. Thus, single carrier transmission based on DFTS-OFDM is used in the LTE uplink. The scheme can combine the desired propeties of OFDM (the spectrum flexibility) and of a single-carrier scheme (small variation in the instantanous power) [30, 31, 32]. The

smaller the Peak-to-Average Power Ratio (PAPR) of the transmitted signal, the higher the average transmission power can be for a given power amplifier.

In contrast to the non-orthogonal WCDMA/HSPA uplink, which is also based on single carrier transmission, the LTE uplink is based on orthogonal separation of uplink transmissions in the time and/or frequency domain. Thus, as the LTE uplink contains a frequency-domain multiple-access component, the uplink transmission scheme is also referred to as Single Carrier FDMA (SC-FDMA) [31].

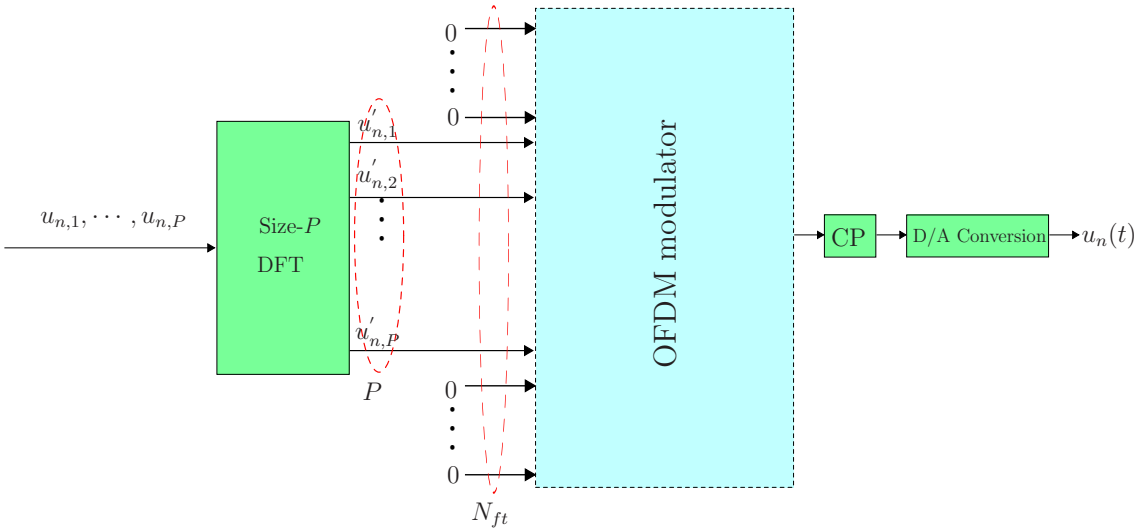

Figure 2.19: DFTS-OFDM signal generation

The basic principle of DFTS-OFDM transmission is shown in Fig. 2.19. The signaling scheme can be interpreted as a normal OFDM with a *Discrete Fourier Transform (DFT)-based precoding*. Similarly to OFDM, a block of P modulation symbols will be transmitted in parallel, however they are firstly applied to a size-P DFT. The output is then applied to consecutive inputs of an OFDM modulator implemented as a size-N_{ft} IFFT. The precoding operation is equivalent to a symbol-to-subcarrier-mapping which spreads each modulation symbol over all mapped subcarriers associated with this OFDM modulator such that:

$$u'_{n,1} = \sum_{p=1}^{P} u_{n,p} \cdot e^{-j2p\pi/P} = u_{n,1} \cdot e^{-j2\pi/P} + u_{n,2} \cdot e^{-j4\pi/P} + \cdots + u_{n,P} \cdot e^{-j2\pi}$$

$$u'_{n,2} = \sum_{p=1}^{P} u_{n,p} \cdot e^{-j4p\pi/P} = u_{n,1} \cdot e^{-j4\pi/P} + u_{n,2} \cdot e^{-j\pi 8/P} + \cdots + u_{n,P} \cdot e^{-j4\pi}$$

$$\vdots \qquad \vdots$$

$$u'_{n,P} = \sum_{p=1}^{P} u_{n,p} \cdot e^{-j2p\pi} = u_{n,1} \cdot e^{-j2\pi} + u_{n,2} \cdot e^{-j4\pi} + \cdots + u_{n,P} \cdot e^{-j2P\pi}$$

will be the inputs associated with the P subcarriers. Keeping the hypothetical implementation with analog OFDM modulators, the signals to be transmitted in parallel would be:

$$\begin{aligned} u_1(t) &= u'_{n,1} \cdot e^{j2\pi\Delta f t} \\ u_2(t) &= u'_{n,2} \cdot e^{j4\pi\Delta f t} \\ \vdots &\qquad \vdots \\ u_P(t) &= u'_{n,P} \cdot e^{j2P\pi\Delta f t} \end{aligned}$$

which summed give the $n-$th DFTS-OFDM symbol:

$$\begin{aligned} u_n(t) &= \sum_{p=1}^{P} u_{n,p}(t) && (2.9) \\ &= \sum_{p=1}^{P}\sum_{q=1}^{P} u_{n,q} \cdot e^{j2\pi[2p\Delta f t - q/Q]} && (2.10) \\ &= u_{n,1} \cdot \left(e^{j2\pi\Delta f t - 1/P} + e^{j4\pi\Delta f t - 1/P} + \cdots e^{j2P\pi\Delta f t - 1/P}\right) && (2.11) \\ &+ u_{n,2} \cdot \left(e^{j2\pi\Delta f t - 2/P} + e^{j4\pi\Delta f t - 2/P} + \cdots e^{j2P\pi\Delta f t - 2/P}\right) && (2.12) \\ &\vdots && (2.13) \\ &+ u_{n,P} \cdot \left(e^{j2\pi\Delta f t - 1} + e^{j4\pi\Delta f t - 1} + \cdots e^{j2P\pi\Delta f t - 1}\right). && (2.14) \end{aligned}$$

Notice in $u_n(t)$ that each modulation symbol $u_{n,p}$ is spread over all subcarriers which are precoded thanks to the previous DFT block. Following the same principles of OFDM modulation in the downlink, DFTS-OFDM is implemented with an IFFT block, which modulates the precoded symbols over the subcarriers and sample the resulting signal. The DFTS-OFDM implementation is depicted in Fig. 2.20.

From this illustration, observe that some inputs of the OFDM modulator are set to zero, and represent the unused part of the spectrum. When $N_{ft} > P$, the transmitted signal has single carrier properties, i.e. a signal with low power variations, and with a bandwidth that depends on P. Assuming a sampling rate f_s at the output of the OFDM modulator, the nominal bandwidth of the transmitted signal will be $BW = (P/N_{fs})f_s$. Thus, by varying the parameter P the instantaneous bandwidth of the transmitted signal can be varied, allowing for flexible bandwidth

assignment.

At the receiver, the operations are basically the reverse of those for DFTS-OFDM signal generation as depicted in Fig. 2.20. The frequency-domain model of Fig. 2.18 is also assumed in the case of DFTS-OFDM transmission, where the DFT precoder has as the main functionality the symbol-to-subcarrier mapping.

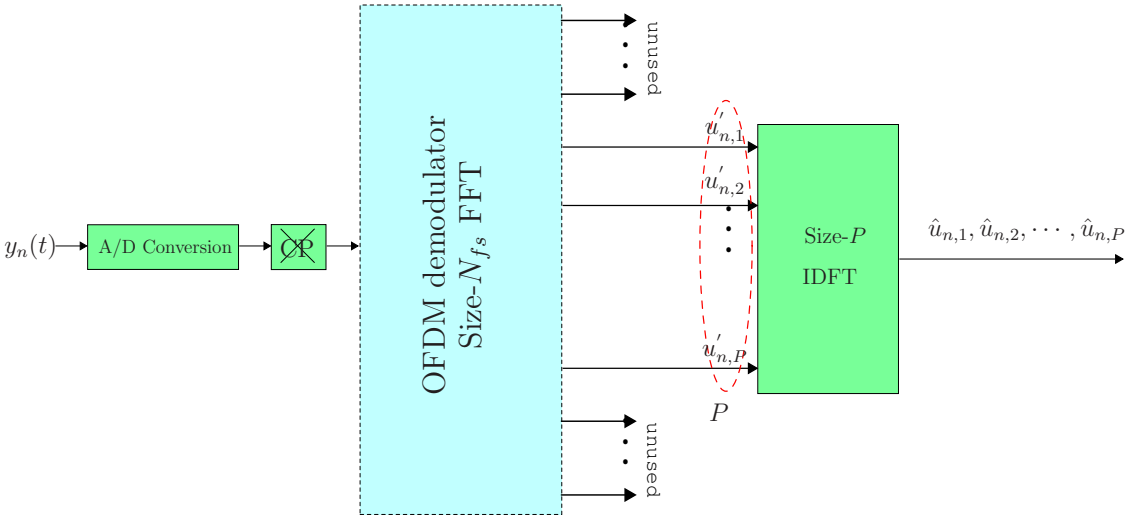

Figure 2.20: Basic principle of DFTS-OFDM demodulation

The basic parameters of the LTE uplink transmission scheme have been chosen to be aligned, as much as possible, with the corresponding parameters of the OFDM-based LTE downlink. Thus, the uplink subcarrier spacing equals $\Delta f = 15$ kHz and resource blocks, consisting of 12 subcarriers are also defined for the LTE uplink [3]. Similar to the downlink, also for the uplink the LTE physical-layer specification allows for a very high degree of flexibility in terms of the overall cell bandwidth by supporting any number of uplink resource blocks ranging from 6 up to a maximum of 110 [3].

Regarding the time-domain structure, the LTE uplink is very similar to the downlink, as illustrated in Fig. 2.15. Each uplink subframe of 1 ms consists of two equally sized slots of length 0.5 ms. Each slot then consists of a number of DFTS-OFDM symbols including the CP. Also similar to the downlink, two CP lengths are defined for the uplink; the normal CP and an extended CP [3]. The resource blocks for LTE uplink have the same structure as the downlink ones, as it was illustrated in Fig. 2.16

In the previous section, we have discussed the need of channel estimation to solve the frequency-domain model of OFDM transmission. The equivalent procedure can

be also applied to DFTS-OFDM, and a similar approach to obtain this one tap channel estimation is considered. The approach is based on known pilot symbols transmitted in specific resource elements distributed over the bandwidth. They are called RS. In the following, the nature of such signals are explained; We also describe their properties and show how they are distributed over a given time-frequency resource grid.

Uplink RS

LTE considers two kinds of RS, being the ones of interest in this work called Demodulation Reference Signals (DRS)[4] needed for coherent demodulation at the eNodeB of the uplink physical channels. An uplink RS is defined as a frequency-domain RS sequence applied to consecutive inputs (consecutive subcarriers) of the OFDM modulator, as depicted in Fig. 2.21. The length of the sequence should be equal to the bandwidth of the corresponding channel in number of subcarriers. Uplink RS should preferably have limited power variations in the frequency to allow for similar channel estimation quality for all frequencies and in the time domain to allow for high power amplifier efficiency. Moreover, many RS sequences of the same length should be available to avoid a planning effort when assigning RS sequences to cells. Such signals are often called specific-cell base sequences or only *base sequences*.

The *Zadoff-Chu sequences* have the property of constant power in both frequency and time domains [33]. Otherwise, due to constraints on the size of the sequences and the number of available sequences, cyclic extensions of Zadoff-Chu sequences are considered for bandwidths larger than or equal to three resource blocks, or 36 subcarriers.

For sequence lengths equal to 12 or 24, corresponding to transmission of one and two resource blocks, respectively, special Quadrature Phase Shift Key (QPSK)-based sequences have instead been found from computer search and are explicitly listed in the LTE specification [3]. An example of sequence is given by $\mathbf{x}^{RS}(1) = [e^{-j\pi/4},\ e^{j\pi/4},\ e^{j3\pi/4},\ e^{-j3\pi/4},\ e^{j3\pi/4},\ e^{j3\pi/4},\ e^{j\pi/4},\ e^{j\pi/4},\ e^{j3\pi/4},\ e^{j\pi/4},\ e^{-j3\pi/4},\ e^{j3\pi/4}]$.

In the case of a sequence length equals 12, there are 30 different base sequences or group of sequences $\mathbf{x}^{RS}(1), \cdots, \mathbf{x}^{RS}(30)$. These base sequences are allocated to a specific cell.

---

[4]There are also the so-called *souding reference signals* (SRS), which are transmitted to allow the network to estimate the uplink *channel quality* at different frequencies

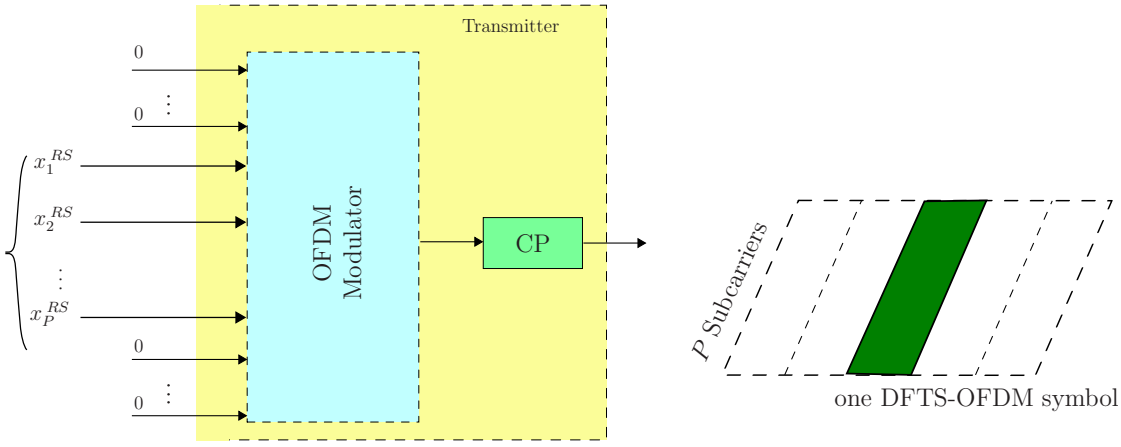

Figure 2.21: Generation of the uplink reference signal from a frequency-domain reference-signal sequence

In some applications where in the uplink the same frequency resource is shared among multiple UEs within the same cell, the cell-specific base sequence $\mathbf{x}^{RS}(c) = [x_1^{RS}(c), \cdots, x_P^{RS}(c)]$ is made orthogonal among the UEs into the same cell through a linear phase rotation in the base sequence. This phase rotation procedure is depicted in Fig. 2.23 where the parameter α takes a value $r\pi/6$ with r ranging from 0 to 11. Then, up to 12 orthogonal RS can be defined from each base sequence.

It is important to mention that the base sequences $\mathbf{x}^{RS}(1), \cdots, \mathbf{x}^{RS}(30)$ have low but still non-zero mutual correlation, but taking any base sequence associated with different phase rotations, the set of sequences generated from the same base sequence can be made completely orthogonal. Then, in the ideal case, there will no be intra-cell interference but it still remains inter-cell interference from neighboring cells using the same phase rotation as illustrated in Fig. 2.22.

Some hopping techniques to avoid or reduce this inter-cell interference can be found in [1, 2], however they are out of the scope of this work.

3 LTE Uplink L1/L2 Signaling

Among the protocol layers of LTE, we are interested in some specific features of Layers 1 and 2 (also denoted as L1 and L2) MAC and PHY. These are the two last layers before the the radio interface.

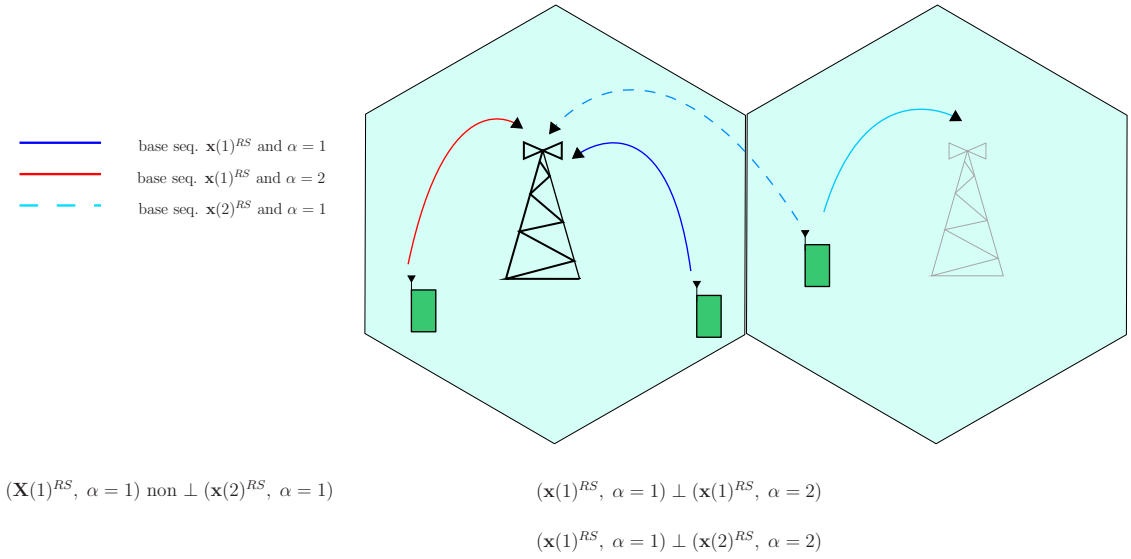

Figure 2.22: Generation of the uplink reference signal from a frequency-domain reference-signal sequence

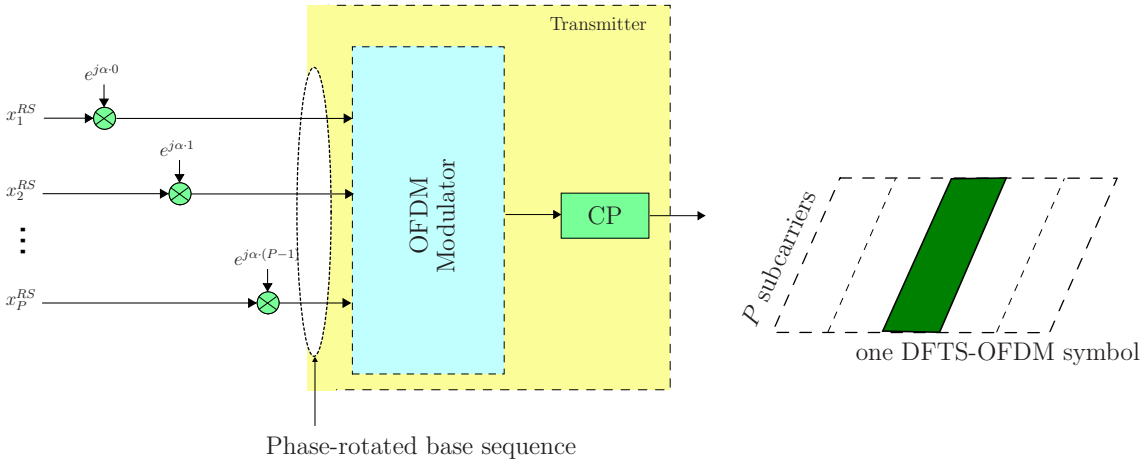

Figure 2.23: Generation of the uplink reference signal from a linear phase-rotation of a base sequence

3.1 MAC Layer

One of the functions of MAC layer is the uplink and downlink scheduling. The scheduler controls to which users the shared resources in the time-frequency grid should be assigned and the data rate to be used for each link.

LTE supports *channel-dependent scheduling*, which consists of allocating resources

to mobile terminals as a function of their channel conditions. This technique is based on a principle called *multiuser diversity*, which basically consists of allocate more resources to terminals with good channel conditions in order to maximizes the system capacity. LTE has access to the channel conditions both on time and frequency domains (resulting from OFDM in the downlink and DFTS-OFDM in the uplink), in contrast to HSPA in which the channel dependent scheduling only considers the time domain channel [1]. To support channel-dependent scheduling in downlink transmission, the terminal may provide the network with *channel-status* reports indicating the instantaneous downlink channel quality in both time and frequency domains.

Channel Status reporting

Although referred to as channel-status reports, what a terminal delivers to the network are not explicit reports of the downlink channel status. Rather, the terminal delivers *recommendations* on what transmission configuration and related parameters the network should use if/when transmitting to the terminal on the downlink shared channel. These reports consist of one or several pieces of information [34]:

- Rank Indication (RI), providing information about the channel rank or, expressed differently, the number of layers that should, preferably, be used for downlink transmission to the terminal, when configured in one of the spatial multiplexing transmission modes supported by LTE.
- Precoding Matrix Indication (PMI), providing a precoder matrix that should, preferably, be used for the downlink transmission. The reported precoder matrix should be determined from the number of layer indicated by the RI.
- Channel Quality Indication (CQI), representing the recommended modulation scheme and coding rate that should preferably be used for the downlink transmission.

Depending on the configuration, the RI, PMI, and CQI in different combinations form the channel status report. The number of bits that represents this report is also defined by the transmission mode and can vary from 1 up to 11 bits [35].

Beyond the channel status reporting, another function of the MAC layer is to provide to the upper layers an error-free reception of transport block, obtained by retransmission schemes of the transport blocks as explained hereafter.

Hybrid Automatic Repeat Request (HARQ)

Link adaptation can be considered to reduce the error rate in a wireless system and to counteract the variations in the received signal [36]. However, receiver noise and unpredictable interference variations cannot be counteracted. Therefore, some form of Forward Error Correction (FEC) is employed in all wireless systems [9]. This technique consists basically in including some redundancy in the transmitted signal.

Another approach to handle transmissions errors is to use Automatic Repeat Request (ARQ), where the receiver uses an error detection code, typically Cyclic Redundancy Check (CRC), to detect if the received packet is in error or not. If no error is detected in the received data packet, the received data is declared error-free and the transmitter is notified by sending a positive Acknowledgement (ACK). On the other hand, if an error is detected, the receiver discards the received data and notifies the transmitter by sending a Negative Acknowledgement (NACK). In response to a NACK, the transmitter retransmits the same information [37]. This principle is illustrated in Fig. 2.24.

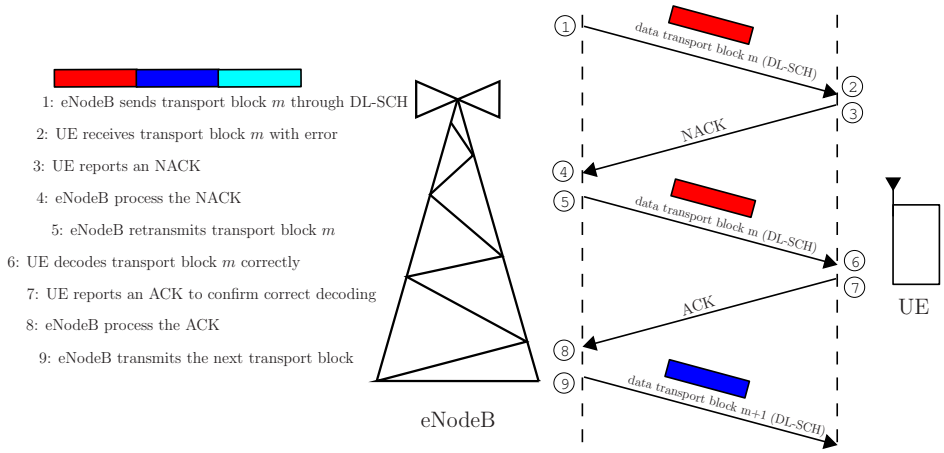

Figure 2.24: ARQ principle

Modern wireless systems, like WCDMA and LTE employ a combination of ARQ and FEC scheme, called *hybrid-ARQ* [38]. Hybrid ARQ uses forward error correcting codes to correct a subset of all errors and rely on error detection to detect uncorrectable errors. Erroneously received packets are discarded and the receiver requests retransmissions of the corrupted packets [37].

In LTE, the hybrid-ARQ acknowledgement bits are received from higher layers. Each positive acknowledgement (ACK) is encoded as a "0" and each negative acknowledgement (NACK) is encoded as a "1" [35].

As mentioned in the first section of this chapter, in LTE radio access network there are specific physical channels without a corresponding transport channel, so-called *L1/L2 control channels*, used for downlink control information, providing the terminal with the necessary information for proper detection and decoding of the downlink data transmission, and uplink control information.

The signaling model of acknowledgements for hybrid-ARQ and the channel status reports in L1/L2 control channels of LTE is one of the focus of this work. In the following, we present the uplink control information and the L1/L2 physical channels.

The uplink L1/L2 control signaling consists of:

- HARQ acknowledgments for received DL-SCH transport blocks.
- Terminal reports related to the downlink channel conditions[5], used as assistance for downlink scheduling
- Scheduling requests, indicating that a mobile terminal needs uplink resources for UL-SCH transmissions.

Uplink L1/L2 control signaling needs to be transmitted on the uplink regardless of whether or not the mobile terminal has any uplink transport channel (UL-SCH) data to transmit and thus regardless of whether or not the mobile terminal has been assigned to any uplink resource for UL-SCH. Then, two different L1/L2 control channels are defined:

- *PUSCH(Physical Uplink Shared Channel) - Simultaneous transmissions on UL-SCH*

  In case the terminal has a valid scheduling grant, that is, resources have been assigned to UL-SCH in the current subframe, the uplink L1/L2 control signaling is time multiplexed with the coded UL-SCH onto the PUSCH prior to DFTS-OFDM modulation. Obviously, as the terminal has been assigned to UL-SCH resources, there is no need to support transmission of the scheduling request in this case.

- *PUCCH(Physical Uplink Control Channel) - No Simultaneous transmissions on UL-SCH*

[5]One or several of CQI, PMI, and RI.

In case the terminal does not have a valid scheduling grant, that is, no resources have been assigned to UL-SCH in the current subframe, a separate physical channel, the PUCCH, is used for transmission of uplink L1/L2 control signaling.

The interest of this work is on the modeling the transmission over PUCCH in its both formats. Moreover, the modeling approach is extended to cover the transmit diversity modes which are under investigation by TSG RAN Work Group one (WG1) of 3GPP.

After this overall description of the LTE radio access network, the next part represents the main focus of this thesis.

3.2 Uplink L1/L2 Control Signaling on PUCCH

The uplink resources are represented in a time-frequency grid with a given number of resource blocks each with 12 subcarriers during 1ms subframe divided in two slots of 0.5 ms. PUCCH is used when no uplink resources has been assigned to a given UE, then, some specific uplink resource must be allocated to transmit L1/L2 control information of this UE. These resources are allocated at the edges of the total available cell bandwidth. Each such resource consists of 12 subcarriers (one resource block) within each of the two slots of an uplink subframe. To provide frequency diversity [39], the resources are frequency hopping on the slot boundary, that is, one frequency resource consists of 12 subcarriers at the upper part of the spectrum within the first slot of a subframe, and an equally sized resource at the lower part of the spectrum during the second slot as illustrated in Fig.2.25.

One resource block (12×15kHz $= 180$ kHz) over 1 subframe (1ms) for control signaling from single UE is a waste of resources. Therefore, to efficiently exploit the uplink resources, multiple UEs share the same resources. In this case, the UEs are multiplexed over the frequency domain by assigning the different UEs to different orthogonal phase rotations of a cell-specific base sequence. Then, the resource used by PUCCH for a given UE is therefore specified not only by the time-frequency resource blocks of Fig. 2.25, but also by the applied phase rotation. Similarly to the case of RS, there are up to 12 different phase rotations specified in LTE, providing up to 12 different orthogonal sequences associated with each base sequence. However, in the case of frequency selective channels, not all the 12 phase rotations can be used if orthogonality is to be ensured. Typically, up to six rotations are considered "usable" in a cell, increasing the capacity of PUCCH by the number of available rotations.

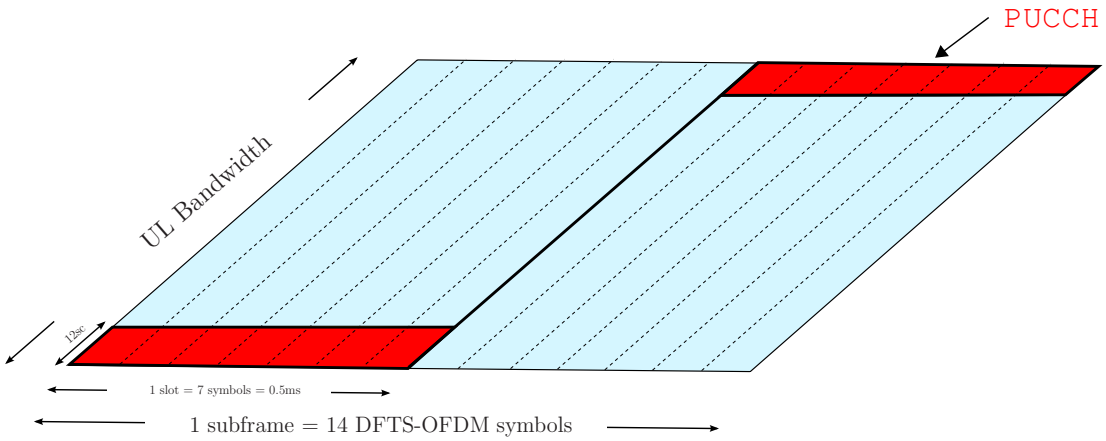

Figure 2.25: Uplink L1/L2 control signaling transmission on PUCCH

As mentioned early, uplink L1/L2 control signaling includes HARQ acknowledgements, channel status reports, and scheduling requests. Different combinations of these types of messages are possible, and there are two general formats for PUCCH, each capable of carrying a different number of bits. The transmissions in both formats are considered in this work using a tensor signal modelling approach, which will be the subject of the next Chapter. In the following, we present PUCCH Format 2.

3.3 PUCCH Format 2: Channel Status Report

Channel status reports are used to provide the eNodeB with an estimate of the channel properties at the terminal to aid channel dependent scheduling. Each report consists of B bits per subframe that ranges from 1 up to 11 bits [35]. These information bits are coded with a linear Reed-Muller block code with code rate given by $B/20$ [37]. Then, these 20 bits are QPSK modulated and converted into 10 symbols. The first five symbols are transmitted in the first slot and the remaining ones in the second slot allocated for PUCCH. Assuming normal CP, 7 DFTS-OFDM symbols, indexed by $n = 1, \cdots, 7$ are transmitted in the first slot. Two out of these seven, associated with $n = 2$ and $n = 6$, are used as reference-signals to allow coherent demodulation at the eNodeB[6]. . The structure of PUCCH

[6]When extended CP is considered, six DFTS-OFDM symbols are transmitted per slot and there is only one reference-signal per slot. This symbol is associated with $n = 4$ concerning the first slot.

Format 2 is illustrated in Fig.3.2

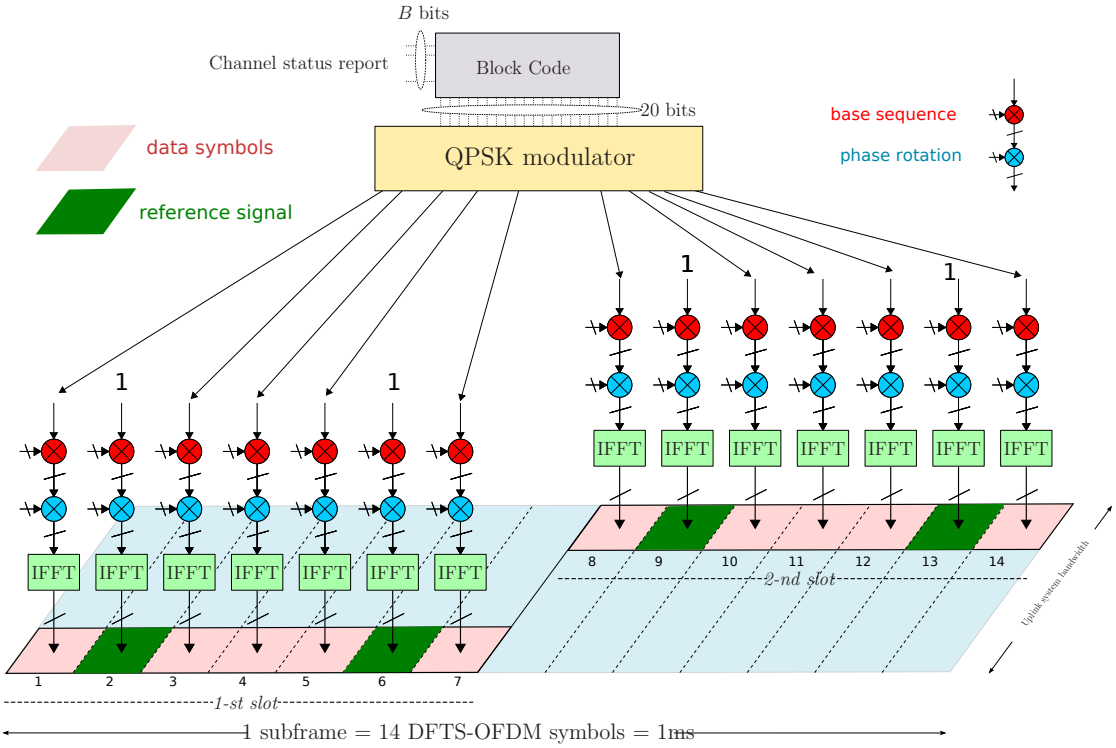

Figure 2.26: Uplink L1/L2 control signaling transmission on PUCCH Format 2

The number of symbols used as reference-signals per slot, denoted N_{RS}, results from a trade-off between channel estimation accuracy and the supportable code rate for the control signalling bits [2]. For a small number of control information bits with a low Signal-to-Noise Ratio (SNR) operating point (for a typical 10^{-2} target error rate), improving the channel estimation accuracy by using more reference-signal symbols (e.g. N_{RS} =3) is more beneficial than being able to use a lower channel code rate. However, with larger numbers of control information bits the required SNR operating point increases, and the higher code rate resulting from a larger overhead of reference-signal symbols becomes more critical, thus favouring fewer symbols. In view of these factors, two reference-signal symbols per slot (in case of normal CP) were considered to provide the best trade-off in terms of performance and reference-signal overhead, given the required payload sizes.

Multiple UEs share the same resources thanks to 12-length orthogonal sequences, composed by a phase rotation of a cell-specific base sequence as depicted in

Fig. 2.21[7]. In conventional OFDM (similar to DFTS-OFDM) transmission, a symbol stream $u_{n,1}, \cdots, u_{n,P}$ is transmitted in parallel through P subcarriers during the n-th symbol period, as it was shown in Fig. 2.19. However, in the case of data symbols, the input stream is a function of the same QPSK symbol which is spread over the 12 subcarriers to obtain a SNR gain. In the case of the RS, the modulation symbol is replaced by ones, which are known at the eNodeB.

3.4 PUCCH Format 1: HARQ acknowledgements and scheduling requests

HARQ acknowledgments are used to acknowledge the reception of one (or two in the case of spatial multiplexing) transport blocks on the DL-SCH. HARQ acknowledgments is only transmitted if the terminal has correctly received the control signaling related to DL-SCH transmission.

Scheduling requests are used to request resources for uplink data transmission. Obviously, a scheduling request should only be transmitted when the terminal is requesting resources, otherwise the terminal should be silent to save battery resources and do not create unnecessary interference. Hence, unlike HARQ acknowledgements, no explicit information bit is transmitted by the scheduling request; the information is instead conveyed by the presence (or absence) of energy on the corresponding PUCCH. However, the scheduling request shares the same PUCCH format as the HARQ acknowledgement. This is referred to as *PUCCH Format 1*. This format has a similar structure as Format 2 with some particular features, as illustrated in Fig. 2.27.

For transmission of a HARQ acknowledgement, a single bit is used to generate a Binary Phase-Shift Keying (BPSK) symbol (in case of downlink spatial multiplexing the two acknowledgement bits are used to generate a QPSK symbol). For a scheduling request, in contrast, the BPSK/QPSK symbol is replaced by a constellation point treated as a negative acknowledgement at the eNodeB. The modulation symbol is then used to generate the signal to be transmitted in each of the two PUCCH slots.

Similar to PUCCH Format 2, there are 7 DFTS-OFDM symbols per slot for normal CP or 6 in the case of extended CP. The same 12-length sequence defined to Format 2 is used to multiplex different UEs over the frequency domain. Reference signals

[7]Notice that it follows the same procedure that handles the reference-signals orthogonal

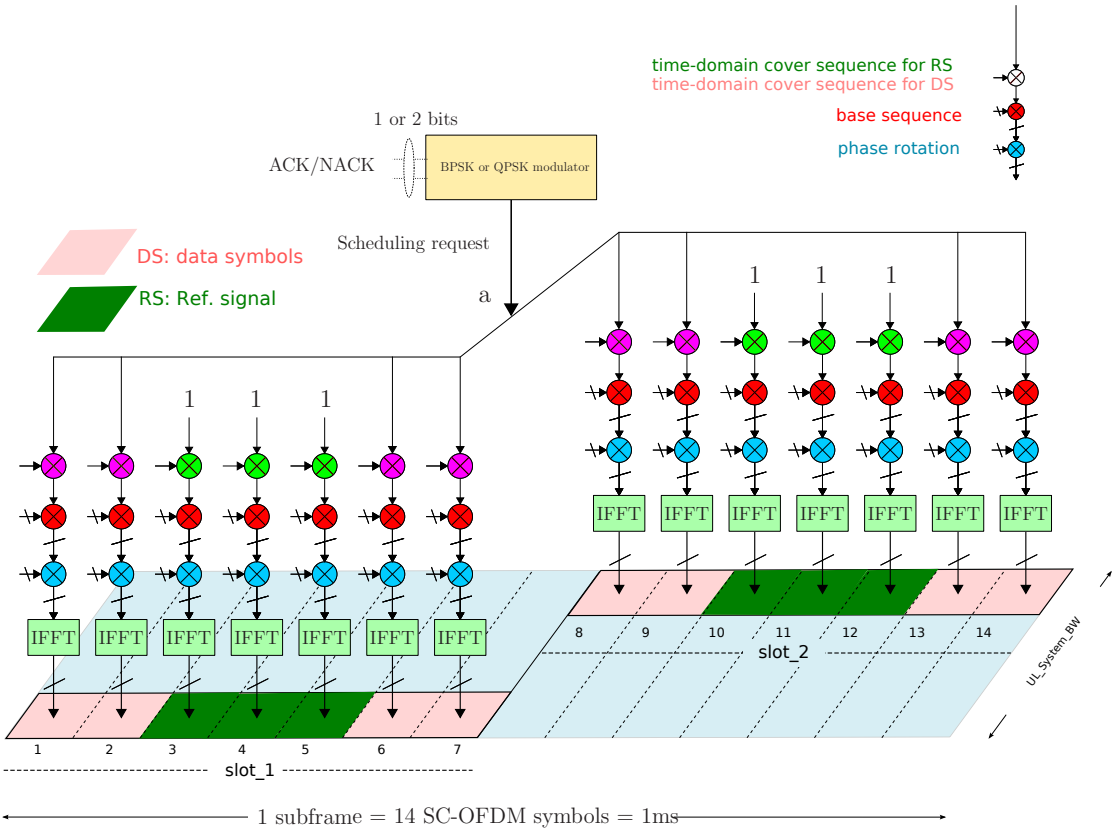

Figure 2.27: Uplink L1/L2 control signaling transmission on PUCCH Format 1

are transmitted in the symbols associated to $n = 3, 4$ and 5. [8]. Due to the small number of ACK/NACK bits, three RS are used to improve the channel estimation accuracy for a lower SNR operating point as compared to Format 2. The use of orthogonal sequences for each UE increases the capacity by a factor of 6. However, in Format 1, this would result in unnecessary low capacity.

The number of supported time-domain cover sequences for ACK/NACK data is limited by the number of RS symbols, as the multiplexing capacity of RS is smaller than that of the data symbols due to a smaller number of RS symbols. For example, in the case of six phase rotations and three time-domain cover sequences, acknowledgments from 18=6 $\times$ 3 different UEs can be multiplexed. Thus, since

[8]For extended CP, there are two reference symbols per slot. They are placed in the third and fourth Single Carrier OFDM (SC-OFDM) symbols in each slot.

each cell-specific base sequence can be used for up to 18 (or 12) different terminals (assuming only 6 phase rotations per base sequence), an up to threefold improvement in the PUCCH capacity is obtained compared to the case with no cover sequence.

The number of supported time-domain cover sequences for ACK/NACK data is limited by the number of RS symbols, as the multiplexing capacity of RS is smaller than that of the data symbols due to smaller number of RS symbols. For example, assuming normnal CP, six phase rotations and three time-domain cover sequences are considered, such that the capacity is increases from 6 to $18{=}6 \times 3$ terminals.

Thus, since each cell-specific base sequence can be used for up to 18 different terminals (assuming only 6 phase rotations per base sequence), a threefold improvement in the PUCCH capacity is compared to the case with no cover sequence.

CHAPTER 3

PUCCH Format 2 and PARAFAC Model

In the first Chapter, the theory behind tensor models has been introduced. In Chapter 2, we reviewed the most important features of the 3GPP LTE RAN, including the uplink control channel PUCCH. Herein, both subjects are linked, i.e., the modeling of PUCCH Format 2 transmission relying on tensor algebra is presented as a new alternative to traditional models based on matrices. Taking advantage of this approach, we propose a multi-user receiver for inter-cell interference reduction in PUCCH LTE Format 2. The proposed receiver is based on the algorithm ALS which exploits the PARAFAC tensor model of PUCCH Format 2. We show that this modeling allow for improved channel estimation at the price of more iterations of the ALS compared to conventional receivers based on LS. We analyze our proposal in both single-cell and multi-cell scenarios. It is shown that in the multi-cell case, the receiver is able to operate in two network configurations. The first one assumes the eNodeBs are connected, having some kind of centralized control. This handle the first configuration very suitable to be deployed in CoMP systems, expected to be included in LTE Release 10. The second configuration consider the eNodeBs have an independent control, which is the case of the existing architeture of LTE Release 8. In the former configuration, we resort to the uniqueness of PARAFAC to apply a semi-blind version of the proposed receiver to estimate and cancel the interference. At the end of the chapter we show some preliminary simulation results in order to justify the further performance gains encountered in Chapter 6.

1 Baseband Model of PUCCH Format 2

As it has been shown in the previous Chapter, the LTE uplink transmission is based on DFTS-OFDM. The baseband model is depicted in Fig. 3.1, where the DFT and Inverse DFT (IDFT) precoders can be interpreted as blocks that respectively handle the subcarriers mapping and demapping [31]. Similarly to the modeling of OFDM transmission described by Eq. (2.7), the combination of subcarrier mapping with IFFT processing, time-dispersive radio channel, FFT processing and subcarrier demapping at the receiver, can be modeled by a flat fading channel coefficient per subcarrier in the frequency domain, i.e.:

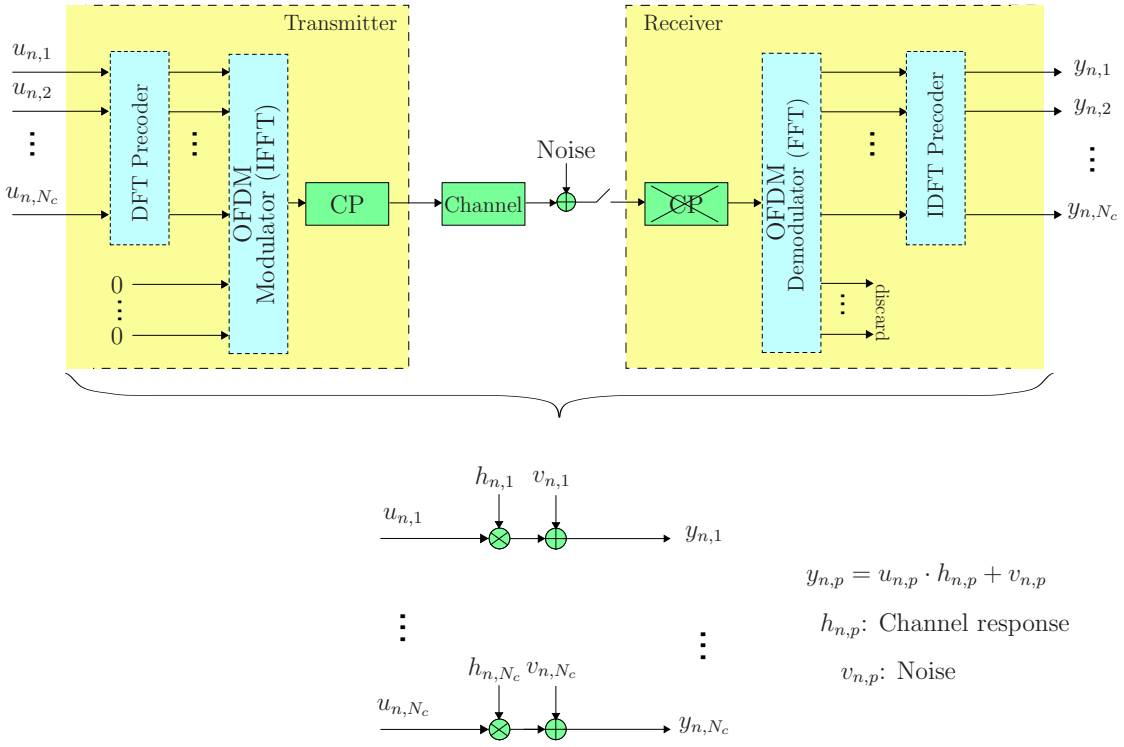

Figure 3.1: Frequency-domain model of DFTS-OFDM transmission/reception

$$y_{n,p} = x_{n,p} + v_{n,p} = u_{n,p} \cdot h_{n,p} + v_{n,p} \tag{3.1}$$

where $u_{n,p}$, $h_{n,p}$ and $v_{n,p}$ are respectively the modulation symbol, channel coefficient and noise sample associated with the n-th DFTS-OFDM symbol at the p-th subcarrier. The term $x_{n,p}$ denotes the received signal in absense of noise. In the baseband model of PUCCH Format 2, we consider the signaling only of the *first slot*. We assume along this Chapter that the UEs are configured with normal

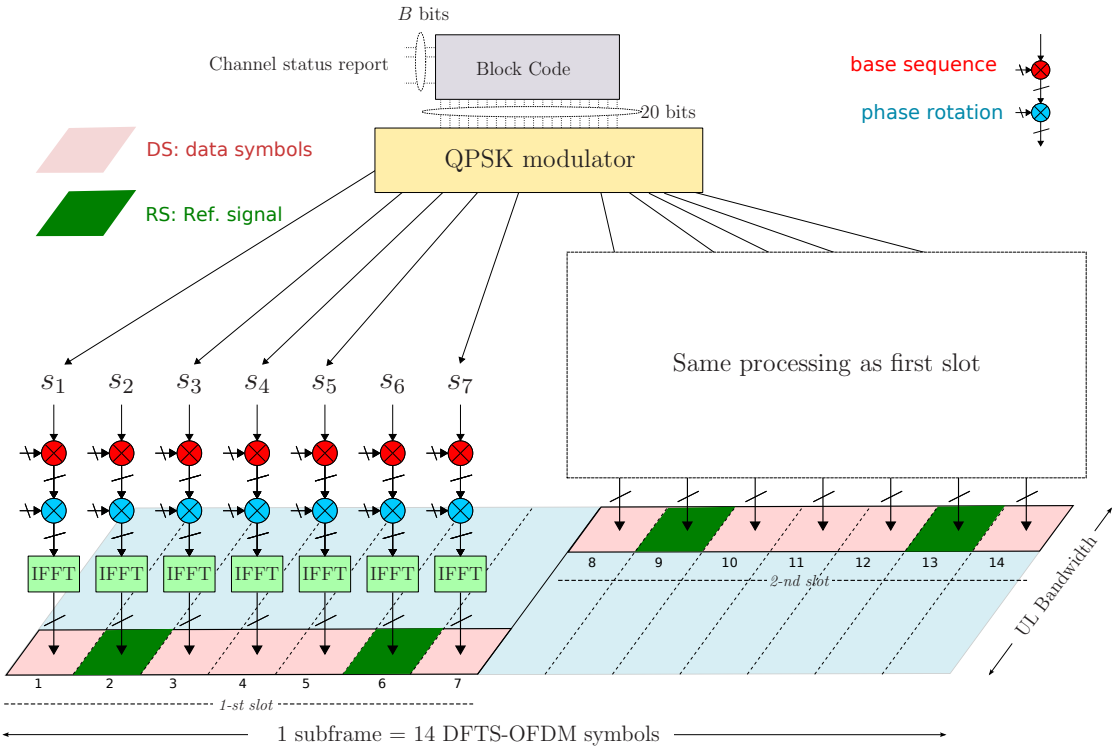

Figure 3.2: Time-frequency structure of PUCCH Format 2

CP, which means that 7 DFTS-OFDM symbols are transmitted per slot where each of these symbols is associated with a QPSK modulation symbol denoted s_n (c.f. Ch. 2 Sec.3.3).

Symbol vector

Considering the processing of the first slot, the modulation symbols are ordered in a vector, called herein *symbol vector*, defined as:

$$\mathbf{s} = \begin{bmatrix} s_1 \\ s_2 \\ s_3 \\ s_4 \\ s_5 \\ s_6 \\ s_7 \end{bmatrix} \in \mathbb{C}^{7\times 1}. \tag{3.2}$$

Two (out of these 7) symbols are used as RS, namely $s_2 = s_6 = 1$[1]. Fig. 3.2 depicts the processing of the first slot in the time-frequency domain.

Coding vector

The physical resources allocated to PUCCH consist of 12 subcarriers in the edges of the bandwidths, as depicted in Fig. 3.3.

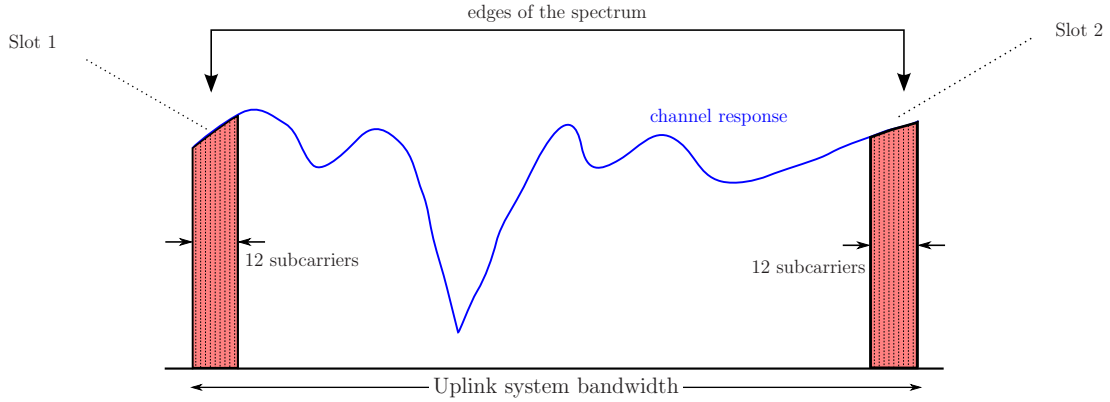

Figure 3.3: Spectrum allocation for PUCCH

Each modulation symbol s_n is spread over the 12 subcarriers through a length-12 frequency-domain sequence composed by the base sequence denoted $\mathbf{x} = [x_1, \cdots, x_{12}]$ which is phase rotated by $e^{j\alpha\cdot 0}, e^{j\alpha\cdot 1}, ..., e^{j\alpha\cdot 11}$ (c.f. Sec. 2.2, Ch. 2). The resulting sequence is organized in the so-called *coding vector*, defined for a given UE as:

$$\mathbf{w} = \begin{bmatrix} w_1 \\ w_2 \\ \vdots \\ w_{12} \end{bmatrix} = \begin{bmatrix} x_1 e^{j\alpha\cdot 0} \\ x_2 e^{j\alpha\cdot 1} \\ \vdots \\ x_{12} e^{j\alpha\cdot 11} \end{bmatrix} \in \mathbb{C}^{12\times 1} \tag{3.3}$$

where $w_p = x_p \cdot e^{j\alpha\cdot(p-1)}$. At this point we assume $\alpha = 1$. In the multi-user model we show how α plays an important role.

[1] In the case of extended CP configuration, 6 DFTS-OFDM symbols are transmitted and there is only one RS per slot. In this case, $s_4 = 1$.

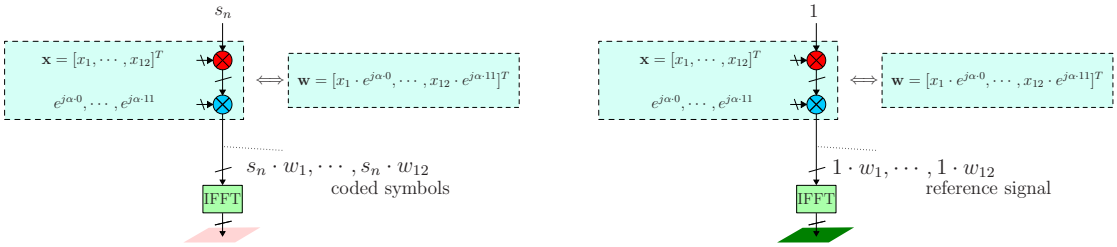

Figure 3.4: Transmit signal composition for PUCCH Format 2

The stream associated with each DFTS-OFDM symbol is composed by the same modulation symbol s_n multiplied by a term of the coding vector, resulting in:

$$x_{n,p} = u_{n,p} \cdot h_{n,p} = s_n \cdot w_p \cdot h_{n,p} + v_{n,p}. \tag{3.4}$$

This operation is illustrated in Fig. 3.4 for both data symbols and RS.

Channel vector h

In the frequency-domain, since the 12 subcarriers in a given resource block are highly correlated, we assume they are associated with the same fading channel coefficient. We also assume the channel is non time-varying following a Rayleigh fading model [9].

We consider the eNodeB is equipped with 2 receive antennas, which is typically the number considered in LTE[2]. Then, the channel coefficients associated with both receive antennas are organized in a *channel vector*, defined as:

$$\mathbf{h} = \begin{bmatrix} h_1 \\ h_2 \end{bmatrix} \in \mathbb{C}^{2\times 1}. \tag{3.5}$$

The channel coefficients are spatially correlated and the Kronecker model [40] is used to model the spatial correlation, in accordance with the LTE specifications [41]. Moreover, three channel models are specified in LTE for performance evaluation: *EPA (Extended Pedestrian A), EVA (Extended Vehicular A) and ETU (Extended Typical Urban)* [41]. These models will be revisited in Chapter 6, where the performance results are presented.

[2]It is worth mentioning that the eNodeB can be equipped with more receive antennas. In that case, our model can be easily adapted.

Hence, the received signal associated with the n-th DFTS-OFDM symbol, p-th subcarrier and k-th receive antenna in absence of noise can be expressed as:

$$x_{n,p,k} = s_n \cdot w_p \cdot h_k. \tag{3.6}$$

2 Tensor Model of PUCCH Format 2

Single-user model as a rank-one tensor

From Eq. (3.4), the signal transmitted in the *first slot* for a given UE can be written as:

$$\mathbf{s}\circ\mathbf{w} = \mathbf{s}\mathbf{w}^T = \begin{bmatrix} s_1 \\ 1 \\ s_3 \\ s_4 \\ s_5 \\ 1 \\ s_7 \end{bmatrix} \begin{bmatrix} w_1 & w_2 & \cdots & w_{12} \end{bmatrix} = \begin{bmatrix} s_1.w_1 & s_1.w_2 & \cdots & s_1.w_{12} \\ 1.w_1 & 1.w_2 & \cdots & 1.w_{12} \\ s_3.w_1 & s_3.w_2 & \cdots & s_3.w_{12} \\ s_4.w_1 & s_4.w_2 & \cdots & s_4.w_{12} \\ s_5.w_1 & s_5.w_2 & \cdots & s_5.w_{12} \\ 1.w_1 & 1.w_2 & \cdots & 1.w_{12} \\ s_7.w_1 & s_7.w_2 & \cdots & s_7.w_{12} \end{bmatrix} \in \mathbb{C}^{7\times 12} \tag{3.7}$$

where $\circ$ denotes the outer product of two vectors (c.f. Def. 1.3.).

Furthermore, notice that (3.6) is equivalent to (1.7), which defines a $7\times12\times2$ third-order tensor of rank one. The received signal on PUCCH Format 2, in absence of noise, can therefore be modeled as follows:

$$\mathcal{X} = \mathbf{s} \circ \mathbf{w} \circ \mathbf{h} \tag{3.8}$$

where $\mathbf{s}$, $\mathbf{w}$ and $\mathbf{h}$ are the *symbol, coding* and *channel* vectors.

Multi-user model as a rank-R tensor

In PUCCH Format 2, the signals of multiple terminals are multiplexed using a specific coding vector associated with the r-th UE defined as:

$$\mathbf{w}^{(r)} = \begin{bmatrix} w_1^{(r)} \\ w_2^{(r)} \\ \vdots \\ w_{12}^{(r)} \end{bmatrix} = \begin{bmatrix} x_1 e^{j\alpha_r \cdot 0} \\ x_2 e^{j\alpha_r \cdot 1} \\ \vdots \\ x_{12} e^{j\alpha_r \cdot 11} \end{bmatrix} \in \mathbb{C}^{12\times 1} \tag{3.9}$$

where $\alpha_r = 2r \cdot \pi/6$ with $r = 0, ..., 5$ in order to guarantee the orthogonality among the coding vectors within the same cell.

Accounting the contribution of the R terminals, the received signal is modeled as a $7 \times 2 \times 12$ tensor of rank R, composed by the sum of R tensors of rank one, i.e.:

$$\mathcal{X} = \sum_{r=1}^{R} \mathcal{X}^{(r)} = \sum_{r=1}^{R} \mathbf{s}^{(r)} \circ \mathbf{w}^{(r)} \circ \mathbf{h}^{(r)} \tag{3.10}$$

where $\mathcal{X}^{(r)}$ is the signal associated with the r-th UE. Alternatively, in scalar notation, this signal is written as:

$$x_{n,p,k} = \sum_{r=1}^{R} s_n^{(r)} \cdot w_p^{(r)} \cdot h_k^{(r)} \tag{3.11}$$

where the system parameters are defined by:

$$\mathbf{s}^{(r)} = \begin{bmatrix} s_1^{(r)} \\ 1 \\ s_3^{(r)} \\ s_4^{(r)} \\ s_5^{(r)} \\ 1 \\ s_7^{(r)} \end{bmatrix} \in \mathbb{C}^{7\times 1} \quad \mathbf{w}^{(r)} = \begin{bmatrix} w_1^{(r)} \\ w_2^{(r)} \\ \vdots \\ w_{12}^{(r)} \end{bmatrix} \in \mathbb{C}^{12\times 1} \quad \mathbf{h}^{(r)} = \begin{bmatrix} h_1^{(r)} \\ h_2^{(r)} \end{bmatrix} \in \mathbb{C}^{2\times 1}.$$

The parameter set that composes the model can be grouped in the following component matrices:

$$\mathbf{S} = \begin{bmatrix} \mathbf{s}^{(1)} & \mathbf{s}^{(2)} & \cdots & \mathbf{s}^{(R)} \end{bmatrix} \in \mathbb{C}^{7\times R} \tag{3.12}$$

$$\mathbf{H} = \begin{bmatrix} \mathbf{h}^{(1)} & \mathbf{h}^{(2)} & \cdots & \mathbf{h}^{(R)} \end{bmatrix} \in \mathbb{C}^{2\times R} \tag{3.13}$$

$$\mathbf{W} = \begin{bmatrix} \mathbf{w}^{(1)} & \mathbf{w}^{(2)} & \cdots & \mathbf{w}^{(R)} \end{bmatrix} \in \mathbb{C}^{12\times R} \tag{3.14}$$

which are respectively, the *symbol*, *channel* and *coding* matrices.

As a third-order tensor, the received signal $\mathcal{X}$ has three unfolded representations

$\mathbf{X}_1, \mathbf{X}_2, \mathbf{X}_3$ defined as (c.f. Def. 1.2):

$$\mathbf{X}_1 = \begin{bmatrix} \mathbf{X}_{1..} \\ \vdots \\ \mathbf{X}_{7..} \end{bmatrix} \in \mathbb{C}^{84\times 2},\ \mathbf{X}_2 = \begin{bmatrix} \mathbf{X}_{.1.} \\ \vdots \\ \mathbf{X}_{.12.} \end{bmatrix} \in \mathbb{C}^{24\times 7} \text{ and } \mathbf{X}_3 = \begin{bmatrix} \mathbf{X}_{..1} \\ \mathbf{X}_{..2} \end{bmatrix} \in \mathbb{C}^{14\times 12}, \tag{3.15}$$

where $X_{n..} \in \mathbb{C}^{12\times 2}$ is the n-th slice considering the time-domain fixed, $X_{.p.} \in \mathbb{C}^{2\times 7}$ is the p-th slice in the frequency-domain, and $X_{..k} \in \mathbb{C}^{7\times 12}$ is the k-th slice in the spatial-domain.

From (1.20)-(1.23), the three unfolded representations $\mathbf{X}_1, \mathbf{X}_2, \mathbf{X}_3$ of the received signal tensor $\mathcal{X}$ can be written compactly as:

$$\mathbf{X}_1 = \mathbf{Z}_1\mathbf{H}^T \in \mathbb{C}^{84\times 2} \tag{3.16}$$

$$\mathbf{X}_2 = \mathbf{Z}_2\mathbf{S}^T \in \mathbb{C}^{24\times 7} \tag{3.17}$$

$$\mathbf{X}_3 = \mathbf{Z}_3\mathbf{W}^T \in \mathbb{C}^{14\times 12} \tag{3.18}$$

where

$$\mathbf{Z}_1 = (\mathbf{S} \diamond \mathbf{W}),\ \ \mathbf{Z}_2 = (\mathbf{W} \diamond \mathbf{H}),\ \ \mathbf{Z}_3 = (\mathbf{H} \diamond \mathbf{S}).$$

Equation (3.11) is well known as the PARAFAC model [8], of which $\mathbf{S}, \mathbf{W}$ and $\mathbf{H}$ are the component matrices. Such a model has been first proposed in [5] for blind multi-user detection of Direct-Sequence CDMA (DS-CDMA) signals. In this work, we resort to the PARAFAC model of (3.11) to propose a *new multi-user receiver for inter-cell interference reduction in PUCCH LTE Format 2*.

Received signal as a tensor

The model is completed when Additive White Gaussian Noise (AWGN) is included [9]. To model the signal using the same notation, the noise is also represented in a $7 \times 12 \times 2$ third-order tensor $\mathcal{V}$, where each term $v_{n,p,k}$ is associated with the n-th DFTS-OFDM symbol, p-th subcarrier and the k-th receive antenna. Therefore, the noisy received signal in scalar notation is written as:

$$y_{n,p,k} = x_{n,p,k} + v_{n,p,k} = \sum_{r=1}^{R} s_n^{(r)} \cdot w_p^{(r)} \cdot h_k^{(r)} + v_{n,p,k}. \tag{3.19}$$

In tensor notation, this signals is represented as:

$$\mathcal{Y} = \mathcal{X} + \mathcal{V} = \sum_{r=1}^{R} \mathbf{s}^{(r)} \circ \mathbf{w}^{(r)} \circ \mathbf{h}^{(r)} + \mathcal{V}. \tag{3.20}$$

The noise samples are modeled as i.i.d. zero mean complex Gaussian random variables with variance:

$$E\left\{|v_{n,p,k}|^2\right\} = \sigma^2_{V,k}.$$

Since $\mathcal{V}$ is a third-order tensor, it has also the three unfolded representations given by:

$$\mathbf{V}_1 = \begin{bmatrix} \mathbf{V}_{1..} \\ \mathbf{V}_{2..} \\ \vdots \\ \mathbf{V}_{7..} \end{bmatrix} \in \mathbb{C}^{84\times 2}, \quad \mathbf{V}_2 = \begin{bmatrix} \mathbf{V}_{.1.} \\ \mathbf{V}_{.2.} \\ \vdots \\ \mathbf{V}_{.12.} \end{bmatrix} \in \mathbb{C}^{24\times 7}, \quad \mathbf{V}_3 = \begin{bmatrix} \mathbf{V}_{..1} \\ \mathbf{V}_{..2} \end{bmatrix} \in \mathbb{C}^{14\times 12}. \tag{3.21}$$

Each slice $\mathbf{V}_{n..}$ of $\mathbf{V}_1$ contains the noise samples associated with the p-th subcarrier, both receive antennas and the 7 DFTS-OFDM symbols, as illustrated in Fig. 3.5.

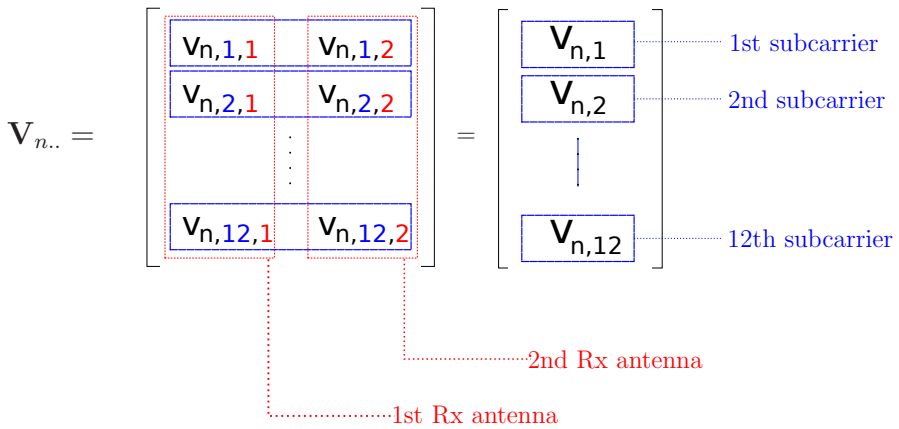

Figure 3.5: Slice $\mathbf{V}_{n..}$ of the tensor $\mathcal{V}$ in its unfolded form $\mathbf{V}_1$

In the same manner, ach slice $\mathbf{V}_{.p.}$ is associated with the n-th DFTS-OFDM symbol, both receive antennas and the 12 subcarriers, as depicted in Fig. 3.6.

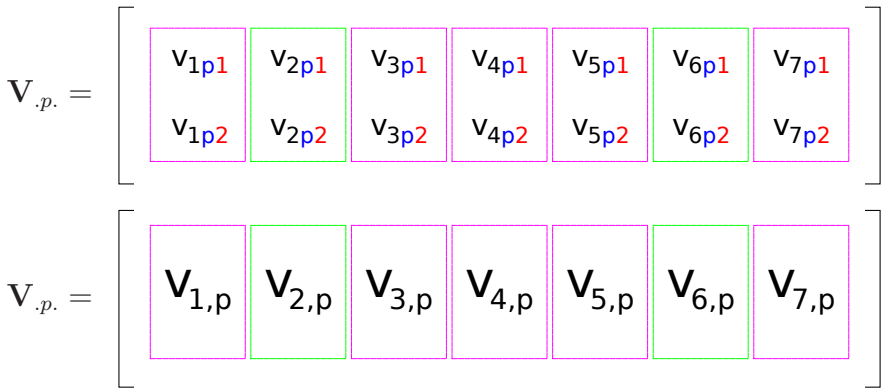

Figure 3.6: Slice $\mathbf{V}_{.p.}$ of the tensor $\mathcal{V}$ in the unfolded form $\mathbf{V}_2$

Then, the unfolded representations of the received signal $\mathcal{Y}$ is expressed as:

$$\mathbf{Y}_1 = \mathbf{Z}_1\mathbf{H}^T + \mathbf{V}_1 \tag{3.22}$$
$$\mathbf{Y}_2 = \mathbf{Z}_2\mathbf{S}^T + \mathbf{V}_2 \tag{3.23}$$
$$\mathbf{Y}_3 = \mathbf{Z}_3\mathbf{W}^T + \mathbf{V}_3. \tag{3.24}$$

3 Tensor-based Receiver for PUCCH Format 2 (TREP-2)

In order to exploit the PARAFAC modeling of the received signal, we make use of the ALS algorithm. As explained in Chapter 1, this algorithm is the classical solution for estimating the component matrices of a PARAFAC model [5, 42] and consists in fitting a third-order tensor model to the received data by alternately minimizing three LS criteria. In our model, the component matrices to be estimated are the *symbol*, *coding* and *channel* matrices, while the received data correspond to the noisy signal measured at the receive antennas.

We make use of the three unfolded representations (3.16)-(3.18) and, at each step of our algorithm, one component matrix is estimated in the LS sense, while the two others are fixed to their values obtained at the two previous steps.

Our receiver is applicable for both *single-cell* and *multi-cell* scenarios. In the

multi-cell case, 2 network configurations are possible so that the initialization of the coding matrix depends on it. In the following, we summarize the general algorithm:

Algorithm 1 TREP for PUCCH Format 2

1. Set $i = 0$; Initialize $\hat{\mathbf{S}}_{(i=0)} = \begin{bmatrix} 0 & 0 & \cdots & 0 \\ 1 & 1 & \cdots & 1 \\ 0 & 0 & \cdots & 0 \\ 0 & 0 & \cdots & 0 \\ 0 & 0 & \cdots & 0 \\ 1 & 1 & \cdots & 1 \\ 0 & 0 & \cdots & 0 \end{bmatrix} \in \mathbb{C}^{7\times R}$ and $\mathbf{W}_{(i=0)} \in \mathbb{C}^{12\times R}$;
2. $i = i + 1$;
3. Using $\mathbf{Y}_1$, find an LS estimate of $\mathbf{H}$:
$$\hat{\mathbf{H}}^T_{(i)} = \left[\hat{\mathbf{Z}}_{1,(i)}\right]^{\dagger} \mathbf{Y}_1$$
4. Using $\mathbf{Y}_2$, find an LS estimate of $\mathbf{S}$:
$$\hat{\mathbf{S}}^T_{(i)} = \left[\hat{\mathbf{Z}}_{2,(i)}\right]^{\dagger} \mathbf{Y}_2$$
5. Using $\mathbf{Y}_3$, find an LS estimate of $\mathbf{W}$:
$$\hat{\mathbf{W}}^T_{(i)} = \left[\hat{\mathbf{Z}}_{3,(i)}\right]^{\dagger} \mathbf{Y}_3$$
6. Repeat steps 2-5 until convergence

where

$$\hat{\mathbf{Z}}_{1,(i)} = \left(\hat{\mathbf{S}}_{(i-1)} \diamond \hat{\mathbf{W}}_{(i-1)}\right), \hat{\mathbf{Z}}_{2,(i)} = \left(\hat{\mathbf{W}}_{(i-1)} \diamond \hat{\mathbf{H}}_{(i)}\right) \text{ and } \hat{\mathbf{Z}}_{3,(i)} = \left(\mathbf{H}_{(i)} \diamond \hat{\mathbf{S}}_{(i)}\right).$$

In the following we apply the proposed algorithm in the single-cell and multi-cell scenarios.

3.1 Single-Cell Scenario

In the single-cell scenario some valid assumptions can be taken into account:

- The coding matrix is known at the eNodeB so that we initialize the algorithm with $\hat{\mathbf{W}}_{(i=0)} = \mathbf{W}$.
- As the coding matrix is known at the eNodeB, Step 5 can be skipped.

In this scenario the coding vectors are orthogonal thanks to the particular phase rotation per UE in the cell-specific base sequence. In the following we show how our proposed receiver improves the channel estimation, ameliorating data detection.

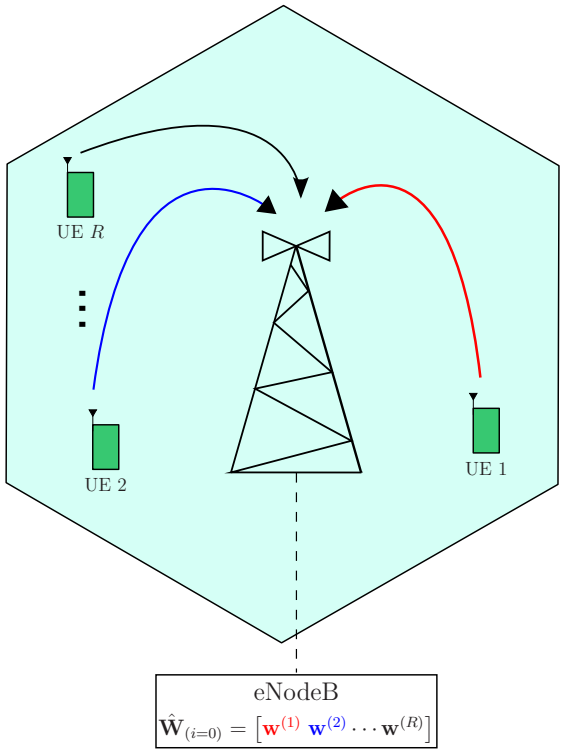

Figure 3.7: Single-Cell Scenario: R orthogonal UEs

Channel Estimation

At the first iteration, the channel matrix is estimated in Step 3 as follows:

$$\hat{\mathbf{H}}^T_{(i=1)} = \left[\hat{\mathbf{Z}}_{1,(i=1)}\right]^{\dagger}\mathbf{Y}_1 = \left[\left(\hat{\mathbf{Z}}^H_{1,(i=1)}\hat{\mathbf{Z}}_{1,(i=1)}\right)^{-1}\hat{\mathbf{Z}}^H_{1,(i=1)}\right]\mathbf{Z}_1\mathbf{H}^T + \left[\hat{\mathbf{Z}}_{1,(i=1)}\right]^{\dagger}\mathbf{V}_1 \tag{3.25}$$

where $\hat{\mathbf{Z}}_{1,(i=1)} = \left(\hat{\mathbf{S}}_{(i=0)} \diamond \mathbf{W}\right) = \begin{bmatrix} \mathbf{0}_R \\ \mathbf{W} \\ \mathbf{0}_R \\ \mathbf{0}_R \\ \mathbf{0}_R \\ \mathbf{W} \\ \mathbf{0}_R \end{bmatrix}$.

Since the coding matrix is orthogonal,

$$\hat{\mathbf{Z}}^H_{1,(i=1)}\hat{\mathbf{Z}}_{1,(i=1)} = 2\ \mathbf{W}^H\mathbf{W} = 24\mathbf{I}_R \tag{3.26}$$

is a diagonal matrix such that Step 3 reduces to:

$$\hat{\mathbf{H}}^T_{(i=1)} = \left[\frac{\hat{\mathbf{Z}}^H_{1,(i=1)}}{24}\right]\mathbf{Y}_1 = \frac{\hat{\mathbf{Z}}^H_{1,(i=1)}\mathbf{Z}_1}{24}\mathbf{H}^T + \frac{\hat{\mathbf{Z}}^H_{1,(i=1)}\mathbf{V}_1}{24}. \tag{3.27}$$

In the previous equation, the term that multiplies the channel matrix is given by:

$$\frac{\hat{\mathbf{Z}}^H_{1,(i=1)}\mathbf{Z}_1}{24} = \frac{2\mathbf{W}^H\mathbf{W}}{24} = \mathbf{I}_R \tag{3.28}$$

and, in the same manner, the filtered noise of Eq. (3.37), denoted by $\mathbf{V}^T_{h,(i=1)}$, is:

$$\mathbf{V}^T_{h,(i=1)} = \frac{\hat{\mathbf{Z}}^H_{1,(i=1)}\mathbf{V}_1}{24} = \frac{\mathbf{W}^H}{24}\left(\mathbf{V}_{2..} + \mathbf{V}_{6..}\right) \tag{3.29}$$

$$= \frac{1}{2}\left(\begin{bmatrix} \bar{\mathbf{v}}^{(1)}_2 \\ \bar{\mathbf{v}}^{(2)}_2 \\ \vdots \\ \bar{\mathbf{v}}^{(R)}_2 \end{bmatrix} + \begin{bmatrix} \bar{\mathbf{v}}^{(1)}_6 \\ \bar{\mathbf{v}}^{(2)}_6 \\ \vdots \\ \bar{\mathbf{v}}^{(R)}_6 \end{bmatrix}\right) \tag{3.30}$$

where

$$\bar{\mathbf{v}}^{(r)}_n = \frac{\sum_{p=1}^{12} w^{(r)*}_p \mathbf{v}_{n,p}}{12}$$

is the noise associated with the n-th DFTS-OFDM symbol and r-th terminal averaged over the 12 subcarriers. From Fig. (3.5) we see that each slice $\mathbf{V}_{n..}$ is composed by the vectors $\mathbf{v}_{n,1}, \cdots, \mathbf{v}_{n,12}$ so that $\mathbf{v}_{n,p} = [v_{n,p,1} \;\; v_{n,p,2}]$.

Thus, the estimated channel matrix is given by:

$$\hat{\mathbf{H}}^T_{(i=1)} = \mathbf{H}^T + \mathbf{V}^T_h \tag{3.31}$$

and the channel estimate associated with the r-th terminal is:

$$\hat{\mathbf{h}}^{(r)}_{(i=1)} = \mathbf{h}^{(r)} + \mathbf{v}^{(r)}_{h,(i=1)} = \mathbf{h}^{(r)} + \frac{\bar{\mathbf{v}}^{(r)}_2 + \bar{\mathbf{v}}^{(r)}_6}{2}. \tag{3.32}$$

Remark that (3.27) represents a classical LS estimator based on RS. Eq. (3.32) shows that the RS from the R terminals are perfectly separated such that its only impairment comes from the noise. Moreover, $\mathbf{v}^{(r)}_{h,(i=1)}$ is the average of the noise samples over the 12 subcarriers and the 2 RS.

In Appendix **A.2** we have proven that the variance of $\mathbf{v}^{(r)}_{h,(i=1)}$ is given by:

$$\sigma^2_{v_{h_k}} = \frac{\sigma^2_{V,k}}{2 \times 12} \tag{3.33}$$

for the k-th channel coefficient.

The accuracy of such a LS estimator is proportional to the number of RS, denoted herein N_{RS}, so that the noise variance from channel estimation can be generalized as follows[3]:

$$\sigma^2_{v_{h_k}} = \frac{\sigma^2_{V,k}}{N_{RS} \times 12}. \tag{3.34}$$

An interesting alternative to conventional estimators only based on known RS consists in using additional energy from estimated data after some post processing, as exploited in recent works [43, 44, 45, 46]. This is the principle of the so-called semi-blind or data-aided estimators. In the following we show that from the second iteration, the proposed ALS receiver uses energy from the estimated symbols to reestimate the channel.

[3]In the case of extended CP, the variance of the channel estimation noise is given by $\sigma^2_{v_{h_k}} = \sigma^2_{V,k}/12$.

From the 2-nd Iteration (Data-aided Estimation)

In the next step, the symbol matrix is calculated as follows:

$$\hat{\mathbf{S}}^T_{(i=1)} = \left[\hat{\mathbf{Z}}_{2,(i=1)}\right]^{\dagger} \mathbf{Y}_2 = \left[\left(\hat{\mathbf{Z}}^H_{2,(i=1)}\hat{\mathbf{Z}}_{2,(i=1)}\right)^{-1}\hat{\mathbf{Z}}^H_{2,(i=1)}\right]\mathbf{Z}_2\mathbf{S}^T + \left[\hat{\mathbf{Z}}_{2,(i=1)}\right]^{\dagger}\mathbf{V}_2 \tag{3.35}$$

where

$$\hat{\mathbf{Z}}_{2,(i=1)} = \left(\mathbf{W} \diamond \hat{\mathbf{H}}_{(i=1)}\right) = \begin{bmatrix} \hat{\mathbf{H}}_{(i=1)}D_1(\mathbf{W}) \\ \hat{\mathbf{H}}_{(i=1)}D_2(\mathbf{W}) \\ \vdots \\ \hat{\mathbf{H}}_{(i=1)}D_{12}(\mathbf{W}) \end{bmatrix}. \tag{3.36}$$

The following product of matrices

$$\hat{\mathbf{Z}}^H_{2,(i=1)}\hat{\mathbf{Z}}_{2,(i=1)} = 12\begin{bmatrix} \|\hat{\mathbf{h}}^{(1)}_{(i=1)}\|^2 & 0 & \cdots & 0 \\ 0 & \|\hat{\mathbf{h}}^{(2)}_{(i=1)}\|^2 & \cdots & 0 \\ \vdots & \vdots & \ddots & \vdots \\ 0 & 0 & \cdots & \|\hat{\mathbf{h}}^{(R)}_{(i=1)}\|^2 \end{bmatrix} \tag{3.37}$$

results in a diagonal matrix, since the orthogonality of the codes eliminates the interference from the other terminals. In the same manner, the product below

$$\hat{\mathbf{Z}}^H_{2,(i=1)}\mathbf{Z}_2 = 12\begin{bmatrix} \hat{\mathbf{h}}^{(1)H}_{(i=1)}\mathbf{h}^{(1)} & 0 & \cdots & 0 \\ 0 & \hat{\mathbf{h}}^{(2)H}_{(i=1)}\mathbf{h}^{(2)} & \cdots & 0 \\ \vdots & \vdots & \ddots & \vdots \\ 0 & 0 & \cdots & \hat{\mathbf{h}}^{(R)H}_{(i=1)}\mathbf{h}^{(R)} \end{bmatrix} \tag{3.38}$$

is also a diagonal matrix which is easily inverted.

The filtered noise of (3.35) is calculated as follows:

$$\left[\hat{\mathbf{Z}}_{2,(i=1)}\right]^{\dagger}\mathbf{V}_2 = \left(\hat{\mathbf{Z}}^H_{2,(i=1)}\hat{\mathbf{Z}}_{2,(i=1)}\right)^{-1}\hat{\mathbf{Z}}^H_{2,(i=1)}\mathbf{V}_2 \tag{3.39}$$

$$= \left(\hat{\mathbf{Z}}^H_{2,(i=1)}\hat{\mathbf{Z}}_{2,(i=1)}\right)^{-1}\sum_{p=1}^{12} D_p(\mathbf{W}^*)\hat{\mathbf{H}}^H\mathbf{V}_{.p.} \tag{3.40}$$

$$= \left(\hat{\mathbf{Z}}^H_{2,(i=1)}\hat{\mathbf{Z}}_{2,(i=1)}\right)^{-1}\sum_{p=1}^{12} D_p(\mathbf{W}^*)\hat{\mathbf{H}}^H\left[\mathbf{v}_{1,p} \;\; \cdots \;\; \mathbf{v}_{7,p}\right] \tag{3.41}$$

$$= 12 \left(\hat{\mathbf{Z}}^H_{2,(i=1)} \hat{\mathbf{Z}}_{2,(i=1)} \right)^{-1} \begin{bmatrix} \hat{\mathbf{h}}^{(1)H} \bar{\mathbf{v}}_1^{(1)} & \hat{\mathbf{h}}^{(1)H} \bar{\mathbf{v}}_2^{(1)} & \cdots & \hat{\mathbf{h}}^{(1)H} \bar{\mathbf{v}}_7^{(1)} \\ \hat{\mathbf{h}}^{(2)H} \bar{\mathbf{v}}_1^{(2)} & \hat{\mathbf{h}}^{(2)H} \bar{\mathbf{v}}_2^{(2)} & \cdots & \hat{\mathbf{h}}^{(2)H} \bar{\mathbf{v}}_7^{(2)} \\ \vdots & \vdots & \ddots & \vdots \\ \hat{\mathbf{h}}^{(R)H} \bar{\mathbf{v}}_1^{(R)} & \hat{\mathbf{h}}^{(R)H} \bar{\mathbf{v}}_2^{(R)} & \cdots & \hat{\mathbf{h}}^{(R)H} \bar{\mathbf{v}}_7^{(R)} \end{bmatrix}.$$

Therefore, the estimated symbol vector associated with the r-th UE can be written as:

$$\hat{\mathbf{s}}^{(r)\,T}_{(i=1)} = \frac{\hat{\mathbf{h}}^{(r)H}_{(i=1)} \mathbf{h}^{(r)}}{\|\hat{\mathbf{h}}^{(r)}_{(i=1)}\|^2} \mathbf{s}^{(r)T} + \frac{\hat{\mathbf{h}}^{(r)H}_{(i=1)} \begin{bmatrix} \bar{\mathbf{v}}_1^{(r)} & \cdots & \bar{\mathbf{v}}_7^{(r)} \end{bmatrix}}{\|\hat{\mathbf{h}}^{(r)}_{(i=1)}\|^2}. \tag{3.42}$$

At the end of the first iteration, the estimated symbol matrix $\hat{\mathbf{S}}_{(i=1)}$ is used as input to the second iteration of ALS and so on.

Thus, at the $(i+1)$-th iteration, the channel estimate is given by:

$$\hat{\mathbf{H}}^T_{(i+1)} = \left[\hat{\mathbf{Z}}_{1,(i+1)} \right]^{\dagger} \mathbf{Y}_1 \tag{3.43}$$

$$= \left[\left(\hat{\mathbf{Z}}^H_{1,(i+1)} \hat{\mathbf{Z}}_{1,(i+1)} \right)^{-1} \hat{\mathbf{Z}}^H_{1,(i+1)} \right] \mathbf{Z}_1 \mathbf{H}^T + \hat{\mathbf{Z}}^{\dagger}_{1,(i+1)} \mathbf{V}_1 \tag{3.44}$$

where $\hat{\mathbf{Z}}_{1,(i+1)} = \left(\mathbf{W} \diamond \mathbf{S}_{(i)} \right)$, such that

$$\hat{\mathbf{Z}}^H_{1,(i+1)} \mathbf{Z}_1 = \sum_{n=1}^{7} D_n(\hat{\mathbf{S}}^*_{(i)}) \mathbf{W}^H \mathbf{W} D_n(\mathbf{S}) \tag{3.45}$$

$$= 12 \sum_{n=1}^{7} D_n(\hat{\mathbf{S}}^*_{(i)}) \mathbf{I}_R D_n(\mathbf{S}) \tag{3.46}$$

$$= 12 \begin{bmatrix} \sum_{n=1}^{7} \hat{s}^{(1)*}_{n,(i)} \cdot s^{(1)}_n & \cdots & 0 \\ \vdots & \ddots & \vdots \\ 0 & \cdots & \sum_{n=1}^{7} \hat{s}^{(R)*}_{n,(i)} \cdot s^{(R)}_n \end{bmatrix} \tag{3.47}$$

and

$$\left(\hat{\mathbf{Z}}_{1,(i+1)}^{H}\hat{\mathbf{Z}}_{1,(i+1)}\right)^{-1} = \frac{1}{12}\begin{bmatrix} \sum_{n=1}^{7}|\hat{s}_{n,(i)}^{(1)}|^2 & \cdots & 0 \\ \vdots & \ddots & \vdots \\ 0 & \cdots & \sum_{n=1}^{7}|\hat{s}_{n,(i)}^{(R)}|^2 \end{bmatrix}^{-1}. \tag{3.48}$$

Alternatively, the estimated channel associated with the r-th UE can be written as:

$$\hat{\mathbf{h}}_{(i+1)}^{(r)} = \left(\frac{\sum_{n=1}^{7}\hat{s}_{n,(i)}^{(r)*}s_n^{(r)}}{\sum_{n=1}^{7}|\hat{s}_{n,(i)}^{(r)}|^2}\right)\mathbf{h}^T + \left(\frac{\sum_{n=1}^{7}\hat{s}_{n,(i)}^{(r)*}\bar{v}_n^{(r)}}{\sum_{n=1}^{7}|\hat{s}_{n,(i)}^{(r)}|^2}\right) \tag{3.49}$$

$$= \eta_{(i+1)}^{(r)}\mathbf{h}^T + \mathbf{v}_{h,(i+1)}^{(r)T}. \tag{3.50}$$

Differently from (3.32), Eq. (3.50) shows that the channel estimate at the $(i+1)$-th itearion, from the second iteration, has a bias given by:

$$\eta_{(i+1)}^{(r)} = \left(\frac{\sum_{n=1}^{7}\hat{s}_{n,(i)}^{(r)*}s_n^{(r)}}{\sum_{n=1}^{7}|\hat{s}_{n,(i)}^{(r)}|^2}\right) \tag{3.51}$$

such a way that *channel estimation noise* is given by:

$$\mathbf{v}_{h,(i+1)}^{(r)} = \left(\frac{\sum_{n=1}^{7}\hat{s}_{n,(i)}^{(r)*}\bar{\mathbf{v}}_n^{(r)}}{\sum_{n=1}^{7}|\hat{s}_{n,(i)}^{(r)}|^2}\right). \tag{3.52}$$

Despite the bias of (3.50), simulation results show that the Mean-Squared-Error (MSE) of channel estimation is improved when the number of iterations of ALS is increased. This happens since the variance of $\mathbf{v}_{h,(i+1)}^{(r)}$ is reduced as it is now averaged over the RS and the data part.

Data Detection

Simplified signaling models usually assume the noise is balanced over the diversity branch. In this case, Step 4 of each iteration of ALS provides an estimate of $\mathbf{S}$. In (3.53), e.g., we have the estimated symbol vector at the end of the first iteration. However, in practical receivers, noise is ususally non-uniform over the receive antennas, i.e., $\sigma_{V,1}^2 \neq \sigma_{V,2}^2 \neq \sigma_{V,3}^2 \neq \sigma_{V,4}^2$.

In this case, Step 4 of ALS is adjusted to account for this unbalanced noise variance. This is done by making the following replacement:

$$\left[\hat{\mathbf{Z}}_{2,(i)}\right]^{\dagger} = \left(\hat{\mathbf{Z}}_{2,(i)}^{H}\hat{\mathbf{Z}}_{2,(i)}\right)^{-1}\hat{\mathbf{Z}}_{2,(i)}^{H} \tag{3.53}$$

$$\Downarrow$$

$$\left(\hat{\mathbf{Z}}_{2,(i)}^{\prime\,H}\hat{\mathbf{Z}}_{2,(i)}\right)^{-1}\hat{\mathbf{Z}}_{2,(i)}^{\prime\,H}. \tag{3.54}$$

where

$$\hat{\mathbf{Z}}_{2,(i)}^{\prime} = \left(\mathbf{W}\diamond\hat{\mathbf{H}}_{(i)}\boldsymbol{\Sigma}^{-2}\right) = \begin{bmatrix} \hat{\mathbf{H}}_{(i)}\boldsymbol{\Sigma}^{-2}D_1(\mathbf{W}) \\ \hat{\mathbf{H}}_{(i)}\boldsymbol{\Sigma}^{-2}D_2(\mathbf{W}) \\ \vdots \\ \hat{\mathbf{H}}_{(i)}\boldsymbol{\Sigma}^{-2}D_{12}(\mathbf{W}) \end{bmatrix}. \tag{3.55}$$

In this case, $\boldsymbol{\Sigma}^2 = \begin{bmatrix} \sigma_{V,1}^2 & 0 \\ 0 & \sigma_{V,2}^2 \end{bmatrix}$ denotes the noise covariance matrix.

Therefore, from (3.54), the estimated symbol vector provided at the end of the i-th iteration of ALS is given by:

$$\hat{\mathbf{s}}_{(i)}^{(r)} = \left(\frac{\hat{\mathbf{h}}_{(i)}^{(r)H}\boldsymbol{\Sigma}^{-2}\mathbf{h}^{(r)}}{\hat{\mathbf{h}}_{(i)}^{(r)H}\boldsymbol{\Sigma}^{-2}\hat{\mathbf{h}}_{(i)}^{(r)}}\right)\mathbf{s}^{(r)} + \frac{\hat{\mathbf{h}}_{(i)}^{(r)H}\boldsymbol{\Sigma}^{-2}}{\hat{\mathbf{h}}_{(i)}^{(r)H}\boldsymbol{\Sigma}^{-2}\hat{\mathbf{h}}_{(i)}^{(r)}}\left[\bar{\mathbf{v}}_1^{(r)}\cdots\bar{\mathbf{v}}_7^{(r)}\right]. \tag{3.56}$$

Thus, using the previous estimate, we form the symbol matrix that is used as input to the next iteration to reestimate the channel.

Denoting by $\hat{\mathbf{H}}$ the estimated channel matrix at the end of the N_{It} iterations of ALS, the estimated symbol vector associated with the r-th UE is multiplied by its respective estimated effective channel, defined as:

$$\hat{h}_{eff}^{(r)} = \sqrt{\sum_{k=1}^{2}\frac{|\hat{h}_k^{(r)}|^2}{\sigma_{V,k}^2}} \tag{3.57}$$

so that the decision variable associated with the n-th estimated symbol can be written as:

$$\hat{D}_n^{(r)} = \frac{1}{\hat{h}_{eff}^{(r)}}\left(\frac{\hat{h}_1^{(r)*}h_1^{(r)}}{\sigma_{V,1}^2} + \frac{\hat{h}_2^{(r)*}h_2^{(r)}}{\sigma_{V,2}^2}\right)s_n + \frac{1}{\hat{h}_{eff}^{(r)}}\left(\frac{\hat{h}_1^{(r)*}\bar{v}_{n,1}^{(r)}}{\sigma_{V,1}^2} + \frac{\hat{h}_2^{(r)*}\bar{v}_{n,2}^{(r)}}{\sigma_{V,2}^2}\right). \tag{3.58}$$

4 Multi-Cell Scenario

Since in PUCCH the same frequency resource is shared among multiple UEs, the cell-specific base sequence $\mathbf{x}(q) = [x_1(q), \cdots, x_{12}(q)]$ is handled orthogonal among the UEs within the same cell through linear phase rotations, according to (3.9). On the other hand, there is still the inter-cell interference as the base sequences defined in the LTE specifications, denoted by $\mathbf{x}(1), \cdots, \mathbf{x}(30)$, have low but still non-zero mutual correlation [3, 1][4]

Herein, we consider that the signals associated with UEs from interfering neighboring cells are summed to the received signal tensor of (3.10). We assume a system with $Q-1$ interfering neighboring cells, such that Z_q terminals are served by the q-th cell. Therefore, the received signal tensor that describes this scenario is given by:

$$\mathcal{X} = \sum_{r=1}^{R} \mathcal{X}^{(r)} + \sum_{q=2}^{Q} \sum_{z_q=1}^{Z_q} \mathbf{s}_q^{(z_q)} \circ \mathbf{w}_q^{(z_q)} \circ \mathbf{h}_q^{(z_q)} \tag{3.59}$$

where $\mathbf{s}_q^{(z_q)}, \mathbf{w}_q^{(z_q)}, \mathbf{h}_q^{(z_q)}$ are respectively the *symbol, coding* and *channel* vectors associated with the z_q-th terminal from the q-th cell.

In this case, the coding vector associated with the z_q-th terminal from the q-th cell is defined as follows:

$$\mathbf{w}_q^{(z_q)} = \begin{bmatrix} w_1^{(z_q)} \\ w_2^{(z_q)} \\ \vdots \\ w_{12}^{(z_q)} \end{bmatrix} = \begin{bmatrix} x_1(q)e^{j\alpha_{z_q}\cdot 0} \\ x_2(q)e^{j\alpha_{z_q}\cdot 1} \\ \vdots \\ x_{12}(q)e^{j\alpha_{z_q}\cdot 11} \end{bmatrix} \in \mathbb{C}^{12\times 1} \tag{3.60}$$

where $\alpha_{z_q} = 2z_q \cdot \pi/6$ with $z_q = 0, ..., 5$ in order to guarantee the orthogonality among the coding vectors composed by the same base sequence. Moreover, the coding vectors associated with the q-th cell are organized in the following coding matrix:

$$\mathbf{W}(q) = \left[\mathbf{w}_q^{(1)} \cdots \mathbf{w}_q^{(Z_q)}\right].$$

Differently from (3.9), the coding vectors associated with the interfering UEs are

[4]It is known that LTE defines interference mitigation techniques in order to randomize the inter-cell interference (e.g. hop the base sequences on a per-slot basis). However this is not taken into account in our model.

composed by different base sequences.

In the following, we analyze the assumption of our algorithm in multi-cell scenarios under two network configurations:

- *Configuration 1*: Neighboring eNodeBs have a common central controller. Thus, the eNodeB associated with the desired UEs knows the coding vectors associated with the interfering UEs. Similarly to the single-cell scenario, Step 5 can be skipped. This configuration assumes that the eNodeBs are connected, similarly to a CoMP architecture.

- *Configuration 2*: Each eNodeB has an independent controller. Then, the eNodeB associated with the desired UEs only knows its served UEs. In this case, the coding vectors assigned to the interfering UEs are estimated using the semi-blind version of our algorithm. This configuration is equivalent to a conventional configuration of LTE Release 8, where the eNodeBs are not connected.

4.1 Configuration 1

This configuration assumes that Q neighboring eNodeBs are connected such a way that each eNodeB knows the coding vectors associated with all the served terminals. This is the case, e.g., of a CoMP systems. In such a case, we benefit from the full knowledge of the coding matrix $\mathbf{W}$ in the ALS algorithm. Then, the coding matrix is initialized as follows:

$$\hat{\mathbf{W}}_{(i=0)} = [\mathbf{W}(1) \cdots \mathbf{W}(q) \cdots \mathbf{W}(Q)] \,. \tag{3.61}$$

In other words, in addition to the coding matrix associated with its served UEs, the desired eNodeB also knows the coding matrix associated with the neighboring cells (or with its access points in the case of CoMP systems).

In the following, we show through a simple case study how the proposed receiver deals with the non-orthogonality of the coding vectors existing in multi-cell scenarios.

Case study 1 (Configuration 1)

We consider $Q = 2$ neighboring cells associated respectively with two fixed base sequences $\mathbf{x}(1)$ and $\mathbf{x}(2)$. We assume one terminal is served by each cell, so that we have a desired UE and a single interferer one.

Fig. 3.8 depicts this case study for configuration 1, where the eNodeBs are connected so that the desired eNodeB knows the coding vector associated with the interfering UE. The coding matrix is initialized as follows:

$$\hat{\mathbf{W}}_{(i=0)} = \left[\mathbf{w}^{(1)}\ \mathbf{w}^{(2)}\right]. \tag{3.62}$$

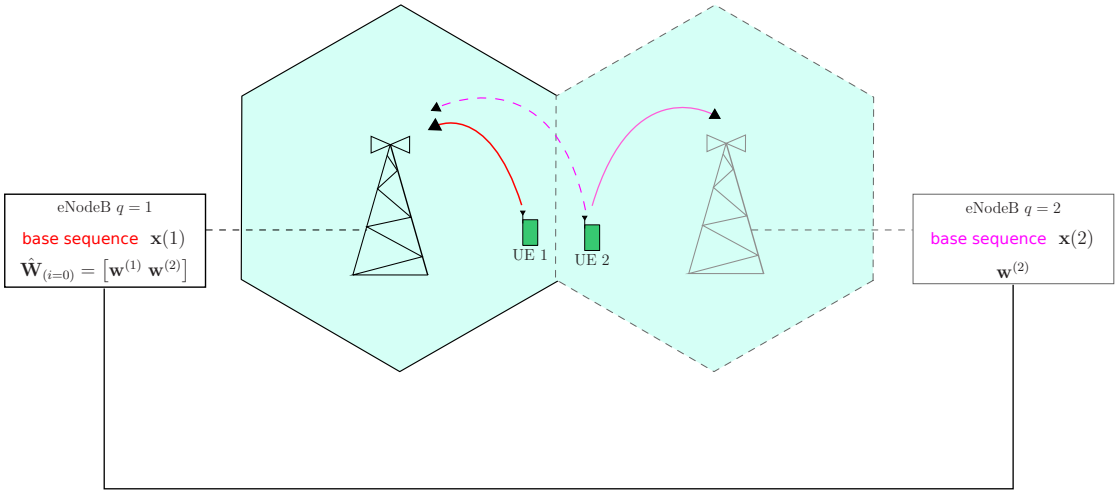

Figure 3.8: Case study 1: 2 neighboring cells x 1 UE (Configuration 1)

Channel Estimation

Channel Estimation at the 1-st iteration

At the first iteration of ALS, the channel matrix is estimated in Step 3 as follows:

$$\hat{\mathbf{H}}^{T}_{(i=1)} = \left[\hat{\mathbf{Z}}_{1,(i=1)}\right]^{\dagger}\mathbf{Y}_1 = \left[\left(\hat{\mathbf{Z}}^{H}_{1,(i=1)}\hat{\mathbf{Z}}_{1,(i=1)}\right)^{-1}\hat{\mathbf{Z}}^{H}_{1,(i=1)}\right]\mathbf{Z}_1\mathbf{H}^{T} + \hat{\mathbf{Z}}^{\dagger}_{1,(i=1)}\mathbf{V}_1 \tag{3.63}$$

where $\hat{\mathbf{Z}}_{1,(i=1)} = \left(\mathbf{S}_{(i=0)} \diamond \mathbf{W}\right)$.

As the coding matrix $\mathbf{W}$ is non-orthogonal, the product $\hat{\mathbf{Z}}_{1,(i=1)}\mathbf{Z}_1$ results in a

non-diagonal matrix, differently from (3.28). It can be shown that:

$$\left(\hat{\mathbf{Z}}^H_{1,(i=1)}\hat{\mathbf{Z}}_{1,(i=1)}\right)^{-1} = \begin{bmatrix} 12 & 12\kappa \\ 12\kappa^* & 12 \end{bmatrix}^{-1} = \frac{1}{12(1-|\kappa|^2)}\begin{bmatrix} 1 & -\kappa \\ -\kappa^* & 1 \end{bmatrix} \tag{3.64}$$

where $\kappa = \mathbf{w}^{(1)H}\mathbf{w}^{(2)}/12$ such a way that Eq. (3.63) gives the following channel estimate:

$$\hat{\mathbf{H}}^T_{(i=1)} = \mathbf{H}^T + \frac{1}{(1-|\kappa|^2)}\begin{bmatrix} 1 & -\kappa \\ -\kappa^* & 1 \end{bmatrix}\frac{1}{2}\left(\begin{bmatrix} \bar{\mathbf{v}}^{(1)}_2 \\ \bar{\mathbf{v}}^{(2)}_2 \end{bmatrix} + \begin{bmatrix} \bar{\mathbf{v}}^{(1)}_6 \\ \bar{\mathbf{v}}^{(2)}_6 \end{bmatrix}\right) \tag{3.65}$$

$$= \mathbf{H}^T + \frac{1}{(1-|\kappa|^2)}\begin{bmatrix} 1 & -\kappa \\ -\kappa^* & 1 \end{bmatrix}\begin{bmatrix} \mathbf{v}^{(1)}_{h,(i=1)} \\ \mathbf{v}^{(2)}_{h,(i=1)} \end{bmatrix} \tag{3.66}$$

$$= \mathbf{H}^T + \frac{1}{(1-|\kappa|^2)}\begin{bmatrix} \mathbf{v}^{(1)}_{h,(i=1)} - \kappa\mathbf{v}^{(2)}_{h,(i=1)} \\ \mathbf{v}^{(2)}_{h,(i=1)} - \kappa^*\mathbf{v}^{(1)}_{h,(i=1)} \end{bmatrix}. \tag{3.67}$$

Alternatively, we can represent the channel estimate associated with the desired UE as:

$$\hat{\mathbf{h}}^{(1)}_{(i=1)} = \mathbf{h}^{(1)} + \frac{1}{1-|\kappa|^2}\left(\mathbf{v}^{(1)}_{h,(i=1)} - \kappa\mathbf{v}^{(2)}_{h,(i=1)}\right). \tag{3.68}$$

The *channel estimation error* in this case is given by:

$$\mathbf{e}_{h,(i=1)} = \frac{1}{1-|\kappa|^2}\left(\mathbf{v}^{(1)}_{h,(i=1)} - \kappa\mathbf{v}^{(2)}_{h,(i=1)}\right), \tag{3.69}$$

and, in Appendix **A.5**, we have shown that the error variance equals:

$$\sigma^2_{e_{h_k}} = \left(\frac{1}{1-|\kappa|^2}\right)\frac{\sigma^2_{V,k}}{12 \times N_{RS}}. \tag{3.70}$$

Channel Estimation from the 2-nd iteration

After obtaining $\hat{\mathbf{H}}_{(i=1)}$, the symbol matrix is estimated in Step 4. However, differently from (3.38), the following product of matrices

$$\hat{\mathbf{Z}}^H_{2,(i=1)}\mathbf{Z}_2 = 12\begin{bmatrix} \hat{\mathbf{h}}^{(1)H}_{(i=1)}\mathbf{h}^{(1)} & \kappa\hat{\mathbf{h}}^{(1)H}_{(i=1)}\mathbf{h}^{(2)} \\ \kappa^*\hat{\mathbf{h}}^{(2)H}_{(i=1)}\mathbf{h}^{(1)} & \hat{\mathbf{h}}^{(2)}_{(i=1)}\mathbf{h}^{(2)} \end{bmatrix} \tag{3.71}$$

results in a non-diagonal matrix which is more complex to be inverted compared to that of (3.38). However, as shown in Step 4, this matrix can be inverted using:

$$\left(\hat{\mathbf{Z}}_{2,(i=1)}^{H}\hat{\mathbf{Z}}_{2,(i=1)}^{H}\right)^{-1} = 12\left[\begin{array}{cc} \|\hat{\mathbf{h}}_{(i=1)}^{(1)}\|^2 & \kappa\hat{\mathbf{h}}_{(i=1)}^{(1)H}\hat{\mathbf{h}}_{(i=1)}^{(2)} \\ \kappa^*\hat{\mathbf{h}}_{(i=1)}^{(2)H}\hat{\mathbf{h}}_{(i=1)}^{(1)} & \|\hat{\mathbf{h}}_{(i=1)}^{(2)}\|^2 \end{array}\right] \tag{3.72}$$

in order to obtain $\hat{\mathbf{S}}_{(i=1)}$, used as input to the next iteration and so on.

At the $(i+1)$-th iteration, the channel estimate is calculated similarly to (3.63). However, differently from (3.45)-(3.47), we have that:

$$\hat{\mathbf{Z}}_{1,(i+1)}^{H}\mathbf{Z}_1 = \sum_{n=1}^{7} D_n(\hat{\mathbf{S}}_{(i)}^{*})\mathbf{W}^H\mathbf{W}D_n(\mathbf{S}) \tag{3.73}$$

$$= 12\sum_{n=1}^{7} D_n(\hat{\mathbf{S}}_{(i)}^{*})\left[\begin{array}{cc} 1 & \kappa \\ \kappa^* & 1 \end{array}\right] D_n(\mathbf{S}) \tag{3.74}$$

$$= 12\left[\begin{array}{cc} \sum_{n=1}^{7}\hat{s}_{n,(i)}^{(1)*}s_n^{(1)} & \kappa\sum_{n=1}^{7}\hat{s}_{n,(i)}^{(1)*}s_n^{(2)} \\ \kappa^*\sum_{n=1}^{7}\hat{s}_{n,(i)}^{(2)*}s_n^{(1)} & \sum_{n=1}^{7}\hat{s}_{n,(i)}^{(2)*}s_n^{(2)} \end{array}\right] \tag{3.75}$$

and

$$\left(\hat{\mathbf{Z}}_{1,(i+1)}^{H}\hat{\mathbf{Z}}_{1,(i+1)}\right)^{-1} = \frac{\left[\begin{array}{cc} \sum_{n=1}^{7}|\hat{s}_{n,(i)}^{(2)*}|^2 & -\kappa\sum_{n=1}^{7}\hat{s}_{n,(i)}^{(1)*}\hat{n}_{n,(i)}^{(2)} \\ -\kappa^*\sum_{n=1}^{7}\hat{s}_{n,(i)}^{(2)*}\hat{s}_{n,(i)}^{(1)} & |\hat{s}_{n,(i)}^{(1)*}|^2 \end{array}\right]}{\dfrac{1}{\det\left(\hat{\mathbf{Z}}_{1,(i+1)}^{H}\hat{\mathbf{Z}}_{1,(i+1)}\right)}}. \tag{3.76}$$

Thus, Step 3 provides the following channel estimate:

$$\hat{\mathbf{H}}_{(i+1)}^{T} = \hat{\mathbf{B}}_{(i+1)}\mathbf{H}^T + \hat{\mathbf{Z}}_1^{\dagger}\mathbf{V}_1 \tag{3.77}$$

where $\hat{\mathbf{B}}_{(i+1)}$ is called the *bias matrix*. We show in the performance results that although this estimator is biased, the MSE of channel estimation decreases with the number of iteration thanks to the reduction in the noise variance, which is now averaged over RS and data symbols.

Data Detection

As in the single-cell scenario, the noise is assume unbalanced over the received

antennas. Then, ALS is adjusted as described in (3.53)-(3.54).

Thus, at the last iteration, the estimated symbol vector is equivalent to the following estimate:

$$\hat{\mathbf{s}}^{(1)} = \left(\frac{\hat{\mathbf{h}}^{(1)H}\boldsymbol{\Sigma}^{-2}\mathbf{h}^{(1)} + |\kappa|^2\hat{\mathbf{h}}^{(2)H}\boldsymbol{\Sigma}^{-2}\mathbf{h}^{(1)}}{1-|\kappa|^2} \right)\mathbf{s}^{(1)}$$

$$+\kappa \left(\frac{\hat{\mathbf{h}}^{(1)H}\boldsymbol{\Sigma}^{-2}\mathbf{h}^{(2)} - \hat{\mathbf{h}}^{(2)H}\boldsymbol{\Sigma}^{-2}\mathbf{h}^{(2)}}{1-|\kappa|^2} \right)\mathbf{s}^{(2)}$$

$$+\frac{\hat{\mathbf{h}}^{(1)H}\boldsymbol{\Sigma}^{-2}\left[\bar{\mathbf{v}}_1^{(1)}\cdots\bar{\mathbf{v}}_7^{(1)}\right] - |\kappa|^2\hat{\mathbf{h}}^{(2)H}\boldsymbol{\Sigma}^{-2}\left[\bar{\mathbf{v}}_1^{(2)}\cdots\bar{\mathbf{v}}_7^{(2)}\right]}{1-|\kappa|^2}. \tag{3.78}$$

TREP-2 vs Conventional Receiver

We call a conventional receiver a low-complexity LS channel estimator based on RS followed by a MRC for data detection. Such receiver is optimum in the single-cell case, where the coding vectors are orthogonal. In a multi-cell scenario, this channel estimate is biased and given by:

$$\hat{\mathbf{H}}^T = \left[\frac{\hat{\mathbf{Z}}^H_{1,(i=1)}}{36}\right]\mathbf{Y}_1 = \begin{bmatrix} 1 & \kappa \\ \kappa^* & 1 \end{bmatrix}\mathbf{H}^T + \mathbf{V}^T_{h,(i=1)} \tag{3.79}$$

where $\mathbf{V}^T_{h,(i=1)}$ is the same defined in (3.30). Alternatively, the channel estimate associated with the desired UE is given by:

$$\hat{\mathbf{h}}^{(1)}_{(i=1)} = \mathbf{h}^{(1)} + \mathbf{v}_{h,(i=1)} + \kappa\mathbf{h}^{(2)}. \tag{3.80}$$

and a *channel estimation error* can be defined as follows:

$$\mathbf{e}_{h,(i=1)} = \mathbf{v}^{(1)}_{h,(i=1)} + \kappa\mathbf{h}^{(2)}. \tag{3.81}$$

We have proven Appendix **A.6** the variance of this error for a channel realization is given by:

$$\sigma^2_{e_{h_k}} = \frac{\sigma^2_{V,k}}{12\times N_{RS}} + |\kappa|^2|h^{(2)}_k|^2. \tag{3.82}$$

The two previous results can be extrapolated to the case of R terminals within

the desired cell and $Q-1$ interfering neighboring cells each one with Z_q terminals. In this case, the channel estimation error associated with the r-th UE within the desired cell will be:

$$\mathbf{e}_h^{(r)} = \mathbf{v}_{h,(i=1)}^{(r)} + \sum_{q=2}^{Q-1} \sum_{z_q}^{Z_q} \kappa_{r,z_q} \mathbf{h}^{(z_q)} \tag{3.83}$$

and the error variance given by:

$$\sigma_{e_{h_k}}^2 = \frac{\sigma_{V,k}^2}{12 \times N_{RS}} + \sum_{q=2}^{Q-1} \sum_{z_q}^{Z_q} |\kappa_{r,z_q}|^2 |h_k^{(z_q)}|^2 \tag{3.84}$$

where $\kappa_{r,z_q} = \mathbf{w}^{(r)H} \mathbf{w}^{(z_q)}/12$.

Therefore, it can be seen from (3.80) that in the channel estimation of conventional receivers, the existing correlation among the coding vectors results in a worse channel estimation compared to the single-cell case. This impairment is proportional to the number of interfering UEs and the level of correlation among the coding vectors.

The channel estimate obtained at the first iteration of TREP has an additional noisy term proportional to the correlation between the coding vectors associated with the desired and the interfering UEs as shown in (3.68). At the subsequent iterations, ALS increases the value equivalent to N_{RS} using the data part as RS when N_{It} is increased.

As our channel estimator has a structure similiar to that of a Zero-Forcing (ZF) filter [40][5], we also expect a poor performance under very low SNRs[6]. We also show in the preliminary results that the proposed receiver provides a better channel estimation within the operating SNR region of PUCCH. As in the single-cell case, we show that the MSE of channel estimation decreases with the number of iterations.

Since the channel has been estimated, data is detected using MRC receiver, rep-

[5]This equivalence provides a good comparison concerning the complexity of our estimator, which is basically the same of an iterative ZF receiver

[6]ZF filters have a poor performance under low SNR thanks to its inherent noise amplification

resented in our tensor modeling by:

$$\hat{\mathbf{S}}^T = \frac{\hat{\mathbf{Z}}_2'^H}{12}\mathbf{Y}_2 = \frac{\hat{\mathbf{Z}}_2'^H\mathbf{Z}_2}{12}\mathbf{S}^T + \frac{\hat{\mathbf{Z}}_2'^H}{12}\mathbf{V}_2. \tag{3.85}$$

This estimator would fit well in the single-cell scenario. However, in the considered multi-cell scenario, where orthogonality among coding vectors is lost, Eq. (3.38) results in:

$$\hat{\mathbf{Z}}_2'^H\mathbf{Z}_2 = 12\begin{bmatrix} \hat{\mathbf{h}}^{(1)H}\boldsymbol{\Sigma}^{-2}\mathbf{h}^{(1)} & \kappa\hat{\mathbf{h}}^{(1)H}\boldsymbol{\Sigma}^{-2}\mathbf{h}^{(2)} \\ \kappa^*\hat{\mathbf{h}}^{(2)H}\boldsymbol{\Sigma}^{-2}\mathbf{h}^{(1)} & \hat{\mathbf{h}}^{(2)H}\boldsymbol{\Sigma}^{-2}\mathbf{h}^{(2)} \end{bmatrix}. \tag{3.86}$$

Therefore, when low-complexity conventional receiver is considered, the estimated symbol vector is given by:

$$\hat{\mathbf{s}}_{(i=1)}^{(1)} = \left(\hat{\mathbf{h}}^{(1)H}\boldsymbol{\Sigma}^{-2}\mathbf{h}^{(1)}\right)\mathbf{s}^{(1)} + \kappa\left(\hat{\mathbf{h}}^{(2)H}\boldsymbol{\Sigma}^{-2}\mathbf{h}^{(1)}\right)\mathbf{s}^{(2)} + \hat{\mathbf{h}}^{(1)H}\boldsymbol{\Sigma}^{-2}\left[\bar{\mathbf{v}}_1^{(r)}\cdots\bar{\mathbf{v}}_7^{(r)}\right]. \tag{3.87}$$

When the channel is perfectly estimated, e.g., the structure of Step 4 of ALS is similar to a ZF receiver which cancels completely the interference from the neighboring cells. Then, the first iteration of the proposed receiver improves the performance over MRC by reducing the interference. Altough, it amplifies the the noise, which handle the proposed receiver suitable for systems limited by interference. Notice that (3.87) results in non-canceled interference which can significantly degrade the performance. Moreover, observe that similarly to the channel estimation, this impairment is proportional to the correlation among the coding vectors.

Furthermore, in the presence of channel estimation error, this inter-cell interference is not completely canceled at the first iteration, but is gradually reduced as the accuracy of the channel estimation is improved, as it can be seen in (3.78). Then, the detection is improved in the subsequent iterations by ameliorating the channel estimation.

4.2 Configuration 2

In this configuration we assume the eNodeBs do not have a common central controller, such that only a part of the coding matrix is known. The other part, associated with the neighboring cells, is initialized with a base sequence and phase rotation chosen randomly from the subset of possibilities. Thus, the algorithm is

initialized as follows:

$$\hat{\mathbf{W}}_{(i=0)} = \left[\mathbf{W}(1) \;\; \hat{\mathbf{W}}(2)_{(i=0)} \cdots \hat{\mathbf{W}}(q)_{(i=0)} \cdots \hat{\mathbf{W}}(Q)_{(i=0)}\right]. \tag{3.88}$$

This configuration is similar to the conventional network configuration of LTE, where the base sequences and phase rotations from neighboring cells are not known. In this situation, our algorithm estimates the coding vectors associated with the interfering UEs at each iteration in order to cancel the inter-cell interference.

Hereafter, case study 1 is analyzed under configuration 2.

Case study 1 (Configuration 2)

As depicted in Fig. 3.9, the eNodeB only knows the first coding vector, such that the coding matrix is initialized as follows:

$$\hat{\mathbf{W}}_{(i=0)} = \left[\mathbf{w}^{(1)} \;\; \hat{\mathbf{w}}^{(2)}_{(i=0)}\right] \tag{3.89}$$

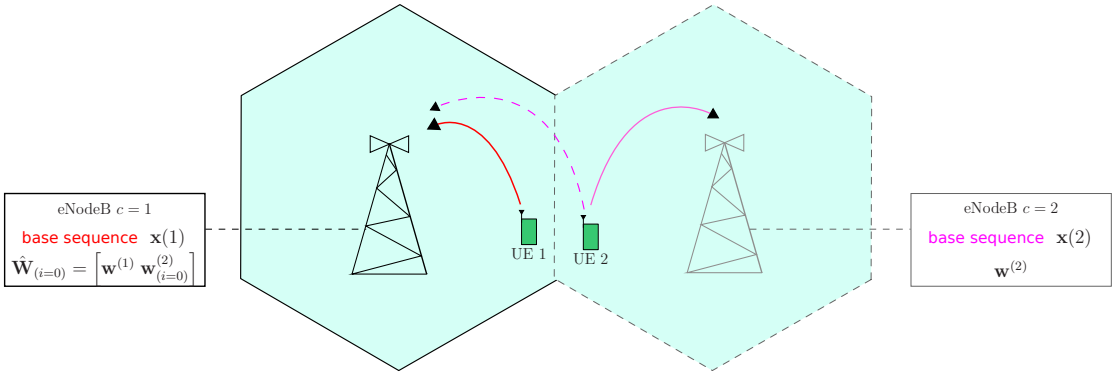

Figure 3.9: Case study 1 - 2 cells x 1 UE (Configuration 2)

In configuration 2, we resort to Step 5 of ALS to estimate the unknown part of the coding matrix. As shown below, at the i-th iteration, the estimated coding matrix is given by:

$$\hat{\mathbf{W}}^{T}_{(i)} = \left[\hat{\mathbf{Z}}_{3,(i)}\right]^{\dagger} \mathbf{Y}_3 \tag{3.90}$$

$$= \left(\hat{\mathbf{Z}}^{H}_{3,(i)} \hat{\mathbf{Z}}_{3,(i)}\right)^{-1} \hat{\mathbf{Z}}^{H}_{3,(i)} \mathbf{Z}_3 \mathbf{W}^{T} + \left[\hat{\mathbf{Z}}_{3,(i)}\right]^{\dagger} \mathbf{V}_3 \tag{3.91}$$

which can be written as:

$$\hat{\mathbf{W}}_{(i)} = \left[\hat{\mathbf{w}}_{(i)}^{(1)} \;\; \hat{\mathbf{w}}_{(i)}^{(2)}\right]. \tag{3.92}$$

The first coding vector is known at the eNodeB, such that at the end of the i-th iteration we can simply replace $\hat{\mathbf{w}}_{(i)}^{(1)}$ by $\mathbf{w}^{(1)}$. Although the second coding vector is not known, we know that $\|\mathbf{w}^{(2)}\|^2 = 12$. Thus, at the end of the i-th iteration we normalize the estimated coding vector such that $\|\hat{\mathbf{w}}_{(i)}^{(2)}\|^2 = 12$.

Thne, the estimated coding matrix $\hat{\mathbf{W}}_{(i)}$ is used at the $(i+1)$-th iterarion to reestimate the channel and so on. Simulation results show the huge gains that are obtained compared to the conventional receivers that ignore the presence of inter-cell interference.

It is of our interest to extend the previous results to multi-cell scenarios with more terminals per cell and more interfering cells. In this sense, other case studies are proposed and evaluated in the Section of performance results. They are:

- **Case study 2** - 2 cells x 2 UEs per cell
- **Case study 3** - 3 cells x 1 UE per cell
- **Case study 4** - 3 cells x 2 UEs per cell

These case studies are illustrated for configuration 2 in Fig. 3.10, Fig. 3.11 and Fig. 3.12.

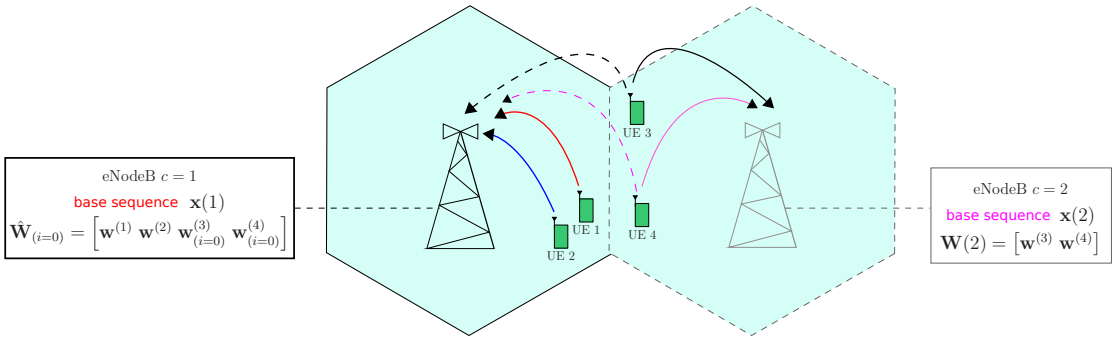

Figure 3.10: Case study 2 - 2 cells x 2 UEs per cell (Configuration 2)

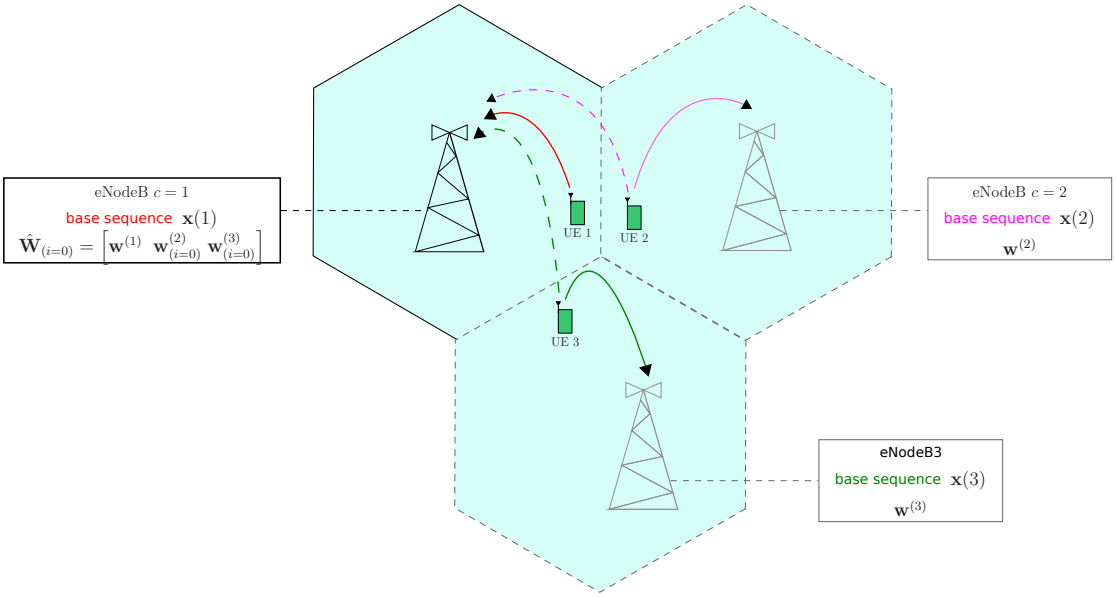

Figure 3.11: Case study 3 - 3 cells x 1 UE per cell (Configuration 2)

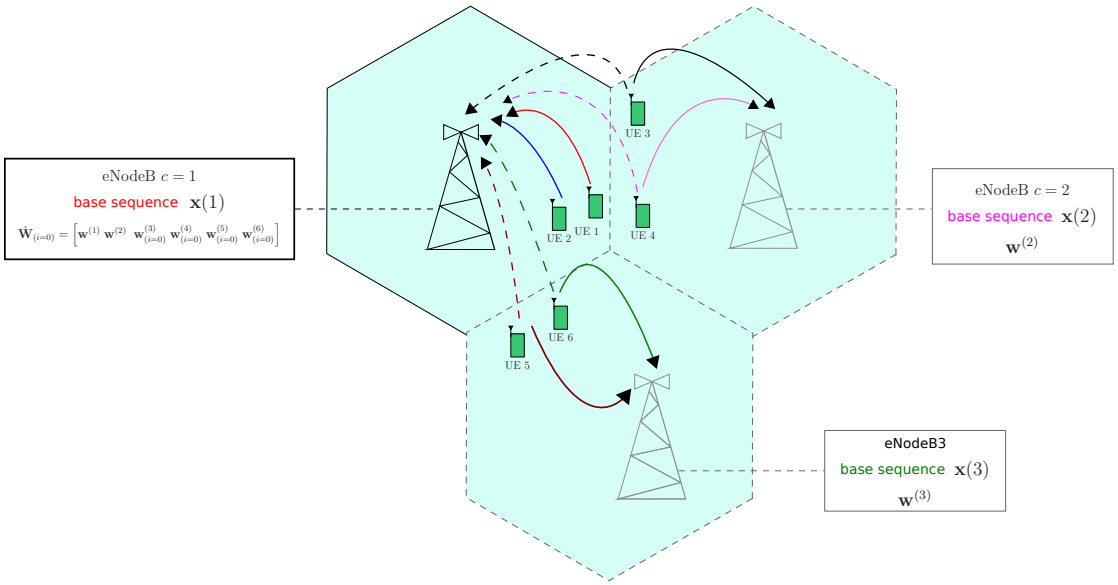

Figure 3.12: Case study 4 - 3 cells x 2 UEs per cell (Configuration 2)

5 Identifiability Issue: PARAFAC Uniqueness

The decomposition of an arbitrary third-order tensor $\mathcal{X}$ in a sum of R rank-one tensors is said to be essentially unique if and only if the component matrices can

be estimated from $\mathcal{X}$ up to trivial permutation and scaling of their columns [5]. In the context of our proposal, uniqueness of the PARAFAC model (3.20) is related to receiver processing and guarantees that the symbol, channel and coding matrices $\mathbf{S} \in \mathbb{C}^{7\times R}$, $\mathbf{W} \in \mathbb{C}^{12\times R}$ and $\mathbf{H} \in \mathbb{C}^{2\times R}$ can be uniquely recovered at the receiver. In the PARAFAC model for PUCCH Format 2, uniqueness is important since it ensures the separation of the signal contributions from multiple terminals at the eNodeB.

Using the fact that $\mathbf{W}$ is full rank by construction, and assuming that the symbol and channel matrices $\mathbf{S}$ and $\mathbf{H}$ are full rank, we can resort to the uniqueness results of the PARAFAC tensor model [8, 10] to obtain an upper bound on the number R of UEs that can be simultaneously supported at the eNodeB. In the following, we provide a necessary and sufficient condition for uniqueness by distinguishing the two presented network configurations:

1. *The eNodeB does not have full knowledge of the coding matrix* $\mathbf{W}$. This is the usual assumption in non-cooperative scenarios where the coding sequences of different cells are not known. In this case, the following condition must be satisfied:

$$min(7, R) + min(12, R) + min(2, R) \geq 2R + 2,$$

   which implies $R \leq 7$, i.e. a maximum of 7 UEs are simultaneously supported;

2. *The eNodeB has full knowledge of the coding matrix* $\mathbf{W}$. This is the case in CoMP systems, where the coding vectors of different cells are known at the eNodeBs. In this case, uniqueness is guaranteed if

$$min(7, R) + min(12, R) \geq R + 1,$$

   which implies $R \leq 19$.

5.1 Combining both slots

The receiver structure of PUCCH Format 2 at eNodeB, must deliver to the higher layers the B bits that represent the channel-status report. Once the modulation symbols $\hat{s}_1^{(r)}, \hat{s}_3^{(r)}, \hat{s}_4^{(r)}, \hat{s}_5^{(r)}, \hat{s}_7^{(r)}$, and $\hat{s}_8^{(r)}, \hat{s}_{10}^{(r)}, \hat{s}_{11}^{(r)}, \hat{s}_{12}^{(r)}, \hat{s}_{14}^{(r)}$ are estimated, the information associated with both slots must be combined at the eNodeB, in such a way that the receiver delivers B bits to the upper layers. The adopted procedure is illustrated in Fig. 3.8. The estimated data symbols and the effective channel associated with both slots are used as input of a soft decoder relying on Maximum

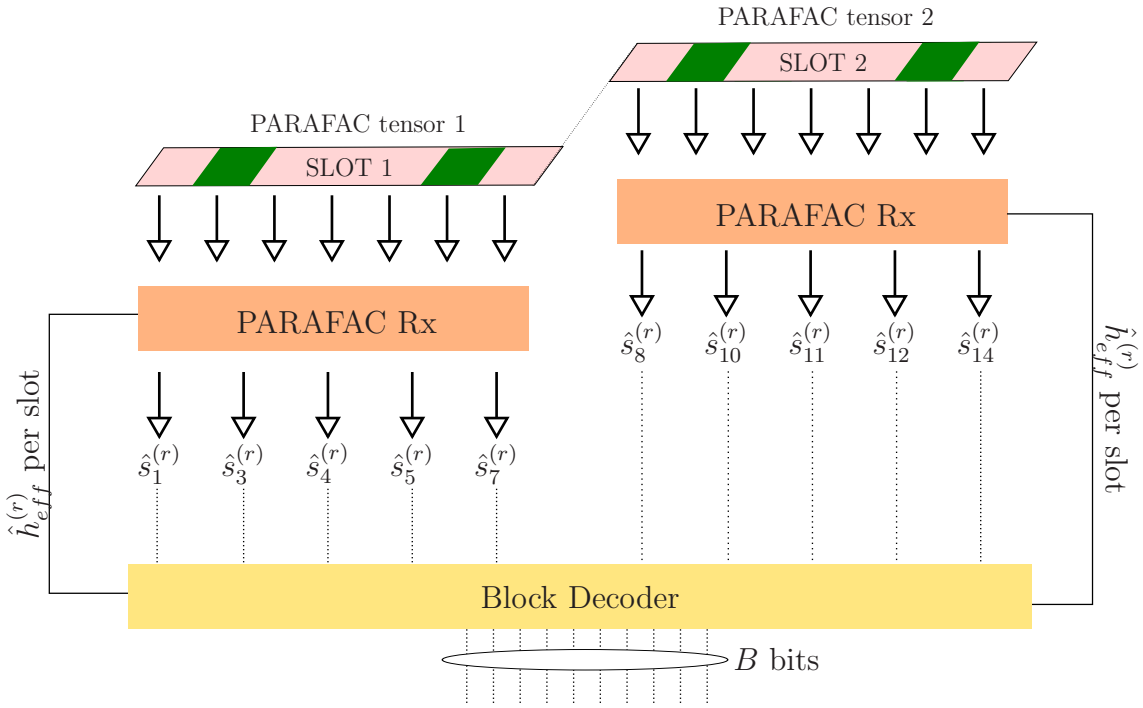

Figure 3.13: Receiver for PUCCH Format 2

Likelihood (ML). The minimum Euclidian distance between the received signal and all possible codewords indicates the decoded B bits [37].

6 Preliminary Results

In this Section we compare through simulation results the *channel estimation accuracy* and the *tensor model matching* when TREP-2 is applied for both single-cell and multi-cell configurations. It is worth pointing out that only the first slot is considered. The following results are presented in order to explain the further performance gains in the error performance of PUCCH Format 2 when TREP-2 is applied. At this chapter, the proposed receiver can be called either TREP or TREP-2.

6.1 Single-Cell Scenario

Channel estimation accuracy

In the following simulations, we compare the channel estimation accuracy provided by the TREP-2 to the one provided by a LS channel estimator based on RS, which is commonly used in conventional receivers. As usually, the channel estimation accuracy is expressed in terms of the MSE defined below as:

$$\mathrm{MSE}(\hat{\mathbf{H}}) = \frac{E\left\{\|\hat{\mathbf{H}} - \mathbf{H}\|_F^2\right\}}{2 \times R}. \tag{3.93}$$

In Fig. 3.14, we show the histogram of $|\eta|$ (bias from channel estimation) for different values of SNR when TREP-2 is applied. The number of iterations is fixed to $N_{It} = 2$ and normal CP is assumed. We can see that the average of $|\eta|$ approaches 1 as the SNR is around 0 dB.

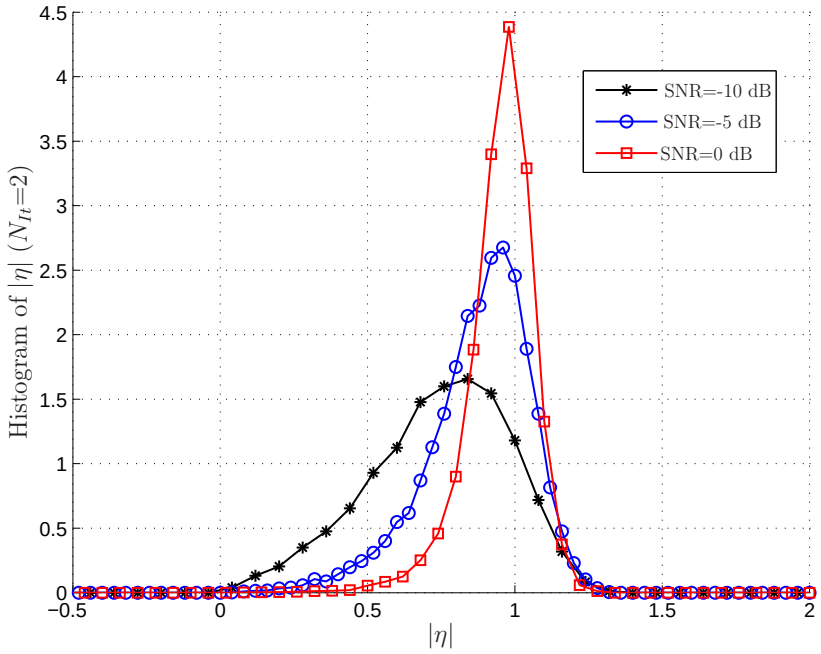

Figure 3.14: Distribution of the channel estimation bias

In Fig. **??**, we show the histogram of $\mathrm{Re}\left\{v_{h_k,(N_{It})}\right\}$, which denotes the real part of the noise from channel estimation. We fixed the SNR=-10 dB and normal CP is assumned. We can observe that the variance of $\mathrm{Re}\left\{v_{h_k,(N_{It})}\right\}$ reduces when the

number of iterations increases. In addition to this, we can see an interesting bound for this noise variance[7]. This reduction is obtained thanks to the use of additional

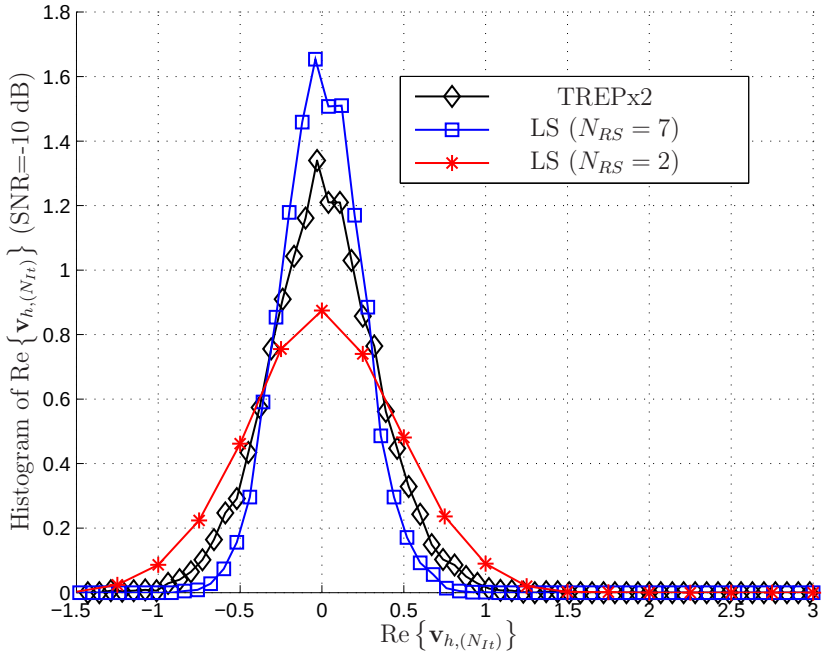

Figure 3.15: Distribution of the Noise from Channel Estimation

energy from the estimated data in the first iteration.

In Table 3.1, we show some values obtained from simulations to the variance of the channel estimation error. We assume normal CP configuration and a variable number of iteratons and RS for a fixed SNR=-10 dB. We can note, e.g., that approximately the energy of 4 symbols is used to reestimate the channel when $N_{It} = 3$.

In Fig. 3.11, we show the MSE($\hat{\mathbf{H}}$) in function of N_{It}. The SNR is fixed to -10 dB and normal CP is assumed. We can note that despite the presence of a bias, the MSE($\hat{\mathbf{H}}$) provided by the TREP-2 decreases with N_{It}, converging to a local minimum in between the valued obtained at the 1-st iteration and the bound for LS estimators.

[7] $N_{RS} = 7$ implies that all the symbols are perfectly known at the eNodeB and used as RS.

N_{It}	N_{RS}	$\sigma^2_{v_{h_k}}$	estimator
1	2	$0.4144 \approx \frac{\sigma^2_{V,k}}{2 \times 12}$	unbiased
1	7	$0.1176 \approx \frac{\sigma^2_{V,k}}{7 \times 12}$	unbiased
2	3.74	$0.2227 \approx \frac{\sigma^2_{V,k}}{3.74 \times 12}$	biased
3	3.86	$0.1925 \approx \frac{\sigma^2_{V,k}}{3.86 \times 12}$	biased

Table 3.1: Variance of Noise from Channel Estimation

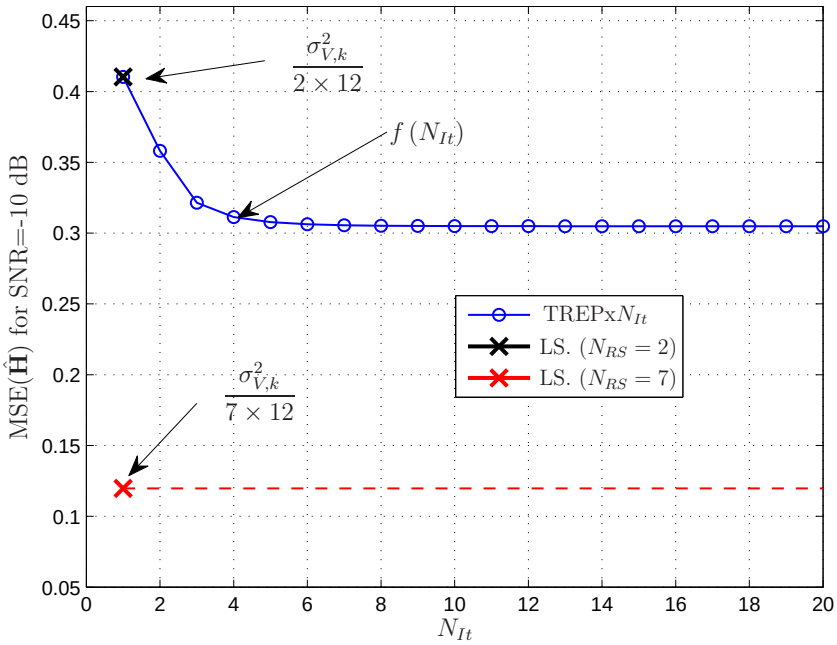

Figure 3.16: MSE from Channel Estimation

Tensor model matching

In the following simulations, we show the model matching between the baseband transmission on PUCCH Format 2 and the PARAFAC tensor model. This matching is measured in terms of MSE between the received signal and the estimated one which is denoted by MSE($\hat{\mathcal{X}}$). As it has been shown in Sec. 3, TREP-2 is based on ALS, which aims to minimize this MSE at each iteration. Therefore, the

PARAFAC model matching is measured as follows:

$$\mathrm{MSE}(\hat{\mathcal{X}}) = \frac{E\left\{\|\mathbf{Y}_2 - \hat{\mathbf{X}}_2\|_F^2\right\}}{7 \times 12 \times 2} \tag{3.94}$$

where $\hat{\mathbf{X}}_2 = \left(\mathbf{W} \diamond \hat{\mathbf{H}}\right) \hat{\mathbf{S}}^T$.

In Fig. 3.14, we show the $\mathrm{MSE}(\hat{\mathcal{X}})$ in function of N_{It}. We assume a single-cell with R=6 terminals with both normal and extended CP configurations. We can see that $\mathrm{MSE}(\hat{\mathcal{X}})$ is a decreasing function of N_{It} for both CP configurations. Moreover, it is worth mentioning that the uniqueness conditions are guaranteed until $R \leq 19$.

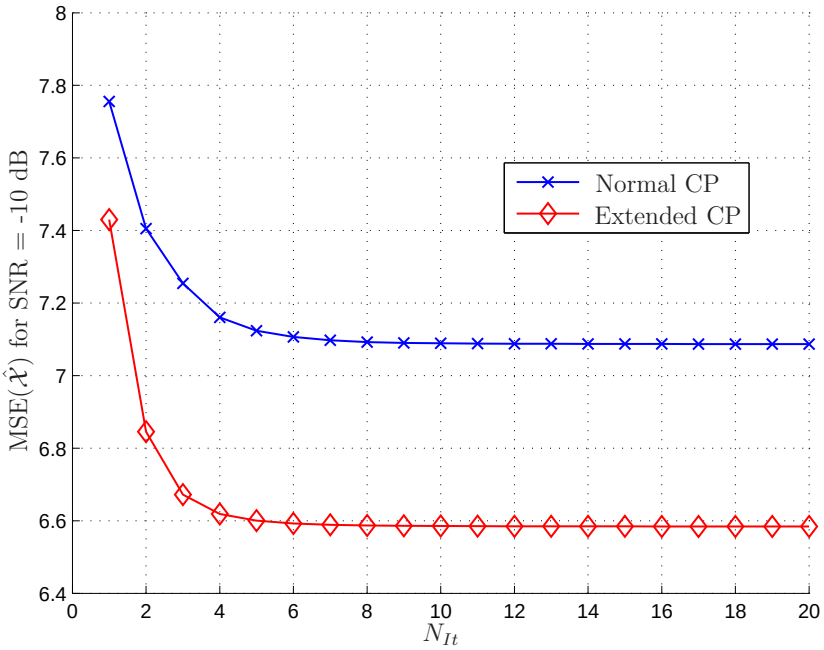

Figure 3.17: PARAFAC model matching of PUCCH Format 2: $R = 6$ UEs

6.2 Multi-Cell Scenario

Channel Estimation

In this part we show a result concerning the study case 1 of Sec. 3.2. In the following simulation, we compare the channel estimation accuracy provided by the TREP-2 to the one provided by a LS channel estimator based on RS, which is

commonly used in conventional receivers.

In Fig. 3.18, we show the MSE($\hat{\mathbf{H}}$) in function of N_{It}. The SNR is fixed to 0 dB and normal CP is assumed. The correlation coefficient is fixed and equals $\kappa = 0.4167 + 0.0833i$. We can note that since the 1-st iteration, TREP-2 provides a smaller MSE($\hat{\mathbf{H}}$). Moreover, this value decays with the number of iterations converging to a local minimum. Comparing Fig. 3.18 to Fig. 3.16, we can observe that in the multi-cell scenario, where the orthogonality is not guaranteed, the MSE($\hat{\mathbf{H}}$) converges to a local minimum closer to the bound for $N_{RS} = 7$ than in the single-cell case.

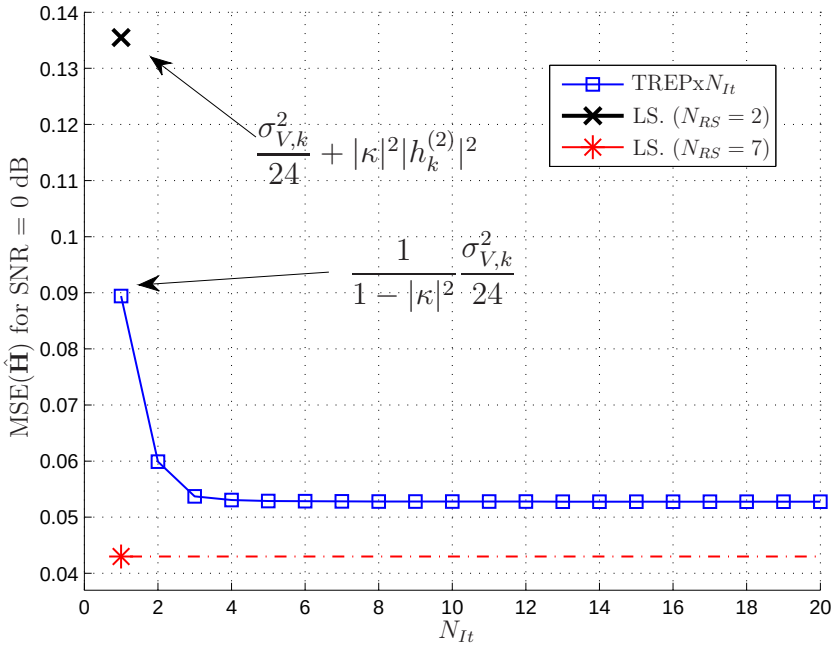

Figure 3.18: MSE from Channel Estimation: Case Study 1

We can conclude from the previous simulation results that the proposed TREP-2 can be an interesting alternative to conventional receivers, as it improves the channel estimation accuracy at the price of more iterations of ALS. In Chapter 5, we evaluate the error performance to confirm the applicability of TREP-2.

CHAPTER 4

PUCCH Format 1 and Constrained PARAFAC Model

In Chapter 3, the baseband model of PUCCH Format 2 has been fitted in a PARAFAC tensor model allowing for improved channel estimation and error performance. This was possible thanks to a proposed receiver, called TREP-2, based on the tensor estimation algorithm ALS. In this Chapter, a new tensor decomposition is derived from PARAFAC to model the baseband transmission in PUCCH Format 1. This new tensor model relies on a fixed constrained matrix that take into account the correlation among the terms of each component matrix. In the case of PUCCH Format 1, e.g., this contrained matrix acts on the design of the symbol matrix, defining the spreading of the ACK/NACK and RS symbols associated with each terminal over the entire time-slot. It is worth mentioning that only the aspects concerning PUCCH Format 1 are covered herein while the complete theoretical formulation of this new tensor model will be presented in the next Chapter. Herein, we show that this new tensor model also allow for improved channel estimation using a modified version of the ALS algorithm, from where we derive a new receiver called TREP-1. Similarly to the previous chapter, we also investigate the behavior of this proposed receiver in both single-cell and multi-cell scenarios. Finally, we conclude showing some preliminary simulation results that justify the further performance gains that will be presented in Chapter 6.

1 Baseband Model of PUCCH Format 1

In the baseband model of PUCCH Format 1 we assume that the 2 slots are taken into account in the signaling model, as the same information is carried on both slots. This information consists of 1 or 2 bits converted into one ACK/NACK modulation symbol associated with the decoded packets in the downlink[1]. We

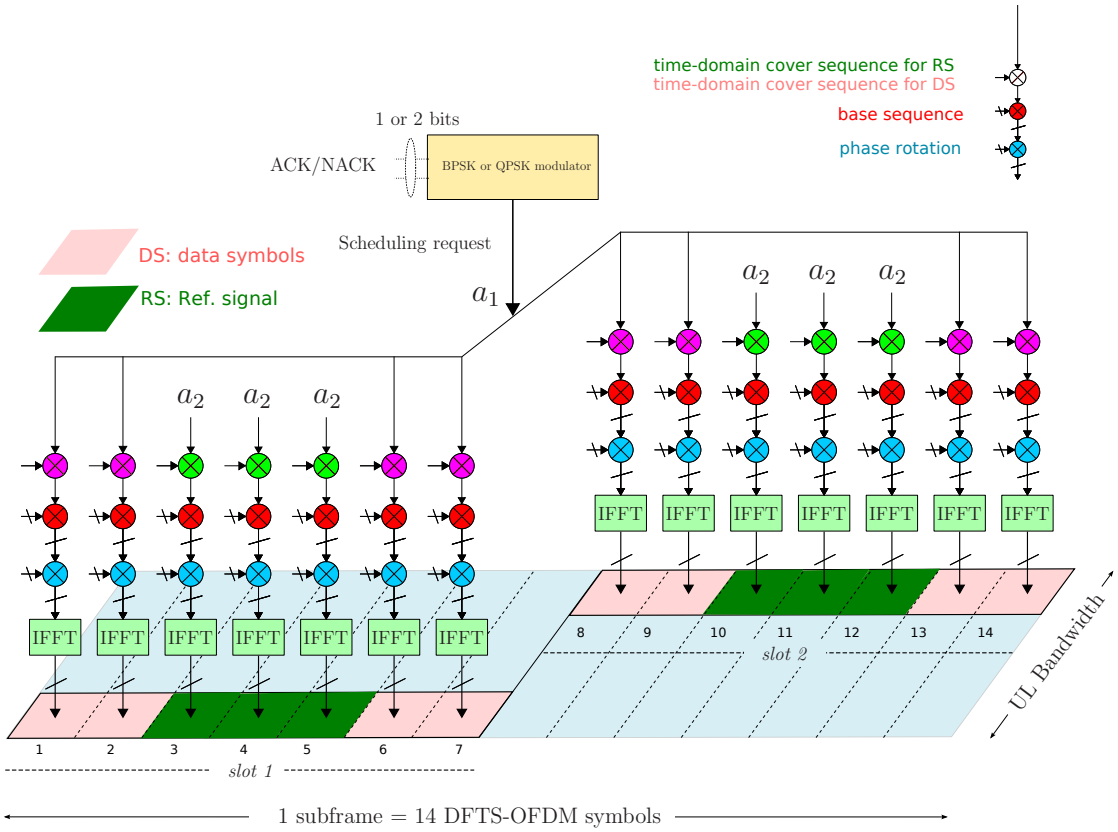

Figure 4.1: Time-frequency structure of PUCCH Format 1

have mentioned that in PUCCH Format 2, each modulation symbol is spread over the frequency domain using a length-12 sequence. In addition to this frequency spreading, in Format 1 the QPSK/BPSK symbol associated with ACK/NACK is also spread over the time domain. Assuming UEs with normal CP configuration, 7

[1]When the terminal is multiplexing information over two antenna ports, there exist 2 ACK/NACK bits, each one associated with a packet transmitted by a given antenna port.

DFTS-OFDM symbols are transmitted in each slot and 3 (out of the 7) are used as RS[2] [3].The time-domain structure of PUCCH Format 1 is illustrated in Fig. 4.1.

Symbol vector

Let a_1 be the modulation symbol associated with the ACK/NACK and a_2 the symbol associated with the RS. The symbol a_1 is spread over an entire time-slot using a *length-4 time-domain cover sequence* denoted $\boldsymbol{\delta} = [\delta_1, \cdots, \delta_4]$ before composing the DFTS-OFDM symbols. In the same manner, the symbol a_2 is spread using a *length-3 time-domain cover sequence* denoted $\boldsymbol{\beta} = [\beta_1, \beta_2, \beta_3]$. Adopting the same notation of Chapter 3, the modulation symbols that compose the 7 DFTS-OFDM symbols are organized in the following symbol vector defined as:

$$\mathbf{s} = \begin{bmatrix} s_1 \\ s_2 \\ s_3 \\ s_4 \\ s_5 \\ s_6 \\ s_7 \end{bmatrix} = \begin{bmatrix} a_1 \cdot \delta_1 \\ a_1 \cdot \delta_2 \\ a_2 \cdot \beta_1 \\ a_2 \cdot \beta_2 \\ a_2 \cdot \beta_3 \\ a_1 \cdot \delta_3 \\ a_1 \cdot \delta_4 \end{bmatrix} \in \mathbb{C}^{7\times 1}. \tag{4.1}$$

The cover sequences $\boldsymbol{\delta}$ and $\boldsymbol{\beta}$ are respectively Walsh sequences of length four and DFT sequences of length three [3, 1]. The length-4 codes are such that the subsets of the code sequences result in the minimum inter-code interference in high Doppler conditions where generally the orthogonality between the code sequences breaks down [47].

Coding vector

The frequency domain length-12 sequences are the same as defined in (3.3), such a way that the data symbols the RS are composed as depicted in Fig. 4.2 and Fig. 4.3 respectively.

[2]If extended CP is used, 6 DFTS-OFDM symbols are transmitted in each slot and 2 are used as RS.

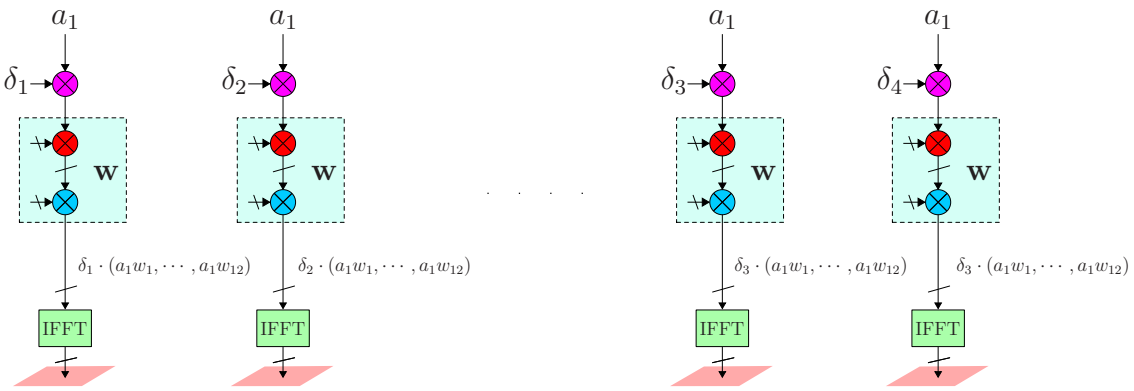

Figure 4.2: Transmit signal composition for PUCCH Format 1: Data part

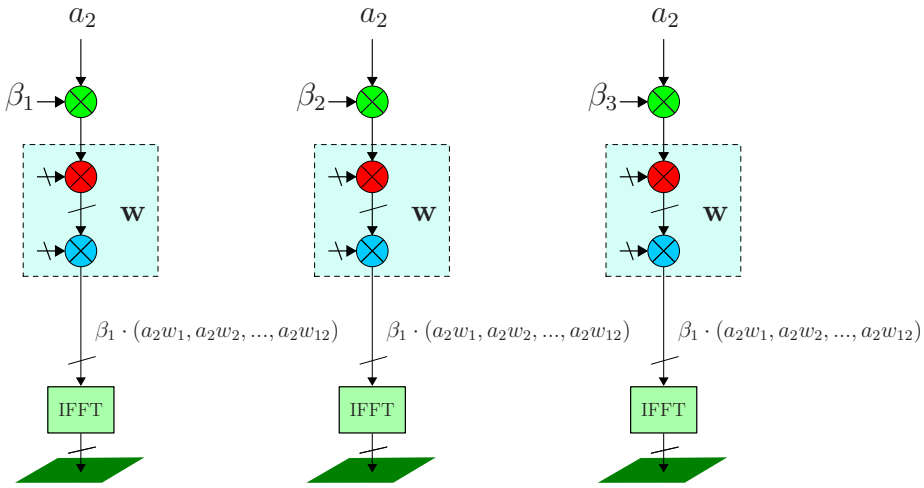

Figure 4.3: Transmit signal composition for PUCCH Format 1: RS

Channel vector

Similarly to the baseband model of PUCCH Format 2, we also consider some simplified assumptions concerning the channel. We assume, e.g., the same fading channel coefficient for a given resource block in the frequency and time domains.

The eNodeB is equipped with 2 receive antennas, which is typically the number considered in LTE. To obtain a diversity gain, the slots are hopped in such a way that our channel model define h_1 and h_2 as the two spatial coefficients associated with the *first slot* and, h_3 and h_4 as the two spatial coefficients associated with the *second slot.*

Then, the channel coefficients associated with the 2 receive antennas and both

slots are organized in the *channel vector* defined as:

$$\mathbf{h} = \begin{bmatrix} h_1 \\ h_2 \\ h_3 \\ h_4 \end{bmatrix} \in \mathbb{C}^{4\times 1}. \tag{4.2}$$

Similarly to (3.4), the received signal associated with the n-th DFTS-OFDM symbol, p-th subcarrier and k-th diversity branch in absence of noise can be expressed as:

$$x_{n,p,k} = s_n \cdot w_p \cdot h_k. \tag{4.3}$$

2 Tensor Model of PUCCH Format 1

Single-user model as a rank-one tensor

Similarly to the modeling of PUCCH Format 2, Eq. (F) defines a third-order tensor of rank one with dimensions $7 \times 12 \times 4$. Then, the received signal, denoted by $\mathcal{X}$, can be written as follows:

$$\mathcal{X} = \mathbf{s} \circ \mathbf{w} \circ \mathbf{h} \tag{4.4}$$

where $\mathbf{s}, \mathbf{w}, \mathbf{h}$ are respectively the symbol, channel and coding vectors defined in this chapter.

Multi-user model as a rank-R tensor

In PUCCH Format 1, the users can be multiplexed both in the time and frequency domains. However, we assume that they are multiplexed only in the frequency domain using a specific coding vector associated with the r-th UE as defined in (3.9).

Then, for a system with R terminals, the multi-user model of PUCCH Format 1 can be written as the sum of R tensor of rank-one, i.e.:

$$\mathcal{X} = \sum_{r=1}^{R} \mathcal{X}^{(r)} = \sum_{r=1}^{R} \mathbf{s}^{(r)} \circ \mathbf{w}^{(r)} \circ \mathbf{h}^{(r)} \tag{4.5}$$

where $\mathcal{X}^{(r)}$ is the signal associated with the r-th terminal. In scalar notation, the

multi-user signal model is given by:

$$x_{n,p,k} = \sum_{r=1}^{R} s_n^{(r)} \cdot w_p^{(r)} \cdot h_k^{(r)} \tag{4.6}$$

where

$$\mathbf{s}^{(r)} = \begin{bmatrix} s_1^{(r)} \\ s_2^{(r)} \\ s_3^{(r)} \\ s_4^{(r)} \\ s_5^{(r)} \\ s_6^{(r)} \\ s_7^{(r)} \end{bmatrix} \in \mathbb{C}^{7\times 1}, \quad \mathbf{w}^{(r)} = \begin{bmatrix} w_1^{(r)} \\ w_2^{(r)} \\ \vdots \\ w_{12}^{(r)} \end{bmatrix} \in \mathbb{C}^{12\times 1}, \quad \mathbf{h}^{(r)} = \begin{bmatrix} h_1^{(r)} \\ h_2^{(r)} \\ h_3^{(r)} \\ h_4^{(r)} \end{bmatrix} \in \mathbb{C}^{4\times 1}$$

are the system parameters associated with the r-th UE.

The parameter set that compose the model can be grouped in the following matrices:

$$\mathbf{S} = \left[\mathbf{s}^{(1)} \;\; \mathbf{s}^{(2)} \;\; \cdots \;\; \mathbf{s}^{(R)}\right] \in \mathbb{C}^{7\times R} \tag{4.7}$$

$$\mathbf{H} = \left[\mathbf{h}^{(1)} \;\; \mathbf{h}^{(2)} \;\; \cdots \;\; \mathbf{h}^{(R)}\right] \in \mathbb{C}^{4\times R} \tag{4.8}$$

$$\mathbf{W} = \left[\mathbf{w}^{(1)} \;\; \mathbf{w}^{(2)} \;\; \cdots \;\; \mathbf{w}^{(R)}\right] \in \mathbb{C}^{12\times R} \tag{4.9}$$

which are respectively, the *symbol*, *channel* and *coding* matrices.

Then, the three unfolded representations $\mathbf{X}_1, \mathbf{X}_2, \mathbf{X}_3$ of the received signal tensor $\mathcal{X}$ can be written as:

$$\mathbf{X}_1 = \mathbf{Z}_1\mathbf{H}^T \in \mathbb{C}^{84\times 4} \tag{4.10}$$

$$\mathbf{X}_2 = \mathbf{Z}_2\mathbf{S}^T \in \mathbb{C}^{48\times 7} \tag{4.11}$$

$$\mathbf{X}_3 = \mathbf{Z}_3\mathbf{W}^T \in \mathbb{C}^{28\times 12} \tag{4.12}$$

where

$$\mathbf{Z}_1 = (\mathbf{S} \diamond \mathbf{W}), \;\; \mathbf{Z}_2 = (\mathbf{W} \diamond \mathbf{H}), \;\; \mathbf{Z}_3 = (\mathbf{H} \diamond \mathbf{S}).$$

Similarly to Eq. (3.10), Eq. (4.5) can be interpreted as a PARAFAC model [8], of which $\mathbf{S}, \mathbf{W}$ and $\mathbf{H}$ are the component matrices. However, PARAFAC does not take into account the time-domain correlation among the rows of the symbol matrix, inherent from the Format 1.

In the following, we extend the PARAFAC approach to define a *new tensor model that takes the time-domain spreading of the ACK/NACK symbols into account. Exploiting this new model, a new multi-user receiver is derived for inter-cell interference reduction in PUCCH LTE Format 1.* The next Section shows the properties of this new tensor model and how PARAFAC is extended.

3 New Constrained Tensor model

In the single-user case, the symbol vector defined in (4.1) can be factored as follows:

$$\mathbf{s} = \begin{bmatrix} a_1 \cdot \delta_1 \\ a_1 \cdot \delta_2 \\ a_2 \cdot \beta_1 \\ a_2 \cdot \beta_2 \\ a_2 \cdot \beta_3 \\ a_1 \cdot \delta_3 \\ a_1 \cdot \delta_4 \end{bmatrix} = \begin{bmatrix} \delta_1 & 0 \\ \delta_2 & 0 \\ 0 & \beta_1 \\ 0 & \beta_2 \\ 0 & \beta_3 \\ \delta_3 & 0 \\ \delta_1 & 0 \end{bmatrix} \begin{bmatrix} a_1 \\ a_2 \end{bmatrix} \tag{4.13}$$

$$= \mathbf{\Theta a}. \tag{4.14}$$

where $\mathbf{\Theta}$ is a new system parameter herein called the *time spreading matrix* and $\mathbf{a} = [a_1 \quad a_2]^T$ is called the *effective symbol vector* containing the modulation symbols a_1 and a_2 associated respectively with the ACK/NACK symbol and the RS. Since in our model the terminals are multiplexed only over the frequency domain, we assume the time-domain sequences are $\boldsymbol{\delta} = [1\ 1\ 1\ 1]$ and $\boldsymbol{\beta} = [1\ 1\ 1]$, so that the symbol vector can be rewritten as:

$$\mathbf{s} = \mathbf{\Theta a} = \begin{bmatrix} 1 & 0 \\ 1 & 0 \\ 0 & 1 \\ 0 & 1 \\ 0 & 1 \\ 1 & 0 \\ 1 & 0 \end{bmatrix} \begin{bmatrix} a \\ 1 \end{bmatrix} = \begin{bmatrix} a \\ a \\ 1 \\ 1 \\ 1 \\ a \\ a \end{bmatrix} \tag{4.15}$$

where $a_1 = a$ and $a_2 = 1$. Notice that the matrix $\mathbf{\Theta}$ controls the density and distribution of RS and the ACK/NACK symbol over both time-slots.

In scalar notation, this operation can be written as:

$$s_n = \sum_{m=1}^{2} \theta_{n,m} a_m \tag{4.16}$$

where $m = 1, 2$ such a that, the received signal of (4.6) accounting the R terminals can be written as:

$$x_{n,p,k} = \sum_{r=1}^{R} \sum_{m=1}^{2} \theta_{n,m} a_m^{(r)} \cdot w_p^{(r)} \cdot h_k^{(r)}. \tag{4.17}$$

Considering its constrained structure, the symbol matrix of (4.7) can be factored as follows:

$$\mathbf{S} = \begin{bmatrix} \boldsymbol{\Theta}\mathbf{a}^{(1)} & \boldsymbol{\Theta}\mathbf{a}^{(2)} & \cdots & \boldsymbol{\Theta}\mathbf{a}^{(R)} \end{bmatrix} \tag{4.18}$$

$$= \boldsymbol{\Theta}\mathbf{A}, \tag{4.19}$$

where $\mathbf{A} = \begin{bmatrix} \mathbf{a}^{(1)} & \mathbf{a}^{(2)} & \cdots & \mathbf{a}^{(R)} \end{bmatrix}$ is called the *effective symbol matrix*.

The set of equation (4.10)-(4.12) can be extended, such a way that the unfolded representations of the tensor () can be written, using the Khatri-Rao product:

$$\mathbf{X}_1 = \mathbf{Z}_1 \mathbf{H}^T \in \mathbb{C}^{84 \times 4} \tag{4.20}$$

$$\mathbf{X}_2 = \mathbf{Z}_2 \mathbf{A}^T \boldsymbol{\Theta}^T \in \mathbb{C}^{48 \times 7} \tag{4.21}$$

$$\mathbf{X}_3 = \mathbf{Z}_3 \mathbf{W}^T \in \mathbb{C}^{28 \times 12} \tag{4.22}$$

where

$$\mathbf{Z}_1 = \left((\boldsymbol{\Theta}\mathbf{A}) \diamond \mathbf{W} \right), \quad \mathbf{Z}_2 = \left(\mathbf{W} \diamond \mathbf{H} \right), \quad \mathbf{Z}_3 = \left(\mathbf{H} \diamond (\boldsymbol{\Theta}\mathbf{A}) \right).$$

Received signal as a tensor

The model is completed when AWGN is included [9]. To model the signal using the same notation, the noise is also represented in a $7 \times 12 \times 4$ tensor $\mathcal{V}$, where each term $v_{n,p,k}$ is associated with the n-th symbol, $p-$th subcarrier and $k-$th diversity branch. Therefore, the noisy received signal in scalar notation is written as:

$$y_{n,p,k} = x_{n,p,k} + v_{n,p,k} = \sum_{r=1}^{R} \sum_{m=1}^{2} \theta_{n,m} a_m^{(r)} \cdot w_p^{(r)} \cdot h_k^{(r)} + v_{n,p,k} \tag{4.23}$$

which in tensor notation is represented as:

$$\mathcal{Y} = \mathcal{X} + \mathcal{V} = \sum_{r=1}^{R} \boldsymbol{\Theta}\mathbf{a}^{(r)} \circ \mathbf{w}^{(r)} \circ \mathbf{h}^{(r)} + \mathcal{V}. \tag{4.24}$$

The noise samples are modeled as i.i.d. zero mean complex Gaussian random variables with variance:

$$E\left\{|v_{n,p,k}|^2\right\} = \sigma_{V,k}^2$$

Since $\mathcal{V}$ is a third-order tensor, it has also the three unfolded representations given by:

$$\mathbf{V}_1 = \begin{bmatrix} \mathbf{V}_{1..} \\ \mathbf{V}_{2..} \\ \vdots \\ \mathbf{V}_{7..} \end{bmatrix}, \quad \mathbf{V}_2 = \begin{bmatrix} \mathbf{V}_{.1.} \\ \mathbf{V}_{.2.} \\ \vdots \\ \mathbf{V}_{.12.} \end{bmatrix} \quad \text{and} \quad \mathbf{V}_3 = \begin{bmatrix} \mathbf{V}_{..1} \\ \mathbf{V}_{..2} \\ \vdots \\ \mathbf{V}_{..4} \end{bmatrix}. \tag{4.25}$$

Thus, the unfolded representations of the received signal $\mathcal{Y}$ are expressed as:

$$\mathbf{Y}_1 = \mathbf{Z}_1\mathbf{H}^T + \mathbf{V}_1 \tag{4.26}$$

$$\mathbf{Y}_2 = \mathbf{Z}_2\mathbf{A}^T\boldsymbol{\Theta}^T + \mathbf{V}_2 \tag{4.27}$$

$$\mathbf{Y}_3 = \mathbf{Z}_3\mathbf{W}^T + \mathbf{V}_3. \tag{4.28}$$

4 Tensor-based Receiver for PUCCH Format 1 (TREP-1)

In order to exploit the new tensor modeling of the received signal, we make use of a modified version of the ALS algorithm. In the version proposed in this Chapter, we take the correlation in the time domain of the ACK/NACK symbols into account such that the component matrices to be estimated are the *effective symbol*, *coding* and *channel* matrices, while the received data correspond to the noisy signal measured at the receive antennas.

Similarly to the classical version of ALS, from where TREP-2 has been derived, this modified version of ALS also makes use of the three unfolded representations (4.20)-(4.22). At each step of our algorithm, one component matrix is estimated in the LS sense, while the two others are fixed to their values obtained at the two previous steps. We assume that $\boldsymbol{\Theta}$ is known and fixed during the iterative

estimation process[3].

TREP-1 can be applied for both *single-cell* and *multi-cell* scenarios. The same 2 network configurations presented in Chapter 3 are also considered herein so that the initialization of the coding matrix in the algorithm depends on it. Then, the general algorithm can be summarized as follows:

Algorithm 2 TREP for PUCCH Format 1

1. Set $i = 0$; Initialize $\hat{\mathbf{A}}_{(i=0)} = \begin{bmatrix} 0 & 0 & \cdots & 0 \\ 1 & 1 & \cdots & 1 \end{bmatrix} \in \mathbb{C}^{2\times R}$ and $\mathbf{W}_{(i=0)} \in \mathbb{C}^{12\times R}$;
2. $i = i + 1$;
3. Using $\mathbf{Y}_1$, find an LS estimate of $\mathbf{H}$:
$$\hat{\mathbf{H}}^T_{(i)} = \left[\hat{\mathbf{Z}}_{1,(i)}\right]^{\dagger} \mathbf{Y}_1$$
4. Using $\mathbf{Y}_2$, find an LS estimate of $\mathbf{A}$:
$$\hat{\mathbf{A}}^T_{(i)} = \left[\hat{\mathbf{Z}}_{2,(i)}\right]^{\dagger} \mathbf{Y}_2 \left[\mathbf{\Theta}^T\right]^{\dagger}$$
5. Using $\mathbf{Y}_3$, find an LS estimate of $\mathbf{W}$:
$$\hat{\mathbf{W}}^T_{(i)} = \left[\hat{\mathbf{Z}}_{3,(i)}\right]^{\dagger} \mathbf{Y}_3$$
6. Repeat steps 2-5 until convergence

where

$$\hat{\mathbf{Z}}_{1,(i)} = \left(\mathbf{\Theta}\hat{\mathbf{A}}_{(i-1)} \diamond \hat{\mathbf{W}}_{(i-1)}\right), \hat{\mathbf{Z}}_{2,(i)} = \left(\hat{\mathbf{W}}_{(i-1)} \diamond \hat{\mathbf{H}}_{(i)}\right) \text{ and } \hat{\mathbf{Z}}_{3,(i)} = \left(\mathbf{H}_{(i)} \diamond \mathbf{\Theta}\hat{\mathbf{A}}_{(i)}\right).$$

In the following we apply the proposed algorithm in the single-cell and multi-cell scenarios.

[3]The CP configuration is also controlled modifying the structure of $\mathbf{\Theta}$

4.1 Single-Cell Scenario

Similarly to TREP-2, the same valid assumptions can be taken into account in the single-cell scenario:

- The coding matrix is known at the eNodeB so that we initialize the algorithm with $\hat{\mathbf{W}}_{(i=0)} = \mathbf{W}$.

- As the coding matrix is known at the eNodeB, Step 5 can be hopped.

Recall that in this scenario the coding vectors are orthogonal thanks to the particular phase rotation per UE in the cell-specific base sequence. In the following we show how our proposed receiver exploits the new tensor model, improving the channel estimation and ameliorating data detection.

Channel Estimation

At the first iteration, the channel matrix is estimated in Step 3 as follows:

$$\hat{\mathbf{H}}^{T}_{(i=1)} = \left[\hat{\mathbf{Z}}_{1,(i=1)}\right]^{\dagger}\mathbf{Y}_1 = \left[\left(\hat{\mathbf{Z}}^{H}_{1,(i=1)}\hat{\mathbf{Z}}_{1,(i=1)}\right)^{-1}\hat{\mathbf{Z}}^{H}_{1,(i=1)}\right]\mathbf{Z}_1\mathbf{H}^{T} + \left[\hat{\mathbf{Z}}_{1,(i=1)}\right]^{\dagger}\mathbf{V}_1 \tag{4.29}$$

where $\hat{\mathbf{Z}}_{1,(i=1)} = \left(\boldsymbol{\Theta}\hat{\mathbf{A}}_{(i=0)} \diamond \mathbf{W}\right) = \begin{bmatrix} \mathbf{0}_R \\ \mathbf{0}_R \\ \mathbf{W} \\ \mathbf{W} \\ \mathbf{W} \\ \mathbf{0}_R \\ \mathbf{0}_R \end{bmatrix}$.

Since the coding matrix is orthogonal,

$$\hat{\mathbf{Z}}^{H}_{1,(i=1)}\hat{\mathbf{Z}}_{1,(i=1)} = 3\ \mathbf{W}^{H}\mathbf{W} = 36\mathbf{I}_R \tag{4.30}$$

is a diagonal matrix such that Step 3 reduces to:

$$\hat{\mathbf{H}}^T_{(i=1)} = \left[\frac{\hat{\mathbf{Z}}^H_{1,(i=1)}}{36}\right]\mathbf{Y}_1 = \frac{\hat{\mathbf{Z}}^H_{1,(i=1)}\mathbf{Z}_1}{36}\mathbf{H}^T + \frac{\hat{\mathbf{Z}}^H_{1,(i=1)}\mathbf{V}_1}{36}. \tag{4.31}$$

In the previous equation, the term that multiplies the channel matrix is given by:

$$\frac{\hat{\mathbf{Z}}^H_{1,(i=1)}\mathbf{Z}_1}{36} = \frac{3\mathbf{W}^H\mathbf{W}}{36} = \mathbf{I}_R \tag{4.32}$$

and, in the same manner, the filtered noise of Eq. (4.31), denoted by $\mathbf{V}^T_{h,(i=1)}$, is:

$$\mathbf{V}^T_{h,(i=1)} = \frac{\hat{\mathbf{Z}}^H_{1,(i=1)}\mathbf{V}_1}{36} = \frac{\mathbf{W}^H}{36}\left(\mathbf{V}_{3..} + \mathbf{V}_{4..} + \mathbf{V}_{5..}\right) \tag{4.33}$$

$$= \frac{1}{3}\left(\begin{bmatrix} \bar{\mathbf{v}}_3^{(1)} \\ \bar{\mathbf{v}}_3^{(2)} \\ \vdots \\ \bar{\mathbf{v}}_3^{(R)} \end{bmatrix} + \begin{bmatrix} \bar{\mathbf{v}}_4^{(1)} \\ \bar{\mathbf{v}}_4^{(2)} \\ \vdots \\ \bar{\mathbf{v}}_4^{(R)} \end{bmatrix} + \begin{bmatrix} \bar{\mathbf{v}}_5^{(1)} \\ \bar{\mathbf{v}}_5^{(2)} \\ \vdots \\ \bar{\mathbf{v}}_5^{(R)} \end{bmatrix}\right) \tag{4.34}$$

where

$$\bar{\mathbf{v}}_n^{(r)} = \frac{\sum_{p=1}^{12} w_p^{(r)*}\mathbf{v}_{n,p}}{12}$$

is the noise associated with the n-th DFTS-OFDM symbol and r-th terminal averaged over the 12 subcarriers and $\mathbf{v}_{n,p} = [v_{n,p,1} \;\; v_{n,p,2}]$.

Hereafter, the estimated channel matrix is given by:

$$\hat{\mathbf{H}}^T_{(i=1)} = \mathbf{H}^T + \mathbf{V}^T_h \tag{4.35}$$

and the channel estimate associated with the r-th terminal is:

$$\hat{\mathbf{h}}^{(r)}_{(i=1)} = \mathbf{h}^{(r)} + \mathbf{v}^{(r)}_{h,(i=1)} = \mathbf{h}^{(r)} + \frac{\bar{\mathbf{v}}_3^{(r)} + \bar{\mathbf{v}}_4^{(r)} + \bar{\mathbf{v}}_5^{(r)}}{3}. \tag{4.36}$$

Similarly to (3.32), Eq. (4.36) shows that the RS from the R terminals are perfectly separated such that the only impairment of (4.36) comes from the noise. However, as in Format 1 we have that $N_{RS} = 3$, $\mathbf{v}^{(r)}_{h,(i=1)}$ is herein the average of the noise samples over the 12 subcarriers and the 3 RS.

Thus, the variance of $\mathbf{v}_{h,(i=1)}^{(r)}$ is given by (c.f. **A.2**):

$$\sigma_{v_{h_k}}^2 = \frac{\sigma_{V,k}^2}{3 \times 12} \tag{4.37}$$

for the k-th channel coefficient.

In the following we show that from the second iteration, the modified version of proposed ALS algorithm uses energy from the estimated symbols to reestimate the channel, working as a data-aided channel estimator [43, 44, 45, 46].

From the 2-nd Iteration (Data-aided Estimation)

In the next step, the symbol matrix is calculated as follows:

$$\hat{\mathbf{S}}_{(i=1)}^{T} = \left[\hat{\mathbf{Z}}_{2,(i=1)}\right]^{\dagger} \mathbf{Y}_2 = \left[\left(\hat{\mathbf{Z}}_{2,(i=1)}^{H}\hat{\mathbf{Z}}_{2,(i=1)}\right)^{-1}\hat{\mathbf{Z}}_{2,(i=1)}^{H}\right]\mathbf{Z}_2\mathbf{S}^{T} + \left[\hat{\mathbf{Z}}_{2,(i=1)}\right]^{\dagger}\mathbf{V}_2 \tag{4.38}$$

where $\hat{\mathbf{Z}}_{2,(i=1)} = \left(\mathbf{W} \diamond \hat{\mathbf{H}}_{(i=1)}\right)$.

Then, considering the results of (3.37)-(3.42), the estimated symbol vector at the end of the first iteration is given by:

$$\hat{\mathbf{s}}_{(i=1)}^{(r)\,T} = \hat{\mathbf{a}}_{(i=1)}^{(r)\,T}\boldsymbol{\Theta}^{T} = \frac{\hat{\mathbf{h}}_{(i=1)}^{(r)H}\mathbf{h}^{(r)}}{\|\hat{\mathbf{h}}_{(i=1)}^{(r)}\|^2}\mathbf{s}^{(r)T} + \frac{\hat{\mathbf{h}}_{(i=1)}^{(r)H}\left[\bar{\mathbf{v}}_1^{(r)} \;\cdots\; \bar{\mathbf{v}}_7^{(r)}\right]}{\|\hat{\mathbf{h}}_{(i=1)}^{(r)}\|^2}. \tag{4.39}$$

such that the estimated effective symbol vector is:

$$\hat{\mathbf{a}}_{(i=1)}^{(r)} = \left(\frac{\hat{\mathbf{h}}_{(i=1)}^{(r)H}\mathbf{h}^{(r)}}{\|\hat{\mathbf{h}}_{(i=1)}^{(r)}\|^2}\right)\mathbf{a}^{(r)} + \frac{\hat{\mathbf{h}}_{(i=1)}^{(r)H}}{\|\hat{\mathbf{h}}_{(i=1)}^{(r)}\|^2}\left[\frac{\bar{\mathbf{v}}_1{}^{(r)} + \bar{\mathbf{v}}_2{}^{(r)} + \bar{\mathbf{v}}_6{}^{(r)} + \bar{\mathbf{v}}_7{}^{(r)}}{4} \quad \frac{\bar{\mathbf{v}}_3{}^{(r)} + \bar{\mathbf{v}}_4{}^{(r)} + \bar{\mathbf{v}}_5{}^{(r)}}{3}\right]. \tag{4.40}$$

At the end of the first iteration, the estimated matrix $\hat{\mathbf{A}}_{(i=1)}$ is used as input to the second iteration of ALS and so on.

Thus, at the $(i+1)$-th iteration the channel estimate is given by:

$$\hat{\mathbf{H}}^{T}_{(i+1)} = \left[\hat{\mathbf{Z}}_{1,(i+1)}\right]^{\dagger} \mathbf{Y}_1 \tag{4.41}$$

$$= \left[\left(\hat{\mathbf{Z}}^{H}_{1,(i+1)}\hat{\mathbf{Z}}_{1,(i+1)}\right)^{-1}\hat{\mathbf{Z}}^{H}_{1,(i+1)}\right]\mathbf{Z}_1\mathbf{H}^{T} + \hat{\mathbf{Z}}^{\dagger}_{1,(i+1)}\mathbf{V}_1 \tag{4.42}$$

where $\hat{\mathbf{Z}}_{1,(i+1)} = \left(\mathbf{W} \diamond \boldsymbol{\Theta}\mathbf{A}_{(i)}\right)$, such that

$$\hat{\mathbf{Z}}^{H}_{1,(i+1)}\mathbf{Z}_1 = \sum_{n=1}^{7} D_n(\boldsymbol{\Theta}\hat{\mathbf{A}}^{*}_{(i)})\mathbf{W}^{H}\mathbf{W}D_n(\boldsymbol{\Theta}\mathbf{A}) \tag{4.43}$$

$$= 12\sum_{n=1}^{7} D_n(\boldsymbol{\Theta}\hat{\mathbf{A}}^{*}_{(i)})\mathbf{I}_R D_n(\boldsymbol{\Theta}\mathbf{A}) \tag{4.44}$$

$$= 12\begin{bmatrix} 3+4\hat{a}^{(1)*}_{(i)}a^{(1)} & \cdots & 0 \\ \vdots & \ddots & \vdots \\ 0 & \cdots & 3+4\hat{a}^{(R)*}_{(i)}\cdot a^{(R)} \end{bmatrix} \tag{4.45}$$

and

$$\left(\hat{\mathbf{Z}}^{H}_{1,(i+1)}\hat{\mathbf{Z}}_{1,(i+1)}\right)^{-1} = \frac{1}{12}\begin{bmatrix} 3+4|\hat{a}^{(1)}_{(i)}|^2 & \cdots & 0 \\ \vdots & \ddots & \vdots \\ 0 & \cdots & 3+4|\hat{a}^{(R)}_{(i)}|^2 \end{bmatrix}^{-1}. \tag{4.46}$$

Alternatively, the estimated channel associated with the r-th UE can be written as:

$$\hat{\mathbf{h}}^{(r)}_{(i+1)} = \left(\frac{3+4\hat{a}^{(r)*}_{(i)}\cdot a^{(r)}}{3+4|\hat{a}^{(r)}_{(i)}|^2}\right)\mathbf{h}^{(r)} + \mathbf{v}^{(r)}_{h,(i+1)} \tag{4.47}$$

$$= \eta^{(r)}_{(i+1)}\mathbf{h} + \mathbf{v}^{(r)}_{h,(i+1)} \tag{4.48}$$

Differently from (4.36), Eq. (4.48) shows that the channel estimate from the second iteration has a bias given by:

$$\eta^{(r)}_{(i+1)} = \left(\frac{3+4\hat{a}^{(r)*}_{(i)}a^{(r)}}{3+4|\hat{a}^{(r)}_{(i)}|^2}\right). \tag{4.49}$$

Furthermore, the channel estimation noise at the end of the $(i+1)$-th iteration is given by:

$$\mathbf{v}_{h,(i+1)}^{(r)} = \frac{\bar{\mathbf{v}}_3^{(r)} + \bar{\mathbf{v}}_4^{(r)} + \bar{\mathbf{v}}_5^{(r)} + \hat{a}_{(i)}^{(r)*}\left(\bar{\mathbf{v}}_1^{(r)} + \bar{\mathbf{v}}_2^{(r)} + \bar{\mathbf{v}}_6^{(r)} + \bar{\mathbf{v}}_7^{(r)}\right)}{3 + 4|\hat{a}_{(i)}^{(r)}|^2}. \tag{4.50}$$

As in Chapter 3, simulation results show that despite the bias of (4.48), the MSE of channel estimation is improved when the number of iterations of ALS is increased. This happens since the variance of $\mathbf{v}_{h,(i+1)}^{(r)}$ is reduced as it is now averaged over the RS and the data part.

Data Detection

Similarly to TREP-2, Step 4 of the modified version of ALS is adjusted to account for the unbalanced noise variance. This is done by making the following replacement:

$$\left[\hat{\mathbf{Z}}_{2,(i)}\right]^{\dagger} = \left(\hat{\mathbf{Z}}_{2,(i)}^{H}\hat{\mathbf{Z}}_{2,(i)}\right)^{-1}\hat{\mathbf{Z}}_{2,(i)}^{H} \tag{4.51}$$

$$\Downarrow \tag{4.52}$$

$$\left(\hat{\mathbf{Z}}_{2,(i)}^{\prime\,H}\hat{\mathbf{Z}}_{2,(i)}\right)^{-1}\hat{\mathbf{Z}}_{2,(i)}^{\prime\,H}. \tag{4.53}$$

where

$$\hat{\mathbf{Z}}_{2,(i)}^{\prime} = \left(\mathbf{W} \diamond \hat{\mathbf{H}}_{(i)}\boldsymbol{\Sigma}^{-2}\right) = \begin{bmatrix} \hat{\mathbf{H}}_{(i)}\boldsymbol{\Sigma}^{-2}D_1(\mathbf{W}) \\ \hat{\mathbf{H}}_{(i)}\boldsymbol{\Sigma}^{-2}D_2(\mathbf{W}) \\ \vdots \\ \hat{\mathbf{H}}_{(i)}\boldsymbol{\Sigma}^{-2}D_{12}(\mathbf{W}) \end{bmatrix}. \tag{4.54}$$

Therefore, the estimated ACK/NACK symbol obtained in this case at the end of the i-th iteration is:

$$\hat{\mathbf{a}}_{(i)}^{(r)} = \left(\frac{\hat{\mathbf{h}}_{(i)}^{(r)H}\boldsymbol{\Sigma}^{-2}\mathbf{h}^{(r)}}{\hat{\mathbf{h}}_{(i)}^{(r)\,H}\boldsymbol{\Sigma}^{-2}\hat{\mathbf{h}}_{(i)}^{(r)}}\right)a^{(r)} + \frac{\hat{\mathbf{h}}_{(i)}^{(r)H}\boldsymbol{\Sigma}^{-2}}{\hat{\mathbf{h}}_{(i)}^{(r)\,H}\boldsymbol{\Sigma}^{-2}\hat{\mathbf{h}}_{(i)}^{(r)}}\left(\frac{\bar{\mathbf{v}}_1^{(r)} + \bar{\mathbf{v}}_2^{(r)} + \bar{\mathbf{v}}_6^{(r)} + \bar{\mathbf{v}}_7^{(r)}}{4}\right). \tag{4.55}$$

Hereafter, the estimated symbol matrix is formed to be used as input to the next iteration to reestimate the channel.

We denote by $\hat{\mathbf{H}}$ the estimated channel matrix after N_{It} iterations of ALS. Each estimated ACK/NACK symbol is multiplied by the its respective estimated effective

channel defined as:

$$\hat{h}_{eff}^{(r)} = \sqrt{\frac{\sum_{k=1}^{4} |\hat{h}_k^{(r)}|^2}{\sigma_{V,k}^2}} \tag{4.56}$$

so that the *decision variable* for the ACK/NACK symbol associated with the r-th UE is given by:

$$\hat{D}^{(r)} = \frac{1}{\hat{h}_{eff}^{(r)}} \left(\frac{\hat{h}_1^* h_1}{\sigma_{V,1}^2} + \frac{\hat{h}_2^* h_2}{\sigma_{V,2}^2} + \frac{\hat{h}_3^* h_3}{\sigma_{V,3}^2} + \frac{\hat{h}_4^* h_4}{\sigma_{V,4}^2} \right) a^{(r)} \tag{4.57}$$

$$+ \frac{1}{\hat{h}_{eff}^{(r)}} \hat{\mathbf{h}}^H \boldsymbol{\Sigma}^{-2} \left(\frac{\bar{\mathbf{v}}_1^{(r)} + \bar{\mathbf{v}}_2^{(r)} + \bar{\mathbf{v}}_6^{(r)} + \bar{\mathbf{v}}_7^{(r)}}{4} \right) \tag{4.58}$$

5 Multi-Cell Scenario

Similarly to TREP-2 (c.f. Sec. 4, Ch. 3), we assume a system with $Q-1$ interfering neighboring cells, such that Z_q terminals are served by the q-th cell. The received signal tensor that describes this scenario is given by:

$$\mathcal{X} = \sum_{r=1}^{R} \mathcal{X}^{(r)} + \sum_{q=2}^{Q} \sum_{z_q=1}^{Z_q} \boldsymbol{\Theta} \mathbf{a}_q^{(z_q)} \circ \mathbf{w}_q^{(z_q)} \circ \mathbf{h}_q^{(z_q)} \tag{4.59}$$

where $\mathbf{a}_q^{(z_q)}, \mathbf{w}_q^{(z_q)}, \mathbf{h}_q^{(z_q)}$ are respectively the *effective symbol, coding* and *channel* vectors associated with the z_q-th terminal from the q-th cell. The coding vector associated with the z_q-th terminal from the q-th cell is the same defined in (3.60) so that the coding vectors associated with the q-th cell are organized in the following coding matrix:

$$\mathbf{W}(q) = \left[\mathbf{w}_q^{(1)} \cdots \mathbf{w}_q^{(Z_q)} \right].$$

In the following, we analyze TREP-1 under the same network configurations 1 and 2, as defined in the previous chapter (c.f. Sec. 4, Ch. 3).

5.1 Configuration 1

Configuration 1 assumes that Q neighboring eNodeBs are connected. Then, the coding matrix is initialized as follows:

$$\hat{\mathbf{W}}_{(i=0)} = [\mathbf{W}(1) \cdots \mathbf{W}(q) \cdots \mathbf{W}(Q)] . \tag{4.60}$$

In the following, we consider a case study similar to that defined for TREP-2 (c.f. Sec. 4.1, Ch. 3).

Case study 1 (Configuration 1)

In this case study, 2 eNodeBs are connected so that the desired eNodeB knows the coding vector associated with the interfering UE and the algorithm is initialized with:

$$\hat{\mathbf{W}}_{(i=0)} = \left[\mathbf{w}^{(1)}\ \mathbf{w}^{(2)}\right] . \tag{4.61}$$

Channel Estimation

Channel Estimation at the 1-st iteration

At the first iteration of ALS, the channel matrix is estimated in Step 3 as follows:

$$\hat{\mathbf{H}}^{T}_{(i=1)} = \left[\hat{\mathbf{Z}}_{1,(i=1)}\right]^{\dagger} \mathbf{Y}_1 = \left[\left(\hat{\mathbf{Z}}^{H}_{1,(i=1)}\hat{\mathbf{Z}}_{1,(i=1)}\right)^{-1} \hat{\mathbf{Z}}^{H}_{1,(i=1)}\right] \mathbf{Z}_1\mathbf{H}^{T} + \hat{\mathbf{Z}}^{\dagger}_{1,(i=1)}\mathbf{V}_1 \tag{4.62}$$

where $\hat{\mathbf{Z}}_{1,(i=1)} = \left(\boldsymbol{\Theta}\mathbf{A}_{(i=0)} \diamond \mathbf{W}\right)$.

As the coding matrix $\mathbf{W}$ is non-orthogonal, $\hat{\mathbf{Z}}_{1,(i=1)}\mathbf{Z}_1$ is a non-diagonal matrix. Thus, as it has been shown in (3.64),

$$\left(\hat{\mathbf{Z}}^{H}_{1,(i=1)}\hat{\mathbf{Z}}_{1,(i=1)}\right)^{-1} = \begin{bmatrix} 12 & 12\kappa \\ 12\kappa^{*} & 12 \end{bmatrix}^{-1} = \frac{1}{12(1-|\kappa|^2)} \begin{bmatrix} 1 & -\kappa \\ -\kappa^{*} & 1 \end{bmatrix} \tag{4.63}$$

where $\kappa = \mathbf{w}(1)H\mathbf{w}^{(2)}/12$ such a way that Eq. (4.62) gives the follwing channel

estimate:

$$\hat{\mathbf{H}}^T_{(i=1)} = \mathbf{H}^T + \frac{1}{(1-|\kappa|^2)} \begin{bmatrix} 1 & -\kappa \\ -\kappa^* & 1 \end{bmatrix} \frac{1}{3} \left(\begin{bmatrix} \bar{\mathbf{v}}_3^{(1)} \\ \bar{\mathbf{v}}_3^{(2)} \end{bmatrix} + \begin{bmatrix} \bar{\mathbf{v}}_4^{(1)} \\ \bar{\mathbf{v}}_4^{(2)} \end{bmatrix} \begin{bmatrix} \bar{\mathbf{v}}_5^{(1)} \\ \bar{\mathbf{v}}_5^{(2)} \end{bmatrix} \right) \tag{4.64}$$

$$= \mathbf{H}^T + \frac{1}{(1-|\kappa|^2)} \begin{bmatrix} 1 & -\kappa \\ -\kappa^* & 1 \end{bmatrix} \begin{bmatrix} \mathbf{v}_{h,(i=1)}^{(1)} \\ \mathbf{v}_{h,(i=1)}^{(2)} \end{bmatrix} \tag{4.65}$$

$$= \mathbf{H}^T + \frac{1}{(1-|\kappa|^2)} \begin{bmatrix} \mathbf{v}_{h,(i=1)}^{(1)} - \kappa \mathbf{v}_{h,(i=1)}^{(2)} \\ \mathbf{v}_{h,(i=1)}^{(2)} - \kappa^* \mathbf{v}_{h,(i=1)}^{(1)} \end{bmatrix}. \tag{4.66}$$

Alternatively, we can represent the channel estimate associated with the desired UE as:

$$\hat{\mathbf{h}}_{(i=1)}^{(1)} = \mathbf{h}^{(1)} + \frac{1}{1-|\kappa|^2} \left(\mathbf{v}_{h,(i=1)}^{(1)} - \kappa \mathbf{v}_{h,(i=1)}^{(2)} \right). \tag{4.67}$$

The *channel estimation error* in this case is given by:

$$\mathbf{e}_{h,(i=1)} = \frac{1}{1-|\kappa|^2} \left(\mathbf{v}_{h,(i=1)}^{(1)} - \kappa \mathbf{v}_{h,(i=1)}^{(2)} \right). \tag{4.68}$$

In Appendix **A.5** we have shown that the error variance equals:

$$\sigma^2_{e_{h_k}} = \left(\frac{1}{1-|\kappa|^2} \right) \frac{\sigma^2_{V,k}}{12 \times N_{RS}}. \tag{4.69}$$

Channel Estimation from the 2-nd iteration

Hereafter, the symbol matrix is estimated in Step 4. However, differently from the single-cell case, the following product of matrices

$$\hat{\mathbf{Z}}^H_{2,(i=1)} \mathbf{Z}_2 = 12 \begin{bmatrix} \hat{\mathbf{h}}_{(i=1)}^{(1)H} \mathbf{h}^{(1)} & \kappa \hat{\mathbf{h}}_{(i=1)}^{(1)H} \mathbf{h}^{(2)} \\ \kappa^* \hat{\mathbf{h}}_{(i=1)}^{(2)H} \mathbf{h}^{(1)} & \hat{\mathbf{h}}_{(i=1)}^{(2)} \mathbf{h}^{(2)} \end{bmatrix} \tag{4.70}$$

results in a non-diagonal matrix. As shown in Step 4, this matrix is inverted using:

$$\left(\hat{\mathbf{Z}}^H_{2,(i=1)} \hat{\mathbf{Z}}^H_{2,(i=1)} \right)^{-1} = 12 \begin{bmatrix} \|\hat{\mathbf{h}}_{(i=1)}^{(1)}\|^2 & \kappa \hat{\mathbf{h}}_{(i=1)}^{(1)H} \hat{\mathbf{h}}_{(i=1)}^{(2)} \\ \kappa^* \hat{\mathbf{h}}_{(i=1)}^{(2)H} \hat{\mathbf{h}}_{(i=1)}^{(1)} & \|\hat{\mathbf{h}}_{(i=1)}^{(2)}\|^2 \end{bmatrix} \tag{4.71}$$

in order to obtain $\hat{\mathbf{A}}^T_{(i=1)}$ which is used as input to the next iteration and so on.

Thus, at the $(i+1)$-th iteration the channel estimate is calculated similarly to (4.41). However, differently from (4.43)-(4.46), we have that

$$\hat{\mathbf{Z}}^H_{1,(i+1)}\mathbf{Z}_1 = \sum_{n=1}^{7} D_n(\hat{\mathbf{S}}^*_{(i)})\mathbf{W}^H\mathbf{W}D_n(\mathbf{S}) \tag{4.72}$$

$$= 12\sum_{n=1}^{7} D_n(\hat{\mathbf{S}}^*_{(i)}) \begin{bmatrix} 1 & \kappa \\ \kappa^* & 1 \end{bmatrix} D_n(\mathbf{S}) \tag{4.73}$$

$$= 12\sum_{n=1}^{7} D_n(\mathbf{\Theta}\hat{\mathbf{A}}^*_{(i)}) \begin{bmatrix} 1 & \kappa \\ \kappa^* & 1 \end{bmatrix} D_n(\mathbf{\Theta}\mathbf{A}) \tag{4.74}$$

$$= 12 \begin{bmatrix} 3+4\hat{a}^{(1)*}_{(i)}a^{(1)} & \kappa\left(3+4\hat{a}^{(1)*}_{(i)}a^{(2)}\right) \\ \kappa^*\left(3+4\hat{a}^{(2)*}_{(i)}a^{(1)}\right) & 3+4\hat{a}^{(2)*}_{(i)}a^{(2)} \end{bmatrix} \tag{4.75}$$

and

$$\left(\hat{\mathbf{Z}}^H_{1,(i+1)}\hat{\mathbf{Z}}_{1,(i+1)}\right)^{-1} = \frac{1}{\det\left(\hat{\mathbf{Z}}^H_{1,(i+1)}\hat{\mathbf{Z}}_{1,(i+1)}\right)} \begin{bmatrix} 3+4|\hat{a}^{(2)*}_{(i)}|^2 & -\kappa\left(3+4\hat{a}^{(1)*}_{(i)}\hat{a}^{(2)}_{(i)}\right) \\ -\kappa^*\left(3+4\hat{a}^{(2)*}_{(i)}\hat{a}^{(1)}_{(i)}\right) & 3+4|\hat{a}^{(1)*}_{(i)}|^2 \end{bmatrix}. \tag{4.76}$$

Thus, Step 3 provides the following channel estimate:

$$\hat{\mathbf{H}}^T_{(i+1)} = \hat{\mathbf{B}}_{(i+1)}\mathbf{H}^T + \hat{\mathbf{Z}}^{\dagger}_1\mathbf{V}_1 \tag{4.77}$$

where $\hat{\mathbf{B}}_{(i+1)}$ is the *bias matrix*. We show in the performance results that although this estimator is biased, the MSE of channel estimation decreases with the number of iteration thanks to the reduction in the noise variance, which is now averaged over RS and data symbols.

Data Detection

As in the single-cell scenario, we also assume the noise is unbalanced over the diversity branches. This assumption is taken into account in the modified version of the ALS algorithm by constructing a filter as described in (4.51)-(4.54).

Thus, at the last iteration, the estimated ACK/NACK symbol is equivalent to the

following estimate:

$$\hat{a}^{(1)} = \left(\frac{\hat{\mathbf{h}}^{(1)H} + |\kappa|^2\hat{\mathbf{h}}^{(2)H}}{1-|\kappa|^2}\right)\boldsymbol{\Sigma}^{-2}\mathbf{h}^{(1)}a^{(1)} + \kappa\left(\frac{\hat{\mathbf{h}}^{(1)H} - \hat{\mathbf{h}}^{(2)H}}{1-|\kappa|^2}\right)\boldsymbol{\Sigma}^{-2}\mathbf{h}^{(2)}a^{(2)}$$
$$+ \frac{\hat{\mathbf{h}}^{(1)H}\boldsymbol{\Sigma}^{-2}}{1-|\kappa|^2}\left(\frac{\bar{\mathbf{v}}_1^{(1)} + \bar{\mathbf{v}}_2^{(1)} + \bar{\mathbf{v}}_6^{(1)} + \bar{\mathbf{v}}_7^{(1)}}{4}\right)$$
$$+ \frac{|\kappa|^2\hat{\mathbf{h}}^{(2)H}\boldsymbol{\Sigma}^{-2}}{1-|\kappa|^2}\left(\frac{\bar{\mathbf{v}}_1^{(2)} + \bar{\mathbf{v}}_2^{(2)} + \bar{\mathbf{v}}_6^{(2)} + \bar{\mathbf{v}}_7^{(2)}}{4}\right). \tag{4.78}$$

TREP-1 vs Conventional Receiver

We call a conventional receiver a low-complexity LS channel estimator based on RS followed by a MRC. This receiver is optimum in the single-cell case, where the coding vectors are orthogonal. However, similarly to (3.79), in the multi-cell scenario, this channel estimate is biased and given by:

$$\hat{\mathbf{H}}^T = \left[\frac{\hat{\mathbf{Z}}_{1,(i=1)}^H}{36}\right]\mathbf{Y}_1 = \begin{bmatrix} 1 & \kappa \\ \kappa^* & 1 \end{bmatrix}\mathbf{H}^T + \mathbf{V}_{h,(i=1)}^T \tag{4.79}$$

where $\mathbf{V}_{h,(i=1)}^T$ is the same defined in (4.34).

Alternatively, the channel estimate associated with the desired UE is given by:

$$\hat{\mathbf{h}}_{(i=1)}^{(1)} = \mathbf{h}^{(1)} + \mathbf{v}_{h,(i=1)} + \kappa\mathbf{h}^{(2)}. \tag{4.80}$$

and a *channel estimation error* can be defined as follows:

$$\mathbf{e}_{h,(i=1)} = \mathbf{v}_{h,(i=1)}^{(1)} + \kappa\mathbf{h}^{(2)}. \tag{4.81}$$

In Appendix **A.6** we show that the variance of this error for a channel realization is given by:

$$\sigma_{e_{h_k}}^2 = \frac{\sigma_{V,k}^2}{12 \times N_{RS}} + |\kappa|^2|h_k^{(2)}|^2. \tag{4.82}$$

The two previous results can be extrapolated to the case of R terminals within the desired cell and $Q-1$ interfering neighboring cells each one with Z_q terminals. In this case, the channel estimation error associated with the r-th UE within the

desired cell will be:

$$\mathbf{e}_h^{(r)} = \mathbf{v}_{h,(i=1)}^{(r)} + \sum_{q=2}^{Q-1} \sum_{z_q}^{Z_q} \kappa_{r,z_q} \mathbf{h}^{(z_q)} \tag{4.83}$$

and the error variance given by:

$$\sigma^2_{e_{h_k}} = \frac{\sigma^2_{V,k}}{12 \times N_{RS}} + \sum_{q=2}^{Q-1} \sum_{z_q}^{Z_q} |\kappa_{r,z_q}|^2 |h_k^{(z_q)}|^2 \tag{4.84}$$

where $\kappa_{r,z_q} = \mathbf{w}^{(r)H}\mathbf{w}^{(z_q)}/12$.

Since the channel has been estimated, data is detected using MRC receiver, represented in our tensor modeling by:

$$\hat{\mathbf{S}}^T = \hat{\mathbf{A}}^T \mathbf{\Theta}^T = \frac{\hat{\mathbf{Z}}_2^{'H}}{12} \mathbf{Y}_2 = \frac{\hat{\mathbf{Z}}_2^{'H} \mathbf{Z}_2}{12} \mathbf{S}^T + \frac{\hat{\mathbf{Z}}_2^{'H}}{12} \mathbf{V}_2. \tag{4.85}$$

This estimator would fit well in the single-cell scenario. However, in the considered multi-cell scenario, where orthogonality among coding vectors is lost, we have:

$$\hat{\mathbf{Z}}_2^{'H} \mathbf{Z}_2 = 12 \begin{bmatrix} \hat{\mathbf{h}}^{(1)H} \mathbf{\Sigma}^{-2} \mathbf{h}^{(1)} & \kappa \hat{\mathbf{h}}^{(1)H} \mathbf{\Sigma}^{-2} \mathbf{h}^{(2)} \\ \kappa^* \hat{\mathbf{h}}^{(2)H} \mathbf{\Sigma}^{-2} \mathbf{h}^{(1)} & \hat{\mathbf{h}}^{(2)H} \mathbf{\Sigma}^{-2} \mathbf{h}^{(2)} \end{bmatrix}. \tag{4.86}$$

Therefore, when low-complexity conventional receiver is considered, the estimated ACK/NACK symbol is given by:

$$\hat{a}^{(1)} = \left(\hat{\mathbf{h}}^{(1)H} \mathbf{\Sigma}^{-2} \mathbf{h}^{(1)} \right) a^{(1)} + \kappa \left(\hat{\mathbf{h}}^{(2)H} \mathbf{\Sigma}^{-2} \mathbf{h}^{(1)} \right) a^{(2)}$$

$$+ \hat{\mathbf{h}}^{(1)H} \mathbf{\Sigma}^{-2} \left(\frac{\bar{\mathbf{v}}_1^{(1)} + \bar{\mathbf{v}}_2^{(1)} + \bar{\mathbf{v}}_6^{(1)} + \bar{\mathbf{v}}_7^{(1)}}{4} \right). \tag{4.87}$$

Similarly to TREP-2, Eq. (4.87) results in non-canceled interference in the estimated ACK/NACK symbol which can degrade the performance. This impairment is proportional to the correlation among the coding vectors.

Comparing this result to that obtained in the the first iteration of TREP-1, we see that when the channel is perfectly estimated, the structure of Step 4 is similar to a ZF receiver which cancels completely the interference from the neighboring cells. Then, the first iteration of the proposed receiver improves the performance

over MRC by reducing the interference altough it amplifies the the noise.

In the presence of channel estimation error, the inter-cell interference is gradually reduced as the accuracy of the channel estimation is improved.

5.2 Configuration 2

In this configuration the eNodeBs are not connected, such that only a part of the coding matrix is known. The other part, associated with the neighboring cells, is initialized with a base sequence and phase rotation chosen randomly from the subset of possibilities. Thus, the algorithm is initialized as follows:

$$\hat{\mathbf{W}}_{(i=0)} = \left[\mathbf{W}(1) \;\; \hat{\mathbf{W}}(2)_{(i=0)} \cdots \hat{\mathbf{W}}(q)_{(i=0)} \cdots \hat{\mathbf{W}}(Q)_{(i=0)}\right]. \tag{4.88}$$

This configuration is similar to the conventional architecture of LTE, where the base sequences and phase rotations from neighboring cells are not known. In this case, our algorithm estimates the coding vectors associated with the interfering UEs during the first iterations in order to cancel the interference in the subsequent ones.

Hereafter, case study 1 is analyzed under configuration 2.

Case study 1 (Configuration 2)

Since the eNodeB only knows the first coding vector, the coding matrix is initialized as follows:

$$\hat{\mathbf{W}}_{(i=0)} = \left[\mathbf{w}^{(1)} \;\; \hat{\mathbf{w}}^{(2)}_{(i=0)}\right] \tag{4.89}$$

In configuration 2, Step 5 of ALS is considered to estimate the unknown part of the coding matrix. As shown below, at the i-th iteration, the estimated coding matrix is given by:

$$\hat{\mathbf{W}}^{T}_{(i)} = \left[\hat{\mathbf{Z}}_{3,(i)}\right]^{\dagger} \mathbf{Y}_3 \tag{4.90}$$

$$= \left(\hat{\mathbf{Z}}^{H}_{3,(i)}\hat{\mathbf{Z}}_{3,(i)}\right)^{-1} \hat{\mathbf{Z}}^{H}_{3,(i)}\mathbf{Z}_3\mathbf{W}^{T} + \left[\hat{\mathbf{Z}}_{3,(i)}\right]^{\dagger} \mathbf{V}_3 \tag{4.91}$$

which can be written as:

$$\hat{\mathbf{W}}_{(i)} = \left[\hat{\mathbf{w}}^{(1)}_{(i)} \;\; \hat{\mathbf{w}}^{(2)}_{(i)}\right]. \tag{4.92}$$

The first coding vector is known at the eNodeB, such that at the end of the i-th iteration we can simply replace $\hat{\mathbf{w}}_{(i)}^{(1)}$ by $\mathbf{w}^{(1)}$. Although the second coding vector is not known, we know that $\|\mathbf{w}^{(2)}\|^2 = 12$. Thus, at the end of the i-th iteration we normalize the estimated coding vector such that $\|\hat{\mathbf{w}}_{(i)}^{(2)}\|^2 = 12$.

This estimated coding matrix is used in the the next iteration to reestimate the channel and so on. .

Similarly to the previous chapter, the previous results to multi-cell scenarios with more terminals per cell and more interfering cells can be also extended. In this sense, the same case studies are also considered herein to evaluate the performance of TREP-1. They are:

- **Case study 2** - 2 cells x 2 UEs per cell
- **Case study 3** - 3 cells x 1 UE per cell
- **Case study 4** - 3 cells x 2 UEs per cell

6 Uniqueness of the new constrained model

The uniqueness conditions of PARAFAC model has been presented in the previous Chapter in the context of TREP-2 for both configurations 1 and 2 (c.f. Sec.5). We have shown that a different number of terminals can be separated depending on the network configuration.

Herein, an equivalent analysis is considered in order to show the conditions under which the new tensor model proposed in Section 3 is said essentially unique, i.e., if and only if the component matrices $\mathbf{A}$, $\mathbf{B}$ and $\mathbf{C}$ can be estimated from $\mathcal{X}$ up to trivial permutation and scaling of their columns.

Using the fact that $\mathbf{\Theta}$ and $\mathbf{W}$ are full rank by construction, and assuming that the symbol and channel matrices $\mathbf{A}$ and $\mathbf{H}$ are full rank, we can resort to the uniqueness results of the PARAFAC tensor model [8, 10] to obtain an upper bound on the number R of UEs that can be simultaneously supported at the eNodeB. The necessary and sufficient condition for uniqueness by distinguishing the two network configurations are:

1. *The eNodeB does not have full knowledge of the coding matrix* $\mathbf{W}$. This is the

usual assumption in non-cooperative scenarios where the coding sequences of different cells are not known. In this case, the following condition must be satisfied:

$$min(2, R) + min(12, R) + min(4, R) \geq 2R + 2,$$

which implies $R \leq 4$, i.e. a maximum of 4 UEs are simultaneously supported;

2. *The eNodeB has full knowledge of the coding matrix* $\mathbf{W}$. This is the case in CoMP scenarios where the coding sequences of different cells are known at the eNodeBs. In this case, uniqueness is guaranteed if

$$min(2, R) + min(12, R) \geq R + 1,$$

which implies $R \leq 13$.

7 Preliminar Results

In this Section we compare through simulation results the *channel estimation accuracy* and the *tensor model matching* when TREP-1 is applied. The following results are presented in order to explain the further performance gains in the error performance of PUCCH Format 1 when TREP-1 is applied. At this chapter, the proposed receiver can be called either TREP or TREP-1.

Channel Estimation

In the following simulations, we compare the channel estimation accuracy provided by the TREP-1 to the one provided by a LS channel estimator based on RS, which is commonly used in conventional receivers.

In Fig. 4.4, we show the histogram of $|\eta|$ (bias from channel estimation) for different values of SNR when TREP-1 is applied. The number of iterations is fixed to $N_{It} = 2$ and normal CP is assumed. The ACK/NACK symbols are modulated with BPSK modulation. We can observe that the average of $|\eta|$ approaches 1 as the SNR is around 0 dB.

In Fig. 4.5, we show the $\text{MSE}_{\hat{\mathbf{H}}}$ in function of N_{It}. The SNR is fixed to -10 dB and normal CP is assumed. We can note that despite the presence of a bias, the MSE($\hat{\mathbf{H}}$) provided by the TREP-1 decreases with N_{It}, converging to a local

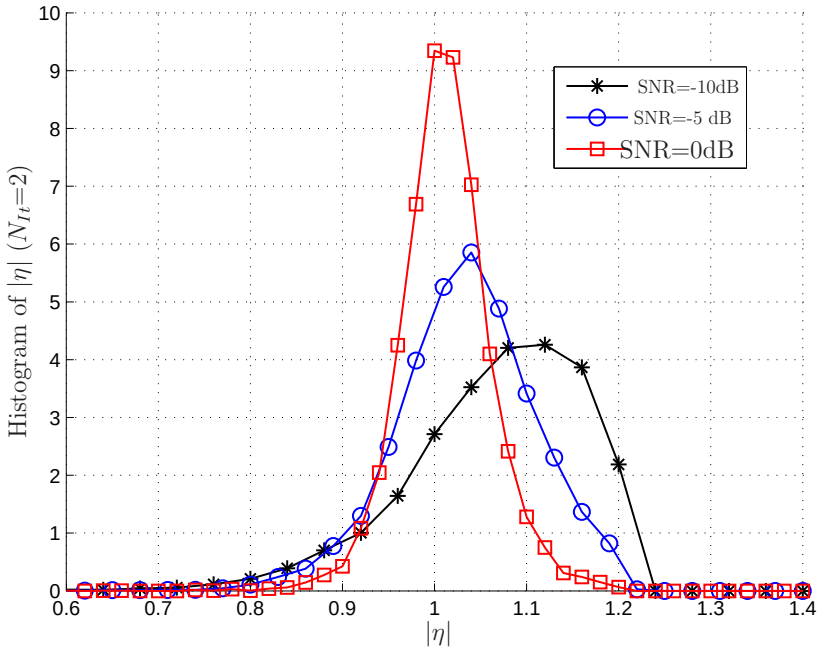

Figure 4.4: Distribution of the channel estimation bias

minimum in between the valued obtained at the 1-st iteration and the bound for LS estimators.

Tensor model matching

In the following simulation, we show the model matching between the baseband transmission on PUCCH Format 1 and the new tensor model, proposed in this Chapter. Similarly to the previous Chapter, this matching is measured in terms of MSE between the received signal and the estimated one which can be expressed as:

$$\text{MSE}(\hat{\mathcal{X}}) = \frac{E\left\{\|\mathbf{Y}_2 - \hat{\mathbf{X}}_2\|_F^2\right\}}{7 \times 12 \times 4} \tag{4.93}$$

where $\hat{\mathbf{X}}_2 = \left(\mathbf{W} \diamond \hat{\mathbf{H}}\right) \hat{\mathbf{A}}^T \mathbf{\Theta}^T$.

In Fig. 4.6, we show the MSE($\hat{\mathcal{X}}$) in function of N_{It}. We assume a single-cell with R=6 terminals with both normal and extended CP configurations. We can see that MSE($\hat{\mathcal{X}}$) is a decreasing function of N_{It} for both CP configurations. Moreover, it is worth mentioning that the uniqueness conditions are guaranteed until $R \leq 13$.

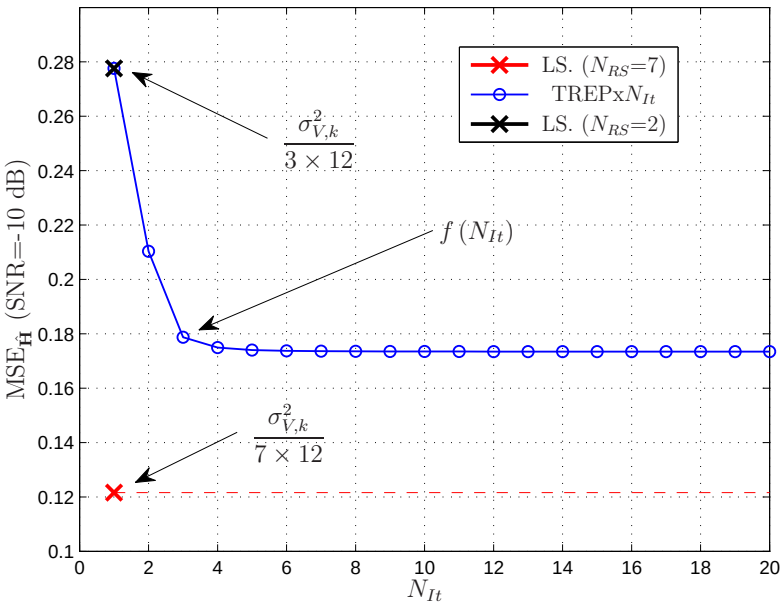

Figure 4.5: MSE of Channel Estimation

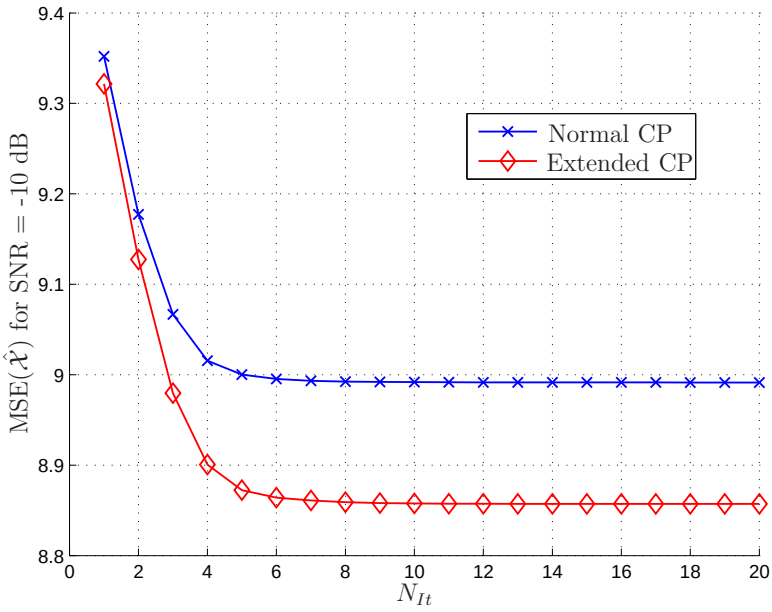

Figure 4.6: Tensor model matching of PUCCH Format 1: $R = 6$ UEs

Similarly to TREP-2, we can conclude from the previous simulation results that the proposed TREP-1 can be an interesting alternative to conventional receivers, as it improves the channel estimation accuracy at the price of more iterations. In the next Chapter, we evaluate the error performance to confirm the applicability of TREP-1 in single-cell and multi-cell scenarios.

CHAPTER 5

Performance Evaluation of PUCCH LTE using TREP-1 and TREP-2

In this Chapter, we evaluate the error performance of PUCCH LTE through simulations when the proposed tensor-based receivers TREP-1 and TREP-2 are respectively applied to Format 1 and Format 2. The proposed receivers are compared to conventional ones composed by a LS channel estimation (based on RS) and MRC for data detection. The simulation results show that both versions of TREP outperform the conventional receivers. On the other hand, the higher complexity of the proposed receivers is better justified in the presence of inter-cell interference. Our results testify the applicability of TREP in LTE eNodeBs for two network configurations. In the first, we consider that the eNodeBs are connected such that they have information concerning the interfering UEs from the neighboring cells. The gains afforded by TREP-1 and TREP-2 make them very suitable in a CoMP configuration, to be considered in LTE Release 10. In the second configuration, we assume the eNodeBs do not know the coding vectors from the neighboring cells. In this case, huge gains can be achieved by TREP and the error floor decreases with the number of iterations. It is worth pointing out that the results we show herein are a representative sample in order to prove the potential of the proposed application. To accomplish this proof of concept, we resort to the case studies proposed in Chapter 3. Differently from the preliminary results of Chapters 3 and 4, we assume a more realistic channel model recommended by 3GPP in the LTE specifications to evaluate the performance of PUCCH. We conclude this Chapter speculating about the effects of the LTE inter-cell interference mitigation techniques, not covered in this work.

1 TREP-2 to PUCCH Format 2

In all the simulations, we evaluate the error performance of PUCCH Format 2 using the proposed TREP-2 in a more practical setting, considering the *ETU (Evolved Typical Urban)* channel model from LTE specification [41]. More specifically, the performance of TREP-2 applied to PUCCH Format 2 is compared to the performance obtained by a conventional receiver composed by a LS channel estimation based on RS followed by a MRC for data detection.

A system bandwidth of 10 MHz and a maximum Doppler frequency of 5 Hz are assumed. Each slot is modeled independently as a PARAFAC tensor so that both slots are combined using the soft decoder described in Chapter 3 (c.f. Sec. 5.1).

The error performance is measured in terms of Block Error Rate (BLER) so that a block is computed wrong when at least one of the B output bits from the soft decoder associated with the channel-status information is incorrect.

The simulations in the following show the BLER provided by each receiver in function of the SNR and the label TREPxN_{It} indicates that the ALS runs during N_{It} iterations while the label CONV. indicates the conventional receivers.

1.1 Single-Cell Scenarios

In Fig. 5.1, we compare the performance of TREP-2 to the performance of conventional receiver in a single-cell with $R = 6$ terminals. Normal CP is assumed for fixed number of uncoded bits $B = 4$ and $B = 8$. The number of iterations of TREP-2 is fixed to $N_{It} = 4$ and the average BLER of the R terminals is plotted in function of the SNR. We can observe a slightly gain provided by TREP-2 over the conventional receiver only when $B = 8$ since the symbols that compose the symbol matrix $\mathbf{S}$ are less correlated than in the case of $B = 4$. This behaviour is due to the fact that PARAFAC model does not take the correlation among the symbols into account.

In Fig. 5.2, we consider the same conditions of the previous simulation except that we assume the terminals are configured with extended CP. Notice that although the gains provided by TREP-2 still remain very small, they are more significant for this CP configuration for both values of B.

This occurs because in conventional receivers, the channel estimation accuracy is proportional to the number of RS, which can be $N_{RS} = 2$ (for normal CP) or $N_{RS} = 1$ (for extended CP). When TREP-2 is applied, the channel estimation is

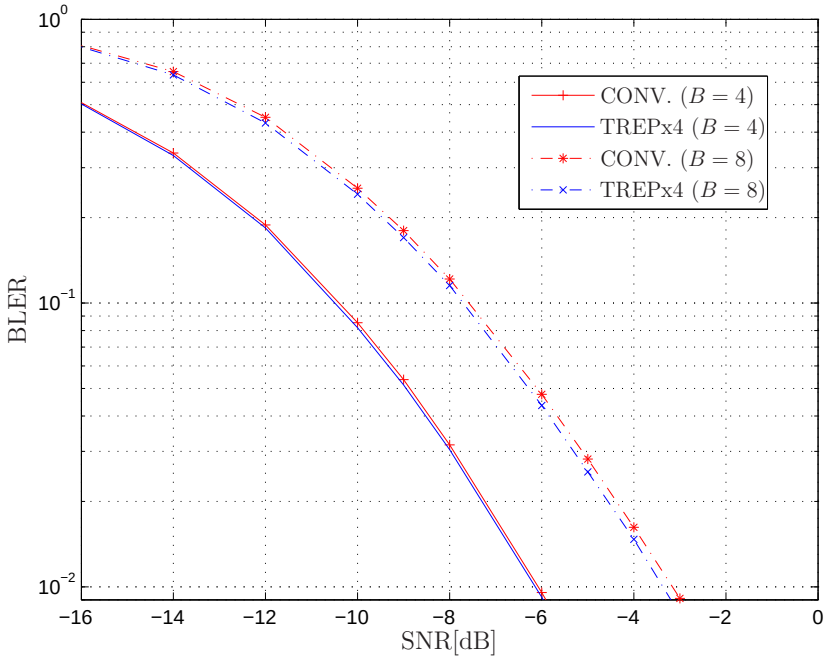

Figure 5.1: Single-Cell with R=6 UEs (Normal CP)

better improved when the density of RS, denoted by ρ_{RS}, is smaller compared to the number of available data symbols that will be used to reestimate the channel in the subsequent iterations. For normal CP, this number equals $\rho_{RS} = 2/7 \approx 0.28$ and, for extended CP $\rho_{RS} = 1/6 \approx 0.16$.

Then, we can conclude that in single-cell scenarios, where TREP-2 has a built-in data-aided channel estimator, the improvements in the channel estimation accuracy shown in the preliminary results of Chapter 3 (c.f. Sec. 6.1) are not translated in significant performance gain compared to the conventional receiver. This happens bacause the conventional receiver separate perfectly the signals from the R terminals as the coding vectors are orthogonal in our frequency-domain baseband model. However, in a more accurate modeling, the orthogonality of the coding vectors is lost when the signals are transmitted over more aggressive channel conditions, like a higher Doppler or frequency selectivity. In this case, TREP-2 will probably improve the performance over the conventional receiver.

In single-cell scenarios, the number of terminals does not affect the performance

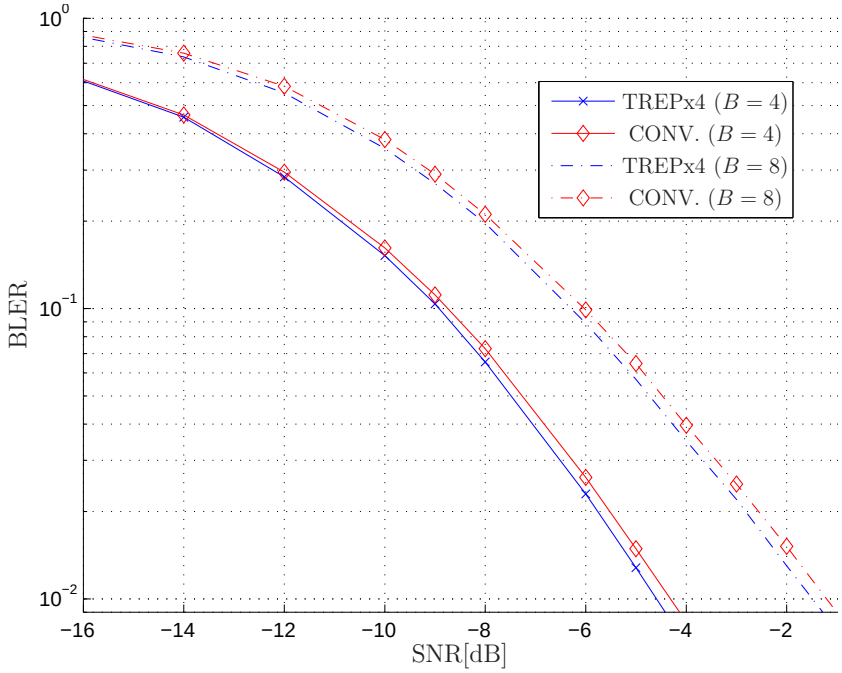

Figure 5.2: Single-Cell with R=6 UEs (Extended CP)

of the proposed receiver as the terminals are perfectly separated thanks to their respective phase rotations in the cell-specific base sequence. However, this is not the case in the multi-cell scenario, as we verify in the following.

1.2 Multi-Cell Scenarios

In all the simulations for multi-cell scenarios, we revisit the case studies defined in Chapter 3 in order to evaluate the performance of TREP-2. They are summarized in Table 5.1. Both network configurations are considered and extended CP is assume. The number of uncoded bits is also assumed fixed $B = 4$. The cell-specific base sequences associated with each cell are randomly chosen and kept fixed during the simulations as the phase rotations that compose the coding vector of each terminal.

In Fig. 5.3, we compare the performance of TREP-2 to the performance of the conventional receiver when case study 1 is considered under configuration 1. The BLER of the desired UE is plotted in function of the SNR. We can see that the conventional receiver performs slightly better than TREPx1 only for very low SNR ranges below -10 dB, as we have speculated in Chapter 3. However, the conventional receiver does not achieve the BLER target of 10^{-2} due to the inter-

Case Study	Number of Cells	UEs per Cell
1	2	1
2	2	2
3	3	1
4	3	2

Table 5.1: Case Studies of Multi-Cell Scenarios

cell interference that remains after MRC, as shown in Chapter 3 (c.f. Sec. 4.1). In order to reduce the inter-cell interference TREP-2 is applied, outperforming the conventional receiver since the first iteration and achieving the BLER target. Moreover, we can observe that a gain of almost 2 dB is achieved from N_{It}=1 to N_{It}=3 for the same BLER target of 10^{-2}.

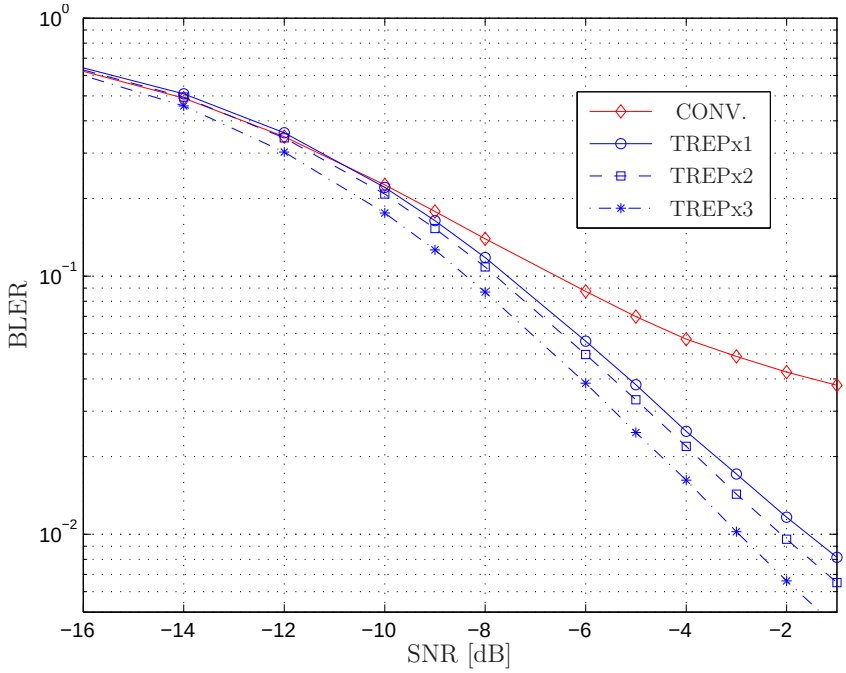

Figure 5.3: Case Study 1 - Configuration 1 (Desired UE)

In Fig. 5.4, we compare the performance of TREP-2 to the performance of the conventional receiver when case study 1 is considered under configuration 2. As in the previous simulation, we can observe that the conventional receiver does not achieve the BLER target of 10^{-2}. The proposed TREP-2 outperforms the conventional receiver since its first iteration. Furthermore, the error floor present in the TREP-2 performance shows that the inter-cell interference is not completely cancelled, but reduced as we increase the number of iterations. A gain around 7 dB

can be observed from the 3-th to the 5-th iteration for the defined BLER target.

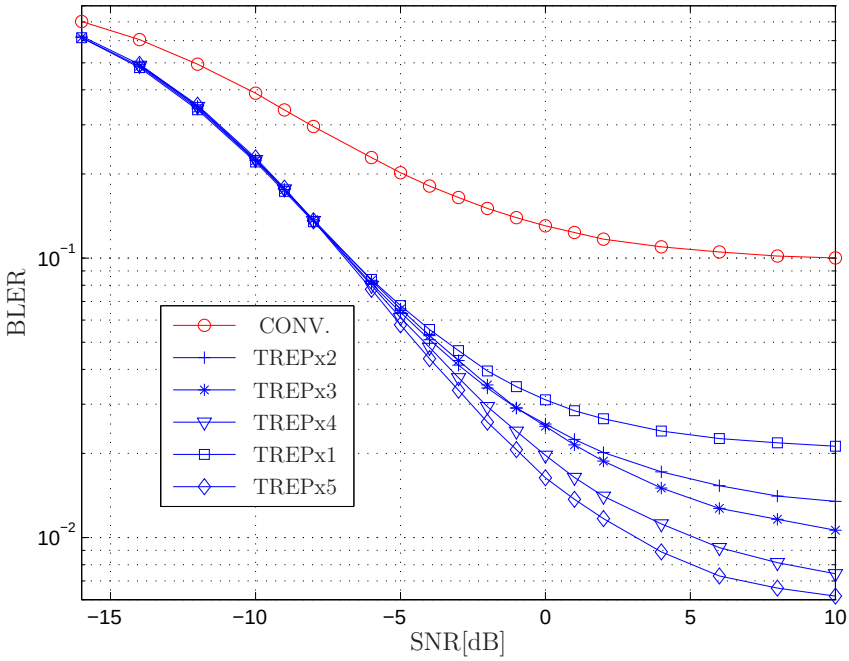

Figure 5.4: Case Study 1 - Configuration 2 (Desired UE)

In Fig. 5.5 the BLER of the interfering UE of the previous simulation is plotted in function of the SNR. We can note that under configuration 2, which is semi-blind by definition, TREP-2 is able to estimate accurately the data symbols of the interfering UE at each iteration. For a target of BLER=10^{-2}, a gain of approximately 4 dB is achieved from the 2-nd to the 3-th iterations.

In Fig. 5.6, we compare the performance of TREP-2 to the performance of the conventional receiver when case study 2 is considered under configuration 1. The BLER of the two desired UEs are plotted in function of the SNR. First of all, note that the UEs have different performances when the same receiver is used. The performance is function of the correlation among the coding sequences of the desired terminals and the interfering ones as it has been discussed in Chapter 3 (c.f. Sec.4.4). This effect will probably disappear when the base sequences and phase rotations are randomly chosen for each transmission [1]. Comparing now the

[1]In addition to this, LTE defines some techniques in order to randomize the inter-cell interference (e.g. hop the base sequences on a per-slot basis). However, these techniques are not considered in our simulations.

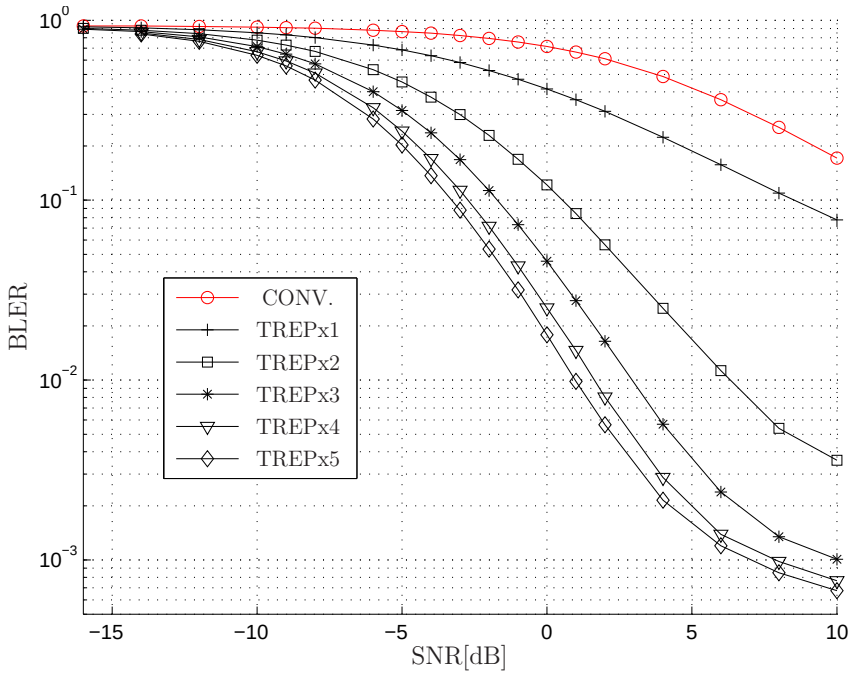

Figure 5.5: Case Study 1 - Configuration 2 (Interfering UE)

performance associated with each UE, we can observe gains around 2 dB for the UE 2 for a BLER below 10^{-2} from the 1-st to the 3-th iteration. Concerning the performance of the UE 1, the error floor due to the inter-cell interference reduces as the number of iterations increases.

In Fig. 5.7, we compare the performance of TREP-2 to the performance of the conventional receiver when case study 3 is considered under configuration 1. The BLER of the desired UE is plotted in function of the SNR. We can observe that since the first iteration TREP-2 outperforms the conventional receiver. The gains achieved from the 1-st to the 3-th iterations are around 1 dB for a BLER target of 10^{-2}.

In Fig. 5.8, we compare the performance of TREP-2 to the performance of conventional receivers when case study 4 is considered under configuration 1. The BLER of the two desired UEs are plotted in function of the SNR. Similarly to case study 2, the 2 desired terminals present different performance, function of the existing correlation between their coding vectors and the interfering ones. We can see that smaller error floors are achieved when the number of iterations of TREP-2 is increased which represents the inter-cell interference reduction provided the proposed receiver.

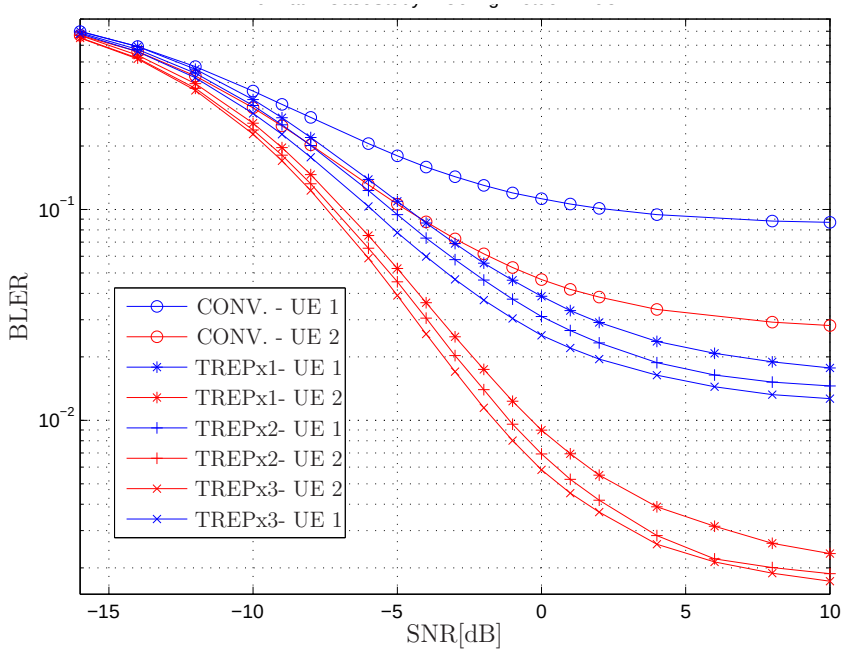

Figure 5.6: Case Study 2 - Configuration 1 (Desired UEs)

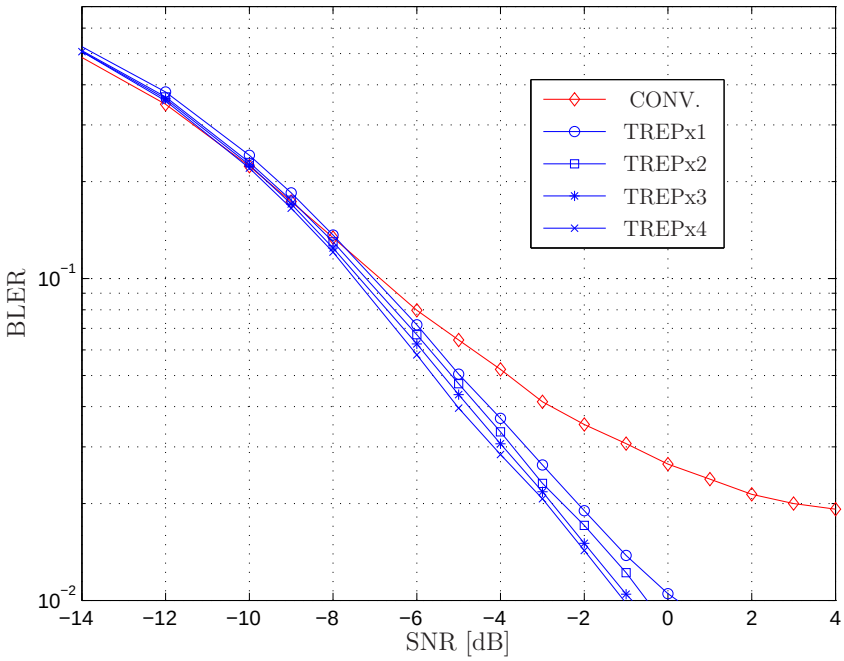

Figure 5.7: Case Study 3 - Configuration 1 (Desired UE)

2 TREP-1 and PUCCH Format 1

In all the simulations, we evaluate the error performance of PUCCH Format 1 using the proposed TREP-1 in a more practical setting, considering the *ETU (Evolved*

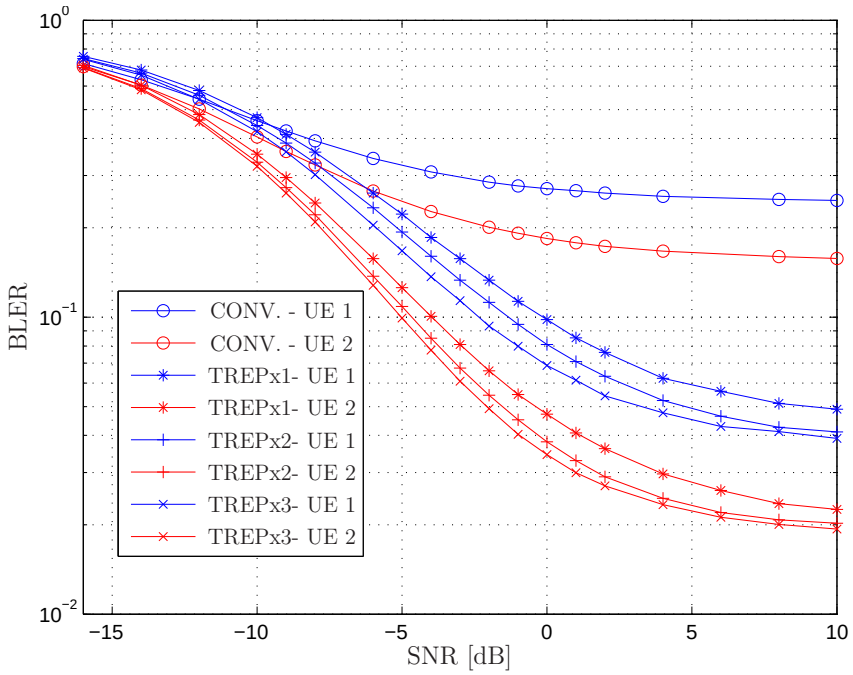

Figure 5.8: Case Study 4 - Configuration 1 (Desired UEs)

Typical Urban) channel model from LTE specification [41]. A system bandwidth of 10 MHz and a maximum Doppler frequency of 5 Hz are assumed.

As described in Chapter 4, both slots are jointly modeled using a constrained tensor model and solved jointly with the aid of TREP-1 (c.f. Sec. 2).

The error performance is measured in terms of the Bit Error Rate (BER) associated with the ACK/NACK symbols. The simulations in the following show the BER furnished by each receiver in function of the SNR. We also compare some algorithmic aspects of TREP-1 and TREP-2 in between the simulation results.

2.1 Single-Cell Scenario

In Fig. 5.9, we compare the performance of TREP-1 to the performance of the conventional receiver in a single-cell with $R = 6$ terminals. Both normal and extended CP configurations are considered. We can note that there is no gain over the conventional receiver when TREP-1 is applied for both CP configurations. Then, we can conclude that although the channel estimation provided by TREP improves as N_{It} increases (as we have shown in the preliminary results of Chapter 4), this better channel estimation accuracy is not translated in a gain in the BER.

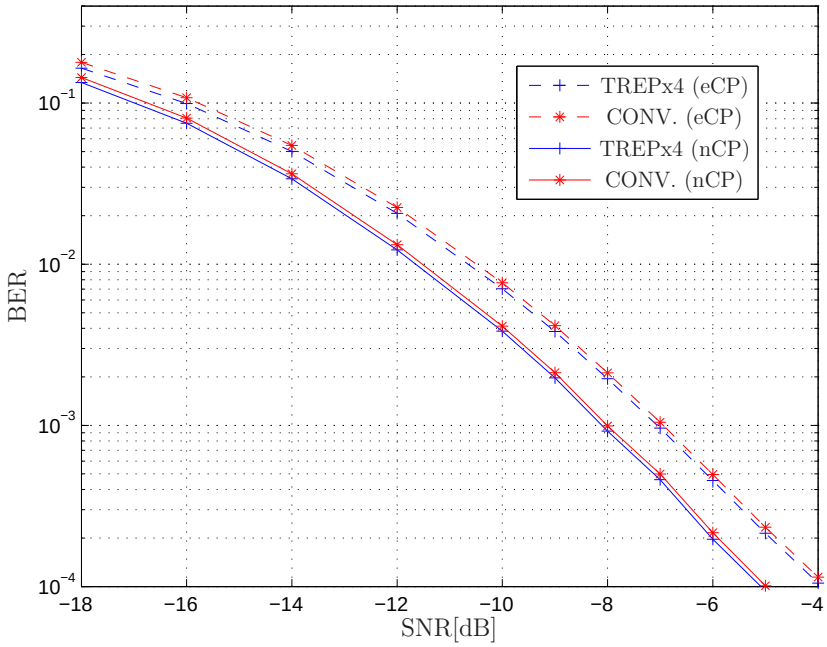

Figure 5.9: Single-cell with $R = 6$ UEs

As mentioned previously, in the single-cell case, the signals from the R terminals are perfectly separated. Both versions of the TREP have a built-in data-aided channel estimator. We have shown that the performance TREP becomes limited when the density of RS increases. Table 5.2 shows that in Format 1, this density is still higher for both CP configurations. For that reason, any gain is afforded when TREP-1 is applied in the single-cell scenario.

Cyclic-Prefix	Format 2	Format 1
Extended CP	$\rho_{RS} = 1/6 \approx 0.16$	$\rho_{RS} = 2/7 \approx 0.33$
Normal CP	$\rho_{RS} = 2/7 \approx 0.28$	$\rho_{RS} = 3/7 \approx 0.42$

Table 5.2: Case Studies of Multi-Cell Scenarios

2.2 Multi-Cell Scenarios

In the simulations for multi-cell scenarios, we reconsider again the case studies of Table 5.1. Both network configurations are considered and normal CP is assumed.

The cell-specific base sequences associated with each cell are randomly chosen and kept fixed during the simulations as the phase rotations that compose the coding vector of each terminals.

In Fig. 5.10, we compare the performance of TREP-1 to the performance of the conventional receiver when case study 1 is considered under configuration 1. We can see that TREP-1 outperforms the conventional receiver, which presents a very poor performance. From the first to the second iteration, we obtain a gain around 0.7 dB for a BER target of 10^{-3}. The gains from the 2-*nd* to the 3-th iterations are not relevant but gives an idea about the convergence of the algorithm.

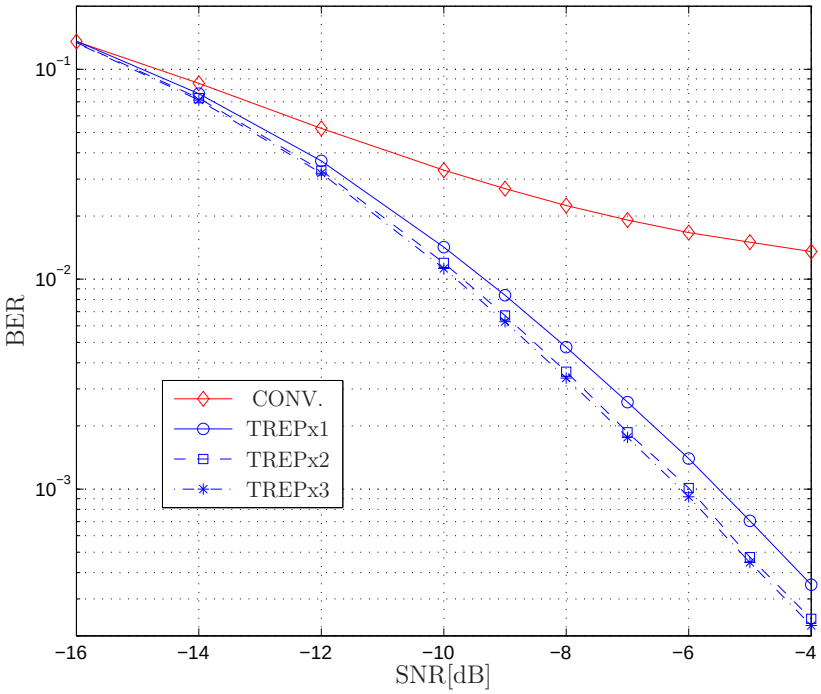

Figure 5.10: Case Study 1 - Configuration 1 (Desired UE)

In Fig. 5.11, we compare the performance of TREP-1 to the performance of the conventional receiver when case study 1 is considered under configuration 2. In this first curve, the BER of the desired UE is plotted in function of the SNR. We can observe that huge gains are obtained when TREP-1 is applied compared to a conventional receiver. Differently from configuration 1, the performance is still significantly improved until the 4-th iteration. The reduction in the error floor indicates the inter-cell interference reduction provided by TREP-1 when the number of iterations increases.

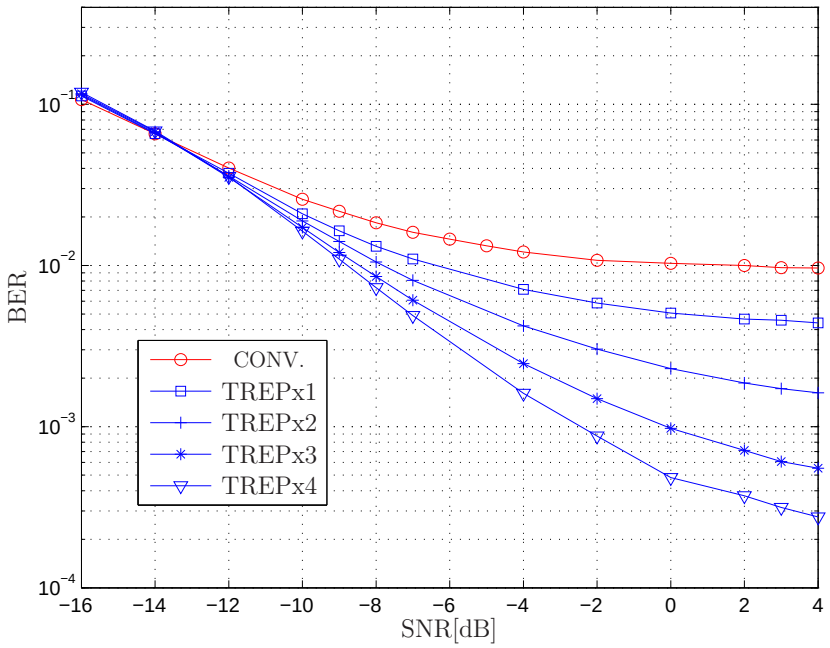

Figure 5.11: Case Study 1 - Configuration 2 (Desired UE)

In Fig. 5.12, the BLER of the interfering UE of the previous simulation is plotted in function of the SNR. Note that TREP-1 ameliorates the performance of the interfering UE at each iteration. Similarly to TREP-2, the benefits of TREP-1 are more significant in scenarios with interference and limited knowledge of the system parameters.

In Fig. 5.13, we compare the performance of TREP-1 to the performance of the conventional receiver when case study 2 is considered under configuration 1. We see that the conventional receiver presents a poor performance with a high error floor. On the other hand, from the first to the second iteration of TREP-1, we observe a gain of 2 dB to the first UE for a BER below 10^{-2}. A similar behaviour is also observed for the UE 2. The difference between the performance between both UEs are related to the fact that their respective coding vectors are differently correlated with the coding vectors associated with the terminals of the interfering cell.

In Fig. 5.14 we compare the performance of TREP-1 to the performance of the conventional receiver when case study 3 under configuration 1. Notice that while the conventional receiver presents an error floor, we see an improvement around 1.5 dB for a BER target of 10^{-3} from the first to the second iteration of TREP-1.

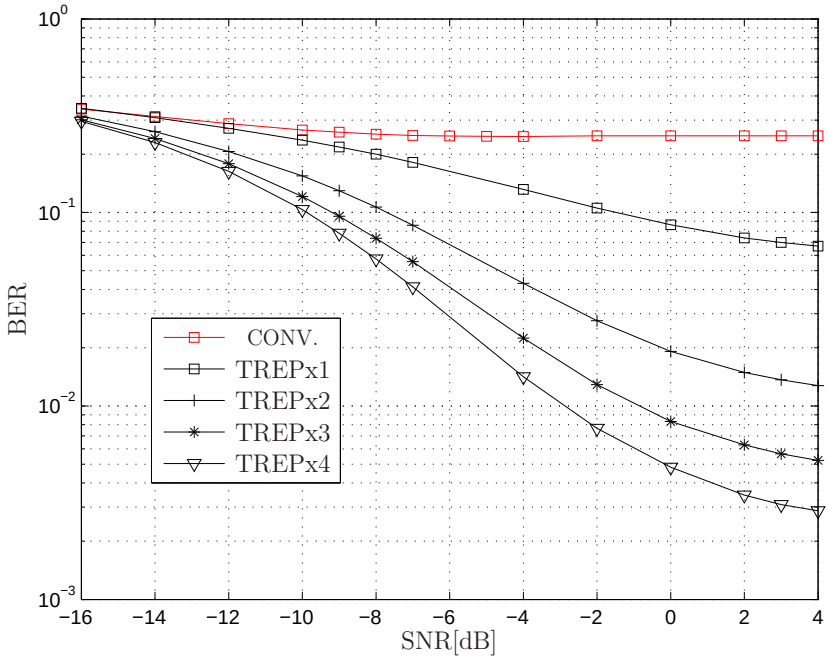

Figure 5.12: Case Study 1 - Configuration 2 (Interfering UE)

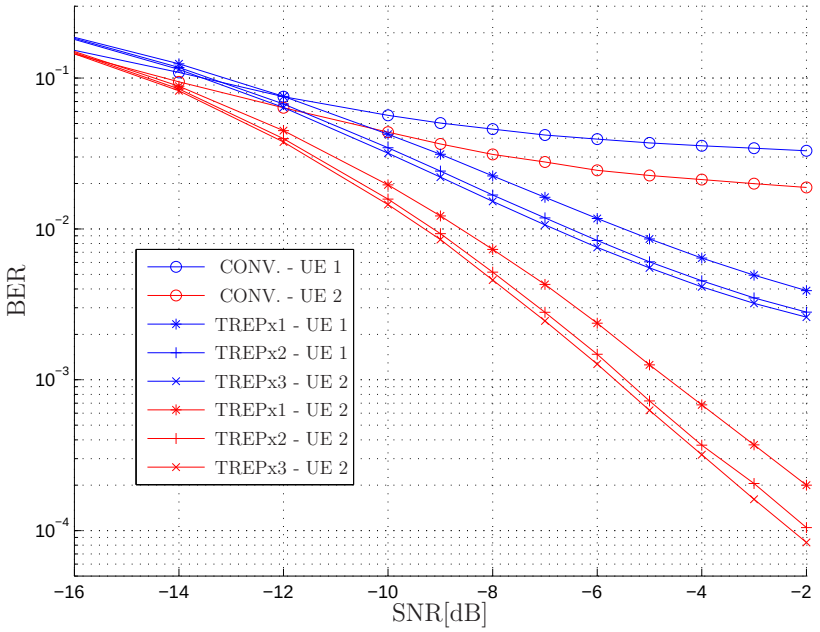

Figure 5.13: Case Study 2 - Configuration 1 (Desired UEs)

In Fig. 5.15 we compare the performance of TREP-1 to the performance of the

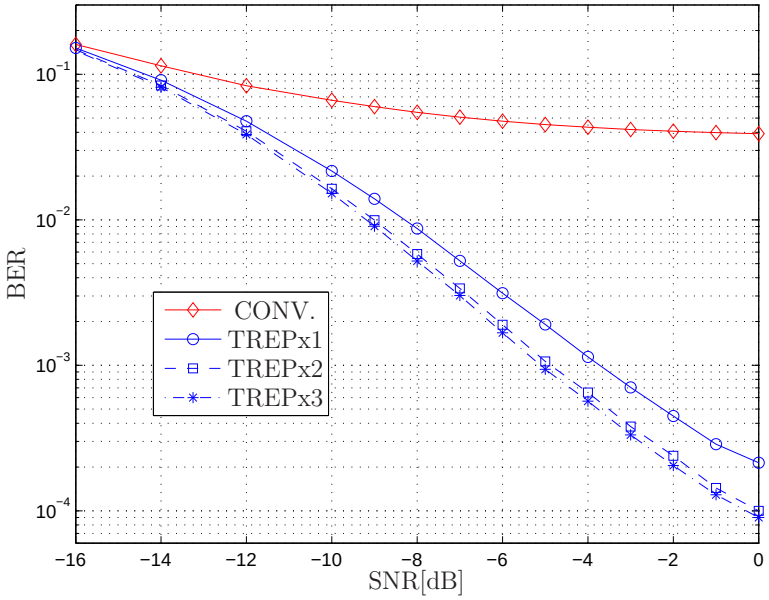

Figure 5.14: Case Study 3 - Configuration 1 (Desired UE)

conventional receiver when case study 4 under configuration 1. We can see that the TREP-1 provides a gain around 3 dB from the 1-st to the 3-th iteration for a BER target of 10^{-3}. In the next Section we conclude this thesis presenting concerning

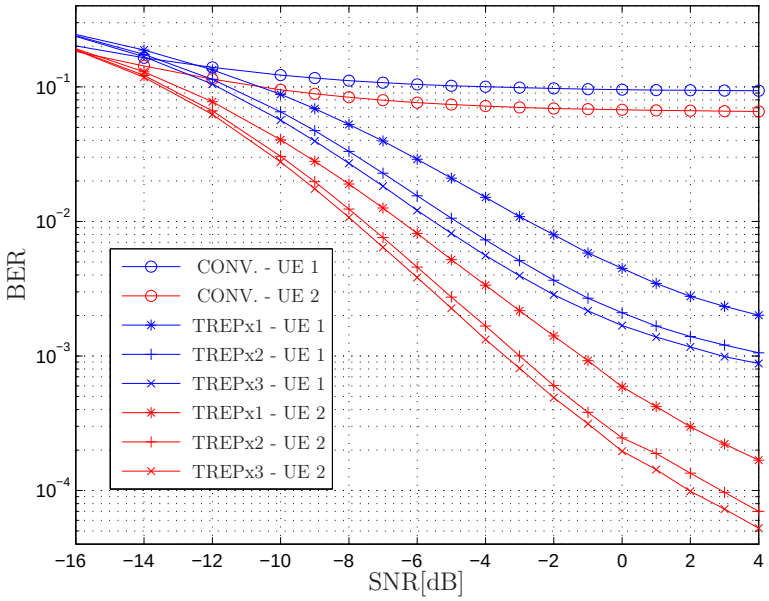

Figure 5.15: Case Study 4 - Configuration 1 (Desired UEs)

the proposed application.

CHAPTER 6

Final Remarks

In this thesis, we have dealt with the baseband model of PUCCH LTE using a tensor approach. From this modeling, we have proposed two multi-user receivers for inter-cell interference reduction in PUCCH LTE: Tensor-based Receiver for PUCCH Format 2 (TREP-2) and Tensor-based Receiver for PUCCH Format 1 (TREP-1), respectively employed to Format 2 and Format 1.

In the first Chapter, we have presented the basis of the tensor modeling used in this thesis, i.e., the basics operations and tensor properties. Then, we have shown how to interpret a multidimensional signal to then propose a tensor model. We have seen that signals that hold a trilinear structure can be written as tensor of rank one, and, when R of these signals are summed, a tensor of rank R is formed. Since the model has been posed, the classical PARAFAC decomposition was introduced as an issue to obtain each rank-one tensor.

APPENDIX A

Appendix

Definition A.1 : (F-th order tensor) *Let be* $\mathbb{V}_1, \mathbb{V}_2, \cdots, \mathbb{V}_F$ *be* F *Euclidian vector spaces of finite dimensions* $I_1, I_2, \cdots, I_F$. *Consider* F *vectors* $\mathbf{u}_1 \in \mathbb{V}_1$, $\mathbf{u}_2 \in \mathbb{V}_2, \cdots, \mathbf{u}_F \in \mathbb{V}_F$ *and denote by* $\mathbf{u}_1 \circ \mathbf{u}_2 \circ \cdots \mathbf{u}_F$ *a multilinear mapping on* $\mathbb{V}_1 \times \mathbb{V}_2 \times \cdots \times \mathbb{V}_F$, *defined as:*

$$(\mathbf{u}_1 \circ \mathbf{u}_2 \circ \cdots \mathbf{u}_F)(\mathbf{x}_1, \mathbf{x}_2, \cdots, \mathbf{x}_F) = \langle \mathbf{u}_1, \mathbf{x}_1 \rangle_{\mathbb{V}_1} \langle \mathbf{u}_2, \mathbf{x}_2 \rangle_{\mathbb{V}_2} \cdots \langle \mathbf{u}_F, \mathbf{x}_F \rangle_{\mathbb{V}_F}, \quad (1.1)$$

in which $\langle \mathbf{u}_f, \mathbf{x}_f \rangle_{\mathbb{V}_f}$ *is a scalar product in* $\mathbb{V}_f$ *and* $\mathbf{x}_f$ *is an arbitrary vector in* $\mathbb{V}_1$, $f = 1, \cdots, F$. *The space generated by all the elements* $\mathbf{u}_1 \circ \mathbf{u}_2 \circ \cdots \mathbf{u}_F$ *is called the tensor product space of* $\mathbb{V}_1 \times \mathbb{V}_2 \times \cdots \times \mathbb{V}_F$. *A* F*-th order tensor is an element of this tensor product space.*

Demonstration A.2 : (Variance of the channel estimation error) *The channel estimation error* $\mathbf{v}_h \in \mathbb{C}^{2\times 1}$ *is a vector containing the error referent to each channel coefficient. Then,* $\mathbf{v}_h = [v_{h,1} \;\; v_{h,2}]^T$ *and the estimation error variance is calculated for each antenna, such that*

$$\hat{\sigma}^2_{\mathbf{v}_h,k} = E\left\{v^*_{h,k} \cdot v_{h,k}\right\} \quad (1.2)$$

When normal CP is considered, $v_{h,k} = \dfrac{\bar{v}_{2,k} + \bar{v}_{6,k}}{2}$ *and*

$$\hat{\sigma}^2_{\mathbf{v}_h,k} = E\left\{\left(\frac{\bar{v}^*_{2,k} + \bar{v}^*_{6,k}}{2}\right)\left(\frac{\bar{v}_{2,k} + \bar{v}_{6,k}}{2}\right)\right\} \quad (1.3)$$

$$\hat{\sigma}^2_{\mathbf{v}_h,k} = \frac{1}{4}\left[E\left\{|\bar{v}_{2,k}|^2\right\} + E\left\{|\bar{v}_{6,k}|^2\right\} + E\left\{\bar{v}^*_{2,k}\bar{v}_{6,k}\right\} + E\left\{\bar{v}^*_{6,k}\bar{v}_{2,k}\right\}\right]. \quad (1.4)$$

The first term can be calculated as follows:

$$E\left\{|\bar{v}_{2,k}|^2\right\} = E\left\{\sum_{p=1}^{12}\frac{w_p^* v_{2,p,k}}{12}\sum_{q=1}^{12}\frac{w_q v_{2,q,k}^*}{12}\right\} = \sum_{p=1}^{12}\sum_{q=1}^{12}\frac{w_p^* w_q E\left\{v_{2,p,k}v_{2,q,k}^*\right\}}{12\times 12}. \quad (1.5)$$

As the noise is uncorrelated over the 12 subcarriers,

$$E\left\{|\bar{v}_{2,k}|^2\right\} = \sum_{p=1}^{12}\sum_{q=1}^{12}\frac{w_p^* w_q \sigma_{V,k}^2}{12\times 12}\delta(p-q), \quad (1.6)$$

$$E\left\{|\bar{v}_{2,k}|^2\right\} = \sum_{p=1}^{12}\frac{|w_p|^2\sigma_{V,k}^2}{12\times 12} \quad (1.7)$$

$$E\left\{|\bar{v}_{2,k}|^2\right\} = \frac{12\times\sigma_{V,k}^2}{12\times 12} \quad (1.8)$$

and finally,

$$E\left\{|\bar{v}_{2,k}|^2\right\} = \frac{\sigma_{V,k}^2}{12}. \quad (1.9)$$

The second term can be calculated using the same idea, and:

$$E\left\{|\bar{v}_{6,k}|^2\right\} = \frac{\sigma_{V,k}^2}{12}. \quad (1.10)$$

The cross-correlation terms can be calculated as:

$$E\left\{\bar{v}_{2,k}^*\bar{v}_{6,k}\right\} = E\left\{\sum_{p=1}^{12}\frac{w_p v_{2,p,k}^*}{12}\sum_{q=1}^{12}\frac{w_q^* v_{6,q,k}}{12}\right\} = \sum_{p=1}^{12}\sum_{q=1}^{12}\frac{w_p w_q^*}{12\times 12}E\left\{v_{2,p,k}^* v_{6,q,k}\right\} = 0 \quad (1.11)$$

as the noise is uncorrelated over all the SC-OFDM symbols. In the same sense, $E\left\{\bar{v}_{6,k}^*\bar{v}_{2,k}\right\} = 0$.

Therefor, the variance of the channel estimation error per antenna is given by:

$$\sigma_{\mathbf{v}_h,k}^2 = \frac{1}{4}\left[\frac{\sigma_{V,k}^2}{12} + \frac{\sigma_{V,k}^2}{12} + 0 + 0\right] \quad (1.12)$$

$$\sigma_{\mathbf{v}_h,k}^2 = \frac{\sigma_{V,k}^2}{24}. \quad (1.13)$$

This result can be easialy extended for a general case, where N_{RS} *SC-OFDM sym-*

bols are being used as reference signals (or pilots) and,

$$\sigma^2_{\mathbf{v}_h,k} = \frac{\sigma^2_{V,k}}{N_{RS} \times 12}. \tag{1.14}$$

Demonstration A.3 : (Convergence of the RS-based noise variance estimator) Considering normal CP, the noise variance estimator for each receive antenna is given by

$$\hat{\sigma}^2_{V,k} = \frac{\left(\frac{\sum_{p=1}^{12} |e_{2,p,k}|^2}{12}\right) + \left(\frac{\sum_{p=1}^{12} |e_{6,p,k}|^2}{12}\right)}{2}. \tag{1.15}$$

then,

$$E\left\{\hat{\sigma}^2_{V,k}\right\} = \frac{1}{2}\left[\frac{1}{12}\sum_{p=1}^{12} E\left\{|e_{2,p,k}|^2\right\} + \frac{1}{12}\sum_{p=1}^{12} E\left\{|e_{6,p,k}|^2\right\}\right] \tag{1.16}$$

where

$$|e_{n,p,k}|^2 = (v_{n,p,k} - w_p v_{h,k})(v^*_{n,p,k} - w^*_p v^*_{h,k}) \tag{1.17}$$

$$= |v_{n,p,k}|^2 + |w_p|^2|v_{h,k}|^2 - w_p v_{h,k} v^*_{n,p,k} - w^*_p v^*_{h,k} v_{n,p,k}. \tag{1.18}$$

Therefor,

$$E\left\{|e_{n,p,k}|^2\right\} = E\left\{|v_{n,p,k}|^2\right\} + |w_p|^2 E\left\{|v_{h,k}|^2\right\} - w_p E\left\{v_{h,k} v^*_{n,p,k}\right\} - w^*_p E\left\{v^*_{h,k} v_{n,p,k}\right\}. \tag{1.19}$$

Observe that

$$E\left\{|e_{n,p,k}|^2\right\} = \sigma^2_{V,k} + |w_p|^2 \sigma^2_{\mathbf{v}_h,k} - w_p E\left\{v_{h,k} v^*_{n,p,k}\right\} - w^*_p E\left\{v^*_{h,k} v_{n,p,k}\right\} \tag{1.20}$$

and the expected value of this noise variance is given by the true value of the noise variance plus the noise variance from channel estimation error minus 2 times the correlation between the true noise and the channel estimation error.

Assuming the result from demonstration **A.2**,

$$E\left\{|e_{n,p,k}|^2\right\} = \sigma^2_{V,k} + \frac{\sigma^2_{V,k}}{24} - w_p E\left\{v_{h,k} v^*_{n,p,k}\right\} - w^*_p E\left\{v^*_{h,k} v_{n,p,k}\right\}. \tag{1.21}$$

The cross-correlation in the previous equation is calculated as follows:

$$E\left\{v_{h,k}v^*_{n,p,k}\right\} = E\left\{\left(\frac{\bar{v}_{2,k}+\bar{v}_{6,k}}{2}\right)v^*_{n,p,k}\right\} = \frac{1}{2}E\left\{\bar{v}_{2,k}v^*_{n,p,k}\right\} + \frac{1}{2}E\left\{\bar{v}_{6,k}v^*_{n,p,k}\right\}. \tag{1.22}$$

As the noise is uncorrelated over the 7 SC-OFDM symbols,

$$E\left\{v_{h,k}v^*_{n,p,k}\right\} = \frac{1}{2}E\left\{\bar{v}_{n,k}v^*_{n,p,k}\right\} \tag{1.23}$$

$$= \frac{1}{2}E\left\{\left(\frac{\sum_{q=1}^{12} w^*_q v_{n,q,k}}{12}\right)v^*_{n,p,k}\right\} \tag{1.24}$$

$$= \sum_{q=1}^{12}\frac{w^*_q}{2\times 12}E\left\{v_{n,q,k}v^*_{n,p,k}\right\} \tag{1.25}$$

and also uncorrelated over the 12 subcarriers,

$$E\left\{v_{h,k}v^*_{n,p,k}\right\} = \sum_{q=1}^{12}\frac{w^*_q}{2\times 12}\sigma^2_{V,k}\delta(p-q) \tag{1.26}$$

Back to Eq,(0.109),

$$E\left\{|e_{n,p,k}|^2\right\} = \sigma^2_{V,k} + \frac{\sigma^2_{V,k}}{24} - w_p\sum_{q=1}^{12}\frac{w^*_q}{2\times 12}\sigma^2_{V,k}\cdot\delta(p-q) - w^*_p\sum_{q=1}^{12}\frac{w_q}{2\times 12}\sigma^2_{V,k}\cdot\delta(p-q). \tag{1.27}$$

and averaging over the 12 subcarriers:

$$\frac{\sum_{p=1}^{12}E\left\{|e_{n,p,k}|^2\right\}}{12} = \sigma^2_{V,k} + \frac{\sigma^2_{V,k}}{24} - 2\times\sum_{p=1}^{12}\frac{|w_p|^2}{2\times 12\times 12}\sigma^2_{V,k} \tag{1.28}$$

$$= \sigma^2_{V,k} + \frac{\sigma^2_{V,k}}{24} - 2\times\frac{\sigma^2_{V,k}}{24} \tag{1.29}$$

$$= \sigma^2_{V,k} - \frac{\sigma^2_{V,k}}{24} = \frac{24-1}{24}\sigma^2_{V,k} \tag{1.30}$$

$$= \frac{23}{24}\sigma^2_{V,k}. \tag{1.31}$$

Therefor, the RS-based noise variance estimator converges in average to:

$$E\left\{\hat{\sigma}^2_{V,k}\right\} = \frac{23}{24}\sigma^2_{V,k} \tag{1.32}$$

This demonstration can be easealy extended to the case where N_{RS} are used as reference signals. In this general case, the estimator converges to:

$$E\left\{\hat{\sigma}^2_{V,k}\right\} = \frac{N_{RS} \times 12 - 1}{N_{RS} \times 12}\sigma^2_{V,k} \tag{1.33}$$

and in the extended CP transmission, $N_{RS} = 1$ and

$$E\left\{\hat{\sigma}^2_{V,k}\right\} = \frac{11}{12}\sigma^2_{V,k} \tag{1.34}$$

Demonstration A.4: (Convergence of the RS-based noise variance estimator for multiples UEs) Consider the case where R UEs are transmitting on PUCCH format 2, considering the extended CP. Considering that the estimated noise matrix is given by $\hat{\mathbf{E}} = \mathbf{Y}_1 - \hat{\mathbf{X}}_1$, where only the part referent to the reference signals is taken, such that each element is given by:

$$\hat{e}_{4,p,k} = v_{4,p,k} - \sum_{r=1}^{R} \bar{v}^{(r)}_{4,k} \cdot w^{(r)}_p \tag{1.35}$$

and the estimated noise power:

$$|\hat{e}_{4,p,k}|^2 = \left(v^*_{4,p,k} - \sum_{r=1}^{R} \bar{v}^{(r)*}_{4,k} w^{(r)*}_p\right)\left(v_{4,p,k} - \sum_{r=1}^{R} \bar{v}^{(r)}_{4,k} w^{(r)}_p\right) \tag{1.36}$$

$$= |v_{4,p,k}|^2 - v^*_{4,p,k} \cdot \sum_{r=1}^{R} \bar{v}^{(r)}_{4,k} w^{(r)}_p - v_{4,p,k} \sum_{r=1}^{R} \bar{v}^{(r)*}_{4,k} w^{(r)*}_p \tag{1.37}$$

$$+ \sum_{r=1}^{R} \bar{v}^{(r)*}_{4,k} w^{(r)*}_p \sum_{r=1}^{R} \bar{v}^{(r)}_{4,k} w^{(r)}_p = |v_{4,p,k}|^2 - \textcircled{i} - \textcircled{ii} + \textcircled{iii} \tag{1.38}$$

The expected value of this estimator can be denoted as:

$$E\left\{|\hat{e}_{4,p,k}|^2\right\} = \sigma^2_{V,k} - E\left\{\textcircled{i}\right\} - E\left\{\textcircled{ii}\right\} + E\left\{\textcircled{iii}\right\} \tag{1.39}$$

such that:

$$\textcircled{1} = v^*_{4,p,k} \cdot \sum_{r=1}^{R} \bar{v}^{(r)}_{4,k} w^{(r)}_p = v^*_{4,p,k} \cdot \sum_{r=1}^{R} \left(\sum_{q=1}^{12} \frac{w^{(r)*}_q v_{4,q,k}}{12} \right) w^{(r)}_p \tag{1.40}$$

$$E\left\{\textcircled{1}\right\} = \sum_{r=1}^{R} \sum_{q=1}^{12} \frac{w^{(r)*}_q w^{(r)}_p}{12} E\left\{ v^*_{4,p,k} v_{4,q,k} \right\} \tag{1.41}$$

$$= \sum_{r=1}^{R} \sum_{q=1}^{12} \frac{w^{(r)*}_q w^{(r)}_p}{12} \sigma^2_{V,k} \delta(p-q) \tag{1.42}$$

$$= E\left\{\textcircled{ii}\right\}. \tag{1.43}$$

and

$$\textcircled{iii} = \sum_{r=1}^{R} \bar{v}^{(r)*}_{4,k} w^{(r)*}_p \sum_{r=1}^{R} \bar{v}^{(r)}_{4,k} w^{(r)}_p = \sum_{r=1}^{R} \sum_{m=1}^{R} w^{(r)*}_p w^{(m)}_p \bar{v}^{(r)*}_{4,k} \bar{v}^{(m)}_{4,k} \tag{1.44}$$

such that:

$$E\left\{\textcircled{iii}\right\} = \sum_{r=1}^{R} \sum_{m=1}^{R} w^{(r)*}_p w^{(m)}_p E\left\{ \bar{v}^{(r)*}_{4,k} \bar{v}^{(m)}_{4,k} \right\} \tag{1.45}$$

$$= \sum_{r=1}^{R} \sum_{m=1}^{R} w^{(r)*}_p w^{(m)}_p \left(\sum_{q=1}^{12} \frac{w^{(r)}_q w^{(m)*}_q}{12 \times 12} \sigma^2_{V,k} \right) \tag{1.46}$$

$$= \sum_{r=1}^{R} \sum_{m=1}^{R} \sum_{q=1}^{12} \frac{w^{(r)*}_p w^{(m)}_p w^{(r)}_q w^{(m)*}_q}{12 \times 12} \sigma^2_{V,k}. \tag{1.47}$$

As the sequences referent to different UEs are orthogonal,

$$E\{\textcircled{iii}\} = \sum_{r=1}^{R}\sum_{m=1}^{R}\sum_{q=1}^{12}\frac{w_p^{(r)*}w_p^{(m)}w_q^{(r)}w_q^{(m)*}}{12\times 12}\sigma_{V,k}^2\delta(m-r) \tag{1.48}$$

$$= \sum_{r=1}^{R}\sum_{q=1}^{12}\frac{|w_p^{(r)}|^2|w_q^{(r)}|^2}{12\times 12}\sigma_{V,k}^2 \tag{1.49}$$

$$= \sum_{r=1}^{R}\frac{|w_p^{(r)}|^2\times 12}{12\times 12}\sigma_{V,k}^2 \tag{1.50}$$

$$= \sum_{r=1}^{R}\frac{1}{12}\sigma_{V,k}^2 \tag{1.51}$$

$$= \frac{R}{12}\sigma_{V,k}^2. \tag{1.52}$$

Back to Eq.(0.149),

$$E\left\{|e_{4,p,k}|^2\right\} = \sigma_{V,k}^2 - 2\times\sum_{r=1}^{R}\sum_{q=1}^{12}\frac{w_q^{(r)*}w_p^{(r)}}{12}\sigma_{V,k}^2\delta(p-q) + \frac{R}{12}\sigma_{V,k}^2. \tag{1.53}$$

Averaging this equation over the 12 subcarriers,

$$\sum_{p=1}^{12}\frac{E\left\{|e_{4,p,k}|^2\right\}}{12} = \sigma_{V,k}^2 - 2\times\sum_{r=1}^{R}\sum_{q=1}^{12}\sum_{p=1}^{12}\frac{w_q^{(r)*}w_p^{(r)}}{12}\sigma_{V,k}^2\delta(p-q) + \frac{R}{12}\sigma_{V,k}^2 \tag{1.54}$$

$$= \sigma_{V,k}^2 - 2\times\sum_{r=1}^{R}\sum_{p=1}^{12}\frac{|w_p^{(r)}|^2}{12\times 12}\sigma_{V,k}^2 + \frac{R}{12}\sigma_{V,k}^2 \tag{1.55}$$

$$= \sigma_{V,k}^2 - 2\times\frac{R}{12}\sigma_{V,k}^2 + \frac{R}{12}\sigma_{V,k}^2. \tag{1.56}$$

Finally, the noise variance estimator, considering extended CP, converges to the value:

$$E\left\{\hat{\sigma}_{V,k}^2\right\} = \left(\frac{12-R}{12}\right)\sigma_{V,k}^2. \tag{1.57}$$

This result can be easealy generalized to the case with N_{RS} symbols are used as reference signals, such that:

$$E\left\{\hat{\sigma}_{V,k}^2\right\} = \left(\frac{12\times N_{RS}-R}{12\times N_{RS}}\right)\sigma_{V,k}^2. \tag{1.58}$$

Therefor, in the case of normal CP, where $N_{RS} = 2$, this estimator converges to $E\left\{\hat{\sigma}^2_{V,k}\right\} = (24 - R)/24\sigma^2_{V,k}$.

Demonstration A.5: (Case study 1: Improved channel estimator) Consider the case where 2 UEs using non-orthogonal coding vectors are transmitting on PUCCH Format 2. Asumme that both terminals are configured with normal CP. From (3.105), the channel estimation error for an improved channel estimation at the end of the first iteration is given by:

$$\mathbf{e}_h = \frac{1}{1 - |\kappa|^2}\left(\mathbf{v}_h^{(1)} - \kappa v_h^{(2)}\right) \tag{1.59}$$

such that for each receive antenna we have:

$$e_{h_k} = \frac{1}{1 - |\kappa|^2}\left(v_{h_k}^{(1)} - \kappa v_{h_k}^{(2)}\right). \tag{1.60}$$

Thus,

$$\sigma^2_{e_{h_k}} = E\left\{|e_{h_k}|^2\right\} = \left(\frac{1}{1 - |\kappa|^2}\right)^2 E\left\{\left(v_{h_k}^{(1)} - \kappa v_{h_k}^{(2)}\right)\left(v_{h_k}^{(1)*} - \kappa^* v_{h_k}^{(2)*}\right)\right\} \tag{1.61}$$

$$= \left(\frac{1}{1 - |\kappa|^2}\right)^2 \left[E\left\{|v_{h_k}^{(1)}|^2\right\} + |\kappa|^2 |E\left\{|v_{h_k}^{(2)}|^2\right\} - \kappa E\left\{\textcircled{i}\right\} - \kappa^* E\left\{\textcircled{ii}\right\}\right] \tag{1.62}$$

where

$$E\left\{\textcircled{i}\right\} = E\left\{v_{h_k}^{(2)} v_{h_k}^{(1)*}\right\} = \kappa^* \sigma^2_{v_{h_k}} \text{ and } E\left\{\textcircled{ii}\right\} = E\left\{v_{h_k}^{(1)} v_{h_k}^{(2)*}\right\} = \kappa \sigma^2_{v_{h_k}}. \tag{1.63}$$

Hence,

$$\sigma^2_{e_{h_k}} = \left(\frac{1}{1 - |\kappa|^2}\right)^2 \left[\sigma^2_{v_{h_k}} + |\kappa|^2 \sigma^2_{v_{h_k}} - 2|\kappa|^2 \sigma^2_{v_{h_k}}\right] \tag{1.64}$$

$$= \left(\frac{1}{1 - |\kappa|^2}\right) \sigma^2_{v_{h_k}} \tag{1.65}$$

$$= \left(\frac{1}{1 - |\kappa|^2}\right) \frac{\sigma^2_{V,k}}{12 \times N_{RS}}. \tag{1.66}$$

Demonstration A.6: (Case study 1: conventional channel estimator) Consider the case where 2 UEs using non-orthogonal coding vectors are transmitting on

PUCCH Format 2. Asumme that both terminals are configured with normal CP. From (3.98), the channel estimation error is given by:

$$\mathbf{e}_h = \mathbf{v}_h^{(1)} - \kappa \mathbf{h}^{(2)}. \tag{1.67}$$

such that for each receive antenna we have:

$$e_{h_k} = v_{h_k} - \kappa h_k^{(2)}. \tag{1.68}$$

Thus,

$$\sigma^2_{e_{h_k}} = E\left\{|e_{h_k}|^2\right\} = E\left\{\left(v_{h_k} - \kappa h_k^{(2)}\right)\left(v_{h_k}^* - \kappa^* h_k^{(2)*}\right)\right\} \tag{1.69}$$

$$= E\left\{|v_{h_k}|^2\right\} + |\kappa|^2|h_k^{(2)}|^2 - \kappa^* h_k^{(2)*} E\left\{v_{h_k}\right\} + \kappa h_k^{(2)} E\left\{v_{h_k}^*\right\} \tag{1.70}$$

$$= \sigma^2_{v_{h_k}} + |\kappa|^2|h_k^{(2)}|^2 \tag{1.71}$$

$$= \frac{\sigma^2_{V,k}}{12 \times N_{RS}} + |\kappa|^2|h_k^{(2)}|^2 \tag{1.72}$$

Bibliography

[1] E. Dahlman, S. Parkvall, J. Skold, and P. Beming, *3G Evolution: HSPA and LTE for Mobile Braodband, 2nd Ed.* Oxford, UK: Elsevier, 2008.

[2] S. Sesia, I. Toufik, and M. Baker, *LTE: The UMTS Long Term Evolution - From theory to practice.* U.S.: Wiley and Sons, 2009.

[3] 3rd Generation Partnership Project (3GPP); Evolved UTRAN (E-UTRAN); Physical Channels and M. R. 8) *Technical Specification Group Radio Access Network (TSG RAN)*, vol. 3GPP TR 36.211, Dec 2008.

[4] I. L. J. Silva, A. L. F. Almeida, C. F. R. P., and G. Favier, *Optimizing Wireless Communication Systems (Chapter 12: MIMO Transceiver Design for Enhanced Performance Under Limited Feedback).* U.S.: Springer, 2009.

[5] N. D. Sidiropoulos, G. B. Giannakis, and R. Bro, "Blind PARAFAC receivers for DS-CDMA systems," *IEEE Trans. Signal Process.*, vol. 48, pp. 810–822, March 2000.

[6] P. Comon, "Tensor decompositions: State of the art and applications," in *IMA Conf. Mathematics in Signal Process.*, (Warwick, UK), Dec. 18-20 2000.

[7] G. Strang, *Linear Algebra and Its Applications, 4-th Ed.* USA: BrooksCole, 2005.

[8] R. A. Harshman, "Foundations of the PARAFAC procedure: Model and conditions for an "explanatory" multi-mode factor analysis," *UCLA Working Papers in Phonetics*, vol. 16, pp. 1–84, Dec. 1970.

[9] J. Proakis, *Digital Communications*. New York, USA: McGraw-Hill, 2001.

[10] A. Stegeman and N. D. Sidiropoulos, "On Kruskal's uniqueness condition for the Candecomp/Parafac decomposition," *Lin. Alg. Appl.*, vol. 420, pp. 540–552, 2007.

[11] E. Acar and B. Yener, "Unsupervised multiway data analysis: A literature survey," *IEEE Trans. on Knowledge and Data Engineering*, vol. 21, no. 1, pp. 6–20, 2009.

[12] L. De Lathauwer, "A multilinear singular value decomposition," *SIAM J. Matrix Anal. Appl.*, vol. 21, no. 4, pp. 1253–1278, 2000.

[13] L. De Lathauwer, "The decomposition of a tensor in a sum of rank-(R_1, R_2, R_3) terms," in *Workshop on Tensor Decompositions and Applications*, (Marseille, France), 2005.

[14] L. De Lathauwer, "A link between the Canonical Decomposition in multilinear algebra and simultaneous matrix diagonalization," *SIAM J. Matrix Anal. Appl.*, to appear, 2007.

[15] M. Rajih and P. Comon, "Enhanced line search: A novel method to accelerate PARAFAC," in *Proc. EUSIPCO*, (Antalya, Turkey), Sep. 2005.

[16] A. L. F. de Almeida, G. Favier, and J. C. M. Mota, "PARAFAC receiver for blind multiuser equalization in wireless communication systems with temporal oversampling," in *European Signal Processing Conference (EUSIPCO)*, (Antalya, Turkey), September 4-8 2005.

[17] A. L. F. de Almeida, G. Favier, and J. C. M. Mota, "Blind multiuser equalization using a PARAFAC-subspace approach," in *GRETSI Symposium on Signal and Image Processing*, (Louvain-la-Neuve, Belgium), September 2005.

[18] A. L. F. de Almeida, G. Favier, and J. C. M. Mota, *An Application of Tensor Modeling to Blind Multiuser Equalization*. IEE-SIAM Workshop on Tensor Decompositions and Applications, Luminy, France, August 2005.

[19] A. de Baynast, L. De Lathauwer, and B. Aazhang, "Blind PARAFAC receivers for multiple access-multiple antenna systems," in *Proc. VTC Fall*, (Orlando, USA), Oct. 2003.

[20] L. De Lathauwer and J. Castaing, "Tensor-based techniques for the blind separation of DS-CDMA signals," *Signal Processing*, vol. 87, no. 2, pp. 322–336, 2007.

[21] T. Jiang and N. D. Sidiropoulos, "Blind identification of out-of-cell users in DS-CDMA," *EURASIP J. on Applied Signal Process.*, vol. 9, pp. 1212–1224, Aug. 2004.

[22] N. D. Sidiropoulos and G. Z. Dimic, "Blind multiuser detection in WCDMA systems with large delay spread," *IEEE Signal Process. Lett.*, vol. 8, pp. 87–89, Mar. 2001.

[23] N. D. Sidiropoulos and X. Liu, "Identifiability results for blind beamforming in incoherent multipath with small delay spread," *IEEE Trans. Signal Process.*, vol. 49, pp. 228–236, Jan. 2001.

[24] D. Nion and L. De Lathauwer, "Levenberg-marquadt computation of the block factor model for blind multi-user access in wireless communications," in *European Signal Processing Conference (EUSIPCO)*, (Florence, Italy), September 4-8 2006.

[25] B. Sklar, "Rayleigh fading channel in mobile digital communication systems. Part II: Mitigation," *IEEE Comm. Magazine*, vol. 49, pp. 148–155, Sep. 1997.

[26] G. Bottomley, T. Ottosson, and Y. P. E. Wang, "A generalized RAKE receiver for interference suppression," *IEEE Journal on Select. Areas in Comm.*, vol. 18, pp. 1536–1545, Aug. 2000.

[27] L. Hanzo, M. Munster, B. J. Choi, and T. Keller, *OFDM and MC-CDMA for Broadband Multi-User Communications, WLANs and Broadcasting*. IEEE Communicatios Society, Wiley, 2003.

[28] 3rd Generation Partnership Project (3GPP); Evolved Universal Terrestrial Radio Access (E-UTRA) and E. U. T. R. A. N. E.-U. O. description; (Release 8) *Technical Specification Group Radio Access Network (TSG RAN)*, vol. 3GPP TS 36.300, Dec 2007.

[29] C. Muschallik, "High-resolution, localization and tracking of multiple frequency hopped signals," *IEEE transactions on consumer electronics*, vol. 41, no. 3, pp. 592–603, 1995.

[30] H. Sari, G. Karam, and I. Jeanclaude, "Channel equalization and synchronization in ofdm systems," in *International Tirrenia Workshop on Digital Communications*, (Pisa, Italy), September 1993.

[31] H. G. Myung, J. Lim, and D. J. Goodman, "Single carrier fdma for uplink wireless transmission," *IEEE Vehicular Tech. Magazine*, vol. 1, pp. 30–38, September 2006.

[32] H. Sari, G. Karam, and I. Jeanclaude, "Transmission techniques for digital terrestrial tv broadcasting," *IEEE Communications Magazine*, vol. 4, pp. 100–109, February 1995.

[33] D. C. Chu, "Polyphase codes with good periodic correlation properties," *IEEE Trans. on Inf. Theory*, vol. 18, no. 4, pp. 531–532, 1972.

[34] 3rd Generation Partnership Project (3GPP); Evolved UTRAN (E-UTRAN); Physical layer procedures (Release 8) *Technical Specification Group Radio Access Network (TSG RAN)*, vol. 3GPP TR 36.213, Dec 2008.

[35] 3rd Generation Partnership Project (3GPP); Evolved UTRAN (E-UTRAN); Multiplexing and channel coding (Release 8) *Technical Specification Group Radio Access Network (TSG RAN)*, vol. 3GPP TR 36.212, Jul 2008.

[36] A. Goldsmith, *Wireless Communications*. Cambridge University Press, 2005.

[37] S. Lin and D. Costello, *Error Control Coding*. Upper Saddle River, NJ, USA: Prentice-Hall, 2005.

[38] J. M. Wozencraft and M. Horstein, "Digitalised communication over two-way channels," in *Fouth London Symp. on Inf. Theory*, (London, UK), Sep 1960.

[39] D. Tse and P. Viswanath, *Fundamentals of Wireless Communications*. New York, USA: Cambridge, 2005.

[40] A. Paulraj, R. Nabar, and D. Gore, *Introduction to Space-Time Wireless Communications*. Cambridge, UK: Cambridge University Press, 2003.

[41] 3rd Generation Partnership Project (3GPP); Evolved Universal Terrestrial Radio Access (E-UTRAN); User Equipment (UE) radio transmission and reception (Release 8), "(release 8)," *Technical Specification Group Radio Access Network (TSG RAN)*, vol. 3GPP TR 36.101, December 2008.

[42] R. Bro, *Multi-way analysis in the food industry: Models, algorithms and applications*. PhD thesis, University of Amsterdam, Amsterdam, 1998.

[43] K. S. Hoher, P. and and P. Robertson, "Pilot-symbol-aided channel estimation in time and frequency," in *in Proc. of IEEE Global Telecommun. Conf. (Globecom)*, (Phoenix, USA), July 1997.

[44] M. Chang and Y. Su, "Blind and semiblind detections of ofdm signals in fading channels," *IEEE Trans. on Communications*, vol. 52, pp. 744–754, May 2004.

[45] T. Cui and C. Tellambura, "Semiblind channel estimation and data detection for ofdm systems with optimal pilot design," *IEEE Trans. on Communications*, vol. 55, pp. 1053–1062, May 2007.

[46] H. Yang, D. Astely, R. Baldemair, and S. Falahati, "Semi-blind multi-user detection for lte pucch," in *Proc. IEEE Wireless Communications and Networking Conference*, (Budapest, Hungary), April 2009.

[47] Samsung, "Selection of orthogonal cover and cyclic shift for high speed ul ack channels," in *Technical Specification Group Radio Access Network (TSG RAN), R1-073564*, August 2007.

Livros Grátis

(http://www.livrosgratis.com.br)

Milhares de Livros para Download:

Baixar livros de Literatura
Baixar livros de Literatura de Cordel
Baixar livros de Literatura Infantil
Baixar livros de Matemática
Baixar livros de Medicina
Baixar livros de Medicina Veterinária
Baixar livros de Meio Ambiente
Baixar livros de Meteorologia
Baixar Monografias e TCC
Baixar livros Multidisciplinar
Baixar livros de Música
Baixar livros de Psicologia
Baixar livros de Química
Baixar livros de Saúde Coletiva
Baixar livros de Serviço Social
Baixar livros de Sociologia
Baixar livros de Teologia
Baixar livros de Trabalho
Baixar livros de Turismo